



Title	<b>Formation of novel biological patterns by controlling cell motility</b>
Advisor(s)	Huang, J; Zhou, Z
Author(s)	Liu, Chenli.; 刘陈立.
Citation	Liu, C. [刘陈立]. (2011). Formation of novel biological patterns by controlling cell motility. (Thesis). University of Hong Kong, Pokfulam, Hong Kong SAR. Retrieved from <a href="http://dx.doi.org/10.5353/th_b4654191">http://dx.doi.org/10.5353/th_b4654191</a>
Issued Date	2011
URL	<a href="http://hdl.handle.net/10722/142016">http://hdl.handle.net/10722/142016</a>
Rights	The author retains all proprietary rights, (such as patent rights) and the right to use in future works.

Abstract of thesis entitled

# **Formation of novel biological patterns by controlling cell motility**

Submitted by

**LIU Chenli**

for the Degree of Doctor of Philosophy  
at The University of Hong Kong  
in August 2011

Pattern formation is one of the most common yet fascinating phenomena in biological world. How do highly ordered patterns arise from a few genetically identical cells? For centuries, scientists have struggled to find the answers. Although advances had been made, the underlying mechanisms of pattern formation remain incompletely understood. The emerging synthetic biology offers us a new way to not only examine current concepts of pattern formations, but also create new ones. Many biological patterns are represented by spatially heterogeneous distribution of cells or gene expression. In these patterning processes, cell movement is often involved. The motility is a fascinating feature of living cells. Cell movement can be controlled according to many cues. If there exists a defined interaction between cell density and cell motility, how this interaction may influence and shape the formation of biological patterns would be an interesting question to ask.

In this study, I rewired genetic circuits in *Escherichia coli* cells so that the local cell density can, through a cell-cell communication module, regulate CheZ gene, a chemotaxis regulator controlling cell tumbling frequency, therefore cell movement. These engineered cells with their movement negatively coupled their local density, if seeded onto a semi-solid agar plate, they grow, spread outwards and sequentially form a self-organized stripe pattern. I quantitatively characterized the pattern, including the geometry and dynamic process, and also identified the critical aspects of the engineered genetic circuit that influence the formation of the pattern.

To better understand the principle underlying the pattern formation by the engineered

cells, a theoretical model was developed in collaboration with phycisits. We identify the mechanism for the pattern formation. It is well consistent with experimental results. More importantly, the model predicts that quantitatively modulations of the density-dependency lead to variation in the number of repetitive elements formed. I validated these predictions by introducing an additional tunable circuitry.

Since the CheZ-cell motility exhibit a bell-shaped relation in soft agar, different from the monotonic relation in liquid media, the alternative design that cell density positively regulates CheZ give rise to a more compacting stripe pattern, which confirmed the findings from our combined experimental and theoretical studies.

Since the quantitative measurement in semi-solid agar was unique and there were no available methods, I developed novel techniques to quantify macroscopic parameters such as cell density, growth, and motility in semi-solid agar plate. Their relation with genetic alternation and the geometry and dynamics of pattern forms have also been systematically studied.

This study provides a new mechanism to develop patterns from a population of genetically identical cells. It will help us understand principles of the natural pattern formation process. The knowledge gleaned here may be applied in various fields like biomaterial fabrication, tissue engineering, and biosensing.

In addition, I included my two other works in this thesis. They are “Salvianolic acid B inhibits hydrogen peroxide-induced endothelial cell apoptosis through regulating PI3K/Akt signaling”, and “cell death caused by single-stranded oligodeoxynucleotide-mediated targeted genomic sequence modification”.

(An abstract of 487 words)

# **Formation of novel biological patterns by controlling cell motility**

BY

**LIU Chenli**

(劉陳立)

B.Sc (BIO, Xiamen University)

M.Sc (BCH, Xiamen University)

A thesis submitted in partial fulfillment of the requirements for  
the Degree of Doctor of Philosophy  
at The University of Hong Kong

August 2011

## **Declaration**

I hereby declare that this thesis represents my own work, except where due acknowledgement is made, and that it has not been previously included in a thesis, dissertation or report submitted to this University or to any other institution for a degree, diploma or other qualification.

*Signed* .....

LIU Chenli

## **ACKNOWLEDGEMENTS**

I am deeply indebted to my supervisor, Dr. Jian-Dong Huang for his unwavering support and guidance, for providing me opportunities to experience different scientific fields, for creating a wonderful and free environment for me to work and try ideas. I am very grateful to Prof. Terence Hwa for introducing me to the world of quantitative biology, for his inspiration to begin this work, for his patient and unique supervision. Thanks must also go to Dr. Wei Huang for intensive discussion, valuable suggestions, and taking time to revise this thesis. Thanks to my co-supervisor, Dr. Zhongjun Zhou for his kind support, for allowing me freely using equipments in his lab. Thanks also go to Mr. Xiongfei Fu for his help in the theoretical analysis of this work.

Special thanks to Dr. Michael S.Y. Huen for evaluable feedback and helps in my manuscripts and for his friendship. Thanks to Charles, Baohua, Rory, Xiao Xin, Andrew, Eleine, Gene, Zai, Maggie, Xiao Yan Gu, and Tiffany for their helps and most importantly for their friendship.

I am also grateful to everyone in JD's lab, Yanxiang, Jin Ye, Judy, Bin-Bin, Joseph, Song-Song, Lu Song, Katherine, Jenny, Mei, Shi-Tou, Miao, Shuang, Qian Xie, Phoenix, Lihong, and Xibin for their support and making lots of fun in lab. Thank you to the team members of HKU iGEM 2008 and 2009 team, Xiaojin, Ma Da, Carlos, Lu Xiang, Bosco, Jubi, Alex, Raymond, and Yinan for their help in my projects. I benefit a lot from the interaction with them.

I would like to thank all our collaborators, Dr. Min Li, Prof. Lei-Han Tang, Dr. Peter Lenz, and Dr. Han-Min Shen for providing materials and advice. Thanks also to Dr. Ron Weiss and Dr. Lingchong You for plasmids, to Prof. Josef Jiricny and Prof. Stefan Zeuzem for cell lines.

Most of all, I thank my parents and my girlfriend who have supported and helped me all along. I am indebted to them for their love and understanding

# TABLE OF CONTENTS

Acknowledgements .....	v
Table of Contents.....	vi
List of Figures .....	x
List of Tables .....	xii
Abbreviations and Symbols .....	xiii
<b>Chapter 1 Introduction.....</b>	<b>1</b>
1.1 Periodic biological pattern .....	3
<i>1.1.1 Drosophila segmentation</i> .....	3
1.2 Coordinated cell movement .....	8
<i>1.2.1 Gastrulation</i> .....	8
<i>1.2.2 Bacterial chemotactic patterns</i> .....	9
1.3 Models for periodic pattern .....	10
<i>1.3.1 Reaction-diffusion model</i> .....	10
<i>1.3.2 The clock and wavefront model</i> .....	11
1.4 Numerical constancy .....	11
1.5 Synthetic biology.....	12
<i>1.5.1 Pattern formation with synthetic biology</i> .....	12
1.6 The motility of <i>E. coli</i> .....	13
<i>1.6.1 E. coli</i> .....	13
<i>1.6.2 The motility of E. coli.</i> .....	14
<i>1.6.3 Flagellum structure</i> .....	15
<i>1.6.4 Chemotaxis</i> .....	17
1.7 Cell-cell communication .....	17
<i>1.7.1 Quorum sensing signals</i> .....	18
<i>1.7.2 luxRI system</i> .....	20
<i>1.7.3 QS in synthetic biology</i> .....	21
1.8 Study objectives .....	22
<b>CHAPTER 2 MATERIALS AND METHOD .....</b>	<b>24</b>
2.1 GENERAL METHODS .....	25
<i>2.1.1 Preparation of bacterial genomic DNA</i> .....	25
<i>2.1.2 Isolation of plasmid DNA using QIAprep® Miniprep kit</i> .....	25
<i>2.1.3 Agarose gel electrophoresis</i> .....	25
<i>2.1.4 Restriction endonuclease digestion</i> .....	26
<i>2.1.5 Extraction of DNA fragments from Agarose gel using QIAquick® Gel Extraction Kit</i> .....	26
<i>2.1.6 Preparation of plasmid vector for ligation</i> .....	26
<i>2.1.7 DNA ligation</i> .....	27
<i>2.1.8 Electrocompetent Cells Preparation</i> .....	27
<i>2.1.9 Electroporation of bacterial cells</i> .....	27
<i>2.1.10 DNA Sequencing</i> .....	27
<i>2.1.11 Recombineering</i> .....	28
<i>2.1.12 Colony PCR screening of recombinants</i> .....	28
<i>2.1.13 Cre-mediated removal of antibiotic resistance cassettes</i> .....	28
<i>2.1.14 P1 transduction</i> .....	29
<i>2.1.15 WESTERN BLOT</i> .....	29
2.2 BUFFER SOLUTION.....	30
2.3 BACTERIAL STRAINS AND PLASMIDS .....	32
2.4 BACTERIAL CELL CULTURE .....	32
2.5 QUANTITATIVE REAL-TIME RT-PCR.....	33

2.6 One-dimensional pattern formation .....	34
2.7 Image capturing.....	34
2.8 Fourier analysis of pattern formation .....	35
<b>CHAPTER 3 METHODS DEVELOPMENT.....</b>	<b>39</b>
3.1 Measurement of cell density in semi-solid agar* .....	40
3.2 Measurement of diffusion coefficient in semi-solid agar <sup>s</sup> .....	42
3.2.1 Principal of the CPB method .....	43
3.2.2 Implementation of CPB .....	44
<b>CHAPTER 4 RESULTS.....</b>	<b>50</b>
4.1 Design of the density-dependent motility genetic circuit.....	51
4.2 Construction of <i>cheZ</i> -knockout strain .....	52
4.3 Genetic circuit I.....	54
4.3.1 Construction of genetic circuit I (GC-I) .....	54
4.3.2 Characterization of genetic circuit I (GC-I).....	54
4.3.3 Pattern formation of cells harboring GC-I .....	56
4.3.4 Spatiotemporal dynamics of patterning process of cells harboring Genetic Circuit-I .....	57
4.3.5 Effect of chromosomal lac operon on the pattern formation.....	59
4.3.6 The intact genetic circuit is required for the pattern formation .....	61
4.3.7 Influence of host-encoded QS factors on pattern formation.....	61
4.3.8 Influence of physical factors on pattern formation .....	62
4.3.9 Cell aggregation driven by density-dependent motility.....	67
4.3.10 Theoretical analysis of the patterning process .....	69
4.3.11 Model-guided controlling of stripe number.....	72
4.4 Genetic circuit II .....	74
4.4.1 Relation between <i>cheZ</i> expression level and cell motility in semi-solid agar.....	74
4.4.2 Construction of genetic circuit positively regulating <i>cheZ</i> (GC-II).....	76
4.4.3 Characterization of GC-II.....	76
4.4.4 Pattern formation of GC-II.....	77
4.4.5 The intact genetic circuit is required for the pattern formation .....	79
4.4.6 Effect of QS in host on the pattern forma- tion .....	80
4.4.7 Cell aggregation driven by GC-II .....	80
4.5 "Fuji mount"-like pattern .....	81
4.6 Other attempts .....	83
4.6.1 Replace <i>cheZ</i> by <i>cheY</i> * .....	83
4.6.2 Mutation-based change of stripe wavelength .....	85
<b>CHAPTER 5 DISCUSSION AND PERSPECTIVES .....</b>	<b>88</b>
5.1 Discussion .....	89
5.1.1 Effects of Chemotaxis .....	89
5.1.2 Effects of pH.....	90
5.1.3 Wavelength.....	91
5.1.4 Adaptive mutation.....	92
5.2 Perspectives .....	93
5.2.1 a general pattern formation strategy.....	93
5.2.2 a simple way to change the number of repeats .....	94
5.2.3 implication in developmental biology .....	94
<b>Appendix I Salvianolic Acid B Inhibits Hydrogen Peroxide-Induced Endothelial Cell Apoptosis through Regulating PI3K/Akt Signalig .....</b>	<b>96</b>
<b>1 INTRODUCTION .....</b>	<b>97</b>
1.1 Apoptosis.....	98
1.1.1 Caspases.....	98

<i>1.1.2 Dysregulation of apoptosis</i> .....	98
1.2 Cerebral microvascular endothelial cells (CMECs).....	98
1.3 Apoptosis of CMECs .....	98
1.4 Reactive Oxygen Species (ROS) .....	99
<i>1.4.1. Oxidative stress</i> .....	99
1.5 Salvia miltiorrhiza Bunge (Danshen).....	99
1.6 Salvianolic acid B (Sal B) .....	100
<b>2 MATERIAL AND METHODS.....</b>	<b>102</b>
2.1 reagents .....	103
2.2 MAMMALIAN PRIMARY CELL CULTURE AND DRUG TREATMENT.....	103
2.3 ANALYSIS OF APOPTOSIS .....	104
2.4 DATA ANALYSIS .....	104
<b>3 RESULTS .....</b>	<b>105</b>
3.1 H <sub>2</sub> O <sub>2</sub> -induced apoptosis in rCMECs .....	106
3.2 Effects of Sal B on H <sub>2</sub> O <sub>2</sub> -induced apoptosis in rCMECs .....	106
3.3 Involvement of caspases.....	107
3.4 H <sub>2</sub> O <sub>2</sub> -induced MEK/ERK signaling .....	109
3.5 Effects of Sal B on H <sub>2</sub> O <sub>2</sub> -induced MEK/ERK signaling .....	110
3.6 PI3K/Akt signaling .....	111
3.7 Effects of SalB on PI3K/Akt/Raf/MEK/ERK signaling .....	113
3.8 Effect of Sal B on Bcl-2 Expression.....	114
<b>4 DISCUSSION AND PERSPECTIVES.....</b>	<b>116</b>
4.1 CMECs as a model .....	117
4.2 Caspase activation by H <sub>2</sub> O <sub>2</sub> .....	117
4.3 ERK: pro-survival or pro-apoptosis.....	118
4.4 PI3K/Akt is pro-survival .....	118
4.5 Akt and ERK represented two independent pathways .....	119
4.6 A balance between PI3K/Akt and PI3K/MEK/ ERK.....	119
4.7 Other mechanism (s) .....	120
4.8 Future work .....	121
<i>4.8.1 is Bcl-2 upregulation responsible for the protective and antioxidant effects of Sal B?</i> .....	121
<i>4.8.2 to test whether the rapid up-regulation of Bcl-2 protein is mediated by Akt/CREB pathway in the Sal B-treated rCMECs.</i> .....	123
<b>Appendix II Cell death caused by single-stranded oligodeoxynucleotides mediated targeted genomic sequence modification .....</b>	<b>125</b>
<b>1 INTRODUCTION .....</b>	<b>126</b>
1.1 Proposed mechanisms of ssODN-mediated gene repair .....	127
<i>1.1.1 Direct nucleotide exchange reaction</i> .....	127
<i>1.1.2 Transcription coupled repair</i> .....	127
<i>1.1.3 Replication based model</i> .....	128
1.2 The fate of corrected cells .....	129
1.3 The possible causes .....	129
<i>1.3.1 ssODN?</i> .....	129
<i>1.3.2 Phosphorothioate linkages?</i> .....	129
<i>1.3.3 D-loop?</i> .....	130
<i>1.3.4 DNA mismatch</i> .....	130
1.4 Study objectives .....	131
<b>2 MATERIAL AND METHODS.....</b>	<b>133</b>
2.1 Cell lines.....	134

2.2 Target gene correction assay.....	134
2.3 Clonogenic survival assay .....	134
2.4 Sequencing of genomic DNA.....	134
2.5 Statistical analysis .....	135
<b>3 RESULTS AND DISCUSSION .....</b>	<b>136</b>
3.1 Corrected cells were more prone to undergo apoptosis than uncorrected cells....	137
3.2 The apoptosis of corrected cells was caspase-dependent and ATM/ATR-independent.....	139
3.3 hMLH1-deficiency increased gene correction efficiency, but not affected the viability of corrected cells .....	140
3.4 Cadmium treatment did not affect the viability of corrected cells.....	142
<b>References .....</b>	<b>145</b>
<b>Publications .....</b>	<b>157</b>

# LIST OF FIGURES

FIGURE 1-1 FASCINATING BIOLOGICAL PATTERNS IN NATURE.....	2
FIGURE 1-2 <i>DROSOPHILA MELANOGASTER</i> SEGMENTATION.....	4
FIGURE 1-3 SEGMENTATION CLOCK OSCILLATOR.....	5
FIGURE 1-4 SYNCHRONIZATION OF THE PSM CELLULAR OSCILLATORS.....	6
FIGURE 1-5 MODEL OF SEGMENTATION IN MOUSE VERTEBRATES.....	8
FIGURE 1-6 SCHEME OF THE FORMATION OF A TURING PATTERN.....	11
FIGURE 1-7 SWIMMING AND TUMBING MOTIONS OF <i>E. COLI</i> .....	14
FIGURE 1-8 MODULATION OF FLAGELLAR ROTATION.....	15
FIGURE 1-9 <i>E. COLI</i> FLAGELLAR STRUCTURE.....	16
FIGURE 1-10 STRUCTURE AND FORMATION OF DPD.....	19
FIGURE 1-11 STRUCTURES OF AHLs.....	20
FIGURE 1-12 FORMATION OF 3-OXO-C6-HSL CATALYZED BY LUXI .....	21
FIGURE 3-1 THE SETUP OF THE CUSTOMIZED DEVICE FOR THE REAL-TIME MEASUREMENT OF THE SPATIOTEMPORAL CELL DENSITY PROFILE IN SEMI-SOLID AGAR DISHES.....	40
FIGURE 3-2 THE CALIBRATION CURVE OF LIGHT TRANSMITTANCE VS. REAL CELL DENSITY IN SEMI-SOLID AGAR PLATES.....	42
FIGURE 3-3 THE SETUP OF THE CONTINUOUS FLUORESCENCE PHOTOBLEACHING (CPB) MICROSCOPY SYSTEM.	44
FIGURE 3-4 TIMELAPSE FLUORESCENCE IMAGE DURING PHOTOBLEACHING.....	45
FIGURE 3-5 MEASUREMENT OF CELL DIFFUSION COEFFICIENT VIA CONTINUOUS FLUORESCENCE PHOTOBLEACHING (CPB). .....	47
FIGURE 3-6 ILLUSTRATION OF THE TRAJECTORY OF ONE CELL IN AND OUT OF THE PHOTOBLEACHING REGION..	48
FIGURE 4-1 THE PROGRAMMED COUPLING OF CELL DENSITY AND MOTILITY.....	51
FIGURE 4-2 PHOTOGRAPHS OF TYPICAL EXPERIMENTAL PATTERN.....	52
FIGURE 4-3 PLASMID MAPS.....	53
FIGURE 4-4 CHARACTERIZATION OF GC-I.....	55
FIGURE 4-5 TIME-LAPSED PHOTOGRAPHS OF A TYPICAL EXPERIMENTAL PATTERN.....	56
FIGURE 4-6 SPATIOTEMPORAL DIAGRAM OF FIG. 4-5A.....	57
FIGURE 4-7 SPATIAL-TEMPORAL DENSITY PROFILE OF STRAIN CL3.....	58
FIGURE 4-8 ONE-DIMENSIONAL PATTERN.....	59
FIGURE 4-9 EFFECT OF CHROMOSOMAL LAC OPERON ON THE PATTERN FORMATION.....	60
FIGURE 4-10 ENTIRE GC-I IS REQUIRED FOR STRIPE PATTERN FORMATION.....	60
FIGURE 4-11 EFFECTS OF HOST-ENCODED QS FACTORS ON STRIPE PATTERN FORMATION.....	61
FIGURE 4-12 PATTERN FORMATION UNDER VARIOUS CONDITIONS.....	63
FIGURE 4-14 THE EFFECT OF pH ON CL-M SWARM DISTANCE.....	64
FIGURE 4-15 EFFECTS OF MEDIUM pH ON PATTERN FORMATION .....	65
FIGURE 4-16 "LOSS-OF-PATTERN" MUTATION.....	65
FIGURE 4-17 CHARACTERIZATION OF "LOSS-OF-PATTERN" PHENOMENUM.....	66
FIGURE 4-18 SCHEME SHOWING THE FORMATION OF AGGREGATION (HIGH-DENSITY REGION) IN SEMI-SOLID AGAR.....	68
FIGURE 4-19 EVIDENCE OF EFFECTIVE AGGREGATION.....	69
FIGURE 4-20 MODELING OF AUTONOMOUS PERIODIC STRIPE PATTERN FORMATION.....	71
FIGURE 4-21 PHASE DIAGRAM OF THE STRIPE NUMBER.....	72
FIGURE 4-22 TUNABLE PERIODIC STRIPE PATTERNS.....	73
FIGURE 4-23 EFFECT OF ATC ON THE PATTERN FORMATION OF CL3.....	74
FIGURE 4-24 RELATIVE <i>CHEZ</i> mRNA LEVEL OR SWARM DISTANCE OF STRAIN CL21 AS A FUNCTION OF IPTG CONCENTRATION.....	75
FIGURE 4-25 GC-II.....	76
FIGURE 4-26 CHARACTERIZATION OF GC-II.....	77
FIGURE 4-27 PATTERN FORMATION OF GC-II.....	78
FIGURE 4-28 ENTIRE GC-II REQUIRED FOR STRIPE PATTERN FORMATION.....	79
FIGURE 4-29 EFFECTS OF HOST-ENCODED QS FACTORS ON GC-II STRIPE PATTERN FORMATION .....	80
FIGURE 4-30 EVIDENCE OF EFFECTIVE AGGREGATION.....	81
FIGURE 4-31 THE REVERSED DESIGN OF PROGRAMMED COUPLING OF CELL DENSITY AND MOTILITY.....	81

FIGURE 4-32 "FUJI-MOUNT"-LIKE PATTERN.....	82
FIGURE 4-33 PATTERN FORMATION OF CL32 AND ITS DERIVATIVES. ....	83
FIGURE 4-34 FLOW CHART OF REPETITIVE SPOTTING EXPERIMENT.....	84
FIGURE 4-35 PATTERN FORMATION OF CELLS FROM DIFFERENT POSITIONS OF DEVELOPED STRIPE PATTERN ...	85
FIGURE 4-36 PATTERN FORMATION OF CELLS FROM SINGLE COLONIES ISOLATED FROM DIFFERENT POSITIONS OF DEVELOPED STRIPE PATTERN AFTER 15 ROUNDS OF PICKING, CULTURE, AND SPOTTING.....	86
FIGURE 4-37 PATTERN FORMATION OF CL22MIDN AND CL22*......	87
FIGURE AI-1 PHOTOGRAPHS OF SALVIA MILTIORRHIZA BUNGE (DANSHEN).....	100
FIGURE AI-2 CHEMICAL STRUCTURE OF SAL B .....	101
FIGURE AI-3 H <sub>2</sub> O <sub>2</sub> -INDUCED RCMECs APOPTOSIS.....	106
FIGURE AI-4 INHIBITION OF H <sub>2</sub> O <sub>2</sub> -INDUCED RCMECs APOPTOSIS BY SAL B. ....	107
FIGURE AI-5 THE INHIBITION EFFECT OF SAL B IS DOSE-DEPENDENT. ....	108
FIGURE AI-6 INVOLVEMENT OF CASPASES. ....	109
FIGURE AI-7 EFFECTS OF SAL B, MEK INHIBITION, OR THEIR COMBINATION ON H <sub>2</sub> O <sub>2</sub> -INDUCED APOPTOSIS..	110
FIGURE AI-8 TIME COURSE OF PHOSPHORYLATED ERK1/2 EXPRESSION IN RCMECS INCUBATED WITH H <sub>2</sub> O <sub>2</sub> (200 MM) ALONE, OR WITH H <sub>2</sub> O <sub>2</sub> (200 MM) AND SAL B (20 MM), OR WITH SAL B (20 MM) ALONE. 111	
FIGURE AI-9 EFFECTS OF PI3K OR MEK INHIBITION ON PHOSPHORYLATED AKT (SER-473) AND PHOSPHORYLATED ERK1/2 EXPRESSION IN THE PRESENCE OR ABSENCE OF H <sub>2</sub> O <sub>2</sub> (200 MM).....	112
FIGURE AI-10 EFFECTS OF c-RAF INHIBITION.....	112
FIGURE AI-11 EFFECTS OF SAL B ON PI3K/AKT/RAF SIGNALING. ....	113
FIGURE AI-12 ROLE OF PI3K SIGNALING. ....	114
FIGURE AI-13 TIME COURSE OF BCL-2 EXPRESSION.....	115
FIGURE AI-14 SCHEMATIC MODEL OF SIGNALING EVENTS INVOLVED IN H <sub>2</sub> O <sub>2</sub> -INDUCED RCMECS APOPTOSIS AND SAL B PREVENTIVE MECHANISM. ....	121
FIGURE AII-1 PROPOSED MODEL OF MMR-DEPENDENT 'CORRECTION-INDUCED' CELL DEATH.....	132
FIGURE AII-2 TIME COURSE OF GREEN/CORRECTED CELLS PRODUCED IN SINGLE-STRANDED OLIGODEOXYNUCLEOTIDES (ssODN)-MEDIATED TARGET GENE REPAIR.....	137
FIGURE AII-3 MEASUREMENTS OF APOPTOSIS IN GREEN CELLS.....	138
FIGURE AII-4 MEASUREMENTS OF APOPTOSIS IN GREEN CELLS.....	139
FIGURE AII-5 EFFECTS OF CASPASES OR ATM/ATR INHIBITIONS ON APOPTOSIS CAUSED BY SSODN-MEDIATED TARGETED GENE REPAIR.....	140
FIGURE AII-6 EFFECTS OF HMLH1 DEFICIENCY.....	141
FIGURE AII-7 EFFECTS OF CADMIUM TREATMENT.....	143

## **LIST OF TABLES**

TABLE 2-1 STRAINS AND PLASMIDS USED IN THIS STUDY .....	36
TABLE 2-2 OLIGONUCLEOTIDES USED IN THIS STUDY .....	37

## ABBREVIATIONS AND SYMBOLS

$^{\circ}\text{C}$	<i>Degree Celsius</i>
$\Delta$	<i>deleted</i>
16S rRNA	<i>16S ribosomal RNA</i>
ABC	<i>ATP-binding-cassette</i>
AHL	<i>N-acylho-moserine lactone</i>
AP	<i>anteroposterior</i>
aTc	<i>anhydrotetracycline</i>
BBB	<i>blood-brain barrier</i>
BioGEE	<i>biotinylated GSH monoethyl ester</i>
bp	<i>base pair</i>
CCW	<i>counterclockwise</i>
cDNA	<i>comlementary DNA</i>
CIP	<i>calf intestine alkaline phosphatase</i>
cm	<i>centimeter</i>
CMECs	<i>cerebral microvascular endothelial cells</i>
CPB	<i>continuous fluorescence photobleaching</i>
CRE	<i>cyclic AMP-responsive element</i>
CREB	<i>cyclic AMP-responsive element-binding protein</i>
CW	<i>clockwise</i>
DAPI	<i>4'6-diamidino- 2-phenylindole</i>
DCF	<i>Carboxy-2',7'-dichlorofluorescein</i>
DEPC	<i>diethylpyrocarbonate</i>
DMEM	<i>Dulbecco's modified Eagle's medium</i>
DMSO	<i>dimethyl sulfoxide</i>
DNA	<i>deoxyribonucleic acid</i>
dNTP	<i>deoxynucleotide</i>
DPD	<i>4,5- dihydroxy-2,3- pentanedione</i>
DSBs	<i>double-stand breaks</i>
DTT	<i>dithiothreitol</i>
Dxs	<i>D-1-deoxyxylulose 5-phosphate synthase</i>
ECGF	<i>Endothelial cell growth factor</i>
ECL	<i>enhanced chemiluminescence</i>
EDTA	<i>ethylene-diamine-tetra-acetic acid</i>
EMT	<i>epithelial-mesenchymal transitions</i>
ERK	<i>extracellular signal-regulated kinase</i>
ES	<i>Embryonic stem</i>
FBS	<i>fetal bovine serum</i>
FGF	<i>fibroblast growth factor</i>
g	<i>gram or gravity (unit of centrifugal force)</i>
GC	<i>genetic circuit</i>
GFP	<i>green fluorescent proteins</i>
gyrB	<i>gyrase subunit B</i>
h	<i>hour</i>
$\text{H}_2\text{O}_2$	<i>hydrogen peroxide</i>
HCl	<i>hydrochloric acid</i>
HEPES	<i>N-2-hydroxyethylpiperazine-N'-2-ethanesulfonic acid</i>
HR	<i>homologous recombination</i>
HRP	<i>horseradish peroxidase</i>
IPTG	<i>Isopropyl-<math>\beta</math>-D-thiogalactopyranoside</i>
Kb	<i>kilobases</i>
KDa	<i>kilodalton</i>
L	<i>liter</i>
LB	<i>Luria-Bertani</i>
M	<i>molar per liter</i>
MAPKs	<i>mitogen-activated protein kinases</i>

MDA	<i>malondialdehyde</i>
MEFs	<i>Mouse embryonic fibroblasts</i>
mg	<i>milligram</i>
min	<i>minute</i>
ml	<i>milliliter</i>
mM	<i>millimolar per liter</i>
MMR	<i>mismatch repair</i>
mRNA	<i>messenger RNA</i>
ng	<i>nanogram</i>
nm	<i>nanometer</i>
OD <sub>600</sub>	<i>optimal density at 600 nm</i>
ORF	<i>open reading frame</i>
PARP	<i>poly (ADP-ribose) polymerase</i>
PBS	<i>phosphate-buffered saline</i>
PCR	<i>polymerase chain reaction</i>
PFA	<i>paraformaldehyde</i>
PI3K	<i>phosphatidylinositol-3-kinase</i>
PS	<i>phosphorothioate</i>
PSM	<i>presomitic mesoderm</i>
PVDF	<i>polyvinylidene difluoride</i>
QS	<i>quorum sensing</i>
R.T.	<i>room temperature</i>
ROS	<i>reactive oxygen species</i>
Rpm	<i>rotation per minute</i>
RT	<i>reverse transcriptase</i>
RT-PCR	<i>reverse transcription-polymerase chain reaction</i>
Sal B	<i>salvianolic acid B</i>
SDS	<i>sodium dodecyle sulphate</i>
sec	<i>second</i>
ssODN	<i>single-stranded oligodeoxynucleotide</i>
Taq	<i>thermus aquaticus DNA (polymerase)</i>
TBA	<i>thiobarbituric acid</i>
TBE	<i>Tris/borate electrophoresis (buffer)</i>
TCR	<i>transcription coupled repair</i>
TE	<i>Tris/EDTA (buffer)</i>
TEMED	<i>N,N,N,N,- tetramethylethylenediamine</i>
Tm	<i>melting temperature</i>
Tris	<i>tris(hydroxymethyl)aminomethane</i>
TUNEL	<i>terminal deoxynucleotidyl transferase-mediated dUTP nick end-labeling</i>
UV	<i>ultraviolet</i>
v	<i>volt</i>
v/v	<i>volume/volume</i>
w/v	<i>weight/volume</i>
WT	<i>wild-type</i>
µg	<i>microgram</i>
µl	<i>microliter</i>
µm	<i>micrometer</i>
µM	<i>micromolar per liter</i>

## **Chapter 1**

### **Introduction**

Biological systems often form intricate spatiotemporal patterns, such as zebra stripes, peacock feather, leopard spots, fish scales, flower petals, and *et al* (**Fig. 1-1**). The biological process that generates these ordered patterns is termed “pattern formation”<sup>9</sup>. It usually involves changes in gene expression, cell movement, proliferation, and death, intricately coordinated by multiple signaling molecules. Pattern formation is a common interest of molecular biologists, developmental biologist, synthetic biologists, tissue engineers, system biologists, and theoretical biologists. Understanding how these patterns arise from the coordinated molecular responses is an outstanding challenge to generations of scientists.



**Figure 1-1 Fascinating biological patterns in nature.**

Figures are from web, and links are indicated.

In the past decade, the synthetic biologists have made great advance in bringing concepts of physics and engineering into biology, engineering cells to have novel functions<sup>10-15</sup>, which is the major aim of synthetic biology. However, the other important aim of this field, “build life to understand it”, is more and more emphasized<sup>16,17</sup>. Biological patterns are traditionally studied via either forward or reverse genetic approach. Applying synthetic biology in investigation of principles of biological pattern formation then would be a paradigm shift.

In this study, I use engineered bacterial cells to explore a novel principle of pattern

formation. I constructed a model system containing the basic ingredients of growth, motility and cell-to-cell signaling for pattern formation. A simple regulatory interaction, involving the inhibition of cell motility at high cell densities, was introduced by controlling the chemotaxis circuit of *E. coli* by a heterologous quorum-sensing system. This interaction, simulating a motility-limiting crowding effect, unexpectedly led to the sequential formation of highly periodic stripe patterns after spotting the engineered strain on a semi-solid agar plate. Detailed experimental and theoretical investigations of the pattern formation process led to the understanding of a new strategy of sequential stripe formation, which may be of relevance not only to the synthetic bacterial patterns but also to similar stripe formation processes in metazoan development.

## 1.1 PERIODIC BIOLOGICAL PATTERN

The biological patterns anatomically may have repeated units, like people have ten fingers, 24 ribs, and 32 teeth. A spatial ‘periodic’ pattern typically comprises repeated units separated by orderly intervals. People can easily see this periodicity in the patterns of zebra stripes, peacock feather, fish scales, *Drosophila* segments, and vertebrate embryo somites. Periodicity also takes place temporally, such as the contraction of our heart muscle, and the oscillation of the harmonic motion<sup>18</sup>.

### 1.1.1 DROSOPHILA SEGMENTATION

The segmentation of the fruit fly *Drosophila melanogaster* is one of the major paradigms in the study of periodic pattern. In the past three decades, about 40 genes have been identified in *D. melanogaster* in the segmentation process. These genes act in a cascade progressively resulting in the subdivision of the anteroposterior (AP) axis<sup>19,20</sup>. The segmentation of *D. melanogaster* can be described in four steps (**Fig. 1-2**)<sup>2</sup>.

Firstly, a ‘ready mix’ cytoplasm has been prepared during the oogenesis. In the cytoplasm of the egg, the maternal transcripts of *hunchback* (*hb*) and *caudal* (*cad*) are uniformly distributed; the transcript of *bicoid* (*bcd*) is mainly localized at the anterior pole, while a protein and RNA complex is localized at the posterior of the egg. After fertilization, these maternal transcripts are translated rapidly, generating protein gradients along the egg (**Fig. 1-2a**). Here, BCD is not only a transcriptional activator of *hb* but also a translational repressor of *cad*, while NOS is a translational repressor of *hb* mRNA. Thus, the anterior half of the egg contains the HB protein, anterior and posterior poles contain high levels of BCD and CAD, respectively.

Secondly, signals embedded in the egg-shell activate Torso, a transmembrane receptor localized at the poles of the egg. Meanwhile, at specific positions along the AP axis of the egg, a group of zygotic ‘gap’ genes, e.g. *tailless* (*tll*), *giant* (*gt*), *Kruppel* (*Kr*), are activated by the signals from maternal proteins (Fig. 1-2b).

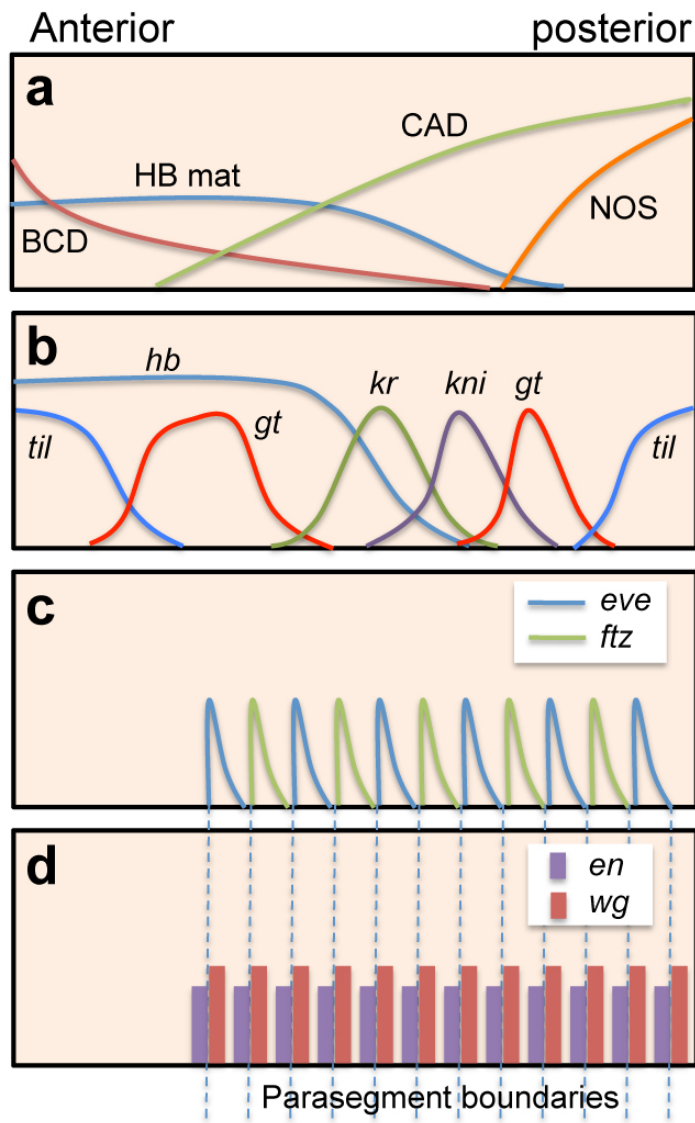


**Figure 1-2 *Drosophila melanogaster* segmentation.**

a, Maternal signals. b, Gap domains. c, Pair-rule pattern, d, Segment polarity pattern. The box indicates a ‘ready mix’ cytoplasm after oogenesis, HB mat, maternal HB. Other abbreviations, see text for details. Adapted from Peel *et al*, 2005<sup>2</sup>.

Thirdly, although the expression profile of the gap genes is not periodic, the interaction of their transcriptional factor products and signals from maternal proteins provides nuclei a specific axial identity. This identity is thereafter interpreted by the pair-rule genes, e.g. *hairy* (*h*), *runt* (*run*) and *even skipped* (*eve*), generating periodic gene expression. Further transcriptional interaction between pair-rule genes and their downstream genes [e.g. *fushi tarazu* (*ftz*)] refine the expression stripes (Fig. 1-2c). The stripe boundaries predict the parasegment boundaries.

Lastly, despite that the gene expression of pair-rule genes is transient, once cell boundaries form, the pair-rule proteins in each parasegment activates the segment polarity genes, whose expression is stable. Some genes like *engrailed* (*en*) is stable even in the adult. Parasegment boundaries form between the cells expressing *en* and *wingless* (*wg*), respectively (Fig. 1-2d). Later on, the segment boundaries are generated based on the parasegments.

### 1.1.2 SOMITOGENESIS

Somitogenesis, an important developmental process of vertebrate embryo, has been extensively studied<sup>21,22</sup>. Somites are segments in embryo, particularly blocks of cells surrounding a cavity structure<sup>21</sup>. The somite appears rhythmically from the presomitic mesoderm (PSM). PSM are two parallel bands of mesenchymal tissue lying alongside the neural tube<sup>21</sup>. With a temporal interval of 30 min in zebrafish, 90 min in chicken, 120 min in mice, and around 4 h in humans, somites are generated periodically along the AP axis<sup>23</sup>. Later on, these somites can develop into skeletal muscles, dermis, and vertebrae.



**Figure 1-3 Segmentation clock oscillator.**

In presomitic mesoderm cells, the expression of the *hairy1* gene (blue) looks like a periodic wave, swiping the PSM, which is correlated with the sequential somite formation. Adapted from Dequeant and Pourquie, 2008<sup>21</sup>.

### 1.1.2.1 SEGMENTATION CLOCK

There's a segmentation clock in PSM involved in the somitogenesis<sup>24</sup>. The first evidence of this clock is that the expression of a chicken embryonic transcriptional factor, HES1, was found to be in an oscillated manner<sup>24</sup>. The mRNA of *hes1* acts like a wave sweeping through the PSM periodically during the somite formation process. This temporal periodicity, termed the segmentation clock, can be translated into the spatial formation of periodic segment pattern (**Fig. 1-3**). Other cyclic genes were increasingly found in mouse, frog, and fish embryos<sup>25-28</sup>, suggesting that the segmentation clock is conserved in vertebrates. Most of these genes belong to the fibroblast growth factor (FGF), Notch, and Wnt signaling pathway. In past decades, much effort has been made to uncover the pacemaker that drives the oscillation of the cyclic gene expression.

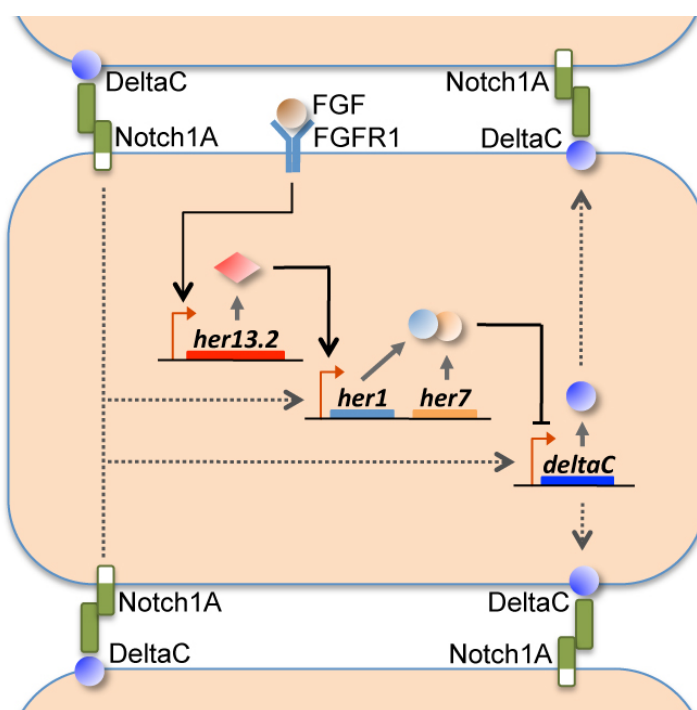


**Figure 1-4 Synchronization of the PSM cellular oscillators.**

The negative feedback loop established by transcriptional factors Her1 and Her7 acts as a pacemaker controlling the dynamic expression of DeltaC. As a result, the Notch signaling in neighboring cells is synchronized. Her13.2, located at the downstream of FGF signaling, is required for Her1-Her7 to receive the signal from Notch. FGFR1, FGF receptor 1. Adapted from Dequeant and Pourquie 2008<sup>21</sup>

In zebrafish, all the identified cyclic genes belong to the Notch pathway, indicating Notch activation plays a central role in the segmentation clock. The rhythmic expression of the Notch ligand *deltaC* was considered to drive the activation of Notch, thereby leading to the oscillated expression of the hairy and enhancer of split-related genes, *her1* and *her7*<sup>29,30</sup>. On the other hand, HER1 and HER7 negatively regulate *deltaC* and their own expression<sup>30,31</sup>. This coupling maintains the synchrony of the PSM cellular oscillators (**Fig. 1-4**)<sup>21</sup>.

In amniotes, homologues of *her1* and *her7* were also detected, e.g. *hes1*, *hairy2* and *hey2* in chicken; *hes1*, *hes7*, and *hey1* in mouse<sup>24,25,32,33</sup>. However, the glycosyl transferase LFNG (Lunatic Fringe) was only found in amniotes<sup>34</sup>. The expression of *lfng* is also activated by Notch signaling and in turn regulates Notch activation by a negative feedback loop<sup>35</sup>. Besides Notch signaling, in mouse, a Wnt signaling inhibitor Axin2 has been identified as a cycling gene<sup>36</sup>. Similarly, the expression of *axin2* is directly activated by Wnt signaling, and in turn negatively regulates Wnt and its own expression. In Notch signaling mutant, *axin2* expression perseveres. On the contrary, the expression of both *axin2* and *lfng* are disrupted in *wnt3a* mutants, showing that Wnt pathway acts upstream of the Notch pathway<sup>37</sup>.

### 1.1.2.2 TRANSLATING CLOCK SIGNAL INTO SEGMENTS

In chick embryo, it has been shown that fibroblast growth factor 8 (FGF8) is involved in the translation of clock signal into segments<sup>38</sup>. The mRNA level of *fgf8* is high in posteriormost PSM and progressively decreases towards anteriormost side, forming a gradient over the PSM (**Fig. 1-5**). Overexpression of *fgf8* blocked the segmentation and kept the PSM cells in an immature state, indicating that the expression level of FGF8 correlates with the fate of PSM cells. Thus, it is proposed that there's a threshold level of FGF8, termed the “determination front” (**Fig. 1-5**). Those cells located in the anterior PSM reach the threshold, and then begin to undergo the segmentation process. In the cells at the determination front, expression of *mesp2/c-meso1* becomes periodic in a domain with one-somite width<sup>39</sup>. Activation of Mesp2 in turn acts on its downstream Notch pathway, the key component of the segmentation clock, ultimately resulting the formation of the somite compartment<sup>40</sup>. As the elongation of the body axis, the determination front recedes, allowing the cells enter the segmentation process. Thus, the distance of boundaries of the somites will be set by the period of the oscillation.

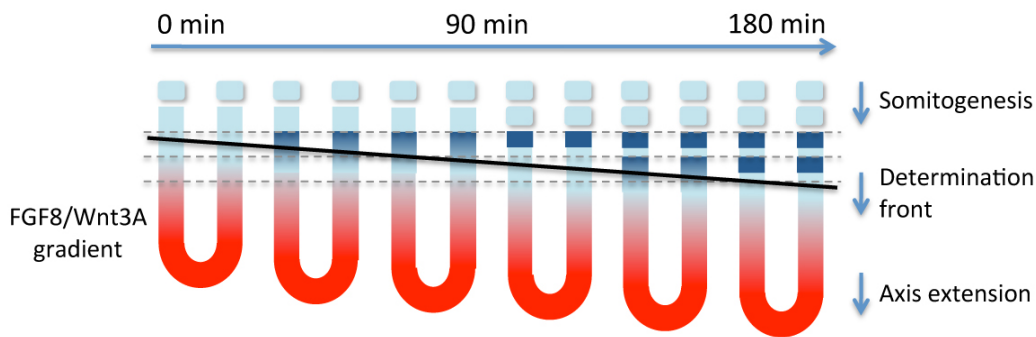


**Figure 1-5 Model of segmentation in mouse vertebrates.**

The FGF8/Wnt3A gradient is shown in red. The expression of *Mesp2/c-meso1* is shown in blue. The determination front is shown as a black line. Adapted from Pourquie, 2003<sup>37</sup>.

## 1.2 COORDINATED CELL MOVEMENT

From mammalian embryonic development<sup>41,42</sup>, *Drosophila* gastrulation<sup>43</sup>, to bacterial chemotactic pattern formation<sup>44,45</sup>, precisely coordinated cell movement is required in pattern formation. Although cell movement is one of the most essential elements in natural patterning process, its regulation and contribution in pattern formation is not fully understood.

### 1.2.1 GASTRULATION

The word gastrulation is from “gaster”, a Greek word meaning gut. Haeckel first used this word to describe the embryonic stage, at which an obvious cell layer becomes visible in the embryo. The cell layer will later develop into the musculature and digestive system. The research on gastrulation is mainly concentrated on three model species, the sea urchin, *Drosophila*, and *Xenopus*. Gastrulation is the earliest developmental event involving massive cellular movements. There’re four types of movement that contribute to the cell rearrangement during gastrulation<sup>46</sup>.

#### a) Epithelial Bending

It is one of the earliest movement events observed in gastrulation, paving a way for the translocation of large mass of cells<sup>46</sup>.

**b) Cell Rearrangement within Sheets**

Cells in epithelia or mesenchymal cells can rearrange, and change the cell sheet dimensions. Cell intercalation generates the force of the movement via the interaction between neighboring cells without the need of a substratum<sup>47</sup>.

**c) Epithelial-Mesenchymal Transitions (EMT)**

Cells undergoing EMT will lose cell adhesion, increase cell motility, and repress E-cadherin expression. Either the delamination of single cells or the transition of an epithelium to a mesenchymal phenotype is considered as EMT<sup>48</sup>. Cells with this mode of movement can move out of the epithelia.

**d) Cell migration**

It requires the substratum, and often occurs at late stages of gastrulation, such as the expanding mesoderm in *Xenopus* and *Drosophila*, the migration of neural crest cells in vertebrates, and so on. In this type of movement, cells can move individually or as groups. Cells are considered to be guided by chemotaxis, however, few cases have been clearly demonstrated in gastrulation<sup>46</sup>. Among them, the primitive streak in avian embryos is an important example of the cell migration guided by chemotaxis<sup>49</sup>. The instructive signal is members of FGF family. Additionally, spatial constraints are another cause of directional movements. For instance, in *Xenopus* or *Drosophila*, the mesodermal cells occupy the site of invagination. The only direction for cell migration is moving away from that site<sup>46</sup>.

### 1.2.2 BACTERIAL CHEMOTACTIC PATTERNS

Bacteria can form intricate spatial patterns in both the laboratory and the natural environment<sup>50</sup>. For instance, in aquatic environments, phototrophic purple bacteria form unique bands, which can migrate in response to light intensity or chemical concentration changes. In laboratory, various bacterial cells have been shown to form complex patterns in semi-solid agar plates. Examples include *E. coli*<sup>44,45</sup>, *Salmonella*<sup>51</sup>, *Pseudomonas*<sup>52</sup>, and so on. In these cases, patterns arise from the directed cellular movement responding to the gradients of chemical cues, i.e. chemotaxis (see 1.7.4). Berg and his co-workers first described that, under specific conditions, *E. coli* cells can form highly ordered patterns when inoculated onto a semi-solid agar plate. It is proposed that the production of chemo-attractants (in this case it is aspartate) causes the aggregation of surrounding cells towards the excreting cell.

## 1.3 MODELS FOR PERIODIC PATTERN

*"I am never content until I have constructed a mechanical model of the subject I am studying. If I succeed in making one, I understand. Otherwise, I do not."* – Lord Kelvin.

Mathematical models can help us understand complex systems and predict the result upon physical or genetic disruptions. So far they have two major forms: 1) analyze every component and simulate every interaction in a system<sup>53</sup>; 2) omit complicated details of a system but extract its nature<sup>54</sup>. The first type of model is used to describe relatively simple systems. If the system were complex, e.g. involving spatiotemporal dynamics, it would be difficult to make a thorough analysis and develop a plausible “detailed” model.

A great diversity of models have been suggested for the periodic patterning phenomena<sup>18</sup>. As Murray drum in his book<sup>55</sup>, these models are not the actual mechanisms of the natural pattern. Similarly, Wolpert shared his Maxim: “do not infer process from pattern, since so many processes can produce the same pattern”<sup>56</sup>. Here, I briefly introduce two important models of theirs.

### 1.3.1 REACTION-DIFFUSION MODEL

Reaction-diffusion or Turing model is one of the most well-known mathematic models for pattern formation<sup>57</sup>. Alan Turing, one of the founders of modern computer<sup>58</sup>, proposed this brilliant model in a seminal paper<sup>59</sup>. Intuitively, people would believe that diffusion always contributes to stabilize the system. But Turing found, in presence of diffusion, it is possible that the origin locally stable state of a reaction system becomes unstable. In other words, the coupling of diffusion and reaction may make small perturbations on the homogenous stable state amplified. In a homogeneous system, small fluctuations of the molecular distribution become unstable. The amplified fluctuations lead to the formation of peak and trough of the molecular concentration. These molecules were termed as morphogens. And their distribution profiles will be the prepattern to develop. It differs from the prepattern models in the reaction term, which produces the morphogens<sup>57</sup>.

The reaction-diffusion model has been considered to be the standard in the mathematic models for biological pattern formation<sup>57</sup>. However, in the experimental biology community, this model is not widely accepted. FitzHugh and Nagumo proposed an important derivative of Turing model to translate the mathematic language into the one biologists use<sup>60</sup>. It is an activator-inhibitor excitable system, such as the neuron. In this two-component system, the production of both components is activated by one of the chemicals, while the other one plays a role to inhibit the growth of the system. With proper parameters and under certain

conditions, the model can produce plain wave, rotating spirals, ring wave, stripe wave, stationary localized pulse, et al. Furthermore, to get a stable spatial pattern, Gierer and Meinhardt proposed that a Turing pattern based on lateral inhibition only requires a short-range positive feedback and a long-range negative feedback (**Fig. 1-6**)<sup>52</sup>, indicating that a faster diffusion of the inhibitor and a slower diffusion of the activator. These refinements make the general principle of Turing model much easier to be applied in complex systems. It has been shown that many systems satisfy this condition and are capable to form Turing Patterns, such as chemotactic cell migration<sup>61</sup>, neuronal interactions<sup>62</sup>, mechanochemical activity<sup>63</sup> and so on.

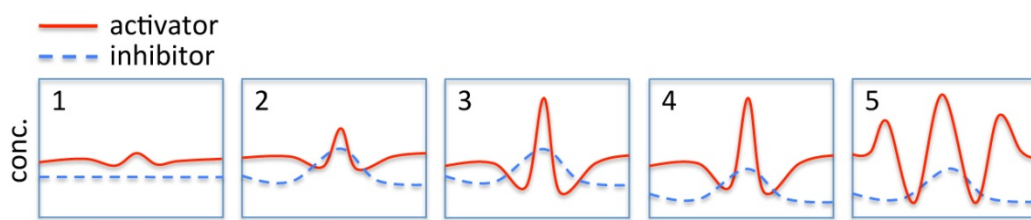


**Figure 1-6 Scheme of the formation of a Turing pattern.**

- 1, The initial condition. The concentration of the activator is supposed to be higher than that of inhibitor. 2, The concentration of activator increases at the center due to the self-enhancing property. 3, The concentration of inhibitor increase. Due to the higher diffusion rate, inhibitor move laterally, leading to the decrease of the concentration of activator at those regions. 4, The decrease of activator concentration in turn results in the decrease of inhibitor. 5, For the outer region, the low concentration of inhibitor causes the increase of activator. This initiates the new peak of activator. Adapted from Kondo and Miura, 2010<sup>57</sup>

### 1.3.2 THE CLOCK AND WAVEFRONT MODEL

The clock and wavefront model was proposed for somitogenesis (see **1.1.2**). It comprises of two components: an oscillating two-state ‘clock’ and a unidirectionally propagating wave<sup>64</sup>. In general, all cells synchronously oscillate between two states. Once the front of the traveling wave reaches, the oscillation stops. As the wave sweeps over the developing zone, a periodic pattern with alternating states is left behind.

### 1.4 NUMERICAL CONSTANCY

Another fascinating question is how precise numbers of modules/elements/body units achieves in periodic patterns, such as ten fingers, 24 ribs, 32 teeth, and 33 vertebrae in humans. What mechanisms guarantee the constancy? Held postulated that there's a 'halt condition' to stop the repetition of the pattern element<sup>18</sup>. If the 'halt condition' were not functional, the pattern element would repeat ceaselessly. Actually, such 'infinite' mutants have been increasingly observed. For instance, in *Caenorhabditis elegans*, *unc-86* mutations caused the cell lineages repeat many times<sup>65</sup>; in *Drosophila*, *bag-of-marbles* mutations increased the cell number of ovarian cyst from 16 to hundreds<sup>66</sup>; in *Antirrhinum, floriscaula* mutation made flowers become repeated meristems<sup>67</sup>.

It is intuitive that, given a constraint of element size, the number of the pattern element could be controlled by the body size. In alligator, there are more stripes on the back of the male alligator due to their longer body size<sup>55</sup>. On the contrary, the element number can be independent of body size, e.g. the somite number in *Xenopus*<sup>68</sup>.

## 1.5 SYNTHETIC BIOLOGY

Synthetic biology is a new and fast growing field that seems still have no a widely accepted definition. In a website (<http://syntheticbiology.org/>), synthetic biology is defined as "the design and construction of new biological parts, devices and systems, and the re-design of existing natural biological systems for useful purposes". In UK Royal Society (<http://royalsociety.org/>), synthetic biology is defined as "an emerging area of research that can broadly be described as the design and construction of novel artificial biological pathways, organisms or devices, or the redesign of existing natural biological systems". Generally, these novel functions were achieved by introducing new genetic networks termed 'genetic circuits'.

In the past decade, synthetic biology has been applied to engineer new functions<sup>69,70</sup>, such as population controlling<sup>14</sup>, cellular counter<sup>71</sup>, 'photoprinter'<sup>12</sup>, edge detector<sup>11</sup>, and so on. The other important aspect of synthetic biology is to understand the life via an engineering approach<sup>16,17</sup>. Various biological phenomena have been studied, including biological oscillator<sup>10,15</sup>, bacterial two-component system<sup>72</sup>, band detection<sup>13</sup>, biofilm development<sup>73</sup>, rebuilt ecosystem<sup>74</sup>, antibiotic resistance<sup>75</sup>, and et al.

### 1.5.1 PATTERN FORMATION WITH SYNTHETIC BIOLOGY

Basu *et al* engineered a ‘band-pass’ filter by separating *luxRI* system into sender [expressing *luxI* and producing N-acylho-moserine lactone (AHL)] and receiver cells (expressing *luxR* and responding to the AHL gradient). They designed an ingenious genetic circuit to make cells responded differently to the different level of AHL, resulting a bull-eye pattern in solid agar. Here, sender cells constitutively produced diffusible AHL. With certain production and decay rate, AHL formed a gradient in solid agar. Receiver cells containing a series of genetic elements (e.g. *luxR*, *cI*, and *lacI*) were in advance mixed in the agar. They only expressed GFP when AHL concentration was in a narrow range. Three LuxR mutants with different sensitivities to AHL were applied to generate various patterns<sup>13</sup>.

More recently, Danino *et al* used *luxRI* system to synchronize *E. coli* population, created a genetic oscillator<sup>10</sup>. Comparing with previous synthetic oscillation systems, their design was simple but led to beautiful temporally periodic patterns. They placed *luxI*, a reporter *yemGFP* and *aiaA* (AHL-degrading enzyme) under the control of *P<sub>luxI</sub>*. LuxR-AHL complex induced *aiaA* expression, which in turn negatively regulated the expression of *luxI*. With the aid of microfluidics devices and fluorescent microscopy, the bulk oscillation was temporally recorded. Moreover, the period and amplitude of the oscillator could be tuned by controlling flow rate in the microfluidics.

Next, I mainly introduce the motility of *E. coli* and the way of cell-cell communication, the two key ingredients of this study.

## 1.6 THE MOTILITY OF *E. COLI*

### 1.6.1 *E. COLI*

*E. coli* is a 1  $\mu\text{m}$  wide and 2  $\mu\text{m}$  long, Gram-negative rod. It weights  $\sim 1^{-12}$  g, and 70% of it is water. The chromosome of *E. coli* is a single chain of double stranded DNA with 4.7 Mb in length. It encodes about 4,000 genes, among which only 60% have known functions<sup>76</sup>. As *E. coli* grows, it elongates along the long axis first and then divides at the middle. Under the optimal condition, e.g. shaking vigorously in rich medium at 37 °C, *E. coli* duplicates itself every 20 min. It means that a 24-h culture produces  $4.7 \times 10^{21}$  *E. coli* cells, beginning with a single cell!

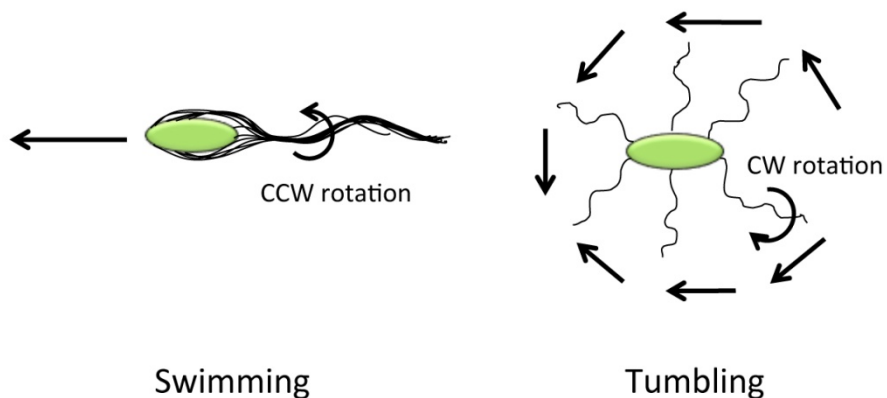


**Figure 1-7 Swimming and tumbling motions of *E. coli*.**

Adapted from Butler and Camilli, 2005<sup>77</sup>.

### 1.6.2 THE MOTILITY OF *E. COLI*

The motility of *E. coli* is realized by the rotation of a set of peritrichous flagella, which randomly locate at the body side. The flagellum is a long, thin, helical filament that extends into external aquatic environment and is driven by a rotary motor at its base<sup>78</sup>. The rotary motor is embedded in the cell envelop and less than 50 nm in diameter. When all flagella rotate counterclockwisely (CCW, viewed from the distal end of flagella to the rotary motor), they assemble into a bundle that propels the cell body move in a direction along its long axis. This motion is called “smooth swimming”. Generally, *E. coli* can run as fast as 35 diameters per second at its top speed. When one or more flagella switch the rotation direction into clockwise (CW), the bundle is disturbed and disassembles and no longer propels the cell body. Cells stop run and move brokenly. This motion is called “tumble” (Fig. 1-7)<sup>79-81</sup>. The default spin direction of flagella is CCW. When phosphorylated CheY binds to the motor, it changes the direction into CW. CheY is phosphorylated by kinase CheA, and dephosphorylated spontaneously in a rather slow rate. Phosphatase CheZ accelerates the dephosphorylation of CheY (Fig. 1-8). All of CheA, CheY, and CheZ are proteins involved in *E. coli* chemotaxis (see 1.6.4)<sup>82,83</sup>.

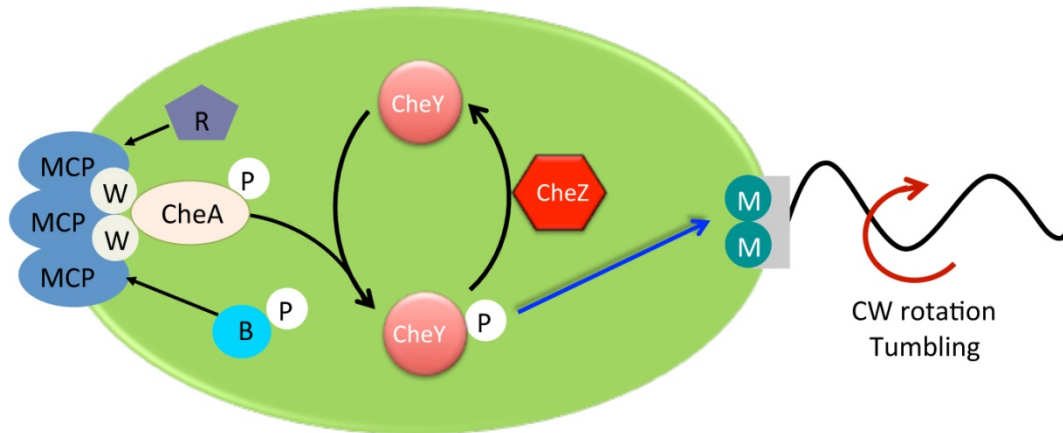


**Figure 1-8 Modulation of flagellar rotation.**

MCP, Methyl-accepting chemotaxis protein; W, CheW; R, CheR; B, CheB; P, phosphyl group.

Adapted from ‘[www.rowland.harvard.edu/.../images/fret1.jpg](http://www.rowland.harvard.edu/.../images/fret1.jpg)’

### 1.6.3 FLAGELLUM STRUCTURE

The structure and function of flagella have been extensively studied<sup>84,85</sup>. The flagella consist of three parts: basal body (rotor and stator), hook, and flagellar filament (**Fig. 1-8**).

#### 1.6.3.1 BASAL BODY

*E. coli* has a multilayered cell envelop comprising the inner membrane, the peptidoglycan layer, and the outer membrane. The basal body is embedded in the cell envelop, from the cytoplasm to the outer membrane. It consists of stator and rotor, two structural elements. The stator comprises the eleven MotA<sub>4</sub>MotB<sub>2</sub> complexes<sup>86,87</sup>. Both MotA and MotB span the inner membrane. About one-third of the MotA span in the inner membrane, while the rest of the molecule is in the cytoplasm. As to the MotB molecule, most is in the periplasm. Close to its C-terminus, a peptidoglycan-binding domain is found. Thus, the stator anchors to the cell wall through MotB<sup>88</sup>.

The rotor comprises MS- and C-ring. C-ring is in cytoplasm, containing about 26 FliG, 34 FliM, and 100 FliN proteins<sup>89,90</sup>. MS-ring (FliF) connects the C-ring and the rod, which links flagellar filament through a hook<sup>91</sup>.

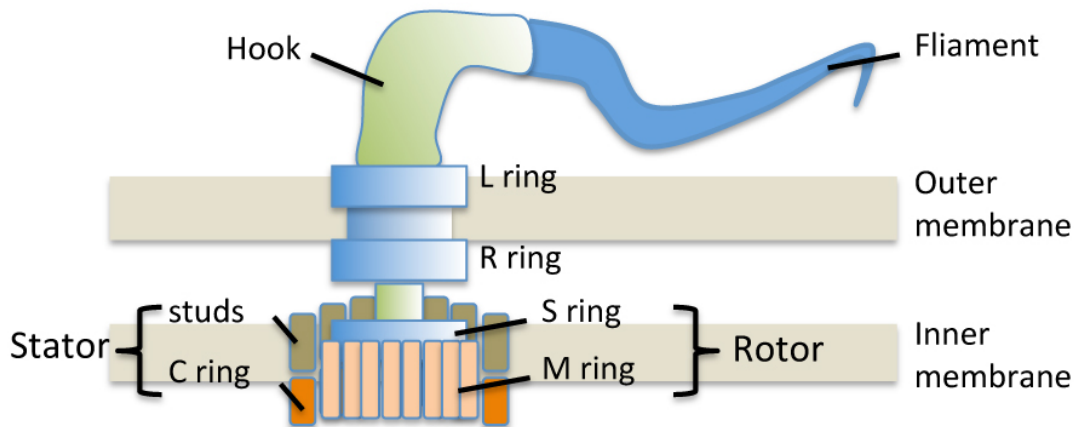


**Figure 1-9 *E. coli* flagellar structure.**

Modified from "<http://www.phy.duke.edu/undergraduate/biophysics/>".

### 1.6.3.2 HOOK

The hook is a flexible joint, located outside the cell, connecting the motor and the filament. It comprises polymers of FlgE, comprising eleven rows of FlgE that abreast give rise to a cylinder. The rows twist slightly to the cylinder axis<sup>92</sup>.

### 1.6.3.3 FILAMENT

The filament is a long and helical propeller<sup>93</sup>. A single helical turn of the filament consists of about 5,000 molecules of flagellin (FliC). And a filament can have six turns. The flagella can be as long as several cell lengths and fragile. If a filament is broken, it can regenerate by assembling FliC at its distal end. Unfolded FliC reaches the distal end of filament by diffusing through its hollow center<sup>92</sup>.

### 1.6.3.4 ASSEMBLY

The motor is assembled from inside out. Suzuki *et al* first analyzed the *Salmonella* mutants in which different *fla* genes were defective, thus different incomplete flagella structures could be observed<sup>94</sup>. In his observation, the simplest structure comprises the MS-ring and the rod. Later on, he observed the similar results in *E. coli*<sup>95</sup>. Kubori *et al* suggested MS-ring alone could be the simpler initial structure<sup>96</sup>. After that, FliG, FliM, and FliN are added<sup>97</sup>, followed by the addition of FlhA, FlhB, FliH, FliI, FliO, FliP, FliQ, and FliR. These proteins form the transport apparatus. What's more, the flagellar proteins are

synthesized in the order in which the flagella are built.

### **1.6.3.5 POWER SOURCE**

The flagellar motor is powered by the flux of proton through the cytoplasmic membrane, but not by ATP<sup>98</sup>. The flagellar rotation rate is proportional to the protonmotive force<sup>92</sup>. Unlike *E. coli*, some bacteria use sodium ion rather than proton<sup>99</sup>, e.g. marine bacteria and those living in high pH environments.

## **1.6.4 CHEMOTAXIS**

In the chromosome of *E. coli*, there're more than 50 genes in 19 operons governing the motility of *E. coli*. About half of these genes are required for the assembly of flagella and half for chemotaxis<sup>100</sup>. As shown in **Fig. 1-8**, the flagellum randomly switches between CCW and CW. The binding of phosphorylated CheY to FliM increases the likelihood of CW. The phosphorylation of CheY is controlled by the kinase CheA, whose activity in turn is modulated by chemoreceptors in the inner membrane. The chemoreceptors comprise of Tar, Tsr, Tap, Trg, and Aer. When an attractant is added, the kinase activity of CheA is depressed. On the contrary, the addition of repellent activates CheA. The macroscopical output is a longer swimming length when cells encounter the change of attractant/repellent concentration. Thus the cell can trace the attractant and keep away from the repellent. CheZ phosphatase is important in readjusting the bacterial behavior. It is localized close to the chemoreceptors by binding CheA, so that the phosphorylated CheY can be dephosphorylated quickly<sup>82,83</sup>. It has been shown that the motility of *E. coli* is very sensitive to intracellular CheZ activity<sup>101-103</sup>.

The adaptation of chemotaxis is achieved by the feedback of CheR and CheB, a methyltransferase and a methylesterase, respectively. CheR adds methyl group to each chemoreceptor monomer, leading to the increase of CheA activity thereby the decrease of sensitivity to attractant. On the other hand, CheB activated by CheA removes the methyl group from the receptors<sup>104</sup>.

## **1.7 CELL-CELL COMMUNICATION**

In multicellular organisms, cell-cell communication is crucial for a wide variety of

cellular behavior. For instance, in mammal cardiac muscle, cell-cell contact signaling enables the delivery of action potential from the pacemaker region to other parts of the heart, resulting in the coordinated contraction of the heart<sup>105,106</sup>. During *Drosophila* development, elaborate cell-cell signaling via BMP, Wnt, Notch, EGF, and Hedgehog gives rise to the vein pattern<sup>107</sup>.

In unicellular organisms, intercellular communication also is common<sup>108-110</sup>. During *Saccharomyces cerevisiae* mating, some cells will secrete a mating factor peptide into environment. Other cells may sense this peptide signal and make preparation for mating<sup>111</sup>. Similarly, bacterial population can sense the change of their density and coordinately alter their behavior. This process is termed as quorum sensing (QS)<sup>112,113</sup>, during which the production of a signaling molecule is required. The cell population density is positively correlated with the extracellular concentration of the signaling molecule. Once the concentration of the signal molecule reaches a critical level, cells can sense and respond to this density change, and then initiate a concerted action.

### **1.7.1 QUORUM SENSING SIGNALS**

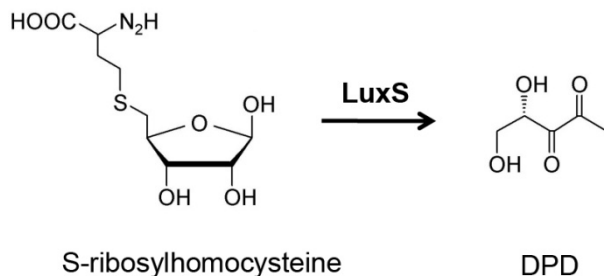
In all QS systems, signaling molecules are produced inside the cell, and then secreted into the extracellular niche. There're three well-defined signaling molecules in bacterial QS. They are oligopeptides<sup>114</sup>, autoinducer-2 (AI-2)<sup>12</sup>, and AHL<sup>115</sup>.

#### **1.7.1.1 OLIGOPEPTIDES**

In 1960s, oligopeptides have been reported as signaling molecules in *Bacillus cereus*<sup>116</sup> and *Pneumococcus*<sup>117</sup>. They are predominantly utilized in Gram-positive bacteria. Generally speaking, oligopeptides are made from precursor proteins, and unable to freely diffuse across the bacterial membrane. So they must be transported into the extracellular environment via ATP-binding-cassette (ABC) systems<sup>114</sup>. On the other hand, to sense the oligopeptides, receptors on the bacterial surface are required<sup>114</sup>.

#### **1.7.1.2 AI-2**

*E. coli* and *Salmonella typhimurium* were unable to produce AHL-like signaling molecules, but AI-2s. The synthesis process of AI-2s involves multiple enzymes. But all AI-2s are synthesized from a common precursor, 4,5- dihydroxy-2,3- pentanedione (DPD), which is the product of *luxS*-encoding enzyme with S-ribosylhomocysteine as substrate (**Fig.1-10**)<sup>118</sup>.

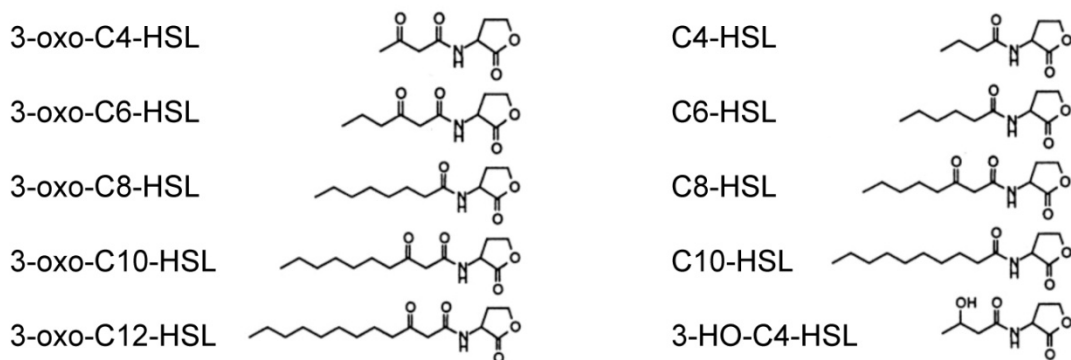


**Figure 1-10 Structure and formation of DPD.**

It is still unclear that how AI-2 is transported to the outside of cells. Recently, Herzberg *et al* showed that AI-2 was actively exported out of the cell via YdgG/TqsA-regulated pathway<sup>119</sup>. As the extracellular concentration of AI-2 increase, it is imported back to the cell via the Lsr ATP binding cassette (ABC) transporter<sup>120</sup>. Subsequently, AI-2 undergoes further phosphorylation by LsrK, followed by the induction of the expression of *lsrACDBFGE* operon or the inactivation of LsrR<sup>120,121</sup>. It is also demonstrated that *luxS/AI-2*-mediated QS system acts on *flhDC* transcription, thus controls the flagella assembly<sup>122</sup>.

### 1.7.1.3 AHL

AHL homologous molecules are used in Gram-negative bacteria and so far the most extensively studied class of communication signals (see structures of AHL in Fig. 1-11)<sup>123</sup>. Small AHLs can freely diffuse across the cell membrane, while large ones secrete out by the active transport as oligopeptides<sup>8</sup>. The first AHL QS system was discovered in *Vibrio fischeri*, the LuxI-LuxR system. *V. fischeri* is a gram-negative bioluminescent marine bacterium. It naturally grows in either seawater or the body of many sea organisms, e.g. the Hawaiian sepiolid squid, *Euprymna scolopes*, and *Monocentris japonica*<sup>125</sup>. In seawater, the cell density of *V. fischeri* is approximately 10 cells l<sup>-1</sup>, cells emit no luminescence. While in the body of marine organisms, it can symbiotically grow to a density as high as 10<sup>10</sup> cells L<sup>-1</sup>, emitting bright bioluminescence (800 photons/second/cell)<sup>126</sup>.

**Figure 1-11 Structures of AHLs**Adapted from Wang et al 2004<sup>124</sup>

### 1.7.2 LUXRI SYSTEM

QS system in *V. fischeri* comprises two major components: an AHL synthetase (LuxI) and an intracellular transcriptional regulator (LuxR). Both of them involves in *V. fischeri* bioluminescence system. The *luxI* is located in operon *luxICDABEG*. Among them, *luxA* and *luxB* encode a heterodimer ( $\alpha\beta$ ) of bacterial luciferase. In presence of a substrate (usually *n*-decanal), the heterogeneous expression of *luxA* and *luxB* renders other bacteria the ability of emitting luminescence<sup>127,128</sup>. The substrate can be produced by the co-expression of a reductase (*luxC*), a transferase (*luxD*), and a synthetase (*luxE*)<sup>127</sup>. Since the bioluminescence can be easily quantified, *LuxCDABE* operon has been widely used as a reporter in various studies.

When cell density is low, the expression level of *luxICDABEG* operon is low. LuxI enzymatically produces N-(3-oxohexanoyl)-homoserine lactone (3-oxo-C6-HSL), the AHL in *V. fischeri*<sup>129,130</sup>. 3-oxo-C6-HSL is small enough and capable to freely diffuse through the cell membrane<sup>8</sup>. As the population density increases, the AHL concentration reaches the critical level and intracellularly activates the transcriptional factor LuxR, which in turn induces the expression of *LuxICDABEG* operon by binding to the promoter  $P_{luxI}$ . The production of AHL thus is amplified, and the luminescence is subsequently produced.

In general, LuxI-homologous enzymes catalyze the production of AHL by directly linking the SAM (S-adenosylmethionine) and acyl-ACP (acyl carrier protein) by an amide linkage (Fig. 1-12). SAM and acyl-ACP are metabolic productions of methionine pathway and fatty acid metabolic cycle, respectively. They are abundant in most Gram-negative bacteria.

LuxR-homologous transcriptional factors consist of two function domains, N-terminal AHL-binding domain and C-terminal helix-turn-helix DNA binding domain<sup>131,132</sup>. The activation of LuxR needs sufficient amount of AHL. When AHL concentration is low, the N-terminal blocks C-terminal's activity. When AHL is abundant in cytoplasm, it binds to the N-terminal, thereby relieves the C-terminal. The activated C-terminal then binds to the *lux* box (a 20-bp inverted repeat) in *P<sub>luxI</sub>* promoter region<sup>131,133</sup>. It is found that LuxR functions as a homodimer<sup>134</sup> and recruits RNA polymerase to activate the transcription of *P<sub>luxI</sub>*<sup>3</sup>.

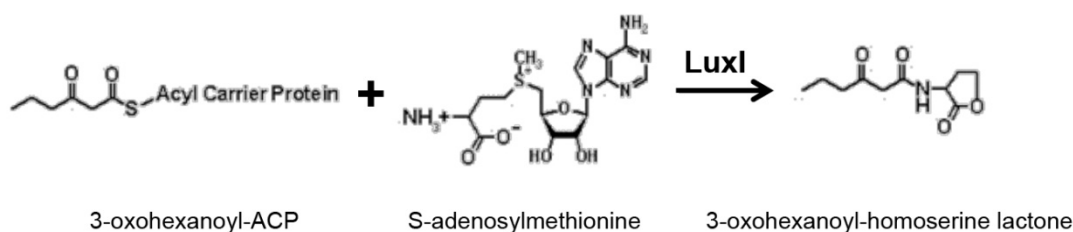


**Figure 1-12 Formation of 3-oxo-C6-HSL catalized by LuxI**

Adapted from “<http://www.photobiology.info/Lin.html>”

In *E. coli*, there's though no AHL-synthesizing gene, *sdiA* encodes a LuxR-homologous transcriptional factor. Recently, Houdt *et al* constructed a promoter-trap library and found that at least 15 promoters were either upregulated or downregulated when *E. coli* cells were exposed to synthetic 3-oxo-C6-HSL (production of LuxI). After deleting *sdiA*, all these responsiveness were eliminated, suggesting SdiA was the LuxR-like factor interacted with AHL<sup>135</sup>.

### 1.7.3 QS IN SYNTHETIC BIOLOGY

An increasing body of studies showed that, as the bacterial speaking approach, QS have attracted great interest of synthetic biologists. By harnessing the QS system, researchers attempted to engineer novel population behaviors, or to understand similar natural systems.

Recently, You and his coworkers made an autonomous cell population controller using luxRI system<sup>14</sup>. They controlled the *E. coli* population density by regulating a killing gene, *ccdB*. Briefly, the expression of *ccdB* was driven by the *P<sub>luxI</sub>*, which was induced by LuxR-AHL complex. As cell density increased, CcdB was expressed to inhibit the growth.

By assembling QS module with recently described light detection module<sup>12</sup>, Voigt and

his coworkers constructed a fascinating ‘edge-detection’ system<sup>11</sup>. They programmed *E. coli* cells to only express *lacZ* gene at the edge of light and dark regions. In brief, light was applied through a mask onto a bacterial lawn. For the cell in light region, the expression of both *luxI* and *cI* was induced. The expressed *CI* repressor blocked the transcription of *lacZ*, which was driven by a hybridized promoter  $P_{lux-\lambda}$ . Meanwhile, AHL was synthesized by *LuxI* and diffused out to the extracellular environment, into the cytoplasm of neighboring cells in dark region. On the other hand, for the cells in dark region, external AHL accumulated and binded to the constitutively expressed *LuxR*, which in turn activate the *lacZ* expression. Thus these ‘neighboring’ cells produced a pigment<sup>11</sup>.

In a biosystem, many nonproducers of ‘common good’ grow faster than producers, since nonproducers never pay any cost in synthesis? To answer this question, Chuang et al programmed two types of cells based on a QS system. Producers contained an intact QS system and a QS controlled *Cm<sup>r</sup>* gene, while non-producers lacked the AHL-producing gene. Here, AHL was the ‘common good’. When grown in *Cm*-containing medium, AHL rendered both types of cells the resistance to the *Cm*. But nonproducers saved the cost of synthesizing AHL. The results showed that nonproducers indeed grew faster than the producers. However, in some circumstances, producers still increased with time. The phenomenon was known as Simpson’s paradigm<sup>136</sup>.

Communication is critical for ecosystems. In a synthetic predator-prey system, predators and preys were designed to constantly secrete 3OC<sub>12</sub>HSL and 3OC<sub>6</sub>HSL into the environment, respectively. Accumulated 3OC<sub>12</sub>HSL activated the killing gene *ccdB* expression in preys, while 3OC<sub>6</sub>HSL initiated *ccdA* expression in the predator when reaching the threshold concentration. The *CcdA* is an antidote that blocks the toxicities of constitutively expressed *CcdB* in predators. Thus, the survival of predators relied on the number of preys. The thrive of predators on the contrary limited the growth of preys<sup>74</sup>.

## 1.8 STUDY OBJECTIVES

Traditionally, pattern formation has been studied with some success by genetic dissection of the gene networks involved<sup>137,138</sup>. However, the origin and mechanism of the patterns formed are difficult to elucidate in many cases due to the overwhelming physiological complexity associated with the natural context. On the other hand, many theoretical models were developed to explain and simulate the organized biological patterns, but few of them can be experimentally tested<sup>55,139,140</sup>. The emerging synthetic biology may offer a way to explore the mechanisms associated and bridge the gap of knowledge. An important determinant in the developmental processes is the coordination of cell movement

by cues which signal various states of the cells<sup>141,142</sup>.

In this study, I mainly study patterns obtained from the simplest signal of this kind, with cell motility controlled by the local cell density, and investigate the underlying mechanism(s).

## **CHAPTER 2**

## **MATERIALS AND METHOD**

## **2.1 GENERAL METHODS**

### **2.1.1 PREPARATION OF BACTERIAL GENOMIC DNA**

1.5 ml of mid-exponential culture was pelleted and washed with PBS once. The cells were resuspended into 567 µl of TE buffer (pH 8.0) supplemented with 10 µg ml<sup>-1</sup> lysozyme, followed by 1 h incubation at 37 °C. 30 µl 10% SDS solution was added and mix thoroughly until cell lysis. 100 µl 1 M NaCl was added and mixed well with vortex. 80 µl CTAB was added and mixed. After that, 780 µl phenol:chloroform:isoamyl alcohol (25:24:1) was added, gently inverted several times, and centrifuged at 13,000 rpm for 5 min in a bench-top microcentrifuge (Eppendorf, NY, USA). The aqueous layer (~650 µl) was carefully pipetted into a new 1.5 ml Eppendorf tube without touching other layers. Equal volume of chloroform was added and gently inverted several times to remove residual phenol. Centrifuged at 13,000 rpm for 5 min, and transfer upper layer into a new 1.5 ml Eppendorf tube. The genomic DNA was precipitated using 2 volumes of ice-cold ethanol. DNA was pelleted and washed twice with 70% ethanol and allowed to air dry for 3 min. 100 µl autoclaved ddH<sub>2</sub>O was added to dissolve the DNA.

### **2.1.2 ISOLATION OF PLASMID DNA USING QIAPREP® MINIPREP KIT**

Single colony was inoculated into 5 ml LB containing appropriate antibiotics, and shaked at 32 °C or 37 °C overnight. Cells were pelleted and resuspended in 250 µl Buffer P1, followed by the addition of 250 µl Buffer P2 and 350 µl Buffer N3, respectively. After centrifugation at 13,000 rpm for 10 min, the supernatant was transferred onto the QIAprep Spin Column. The loaded column was centrifuged for at 3,000 for 0.5 min, and the flow-through was discarded. The column was then washed using 750 µl Buffer PE, centrifuged for 30 s at 3,000 for 1 min the flow-through discarded. 1 min centrifugation at maximum speed was carried out to remove residual ethanol. The column was placed in a 1.5 ml Eppendorf tube and allowed to air dry for 2 min. The DNA was then eluted with 50 µl EB solution.

### **2.1.3 AGAROSE GEL ELECTROPHORESIS**

Firstly, 0.7-2% (w/v) low melting temperature agarose was completely dissolved in

1xTAE solution by microwave. After the solution was cool down to 50-55 °C, 0.5 g ml<sup>-1</sup> of EB was added, mixed well, and poured into an agarose gel casting tray. Appropriate number of combs was placed into the gel tray. The agarose gel was allowed to harden for 15-20 min. and then, the combs were removed, the gel can be stored at 4 °C for two weeks or directly placed into a gel tray covered with 1xTAE buffer solution. Loading buffer was added to DNA samples, mixed well, and loaded into the gel wells with 1 kb plus DNA ladder as molecular weight marker. Electrophoresis at 80-130 V for appropriate time. DNA bands were visualized using UV gel imaging system (Chinetec Scientific, HK, China).

#### **2.1.4 RESTRICTION ENDONUCLEASE DIGESTION**

Restriction digestion of DNA was carried out following the conditions recommended by the manufacturer. For multiple enzyme digestions, the most favorable condition for all the enzymes was chosen. If the conditions were incompatible, the digestions were carried out separately from low to high in terms of the salt concentrations in corresponding enzyme buffers.

#### **2.1.5 EXTRACTION OF DNA FRAGMENTS FROM AGAROSE GEL USING QIAQUICK® GEL EXTRACTION KIT**

DNA was first separated by agarose gel electrophoresis. The ethidium bromide stained gel was placed on a UV trans-illuminator (UVP, CA, USA). The trans-illuminator was set to long-wavelength UV to prevent mutagenesis. Bands of interest were cut out with a blade. The empty agarose gel was removed from the DNA-containing gel as much as possible. The excised band was then placed into a 1.5 ml Eppendorf tube. The recovery of the DNA was carried out with QIAquick® Gel Extraction Kit according to the manufacturer's protocol.

#### **2.1.6 PREPARATION OF PLASMID VECTOR FOR LIGATION**

When a single restriction endonuclease digestion or blunt end digestion was carried out, 0.2 µl of CIP was added to 50 µl digestion mixture at the end of digestion incubation, and incubated at 50 °C for 1 h. Subsequently, the DNA was immediately applied to agarose gel electrophoresis, and followed by purification using QIAquick® Gel Extraction Kit.

### **2.1.7 DNA LIGATION**

In the case of sticky ends, the ligations were carried out in 5 µl volume in the presence of 0.5 µl 10 × T4 DNA ligase buffer, 1 U of T4 DNA ligase, appropriate amount of vector and insert DNA. The ligation mixture was incubated at 16 °C for 4 h. In the case of blunt ends, 5% (w/v) PEG 4000 and double amount of T4 DNA ligase were added, and incubated overnight at 16 °C. Generally, the mole ratio of insert and vector is 1:1.

### **2.1.8 ELECTROCOMPETENT CELLS PREPARATION**

The day before the experiment, cells were streaked onto LB agar supplemented with appropriate antibiotics from a frozen glycerol stock. One single colony was picked and inoculated into 1 ml LB broth with appropriate antibiotics. After around 3-4 h incubated at 37 °C and spun at 230 rpm, 500 µl of the culture was subcultured into 50 ml medium in a 250 ml conical flask and grown at 37 °C in a rotating incubator till OD<sub>600</sub> reached ~0.3. Bacterial cultures were chilled in an ice/water bath for 15 min, and then transferred to a pre-cold 50-ml Falcon tube (Iwaki) and pelleted at 4,200 rpm at 0 °C for 2 min. The supernatant was poured off and the pellet was resuspended in 50 ml ice-cold ddH<sub>2</sub>O. Cells were pelleted and suspended again in 50 ml ice-cold ddH<sub>2</sub>O. Lastly, the pellet was resuspended in 400 µl 10% ice-cold glycerol, stored at -80 °C in 100 µl aliquots until use.

### **2.1.9 ELECTROPORATION OF BACTERIAL CELLS**

DNA was added into an Eppendorf tube, and put in an ice-water mixture. An aliquot of 50 µl electrocompetent cells was thawed on ice and mixed with the DNA. The DNA-cell mixture was then added into a pre-cold 0.1-cm cuvette (BioRad, Hercules, CA, USA). The electroporation was carried out with the pulse condition of 25 µF, 1.80 kV and 200 Ω using an *E. coli* pulser (BioRad, Hercules, CA, USA). After the pulse, the bacterial cells were collected with 1 ml LB and recovered at 32 or 37 °C with shaking for 1 h. Finally, the cells were briefly spun at 8,000 rpm in a bench-top microcentrifuge for 0.5 min and spread onto LB agar plates supplemented with appropriate antibiotics.

### **2.1.10 DNA SEQUENCING**

Sequencing reactions were performed using the ABI PRISM® Big-dye™ terminator cycle sequencing ready reaction kit following the manufacturer's recommendation. Briefly, 4

$\mu$ l Big-dye terminator ready reaction mix, 0.3-0.5  $\mu$ g of DNA, and 10  $\mu$ g of sequencing primer was mixed, and adjusted to final 10  $\mu$ l volume with ddH<sub>2</sub>O. PCR was carried as 25 cycles of denaturing (96 °C, 10s), primer annealing (50 °C, 5s) and extension (60 °C, 4 min). And then, the sequencing reaction products were purified using DyeEx™ 2.0 Spin Kit. The column was first thoroughly mixed and centrifuged at 2, 000  $\times$  g for 1 min. The volume of the sequencing reaction product was increased to 20  $\mu$ l by adding ddH<sub>2</sub>O. The sequencing product was mixed well and loaded onto the center of the column. The sample-containing column was centrifuged again at 2, 000  $\times$  g for 1 min. The elution was then ready for analysis using the ABI PRISM® 310 genetic analyzer.

### **2.1.11 RECOMBINEERING**

One single colony was picked and inoculated into 1 ml LB broth with appropriate antibiotics. After around 3-4 h incubated at 37 °C and spun at 230 rpm, 500  $\mu$ l of the culture was subcultured into 50 ml medium in a 250 ml conical flask and grown at 37 °C in a rotating incubator till OD<sub>600</sub> reached 0.2-0.3. Flasks were then incubated in a water-bath at 42 °C for 15 min with shaking. Subsequently, flasks were put into ice-water mixture quickly and incubated for 15-30 min. Following steps were the same as those of preparation electrocompetent cells. After spreading cells onto LB plates supplemented with appropriate antibiotics, the plates were incubated at 32 °C to avoid expressions of  $\lambda$  proteins.

### **2.1.12 COLONY PCR SCREENING OF RECOMBINANTS**

Colony PCR was used to confirm if recombineering was successful using a pair of primers with one homologous to the bacterial chromosome and the other homologous to the antibiotics resistant cassette. Each PCR reaction included: ExTaq DNA polymerase and Ex buffer; 250 mM dNTP; 200 nM of each primer. Small portion of each fresh bacterial colony was transferred into the reaction tube by sterilized tips. The program was: 95 °C for 5 min; 30 cycles of: 95 °C for 30 s, 55 °C for 30 s, 72 °C for 2 min; 72 °C for 5 min.

### **2.1.13 CRE-MEDIATED REMOVAL OF ANTIBIOTIC RESISTANCE CASSETTES**

Cre- (in p705Cre) mediated removal of chloramphenicol resistance cassette was performed as described by Buchholtz et al<sup>143</sup>. Plasmids p705cre were electroporated into the

correct recombinants, spread onto LB agar plate supplemented with chloramphenicol (25 mg ml<sup>-1</sup>), and incubated overnight at 32 °C. One single colony was inoculated into 1 ml LB broth without antibiotics, incubated at 32 °C, spun at 230 rpm for 3-4 h. The 1-ml culture was then shifted into 37 °C rotary incubator and incubated overnight. Aliquot was streaked onto a LB agar plate without antibiotics, and incubated overnight at 32 °C. Several single colonies were picked and streaked onto LB plates containing no antibiotics or chloramphenicol (25 mg ml<sup>-1</sup>) or kanamycin (50 mg ml<sup>-1</sup>). If no growth was observed on both selective LB agar plates, it indicated that both antibiotic resistant cassette on the chromosome and p705Cre had been successfully removed.

### **2.1.14 P1 TRANSDUCTION**

#### **2.1.15.1 PREPARATION OF LYSATE**

Overnight culture was 1:100 diluted into 5-ml LB broth until it reaches OD<sub>600</sub> of 0.1-0.2. 50 µl of 1 M CaCl<sub>2</sub> and 15 µl of P1vir (prepared from wild type MG1655 strain) were added. The cell-virus mixture was incubated at 37 °C for 3 h with vigorous shake until cells lyse. Subsequently, 1 drop of chloroform was added. After 10 min at 37 °C, 1 ml of cell lysis was transferred into a 1.5-ml Eppendorf tube, centrifuged for 2 min at maximum speed. Supernatant was transferred into a new tube, into which two drops of chloroform was added. Then, the lysate was ready to use and also could be stored at 4 °C until use.

#### **2.1.15.2 TRANSDUCTION**

Overnight culture of recipient was 1:100 diluted into 5-ml LB broth until it reaches OD<sub>600</sub> of 0.7. 50 µl CaCl<sub>2</sub> was added to the cells with gentle shaking. 200 µl culture was then transferred into an Eppendorf tube, followed by adding 30 µl prepared lysate, incubated at 37 °C for 20 min. After that, 100 µl 30% citrate and 0.5 ml LB was added, and incubated at 37 °C for 1 h. The cells were pelleted using microcentrifuge. Supernatant was discarded. The pellet was then washed twice with LB broth, and resuspended with 30 µl 30% citrate and 70 µl LB broth. Finally, the cells were spreaded onto LB agar plates supplemented with appropriate antibiotics and citrate, incubated at 37 °C overnight.

### **2.1.15 WESTERN BLOT**

Protein extracts were prepared and subjected to Western blot analysis as described by Sambrook et al<sup>144</sup>. In brief, after designated treatment, cells were scraped off the plates,

washed with PBS and dispersed in 5 volumes of ice-cold suspension buffer. An equal volume of SDS gel-loading buffer was added, and the samples were boiled for 10 min. After centrifugation, protein extracts were resolved on SDS-PAGE and transferred onto PVDF membranes. After blocking with 5% skim milk in 1×TBS-T for 1 h, the membranes were probed with various first and second antibodies and developed with enhanced chemiluminescence by following the manufacturer's instructions (Pierce, IL, USA). The levels of proteins were determined using densitometry with Image J software, which allowed direct comparisons between experimental sets.

## **2.2 BUFFER SOLUTION**

### **Ammonium persulfate (AP), 10%**

Dissolve 5 g ammonium persulfate in ddH<sub>2</sub>O with final volume of 50 ml and store at -20 °C in 1 ml aliquots

### **DTT, 1 M**

Dissolve 15.45 g DTT into 100 ml autoclaved ddH<sub>2</sub>O and store at -20 °C in 1 ml aliquots

### **EDTA pH 8.0, 500 mM**

Dissolve 186.1 g Na<sub>2</sub>EDTA.2H<sub>2</sub>O in 800 ml H<sub>2</sub>O, adjust pH to 8.0 with 10 N NaOH, adjust final volume to 1 L, autoclave and store at room temperature

### **Ethidium bromide (EB), 10 mg ml<sup>-1</sup>**

Dissolve 0.2 g EB in 20 ml ddH<sub>2</sub>O, mix well and store at room temperature in dark

### **Freezing Medium for mammalian cells**

5.0 ml DMEM or MEM

4.0 ml FBS

1.0 ml DMSO

Prepare freshly

### **HEPES pH 8.0, 1 M**

Dissolve 238.3 g HEPES free acid in 800 ml of ddH<sub>2</sub>O and adjust the pH to 8.0 with NaOH. Add ddH<sub>2</sub>O to 1 L, autoclave and store at room temperature.

### **Loading Buffer for Total Protein Extraction**

50 ml 1 M Tris-Cl, pH 7.0

200 ml 10% SDS

100 ml Glycerol

Add ddH<sub>2</sub>O to 500 ml, autoclave and store at 4 °C

Add 1 M DTT to final 200 mM prior to use

### **Paraformaldehyde (PFA), 4%**

4.0 g paraformaldehyde  
100 ml 1×PBS  
Incubate at 55 °C for 5 h until completely dissolved  
Store at 4 °C for up to 2 weeks

**Phosphate-buffered Saline (PBS), 10×**

80.0 g NaCl  
2.0 g KCl  
26.8 g Na<sub>2</sub>HPO<sub>4</sub>.7H<sub>2</sub>O  
2.4 g KH<sub>2</sub>PO<sub>4</sub>  
Adjust pH to 7.4 with 10 N NaOH  
Add ddH<sub>2</sub>O to 1 L, autoclave and store at room temperature.

**Protease Inhibitors, 25×**

Dissolve one tablet of Complete® Protease Cocktail (Roche) into 2.0 ml ddH<sub>2</sub>O  
Store at -20 °C up to one month

**Rnase A, 10 mg ml<sup>-1</sup>**

Dissolve 50 mg Rnase A in 5 ml 10 mM Tris-Cl (pH 7.5) and 15 mM NaCl, boil for 15 min, and store at -20 °C in 1 ml aliquots.

**SDS-PAGE Tris-glycine Buffer, 5×**

15.1 g Tris base  
72.0 Glycine  
5.0 g SDS  
Add ddH<sub>2</sub>O to 1 L and store at room temperature

**SDS Sample Buffer, 6×**

14 ml 4×Tris-Cl/SDS (pH 6.8)  
  
6.0 ml Glycerol  
2.0 g SDS  
1.86 g DTT  
9.6 mg Bromphenol Blue  
Add ddH<sub>2</sub>O to 20 ml and store 4 °C in 1 ml aliquots

**Suspension Buffer for Total Protein Extraction**

10.0 ml 5 M NaCl  
5.0 ml 1 M Tris-Cl (pH 7.5)  
1.0 ml 500 mM EDTA (pH 8.0)  
Add ddH<sub>2</sub>O to 500 ml and store at 4 °C

**TE Buffer, pH 8.0**

5.0 ml 1 M Tris-Cl (pH 8.0)  
1.0 ml 500 mM EDTA (pH 8.0)  
Add ddH<sub>2</sub>O to 500 ml, autoclave and store at room temperature

**Transfer Buffer for SDS-PAGE, 10×**

60.5 g Tris base  
288.3 g Glycine  
Add ddH<sub>2</sub>O to 2 L and store at room temperature

### **Tris-Cl pH 8.0, 1 M**

Dissolve 121.14 g Tris base in 1 L ddH<sub>2</sub>O  
Adjust pH to 8.0 with 1 N HCl  
Autoclave and store at room temperature

### **Tris-Cl/SDS, pH 6.8, 4×**

30.25 g Tris base  
Adjust pH to 6.8 with 1 N HCl  
20.0 ml 10% SDS  
add ddH<sub>2</sub>O to 500 ml  
Sterilize with 0.45 µm filter and store at room temperature

## **2.3 BACTERIAL STRAINS AND PLASMIDS**

Strains and plasmids used in this study are listed in **Table 2.1**. Oligonucleotides used are listed in **Table 2.2**. Strain CL-M is a motile *E. coli* K12 MG1655 strain, and strain CL-IM is a flagella-lacking mutant of *E. coli* K12 MG1655 strain. Both are kindly provided by Prof. Antoine Danchin (Institute Pasteur, Paris). Strain EQ44 is kindly provided by Prof. Terrence Hwa (UCSD). A single frozen glycerol stock was used throughout this study for each bacterial strain. For each experiment, cells were streaked onto LB agar with appropriate antibiotics from corresponding frozen glycerol stock. 3 to 5 colonies were randomly picked for following experiments. Plasmids pLD and pCRT-1 are kindly provided by Dr. Ron Weiss (MIT). Plasmid pLuxRI2 is kindly provided by Dr. Lingchong You (Duke).

## **2.4 BACTERIAL CELL CULTURE**

Unless otherwise stated, the following conditions were used throughout this study. Plasmids were maintained with 50 µg ml<sup>-1</sup> Kanamycin and 25 µg ml<sup>-1</sup> Chloramphenicol (Sigma, MO, USA). It had been shown that both AHL degradation rate and *E. coli* cell motility were influenced by pH change in media. To minimize the effects of pH, for bulk culture, we used Luria–Bertani (LB) medium containing 2.5 g Yeast extract, 5 g Bacto Tryptone, 5 g NaCl per liter, buffered by 0.1 M HEPES (pH 8.0). The pH variation was less than 0.3 (measured with PB-10 pH Meter, Sartorius, Goettingen, Germany). To prepare semi-solid agar, 10-ml of the above medium containing 0.25% agar was poured into a Petri dish, and allowed to harden at room temperature for 90 min. For the experiments with varying degree of cI expression, various concentrations of the inducer anhydrotetracycline (aTc, Clontech) were added to the same media before the agar hardened. Unless otherwise

stated, all other reagents were from Sigma. All experiments were carried out at 37°C.

Before each experiment, cells underwent seed culture, pre-culture, and then into experimental culture. Medium was pre-warmed prior to use. Strains were first inoculated from fresh single colonies and cultured in 14-ml tubes (Falcon) with vigorous shaking (seed culture), followed by a round of preculture growth in the same medium (till mid-exponential phase). After that, cells were subcultured (1:200 dilution) into fresh pre-warmed medium with appropriate antibiotics and aTc, when applicable. For gene expression experiments, samples were taken at different time points for measurements of OD<sub>600</sub> (measured with Cary Bio 300 UV-Vis Spectrophotometer, Varian) and RT-qPCR (see Method 2.6). For pattern formation experiments, when OD<sub>600</sub> reached 0.1-0.2, a suspension of cells (2-μl) was spotted at the centre of a pre-warmed semi-solid agar plate. To measure relative diffusion coefficient in semi-solid agar, after preculture growth, cells were diluted 200-fold into the same pre-warmed media containing 0.25% agar. Cell-agar mixtures were poured into Petri dishes and allowed to harden at room temperature for 90 min, and then moved back into 37 °C incubator. After various duration of incubation, plates were taken out for measurements of cell density (see **Method 2.9**) and diffusion coefficient (see **Method 2.10**) in triplicate and discarded after use. Similarly, for the aggregation test, receiver cells were diluted 10-fold into a fresh medium containing 0.25% agar when OD<sub>600</sub> reached 0.1-0.2. Sender cells were grown to the same OD value and concentrated 16-fold, unless otherwise stated. After the cell-agar mixture solidified, 5-μl of sender cells was spotted at the center, followed by 12-h incubation at 37 °C.

## 2.5 QUANTITATIVE REAL-TIME RT-PCR

Approximately 10<sup>8</sup> cells from each condition were immediately mixed with RNA Bacteria Protect Reagent (Qiagen). Total RNA was extracted using the Rneasy Mini kit (Qiagen) according to the manufacturer's protocol, followed by treatment with Amplification Grade Dnase I (Invitrogen). RNA quality was checked by electrophoresis on agarose gel and the absence of DNA contamination was confirmed by PCR. RNA yield was estimated using a NanoDrop 1000 spectrophotometer (Thermo Scientific). To reverse transcribe RNA, about 0.4 μg RNA, 200 ng random primer (Invitrogen), 0.5 mM dNTP Mix, and up to 13 μl Rnase-free distilled water was mixed and heated to 65°C for 5 min and chilled in ice for 1 min. And then 10 μM DTT, 10 unit SuperScript™ III Reverse Transcriptase (Invitrogen) and 1 μl RNaseOUT™ Recombinant Rnase Inhibitor (Invitrogen) were added. The reaction was incubated 5 min at 25 °C, 60 min at 50 °C, and 15 min at 80 °C. Reactions without reverse transcriptase were conducted as controls for the following qPCR reactions. The cDNA

samples were diluted 1:40 with PCR grade water and stored at -20 °C until use. Power SYBR Green PCR Master Mix (ABI) was used for qPCR amplification of the amplified cDNA. 1 µl of the 1:10 cDNA dilution; 200 nM of forward and reverse qPCR primers; 10 µl of SYBR Green PCR Master Mix and up to 20 µl of PCR grade water were mixed in a well of a MicroAmp Fast Optical 96-well reaction plate (ABI). The non-template control (NTC) contained sterile water instead of cDNA template was included during each qPCR experiment to check the purity of the reagents. Each reaction was performed in triplicate. The qPCR reactions were performed using StepOnePlus™ Real-time PCR system (ABI) with the following programme: 2 min at 50 °C, 10 min at 95 °C, and 40 cycles of denaturation (10 s, 95 °C), annealing and elongation (30 s, 60 °C). Data were acquired at the end of the elongation step. The specificities of accumulated products were verified by melting-curve analysis. A melting curve was run at the end of the 80 cycles to test for the presence of a unique PCR reaction. The qPCR products were checked by electrophoresis on 2% agarose gels. The primers for real-time PCR were designed with the Primer premier 5.0 software package (<http://www.Premierbiosoft.com/>) and synthesized by Invitrogen (**Table 2.2**). DNA gyrase subunit B (*gyrB*), D-1-deoxyxylulose 5-phosphate synthase (*dxs*) and 16S ribosomal RNA (*16S rRNA*) were tested as reference genes. They were analyzed in various cell density conditions ( $OD_{600}=0.05-1.2$ ) and aTc concentrations (0-3 ng ml<sup>-1</sup>). All of them showed comparative low variation in various conditions. Unless otherwise stated, 16S rRNA was used to normalize the abundance of various genes of interest. The relative fold change in mRNA quantity was calculated for each gene using the relative standard curve method<sup>10</sup>. To construct the standard curves for 16S rRNA, cI, and cheZ, pCIcheZ16S (see **Table 2.1**) was 10-fold serially diluted, ranging from  $10^{-5}$  to 10 ng µl<sup>-1</sup>. For each RNA preparation, at least three independent real-time PCR measurements were performed.

## 2.6 ONE-DIMENSIONAL PATTERN FORMATION

I made rectangle plastic plates in two sizes: 3 cm by 7 cm and 6 cm by 10 cm. 3- and 10-ml of 0.25% agar was added to the small and large size plates, respectively. After agar hardened, cells were horizontally inoculated as a line of 3 or 6 cm using a sterile coverslip<sup>15</sup> and incubated overnight at 37 °C.

## 2.7 IMAGE CAPTURING

The bright field images were taken using Canon EOS 450D digital camera with a Canon

EF 50mm f/1.8 II lens and an exposure setting of f5.6/0.6s/ISO200. The agar plates were illuminated by a circular white LED array with the diameter of 30 cm 10cm bellow, similar to what was described by Budrene and Berg<sup>45</sup>. The time-lapse photographs were acquired with an aid of a timer shutter release controller (TC-80N3a, YongNuo, HK, China). Fluorescence images of the agar plates were captured using a Xenogen IVIS 100 imaging system (Caliper LifeSciences, Hopkinton, MA, USA) with the exposure time of 30 s.

## **2.8 FOURIER ANALYSIS OF PATTERN FORMATION**

The time-lapse imaging for 1-D stripe formation was used for Fourier analysis. At each time point, a 1-D intensity profile was computed perpendicular to the stripes. These 1-D profiles were padded with mean intensity to 1,024 pixels and applied with a Hamming window. Standard MATLAB (Mathworks, Natick, MA, USA) build-in Fast Fourier Transform (FFT) function was used to computer the mean square power spectra from the 1-D intensity profiles.

**Table 2-1 Strains and plasmids used in this study**

<b>Strains or plasmids</b>	<b>Genotype or description</b>	<b>Reference or source</b>
<b>Strains</b>		
CL-M	CL-M is also named as AMB1655 by Prof. Antoine Danchin. It is derived from CL-IM by selecting for motility on soft agar, and CL-M was purified as a strain that was stably motile by Dr. Agnieszka Sekowska in Prof. Danchin's lab. This mobile strain was sequenced using Solexa. Only one G>T mutation in the <i>gudd</i> gene at 2917303 was found when compared to the parent strain (CL-IM). Later, Dr. Jin Ye in the Huang lab found an IS inserted upstream of <i>fkhDC</i> gene in the motile CL-M whilst the nonmobile strain, CL-IM, does not have the IS insertion.	Prof. Danchin
CL-IM	This strain was obtained from <i>E. coli</i> Genetic Resources at Yale CGSC, the Coli Genetic Stock Center by Prof. Danchin as an immotile <i>E. coli</i> K12 strain MG1655 (F-, $\lambda$ , <i>rph-I</i> ). This <i>fnr</i> - subculture of MG1655 was sent as MG1655 (CGSC #6300) from 1986 to Oct. 2003. It is now given a new CGSC # of 8003. The genome of CL-IM was sequenced in Prof. Danchin's lab and the following mutations were found: a deletion spans 1395405-1409159 (13,755 bp). This is in the region of <i>ynaJ uspE fnr ogt abgT abgB abgA abgR isrA ydaL ydaM ydaN C0343sncRNA dbpA</i> .	Prof. Danchin
CL-M $\Delta$ <i>cheZ</i>	$\Delta$ <i>cheZ</i>	CL-M, this study
CL1	$\Delta$ <i>cheZ</i> , $\Delta$ <i>lac</i>	CL-M, this study
CL2	$\Delta$ <i>cheZ</i> , $\Delta$ <i>lac</i> , <i>bla</i> :P <sub>Ltet-OI-tetR</sub> at the <i>attB</i> site	CL1, this study
CL3	pCI <i>cheZ</i> , pLuxRI2	CL1, this study
CL3GFP	pCI <i>cheZ</i> , pLuxRI/GFP	CL1, this study
CL4	pLuxRI/GFP	CL-M, this study
CL5	pCI <i>cheZ</i> , pLuxRI/CI	CL2, this study
CL6	pCI <i>cheZ</i> $\Delta$ <i>cheZ</i> , pLuxRI/GFP	CL1, this study
CL7	pCI <i>cheZ</i> $\Delta$ <i>clI</i> , pLuxRI2	CL1, this study
CL8	pCI <i>cheZ</i> , pLuxR	CL1, this study
CL9	pCI <i>cheZ</i> , pLuxI	CL1, this study
CL10	pCI <i>cheZ</i> $\Delta$ <i>clI</i> , pLuxR	CL1, this study
CL11	pCI <i>cheZ</i> $\Delta$ <i>cheZ</i> , pLuxR/GFP	CL1, this study
CL12	pCI <i>cheZ</i> $\Delta$ <i>cheZ</i> , pLuxRI2	CL-M, this study
CL13	pCI <i>cheZ</i> $\Delta$ <i>cheZ</i> , pLuxR	CL-M, this study
CL14	pLuxRI/GFP	CL-IM, this study
CL15	pLacheZ	CL1, this study
CL16	$\Delta$ <i>cheZ</i> , $\Delta$ <i>lac</i> , $\Delta$ <i>sdiA</i>	CL1, this study
CL17	$\Delta$ <i>cheZ</i> , $\Delta$ <i>lac</i> , $\Delta$ <i>luxS</i>	CL1, this study
CL18	pCI <i>cheZ</i> , pLuxRI2	CL16, this study
CL19	pCI <i>cheZ</i> , pLuxRI2	CL17, this study
CL20	$\Delta$ <i>cheZ</i> , $\Delta$ <i>lac</i> , P <sub>lacIq-lacI</sub>	CL1, this study
CL21	pLacheZ	CL20, this study
CL22	pLux <i>cheZ</i> , pLuxRI2	CL1, this study

CL22GFP	pLuxcheZ, pLuxRI/GFP	CL1, this study
CL23	pLuxcheZΔcheZ, pLuxRI2	CL1, this study
CL24	pLuxcheZ, pLuxR	CL1, this study
CL25	pLuxcheZ, pLuxI	CL1, this study
CL26	pLuxcheZ, pLuxRI2	CL16, this study
CL27	pLuxcheZ, pLuxRI2	CL17, this study
CL28	<i>P<sub>luxI</sub>-cheZ</i> at <i>attTn7</i> site	CL1, this study
CL29	pLuxRI2	CL28, this study
CL30	pLuxcheZLAA, pLuxRI2	CL1, this study
CL31	pCIcheZ, pLuxRI2	CL-MΔ <i>cheZ</i>
CL32	Δ <i>cheY</i>	CL-M, this study
CL33	pCIcheY	CL32, this study
CL34	pCIcheY, pLuxRI2	CL32, this study
EQ44	Δ <i>lacY</i> , <i>bla</i> :PLTet-O1-tetR at the <i>attB</i> site	<sup>145</sup>
DH10B	Cloning strain	Invitrogen
<b>Plasmids</b>		
pSim6	Ap <sup>r</sup> , pSC101 <i>ori</i> , λRed	146
pEGFP-loxP-CmR-loxP	Ap <sup>r</sup> , Cm <sup>r</sup> , pUC <i>ori</i> , <i>loxP</i> -Cm <sup>r</sup> - <i>loxP</i>	147
p705cre	Km <sup>r</sup> , pSC101 <i>ori</i> , <i>cre</i>	148
pLuxRI2	Cm <sup>r</sup> , ColE1 <i>ori</i> , Pcon- <i>luxR-luxI</i>	14
pLD	Km <sup>r</sup> , p15A <i>ori</i> , P <sub>λ(0-12)</sub> - <i>lacI</i> , P <sub>luxI</sub> - <i>cI</i>	13
pLacheZ	Cm <sup>r</sup> , pMB1 <i>ori</i> , Pcon- <i>cheZ</i>	This study
pCIcheZ	Km <sup>r</sup> , p15A <i>ori</i> , P <sub>λ(0-12)</sub> - <i>cheZ</i> , P <sub>luxI</sub> - <i>cI</i>	This study
pLuxRI/CI	pLuxRI2 carring P <sub>tet</sub> - <i>cI</i>	This study
pLuxRI/GFP	pLuxRI2 carring Pcon-superfolder gfp	This study
pLuxR/GFP	pLuxR carring Pcon-superfolder gfp	This study
pCIcheZΔcheZ	pCIcheZ lacking <i>cheZ</i> -coding region	This study
pCIcheZΔcI	pCIcheZ lacking <i>cI</i> -coding region	This study
pLuxR	pLuxRI2 lacking <i>luxI</i> -coding region	This study
pLuxI	pLuxRI2 lacking <i>luxR</i> -coding region	This study
pCIcheZ16S	pCIcheZ carring a copy of 16S rRNA gene	This study
pLuxcheZ	Km <sup>r</sup> , p15A <i>ori</i> , P <sub>luxI</sub> - <i>cheZ</i>	This study
pLuxcheZΔcheZ	pLuxcheZ lacking <i>cheZ</i> -coding region	This study
pLuxcheZLAA	<i>cheZ</i> in pLuxcheZ was tagged a LAA peptide	This study

**Table 2-2 Oligonucleotides used in this study**

Name	Sequence	Use
cheZ-del-f	ggaaaaactcaacaaaatctttagaaactggccatg tgaggatgcgactctcgagccatcatattcaataa	<i>cheZ</i> deletion
cheZ-del-r	ttatcagaccgcctgatatgacgtggtcacgccccatc aggcaatacaaagacacctcgaggactagtgaacctc	<i>cheZ</i> deletion
cheZ-del-conf-f	aactggccatgtgaggat	Confirmation
cheZ-del-conf-r	gccacatcaggcaataca	Confirmation
lacIZYA-del-f	gccccatggcatatgcgcggccaagagaggtaat tcagggttgtaatctcgagccatattcaataaac	<i>lac</i> operon deletion
lacIZYA-del-r	tccatgcggatggctaatgttagatcgctgaacttgc taggcctgataagacacctcgaggactagtgaacctc	<i>lac</i> operon deletion
lac-del-conf-f	ggcagaatgttaatgaatta	Confirmation
lac-del-conf-r	tccctgcgtttgttcat	Confirmation
cheZ-f	atgatgcaccaatcaatcaa	Cloning <i>cheZ</i> into pLD
cheZ-r-Nhe	ctagctagctaaaatccaagactatccaac	Cloning <i>cheZ</i> into pLD

pLD-rot-f-xba	gctctagagtttccataggctccgc	Linearing <i>P<sub>luxI</sub>-cI</i>	pLDcheZ	flanking
pLD-rot-r-cla	ccatcgatgagtaggacaaatccgcgg	Linearing <i>P<sub>luxI</sub>-cI</i>	pLDcheZ	flanking
cl-f-cla	ccatcgatcttacgtcacactattgtatcg	Cloning <i>P<sub>luxI</sub>-cI</i> into linearized pLDcheZ		
cl-r-xba	gctctagaagaacacccgtccgatcattaa	Cloning <i>P<sub>luxI</sub>-cI</i> into linearized pLDcheZ		
cl-f-sca	aaaagtactgagaattcacacagggtac	Cloning <i>cI</i> into pCRT-1		
cl-r-not	aaagccgcgtagaagaacaccctgcccga	Cloning <i>cI</i> into pCRT-1		
gfp-f-sac	<u>cgagcttgcggctagctcagtcctagtg</u> <u>ctagctggctagctactagagaaagag</u>	Cloning superfolder-gfp into pLuxRI2, the synthetic promoter is underlined		
gfp-f-sac	cgagcttttatcatcattgtacagttcatcc	Cloning superfolder-gfp into pLuxRI2		
gfp-conf-r	acgcacggaaaacttatgac	confirmation		
delcl-f-cla	acaatagtgtgaacgtaaagcatc	Deleting <i>cI</i> from pCIcheZ		
delcl-r-cla	gcatcgatcgcaagggtttcttag	Deleting <i>cI</i> from pCIcheZ		
lux-f	accaaccccttgcgttat	Linearing pLuxcdB flanking <i>lacZ-ccdB</i>		
lux-r-xho	ccgctcgagtaatgtcaggcgtcgacaag	Linearing pLuxcdB flanking <i>lacZ-ccdB</i>		
cheY-del-conf-f	atacgatttaaatcaggagtg	Confirmation		
cheY-del-conf-r	attgtggttgcacatcatagt	Confirmation		
cheY-f-DM	atggcgataaagaacttaattttggtgtggataaaa ttttccaccatcgacgcata	Generating double mutant cheY		
cheY-r-DM	tcacatgcccagttctcaaaggattttgtgagttttcc ccagctgcggcggtaaatggctcaccacccagc cactggcccccg	Generating double mutant cheY		
cheY-f	atggcgataaagaacttaaa	Cloning cheY** into pCI		
cheY-r-nhe	ctagctagctcacatgccaggttctcaa	Cloning cheY** into pCI		
16S-f-cla	ccatcgatattgaagagttgtatcatggc	Cloning 16S rRNA into pCIcheZ		
16S-r-xho	ccgctcgagaggagggtatccaacccg	Cloning 16S rRNA into pCIcheZ		
cheZ-LAA-f	atgatgeaaccatcaatca	Cloning cheZ-LAA into pluxcheZ		
cheZ-LAA-r-nhe	ctagctagttattaagctgtcaaagcttagttcg gtttgtcgaggctaaatccaagactatccaacaaa	Cloning cheZ-LAA into pluxcheZ		
RT-cheZ-f	ctgaaatcatgtggcg	Real-Time RT PCR primer for <i>cheZ</i>		
RT-cheZ-r	tgcgttatcgacactgagg	Real-Time RT PCR primer for <i>cheZ</i>		
RT-cl-f	ggtagtatgcagccgtactt	Real-Time RT PCR primer for <i>cI</i>		
RT-cl-r	caacctcaagccagaatgc	Real-Time RT PCR primer for <i>cI</i>		
RT-rrn-r	gtacaaatggcgcatacaaa	Real-Time RT PCR primer for 16S rRNA <sup>149</sup>		
RT-rrn-f	ttcatggagtcgagttgcag	Real-Time RT PCR primer for 16S rRNA <sup>149</sup>		

# **CHAPTER 3**

## **METHODS DEVELOPMENT**

### 3.1 MEASUREMENT OF CELL DENSITY IN SEMI-SOLID AGAR\*

Follow the same principle used in the regular spectrophotometer, we determine the cell density by measuring light transmittance of the cell-containing agar plate. Specifically, we positioned a parallel laser beam from 2 mW/650 nm laser diode (DA650-2-3, Huanic Co., Xi'an, China) perpendicularly to the agar plates and collected the light with a convex lens ( $f = 75$  mm) with an amplified Si photodetector (PDA36A, Thorlabs, NJ, USA). In order to ensure spatial resolution, the laser beam was passed through a 300- $\mu\text{m}$  pinhole. The Petri dish was placed on a motorized stage controlled by a computer running a customized LabVIEW program (National Instruments, Austin, TX, USA) to facilitate spatial and temporal measurements. The whole setup was kept in a warm room ( $37^\circ\text{C}$ ) throughout the experiment. See **Fig. 3-1**.

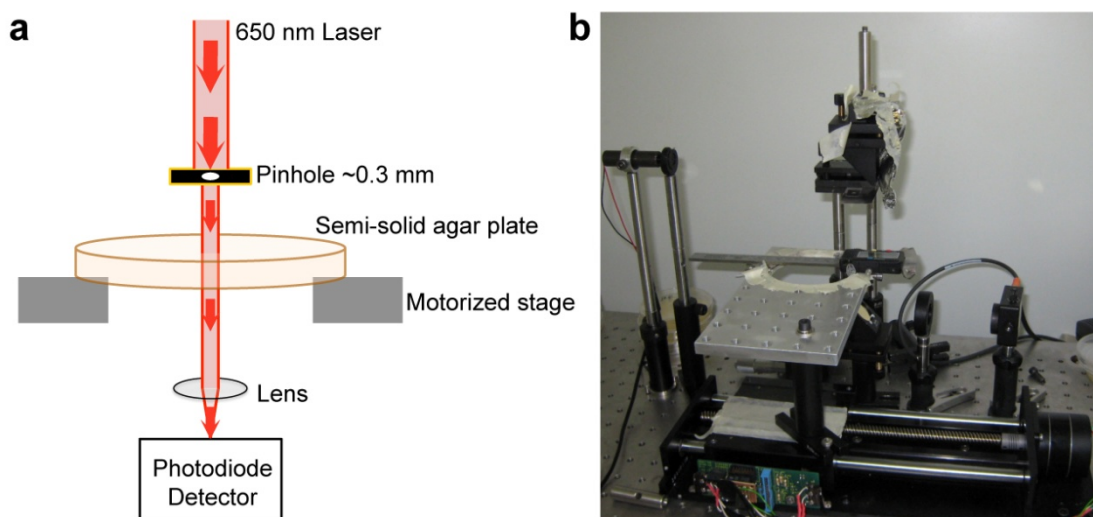


**Figure 3-1 The setup of the customized device for the real-time measurement of the spatiotemporal cell density profile in semi-solid agar dishes.**

A parallel 650-nm laser beam is guided through a 300- $\mu\text{m}$  pinhole, passed through the sample in semi-solid agar on the Petri dish, and collected via a convex lens to a photodiode detector. The light intensity is digitized with a DAQ device and stored on a personal computer. The spatiotemporal scanning is realized with a motorized stage controlled with the PC. The whole apparatus was placed in a warm room ( $37^\circ\text{C}$ ) throughout the experiment. **a**, Schematic diagram. **b**, Photograph of the experimental setting

---

\* This method was developed with the help of Mr. Xiongfei Fu, Mr. Hualing Zeng, Dr. Xiaodong Cui in Dept. of Physics, HKU

The 10-ml 0.25% agar in Petri dish usually forms an inverse-taper-shape with the lowest depth at the center. To avoid such systematic error on the optical path length, we measure the location-dependent transmittances for known standard cell densities. Hence we established a series of standard curves for any given radical positions. The agar plates with standard cell densities were generated with cells collected at mid-exponential phase ( $OD_{600} = 0.1\text{-}0.2$ ). The cell growth was stopped by washing twice with nutrient depleted LB<sup>4</sup>, and concentrated to  $9.6\times10^9$  cells ml<sup>-1</sup>. Subsequently, serial dilutions were carried out.

For each cell density, 15 ml of cells was vigorously mixed with equal volume of pre-warmed nutrient depleted medium containing 0.5% agar and poured into 3 Petri dishes with 10 ml each. All dishes were allowed to harden at room temperature for 90 min. The final cell densities ranged from 0.03 to  $9.6\times10^9$  cells ml<sup>-1</sup>. Dishes were moved into warm room (37 °C) and placed on the motorized stage, and light transmittance measurements were taken every 0.2-mm along the line across the centre of the dish.

The output laser intensities were digitized at 10 KHz (12 bit) using a DAQ device from National Instruments (NI USB-6009, National Instruments, Austin, TX, USA). The average of 1,000 data points was used to reduce the noise in the measurements at each position. The constant input laser intensity was ensured throughout the experiments with a regulated 5V power supply, verified using the photodetector. At each position along the radius, the ratio of the output intensities to the input intensities (measured using a blank agar plate), namely the transmittances ( $T$ ), were plotted against the known cell densities  $\rho$  for 21 different seeding densities (an example curve is shown in **Fig. 3-2a**). In total we generated 376 position-dependent density-transmittance standard curves (using a step size of 0.2 mm for a scanning range of 75 mm) and fitted the results to an exponential function for each position  $x$ :

$$T(x) = A(x) \exp[B(x) \cdot \rho] \quad [1]$$

where  $A(x)$  and  $B(x)$  are the position-dependent fitting parameters (**Fig. 3-2b**). From these experimentally determined standard curves, we could invert them to compute the real cell density profile  $\rho(x)$  from the measured transmittance profile  $T(x)$ . In subsequent experiments, we scanned the transmittances across the Petri dish for every experiment samples, and compute the spatial cell density profiles. The temporal density profiles were obtained by scanning the agar dish every 10 min with the help of a customized LabVIEW program.

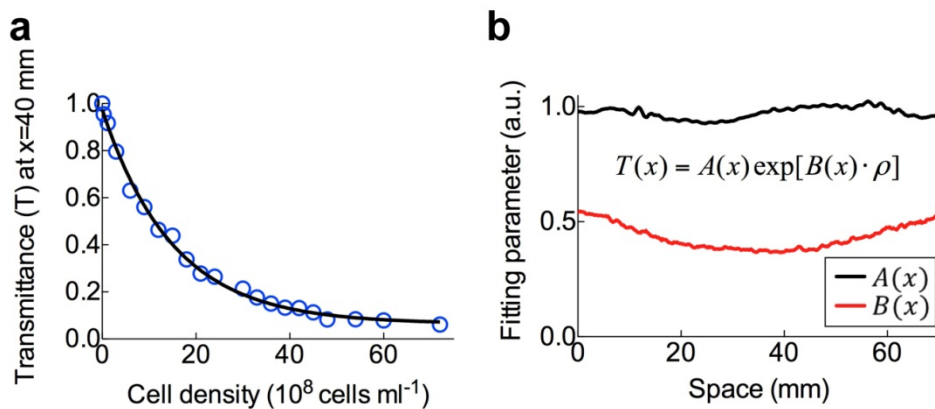


**Figure 3-2 The calibration curve of light transmittance vs. real cell density in semi-solid agar plates.**

**a**, An example of the fitted curve of the transmittance as the function of cell density at a specific position. **b**, The spatial distribution across the center of the dish, of the two fitting parameters for the standard curve,  $A(x)$  (black line) and  $B(x)$  (red line). This is derived from 376 standard curves (scanning range = 75 mm; step size = 0.2 mm).

### 3.2 MEASUREMENT OF DIFFUSION COEFFICIENT IN SEMI-SOLID AGAR<sup>§</sup>

A crucial feature needed to characterize for the engineered strain is the density dependence of cell motility in semi-solid agar. Microscopy-based single-cell tracing methods are technically challenging to implement at high cell densities where the cells frequently run into each other, and in thick agar where the cells move in-or-out of focus in the  $z$ -direction. Also, a large number of single-cell tracing experiments need to be carried out over long times to obtain good statistics. Since the swim-and-tumble motion of *E. coli* cells could be described macroscopically as a diffusive process<sup>150</sup>, we aimed to directly quantify the density dependence of diffusion with a population of *E. coli* cells.

Here, we modified a Continuous Fluorescence Photobleaching method (CPB)<sup>151</sup> to quantify the random motion of *E. coli* cells in semi-solid agar. This method utilized a fine laser beam to photobleach green fluorescent proteins (GFP) expressed by *E. coli* cells, and deduces the diffusion coefficient from the decay time of photobleaching. This is based on the fact that the diffusion of *E. coli* cells in and out of the photobleaching region affects the decay of fluorescent intensity. The faster the diffusion, the faster the unbleached

<sup>§</sup> This method was developed with the help of Mr. Xiongfei Fu and Mr. Sihong Li in Dept. of Physics, HKU

GFP-carrying *E. coli* cells refreshed the bleaching region, which leads to slower decay of the total fluorescent intensity observed.

### 3.2.1 PRINCIPAL OF THE CPB METHOD

Quantitatively, we considered a homogeneous distribution of cells diffusing in a semi-solid agar. The fluorescent intensity of GFP-expressing *E. coli* cells were collected from a cylindrical volume of  $R^2z$ , where  $R$  is the radius of the beam,  $z$  is the depth of the field of the objective. Without photobleaching, the total fluorescent intensity observed should be constant over time. However, if the laser power was high, photobleaching would take place over a cylindrical volume of  $R^2Z$ , where  $Z$  is the thickness of the LB agar ( $\sim 1.6$  mm). The rate of fluorescent intensity decay would be expected to depend on three parameters: the photostability of GFP molecules, the laser intensity, which causes photobleaching, and the diffusion coefficient of *E. coli* cells. Out of the three parameters, the first two are constant in our experiments.

To establish the relation between the time-dependent fluorescent intensity and the diffusion coefficient, we first assumed the fluorescent intensity to be proportional to the cell density. Although the photobleaching of one GFP molecule is a stochastic event, the photobleaching of GFP-expression cells can be simplified as a continuous process throughout the laser-illuminated region, as each cell contains a relatively large number of GFP molecules. Giving a fluorescent photobleaching rate  $\zeta$ , the dynamics of the fluorescent intensity of the cells can be described by the differential equation

$$\frac{\partial \rho}{\partial t} = \begin{cases} D\nabla^2\rho - \zeta\rho & \text{for } r \leq R \\ D\nabla^2\rho & \text{for } r > R \end{cases} \quad [2]$$

where  $\rho(\vec{r}, t)$  is the fluorescent density,  $D$  is the cells' diffusion coefficient. Eq. [2] is supplemented by the initial condition  $\rho(\vec{r}, 0) = \rho_0$  and the boundary conditions that  $\rho$  is continuous at  $r = R$ .

In the long-time limit, Eq. [2] has a steady state that the rate of fresh cells (unbleached) into this laser-illuminated region (proportional to  $D/R^2$ ) balances out the photobleaching rate  $\zeta$ . The faster diffusion corresponds to the larger the steady state of fluorescent intensity. Dynamically, the flow of fresh cells will slow down the decay of fluorescent intensity. Therefore, in principle we can compute the diffusion coefficient from the temporal fluorescent intensity curve by Eq. [2] for given  $R$  and  $\zeta$ . However, the photobleaching

response of GFP in cells is more complex than a single component exponential decay assumed in Eq. [2] (see below). Therefore computer simulation approach is used instead to interpret the experimental results and compute the diffusion coefficient.

### 3.2.2 IMPLEMENTATION OF CPB

A fluorescence photobleaching microscopy was set up using a Nikon inverted microscope (Eclipse TE2000-E, Nikon Instruments, Kawasaki, Kanagawa, Japan) as illustrated in **Fig. 3-3**.

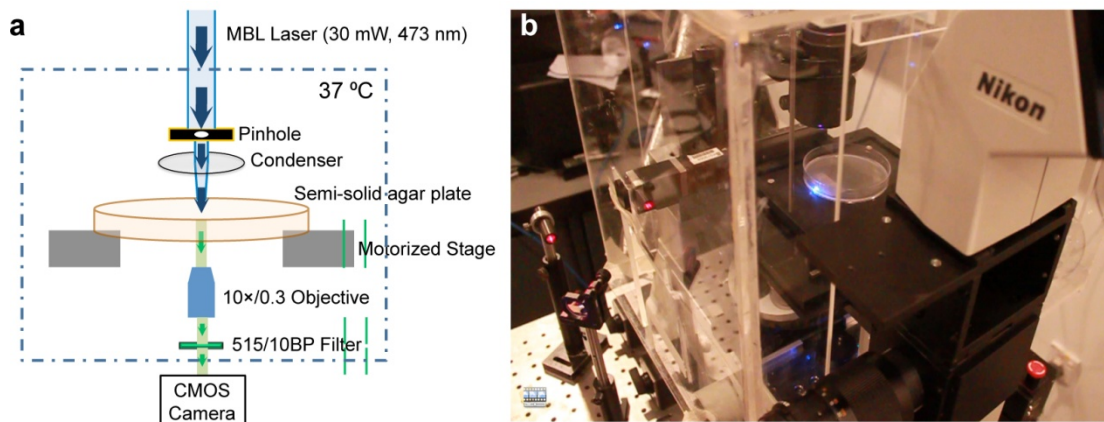


**Figure 3-3 The setup of the continuous fluorescence photobleaching (CPB) microscopy system.**

A parallel 473-nm laser beam is guided through a pinhole and a condenser to excite the GFP molecules in the cells in a cylindrical volume. The emitted fluorescence is collected via an objective lens, passed through a narrow band green filter, and detected with a CMOS camera. Throughout the measurement, the semi-solid agar plate was placed on a motorized stage within an environmental chamber, which is kept constant at 37 °C. **a**, Schematic diagram. **b**, Photograph of the experimental setting

An environmental chamber was built with a heated-air circulating system, which is under the control of a PID temperature controller (ZNHW-IV, Truelab, Shanghai, China). The temperature inside the chamber was maintained at 37 °C throughout the experiments. Sample agar plate was placed on a Thorlabs motorized x-y stage (Max200, Thorlabs, NJ, USA) under the control of a customized LabVIEW program. A laser beam from a 473-nm

solid-state laser (MBL-III-473/30mW, Changchun New Industries Co., Changchun, China) illuminated through the semi-solid agar from the top to the bottom, to excite and bleach fluorescent proteins in cells. The emitted fluorescence signal was collected with a  $10 \times$  objective (Nikon Plain Fluor  $10\times/\text{NA}0.3$ ) and filtered through a narrow green bandpass filter (515BP10, Omega Optical, Brattleboro, VT, USA). The fluorescent image was recorded every second with a CMOS camera (DCC1545M, Thorlabs, NJ, USA).

In our experiments, CL3GFP, CL4 (CL-M expressing GFP), or CL14 (CL-IM expressing GFP) cells were uniformly mixed in 0.25% agar at low cell density and cultured at  $37^\circ\text{C}$  (see **Method 2.4**), at each time point, agar plates were taken out and placed on the motorized x-y stage of modified microscope. Once the location was set, the camera and laser were turned on simultaneously.

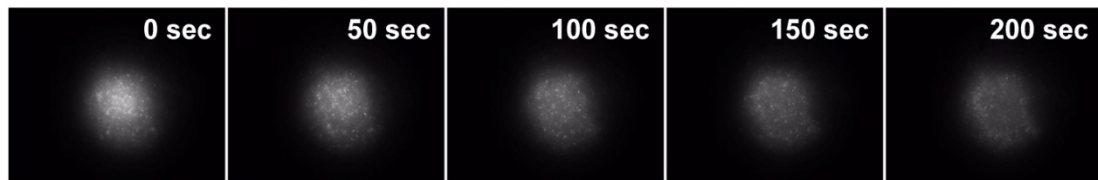


**Figure 3-4 Timelapse fluorescence image during photobleaching**

A series of fluorescent images of CL3GFP were taken with a monochromatic CMOS camera for every 0.7 sec. The brightness represents the intensity of the GFP fluorescence. With a pinhole, only the center region is shined in laser and being photobleached. The fluorescent intensity decays with time due to the continuous photobleaching.

The camera was normally set to record every second. We calculated the average fluorescent intensity in the photobleaching region for each fluorescence image, and obtained a time series of fluorescent intensity for each location of each sample,  $i(t)$  (**Fig. 3-4**). In order to control for variations in cell densities and obtain specific GFP signals, we defined a GFP-specific relative fluorescent intensity ( $I(t)$ ) as

$$I(t) = \frac{i(t) - i_B(t)}{i(0) - i_B(0)} \quad [3]$$

where  $i(t)$  the average of the fluorescent intensity,  $i(0)$  is the value at  $t=0$ . Agar plates with similar cell densities but no GFP expression were measured in parallel as  $i_B(t)$ , The background signal  $i_B(t)$  is constituted of autofluorescence from LB medium, agar and cells.

The later has minimal contribution. Examples of the continuous fluorescence photobleaching curve with various fitted values of cell diffusion coefficients are shown in **Fig. 3-5a**.

We used strain CL14, a flagella-lacking mutant, as an immobile reference ( $D=0$ ) throughout the study. It provides us with a pure GFP photobleaching curve  $I(t)=f(t)$  (**Fig. 3-5a**). The curve is best described by a double-exponential decay, with the half-lives of  $\sim 20$  s and  $\sim 170$  s, respectively (**Fig. 3-5a**). This two-component photobleaching has been observed in a number of fluorescent proteins<sup>152</sup>, especially for the GFP variant (superfolder GFP) we used<sup>5</sup>. As we kept the laser power constant, the two decay constants remained the same throughout all our experiments. For the mobile strains, the decays are slower as we expected (**Fig. 3-5a**). However, the double exponential decay is difficult to be implemented into Eq. [2]. As the cells move in/out of the laser-illuminated zone, the fluorescent intensity of each cell is determined by the accumulated time it located in the laser-illuminated zone (**Fig. 3-6**). The accumulated time is different for each cell and not correlated with the total time. Therefore it is hard to integrate all these independent photobleaching processes to get a time-dependent curve of total fluorescent intensity. We then adapted an alternative single-cell simulation-based process to derive the diffusion coefficients from experiments (**Fig. 2-4a**). For a given diffusion coefficient, we performed computer simulations to mimic the Brownian motion of many cells, and assign the time-dependent fluorescent intensity for each cell based on the accumulated time it located in the bleaching zone and the two decay constants. Both the decay constants and the size of the bleaching zone used in the simulation were determined experimentally (**Fig. 3-5a**). With the trajectories of fluorescent intensities of many cells, we can compute the total fluorescent intensity in the photobleaching zone. The simulated relative intensity for different diffusion coefficients is shown in **Fig. 3-5b**.

Specifically we defined a square box with the size of 3 mm by 3 mm. The region of photobleaching is set as a circle at the center of the box. The scale of the circle  $R$  ( $\sim 100$   $\mu\text{m}$ ) is significantly smaller than the scale of the box,  $L$  ( $=3$  mm). For the range of the diffusion coefficients  $D$  ( $0\text{-}500$   $\mu\text{m}^2 \text{s}^{-1}$ ), the time scale  $L^2/D$  is significantly larger than the bleaching time constants. For each diffusion coefficient  $D$ , we started with more than 100,000 random positioned cells in this square box and simulated their random walks (trajectories) using a 2D stochastic process and a time step of 1 second.

$$\vec{r}(t+dt) - \vec{r}(t) = \sqrt{2Ddt}\vec{Z}_t \quad [4]$$

where  $\vec{Z}_t$  is a vector of normally distributed pseudorandom numbers.

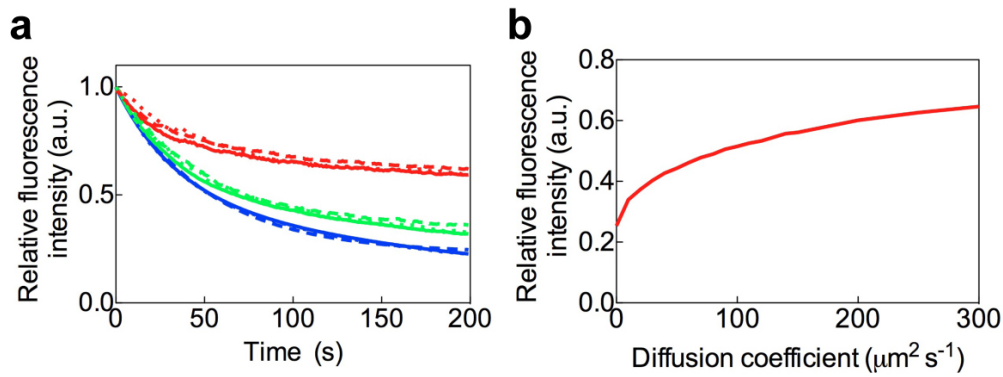


**Figure 3-5 Measurement of cell diffusion coefficient via continuous fluorescence photobleaching (CPB).**

**a**, The representative CPB curves of different diffusion coefficients. Blue dots are experimental data of immobile strain CL14. Red and green dots are representative data of CL3GFP with fast and slow diffusion coefficients, respectively. Blue lines are fitting curves of blue dots ( $D=0 \mu\text{m}^2 \text{s}^{-1}$ ) using double component decay function  $f(t) = 0.48e^{0.03t} + 0.52e^{0.004t}$  (solid) and single decay function  $f'(t) = 0.75e^{0.018t} + 0.25$  (dashed). Red and green lines are the simulation results of  $D=110 \mu\text{m}^2 \text{s}^{-1}$  and  $D=5 \mu\text{m}^2 \text{s}^{-1}$ , respectively, with the corresponding blue lines as  $D=0$  standard. **b**, The relationship between diffusion coefficient and relative fluorescence intensity (mean value from 175 to 180 s) by using  $f(t)$  as the  $D=0$  standard.

As shown in **Fig. 3-6**, for a hypothetical cell trajectory, the photobleaching should only happen when the cell locates in the laser-illuminated region (the green region). If the cell is immobile and just locates in this photobleaching region initially, its fluorescent intensity will decay the same as the experimental immobile strain (**Fig. 3-5a**). If cell moves, its fluorescent intensity decay should be determined by its accumulated time in the laser-illuminated time. Taking the trajectory shown in **Fig. 3-6** as an example, it has three segments in the photobleaching region. The calculation of the accumulated time for each time point only takes the three segments into consideration.

We calculated the time-dependent fluorescent intensity  $F(t)$  of each trajectory by a stochastic process as Eq. [5]

$$F(t) = F(0) \cdot f(\tau^i(t)) \quad [5]$$

where  $f(t)$  is the pure photobleaching function obtained by the fitting of the experimental

data (**Fig. 3-5a**). And  $\tau^i(t)$  is the accumulated time that the trajectory locates in the laser-illuminated region from 0 to  $t$  for cell  $i$ .

$$\tau^i(t) = \sum_0^t P(t') dt' \quad [6]$$

where  $P(t')$  = 1 if the cell locates in the photobleaching region at time  $t'$ , and  $P(t') = 0$  if the cell is outside this region. And the relative mean fluorescent intensity  $I(t)$  in the laser illuminated region is calculated by averaging the fluorescent intensity  $F(t)$  for all the trajectories in this region at time  $t$  as Eq. [7].

$$I(t) = \langle F(t) \rangle / \langle F(0) \rangle \quad [7]$$

We simulated  $I(t)$  for many different diffusion coefficients and found good fitting to the experimental data quite well (**Fig. 3-5a**). Similarly we were also able to use a single exponential decay with a basal level of  $f(t)$  to fit both the immobile and mobile strain (**Fig. 3-5a**). Here we chosen the two exponential component fitting  $f(t)$  as our immobile standard for its better fitting. We also simplified the fitting method.

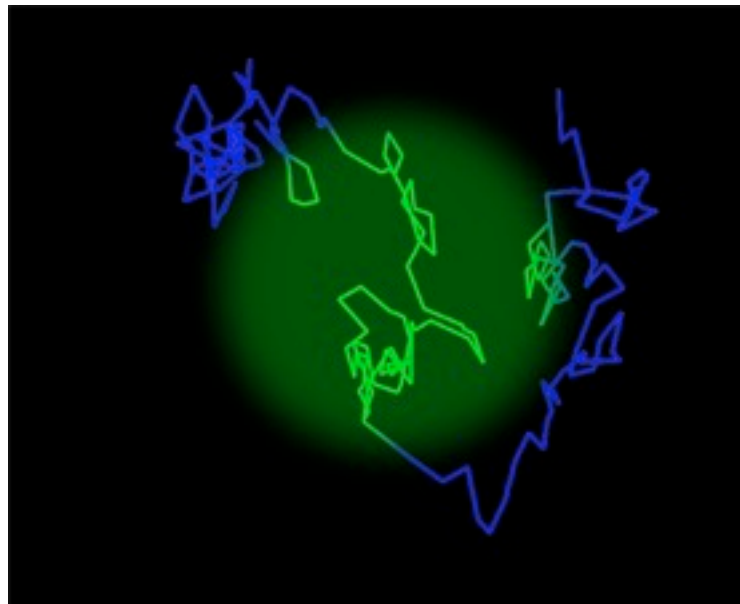


**Figure 3-6 Illustration of the trajectory of one cell in and out of the photobleaching region.**

The line represents a simulated 2D random walk trajectory of an *E. coli* cell. The GFP molecules would undergo photobleaching only when the cell locates in the laser-illuminated region (green). The accumulated photobleaching time ( $\tau$ ) was derived from the portions of the trajectory in the green region.

We plotted the relation between diffusion coefficients and the averages of relative fluorescent intensities from 175 to 180 s (**Fig. 3-5b**). This was used as the standard curve to compute the diffusion coefficients from experimentally measured bleaching curves. However, the exact value of diffusion coefficient depends on the value of  $R^2$ . Its exact value is hard to determine because it lacks the well-defined boundary due to the fact that laser beam exhibits cross-sectional Gaussian intensity profile. Therefore, we used relative diffusion coefficients in following study.

To measure the relative fluorescent intensity curves for different cell densities in semi-solid agar, cell-containing semi-solid agar plates were prepared as described in **Method 2.4**. For every 20-30 min, two plates were taken out to measure the cell density (see **Method 3.1**), followed by the measurement of the fluorescent intensity curves for 200 s. Three positions were randomly measured for each plate. The exposure time varies from 0.05 to 1 s to optimize the dynamic range of the camera. The boundary for the photobleaching region was computed using the segmentation algorithm developed by Otsu *et al*<sup>153</sup>.

## **CHAPTER 4**

## **RESULTS**

## 4.1 DESIGN OF THE DENSITY-DEPENDENT MOTILITY GENETIC CIRCUIT

I first programmed that the local cell density suppresses the motility of *E. coli* cells, particularly, if cell density is low, move. If cell density is high, stop (**Fig. 4-1a**). It is known that *cheZ* deletion causes cells to tumble incessantly, resulting in a non-motile phenotype in semi-solid agar<sup>154-156</sup>. Reintroducing of *cheZ* restores cell motility<sup>102,103</sup>. Based on these findings, I devised strategies to control cell motility by controlling the transcription of *cheZ* (**Fig. 4-1b**). The quorum-sensing system in *V. fischeri* was adopted to signal the local cell density: This system synthesizes and excretes a small molecular acyl-homoserine lactone (AHL), which, at high extracellular levels (due e.g., to high cell density), is expected to accumulate intracellularly and activate a constitutively expressed cytoplasmic regulator, LuxR.

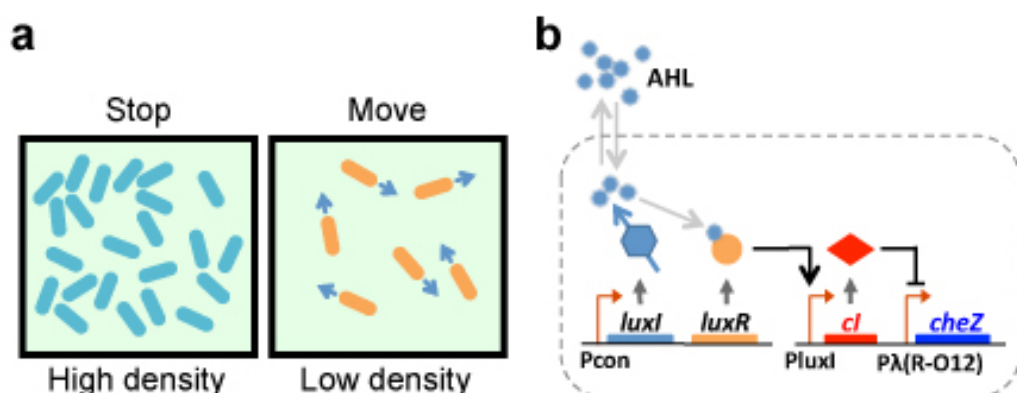


**Figure 4-1 The programmed coupling of cell density and motility.**

**a**, Illustration of the design. **b**, Genetic circuit I. *cheZ* is driven by  $P_{\lambda(R-O12)}$ , which is repressed by CI. The expression of *cl* is in turn under the control of  $P_{luxI}^3$ . The constitutively expressed LuxI synthesizes AHL, which diffuses freely across the cell membrane<sup>8</sup>. At high cell density, increased intracellular AHL binds to the cytoplasmic transcriptional regulator, LuxR, and the LuxR-AHL complex subsequently activates the *luxI* promoter<sup>3</sup>. Dashed line indicates cell membranes.

To exert the control of cell motility by density, AHL-activated LuxR was used to drive the expression of the lambda repressor (CI), which in turn represses *cheZ* transcription. This genetic circuit was designated as genetic circuit I (**Fig. 4-1b**).

## 4.2 CONSTRUCTION OF *CHEZ*-KNOCKOUT STRAIN

Strain CL-M is a motile *E. coli* K12 MG1655 strain that are kindly provided by Prof. Antoine Danchin (Institute Pasteur, Paris). To rewire the motility regulation, full-length *cheZ* in CL-M was deleted “seamlessly” using a recombineering protocol<sup>147</sup> with the aid of pSIM6<sup>146</sup>. Briefly, *loxP* flanked chloramphenicol resistance cassette was PCR amplified from pEGFP-loxP-CmR-loxP<sup>147</sup> with primers cheZ-del-f and cheZ-del-r (**Table 2-2**), each composed of a 50-bp sequence at the 5'-end homologous to the *cheZ* gene region. The PCR products were treated with *Dpn*I, gel purified and then electroporated into CL-M cells containing pSIM6<sup>146</sup> that encodes lambda-Red proteins. Cm<sup>r</sup> colonies were verified for replacement of *cheZ* with loxP-CmR-loxP cassette using colony PCR with primers cheZ-del-conf-f and cheZ-del-conf-r, and followed by direct sequencing. Removal of the chloramphenicol gene insertion was mediated by p705Cre as described previously<sup>147</sup>. pSIM6 and p705Cre were removed from the host by growing the mutants overnight at 37°C, since they both carried temperature-sensitive origin of replication, pSC101. Furthermore, I made seamless deletion of the *lac* operon (including *lacI*) using the same recombineering protocol, to avoid possible interference with the synthetic *P<sub>lac/ara-1</sub>* promoter used to drive the expression of *luxRI* in pLuxRI2 and its derivatives (See **4.3.5**). The final mutant, designated as CL1, contains seamless deletion of *cheZ* and the *lac* operon.

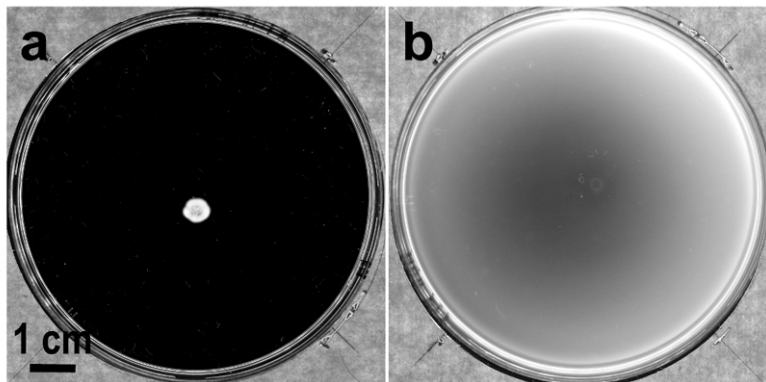


**Figure 4-2 Photographs of typical experimental pattern.**

**a**, CL1. **b**, CL-M. A suspension of mid-exponential growing cells (2  $\mu$ l) was spotted onto the center of 0.25% LB agar plate, incubated at 37 °C for 12 h. Images were captured against a black background, illuminated from below by a circular LED array (see **Method 2.7** for details).

The motility of CL1 was examined under microscope and tested by swimming assay. As shown in **Fig. 4-2a**, CL1 cells showed only tumbling motion in bulk culture and failed to migrate outwards when spotted at the center of a semi-solid agar plate. On the contrary, its parental cells, CL-M, exhibited both tumbling and smooth swimming, and migrated radially outwards like a plain disk (**Fig. 4-2b**). Thus, the motility of CL1 in agar has been successfully abolished.

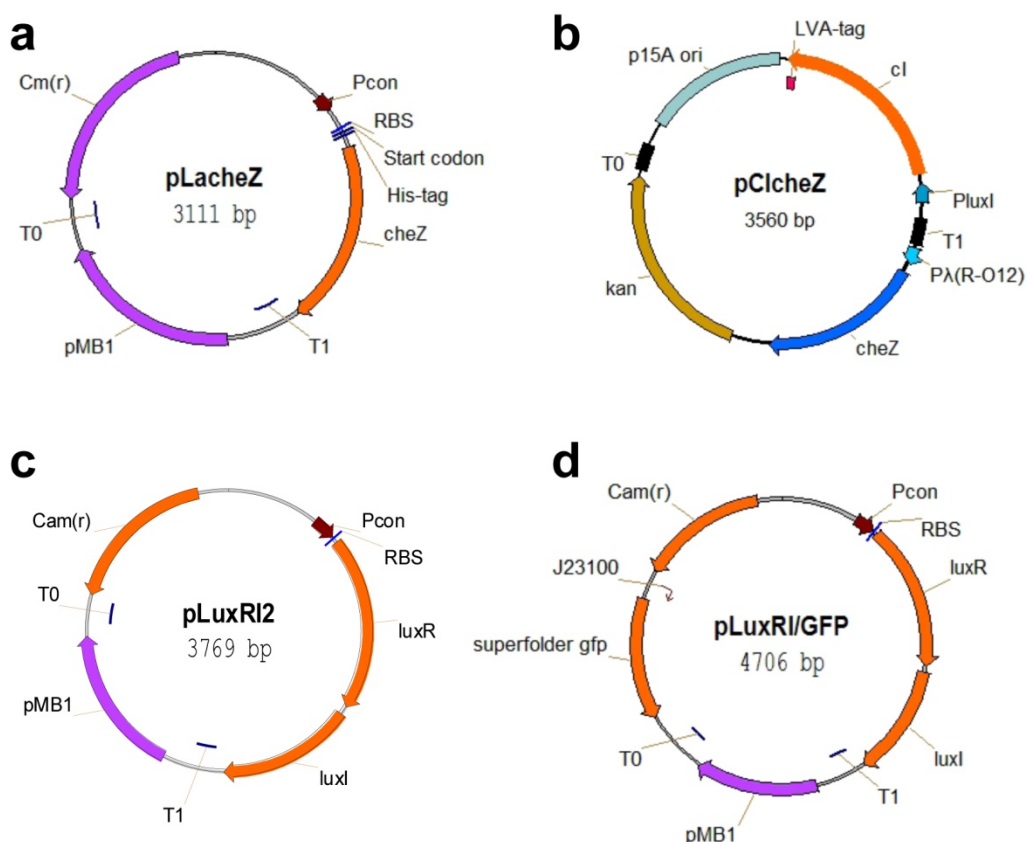


**Figure 4-3 Plasmid maps.**

**a**, pLacheZ. N-terminal of CheZ is fused to a His-tag, the whole ORF is under the control of a constitutively expressed promoter. **b**, pClcheZ. *cheZ* and *cl* are under the control of CI repressible promoter,  $P_{\lambda(R-O12)}$  and cell density-inducible promoter  $P_{luxI}$ , respectively. They are oriented in back to back. LVA-tag at the C-terminal of CI coding region will facilitate the turnover of CI in cells<sup>6</sup>. **c**, pLuxRI2. *luxR* and *luxI* are constitutively expressed (see 4.3.5 for details). **d**, pLuxRI/GFP, superfolder gfp driven by a strong constitutive promoter (BBa\_J23100) is inserted at the downstream of the chloramphenical resistant gene. T0 and T1 indicate transcriptional terminators.

## 4.3 GENETIC CIRCUIT I

### 4.3.1 CONSTRUCTION OF GENETIC CIRCUIT I (GC-I)

To test if reintroduction of *cheZ* can restore CL1's motility, pLacheZ (**Fig. 4-3a**) was constructed by inserting pLa *cheZ* structure gene amplified by PCR from the genomic DNA of strain CL-M at *Bam*HI and *Nhe*I sites. Strain CL15 was created by transforming pLacheZ into strain CL1. CL15 exhibited a similar behavior as CL-M, swimming outwards in semi-solid agar (**Fig. 4-2b**). Next, to establish the density-dependent motility control, pCIcheZ (**Fig. 4-3b**) was constructed in two steps. Firstly, *luxI* in pLD<sup>13</sup> was replaced by the *cheZ* structure gene amplified by PCR from the genomic DNA of strain CL-M. The ribosomal binding site (RBS) of *cheZ* was kept the same as that of *luxI* in pLD. Secondly, the resultant plasmid was linearized by inverse PCR with primers pLD-rot-f-xba and pLD-rot-r-cla, creating *Xba*I and *Clai* sites, and ligation with PCR-amplified *P<sub>luxI</sub>-cI* from pLD. pCIcheZ and pLuxRI2 (**Fig. 4-3c**)<sup>14</sup> were then cotransformed into CL1, generating CL3.

### 4.3.2 CHARACTERIZATION OF GENETIC CIRCUIT I (GC-I)

To verify features of our design, we characterized various properties of the programmed strain CL3 biochemically and physically. The expression profiles of *cheZ* and *cI* were measured in bulk culture at various cell densities using quantitative Real-Time RT-PCR. As evident in **Fig. 4-4a**, *cI* expression level (red) elevated over 40-fold as cell density increased from  $0.5 \times 10^8$  to  $16 \times 10^8$  cells ml<sup>-1</sup> whilst *cheZ* expression (blue) decreased sharply to 5% of the high level.

To characterize cell motility in semi-solid agar quantitatively, we developed an approach analogous to the Continuous-Fluorescence-Photobleaching method<sup>151</sup>, but applying it to fluorescently labeled cells rather than fluorescent molecules (see **Method 3.2** for details). Briefly, pLuxRI/GFP (**Fig. 4-3d**) was constructed as follows: superfolder-gfp<sup>5</sup> was PCR-amplified from BBa\_I746916 (Biobrick) with primers gfp-r-sac and gfp-f-sac, composed of a 35-bp sequence of a synthetic constitutive promoter (Biobrick, BBa\_J23100) at the 5' end. The fragment was then inserted into pLuxRI2 at the *Sac*I site. The colonies with the correct orientation were confirmed by PCR with primers lac-del-conf-f and gfp-conf-r. pLuxRI/GFP was cotransformed with pCIcheZ into CL3 cells, generating strain CL3GFP.

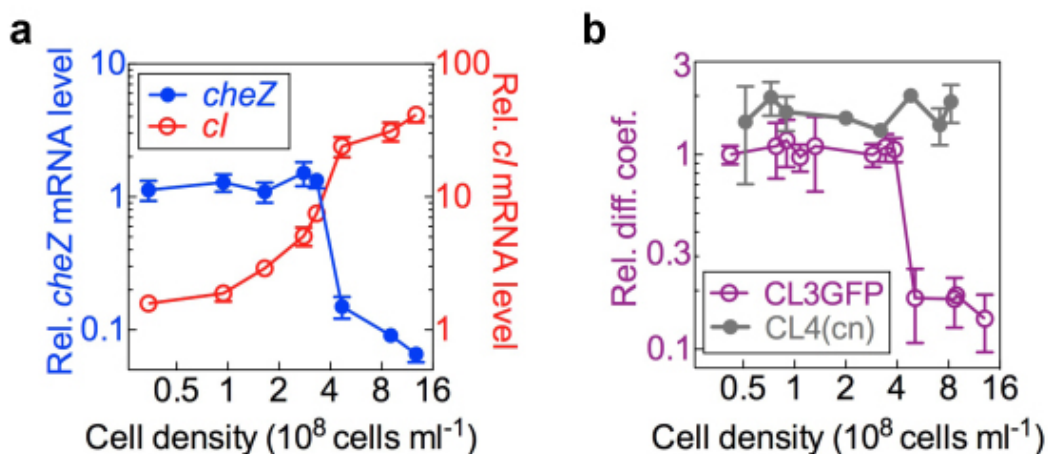


**Figure 4-4 Characterization of GC-I.**

**a**, Relative *cheZ* and *cl* mRNA level in strain CL3 as a function of cell density in bulk culture by Quantitative Real-Time RT-PCR. Data are normalized by the mean value of cells at  $0.3 \times 10^8$  cells  $\text{ml}^{-1}$ . **b**, the relative diffusion coefficient as a function of cell density for cells uniformly grown in 0.25% agar, measured by CPB method (Appendix 2). CL3GFP, strain CL3 carrying superfolder GFP<sup>5</sup>. CL4 (Cn), strain CL4 as a control (harboring quorum-sensing module but with native *cheZ* regulation). Relative diffusion coefficient values are normalized by the mean value of CL3GFP at  $0.4 \times 10^8$  cells  $\text{ml}^{-1}$ . Results are representative data from three independent experiments. Error bars represent s.d. of three replicates.

To measure the motility of CL3GFP cells in semi-solid agar, cells were uniformly mixed with 0.25% agar at low density, and then at various times during the course of cell growth, laser was applied to photo-bleach fluorescent cells in small areas on the agar plate. Cell motility was deduced from the subsequent (rapid) decrease in fluorescence in the bleached area. The absolute cell density in agar at each time was determined by the transmittance of laser light through the agar plate, calibrated against serial dilutions of cell suspensions uniformly mixed in nutrient-depleted<sup>4</sup> agar plates. Consistent with our design and the gene expression results, strain CL3GFP exhibited motility (characterized by an effective diffusion coefficient  $D$ ) comparable to that of the wild type *E. coli* cells at low cell densities, dropping abruptly around a density of  $\sim 4 \times 10^8$  cells  $\text{ml}^{-1}$  (Fig. 4-4b, purple symbols). As a control, strain CL4 carrying quorum-sensing module but with the native *cheZ* regulation showed a density-independent motility in the same cell density range (Fig. 4-4b, brown symbols). Thus strain CL3 exhibits a reduced motility at high cell density as designed.

### 4.3.3 PATTERN FORMATION OF CELLS HARBORING GC-I

To characterize spatiotemporal patterns formed by CL3, I inoculated a suspension of exponentially growing CL3 cells (2  $\mu$ l, OD<sub>600</sub>~0.1-0.2) at the centre of a 8.5-cm Petri dish containing 10-ml LB medium and 0.25% agar. A stripe pattern of alternating white (high cell density) and dark (low cell density) bands developed overnight and was recorded by a camera under the illumination of a circular LED light from below (see **Method 2.7** for details).

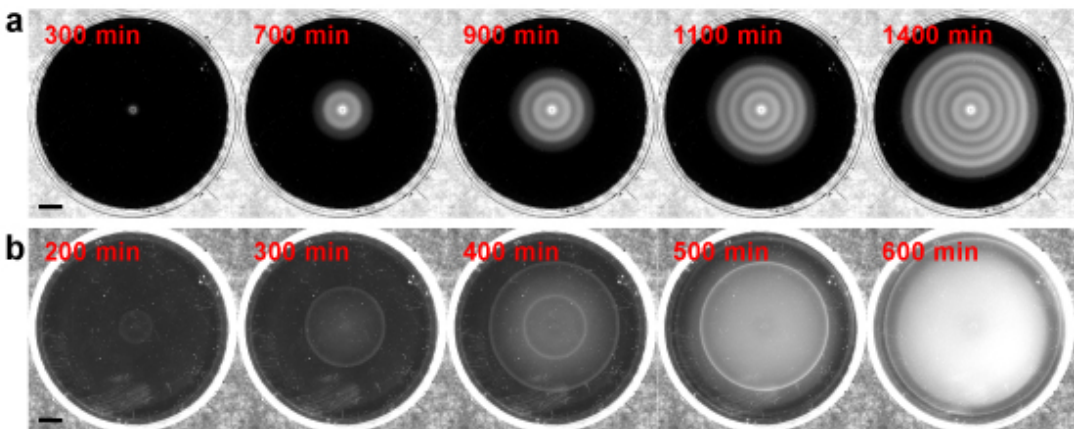


**Figure 4-5 Time-lapsed photographs of a typical experimental pattern.**

**a**, CL3. Sequential and periodic stripe pattern. **b**, CL4. Harbors quorum-sensing module but with native *cheZ* regulation, disk-like pattern. Images were captured every 10 min against a black background, illuminated from below by a circular LED array. Scale bars, 1 cm.

As shown in **Fig. 4-5a**, the bands formed sequentially, at a spacing of ~6 mm. In the first 200 min, cells grew and the cell density increased at the point of inoculation. Two travelling waves could be visible from 400 min. The outer wave was weaker but larger in width than the inner one. As it migrated to a radius of 9 mm, it appeared to be frozen and waited for the coming of the inner wave, which travelled toward the outer wave. During this period, cells behind the inner wave continued growing. Two high-density regions emerged at the point of inoculation and at the place where the outer wave got frozen. Later on, these two regions became denser and denser. Nevertheless, the cell density of the region between them kept unchanged or even decreased a little bit. As the inner wave continued on its way, an outer wave appeared again near the edge of bacteria lawn. It is difficult to determine if the cells in this outer wave is the same population as those in the previous one. This wave expanded for a distance and freeze again. Then the high- and low- density regions appeared

periodically with a constant interval time of about 200 min. Once a stripe (region of high cell density) forms, it doesn't move but remained in the position. Observation under an optical microscope revealed that cells in the outer dark band were motile but the ones in the outer white band could hardly move. All cells in inner stripes were non-motile. The patterns in Petri dish were stable for days until the agar was totally dried up.

As a control, strain CL4 (carrying quorum-sensing module but with the native *cheZ* regulation) behaved like wild type cells<sup>154,157</sup>: from the position of the inoculum, two traveling waves successively moved radially outwards, followed by an uniform expansion of cell density (**Fig. 4-5b**).

#### 4.3.4 SPATIOTEMPORAL DYNAMICS OF PATTERNING PROCESS OF CELLS HARBORING GENETIC CIRCUIT-I

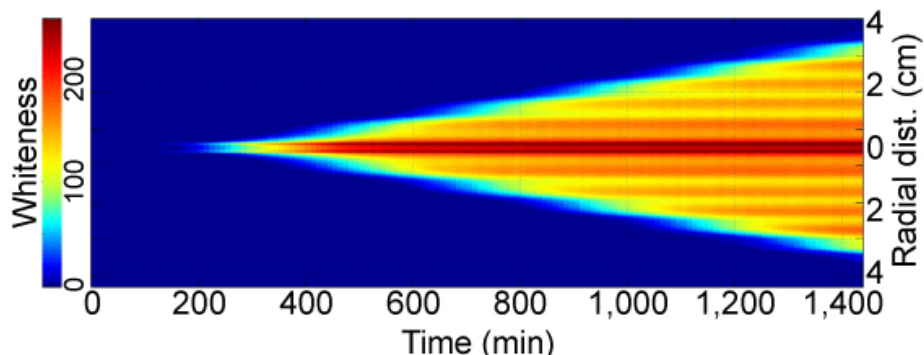


**Figure 4-6 Spatiotemporal diagram of Fig. 4-5a.**

Showing the light intensity along a vertical line through the center of the Petri dish as a function of time.

The spatiotemporal dynamics of the stripe formation process may be revealed in more detail by displaying the light intensities along a vertical line through the center of the plates; see **Fig. 4-6**, color codes indicating the intensity of whiteness in **Fig. 4-5a**. The light intensities extracted from photos taken every 10 min from the time of inoculation (time=0) until 1,400 min were successively displayed to form the spatiotemporal diagram of **Fig. 4-6**. The diagram clearly shows that the positions of the bands are fixed in space once formed. Furthermore, the bands initiated at a regular time and spatial interval.

To further quantify the patterning process, the Petri dish was placed on a motorized stage, and cell density profile was obtained by periodically scanning along a line through the center of the agar plate with a fine laser beam while the pattern is forming, and comparing the transmitted light with the standard; see **Method 2.7**. The spatiotemporal density profile (**Fig. 4-7**) showed initially small density variations gradually amplified into a 2-fold difference between the densities of the neighboring peaks and troughs at late times.

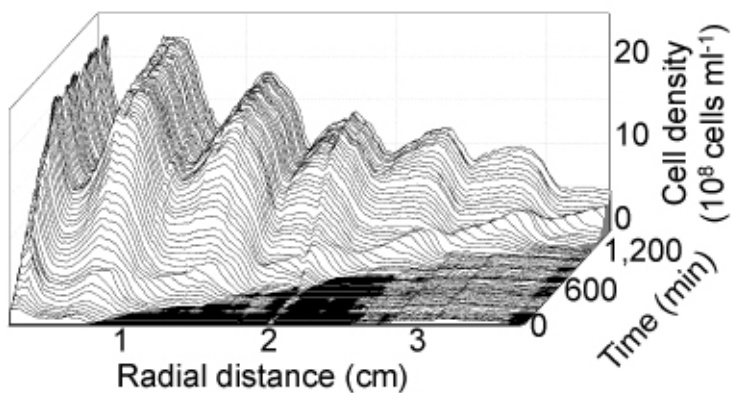


**Figure 4-7 Spatial-temporal density profile of strain CL3.**

The absolute cell density profile across the center of the Petri dish as a function of time. After 2  $\mu$ l mid-exponential growing cells was spotted onto the center of a 0.25% LB agar plate, the plate was scanned every 10 min along a line through the center of the agar plate with a fine laser beam. The cell density in agar was calibrated against serial dilutions of cell suspensions uniformly mixed in nutrient-depleted<sup>4</sup> agar plates (see **Method 3.1** for details).

To investigate pattern formation in one-dimensional geometry, I modified the shape of the regular Petri dish into rectangle, and found that plate sizes of 3 cm  $\times$  7 cm to 6 cm  $\times$  10 cm were ideal for patterning process, as they well prevented the interference of boundary and the evaporation of medium in a long term. A line (~2.3-4.5  $\times$  10<sup>5</sup> cells), but not a spot, was inoculated at the middle of the plate by using a cover slip as described<sup>158</sup>.

The cells grew at the position of inoculum for about 4 h, and then two bands appeared at both sides. Later on, stripes were developed periodically at the left and the right with a similar dynamic process to cells inoculated at Petri dishes. A similar stripe pattern developed and propagated towards the two sides for CL3 (**Fig. 4-8a and c**) but not for wild type or CL4

cells (**Fig. 4-8b**).

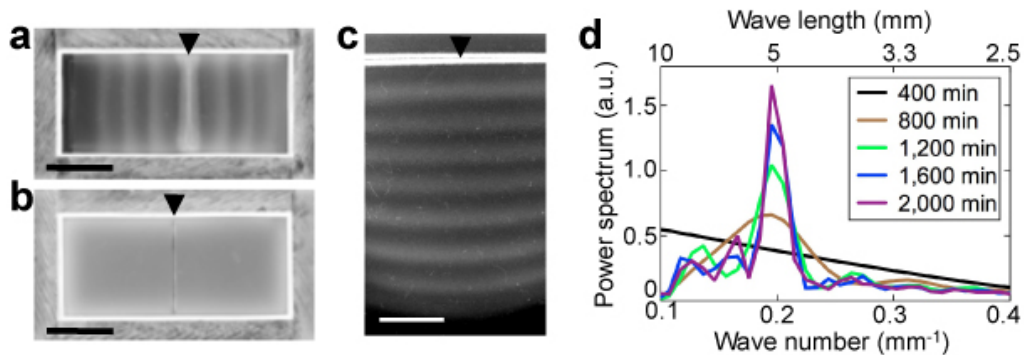


**Figure 4-8 One-dimensional pattern.**

**a, c, CL3. b, CL4. a, b,** Photographs were taken after 1,200 min growth at 37 °C. The white boundary is an artifact due to the illumination. **c,** Photographs were taken after 2,000 min growth at 37 °C. **a, b, c,** Arrow indicates the position of inoculation. Scale bars, 1 cm. **d,** Fourier power spectra of **c**, indicating the sequential formation of stable periodic stripe pattern with a wavelength of ~5 mm.

To evaluate the periodicity of the stripe pattern, we used Fourier analysis to transform the light intensity of stripe pattern (**Fig. 4-8c**) from space to wave number domain (see **Method 2.8** for details). The frequency spectrums via a Fourier transform at various time points are shown in **Fig. 4-8d**. A peak around wave number of  $\sim 0.2 \text{ mm}^{-1}$  appeared at time 800 min (Brown line in **Fig. 4-8d**) and getting narrower and taller overtime, indicating an expanding stripe pattern with an almost constant wavelength of  $\sim 5 \text{ mm}$ .

#### 4.3.5 EFFECT OF CHROMOSOMAL LAC OPERON ON THE PATTERN FORMATION

Both the *luxR* and *luxI* genes in the genetic circuits were driven by a synthetic promoter  $P_{\text{lac/ara-1}}^{159}$ , which is repressible by LacI. However, there is a copy of *lacI* gene on the chromosome of CL-M, it may exert an effect on the expression of *luxRI* expression.

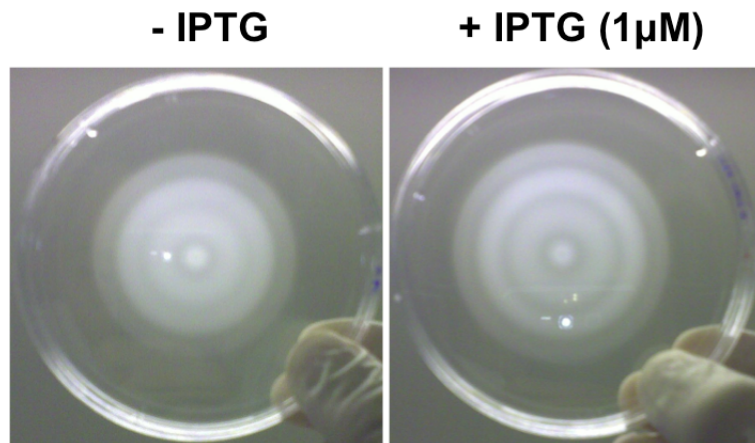


**Figure 4-9 Effect of chromosomal lac operon on the pattern formation.**

Cells were cultured till mid-exponential phase ( $OD_{600}=0.1\text{-}0.2$ ), then inoculated 2- $\mu\text{l}$  cell suspension at the center of 0.25% agar plates, followed by 20-h incubation at 37 °C. Photographs were taken against a grey wall illuminated by a fluorescent lamp from below.

To test if this is the case, I transformed GC-I into CL-M $\Delta cheZ$ , resulting strain CL31. As shown in Fig. 4-9, comparing with the agar plate supplemented with IPTG, the stripe pattern formed without IPTG was much unclear, suggesting that the endogenous *lacI* might influence the expression of *luxRI*. Thus, throughout this study, strain CL1 was utilized (Table 2-2).

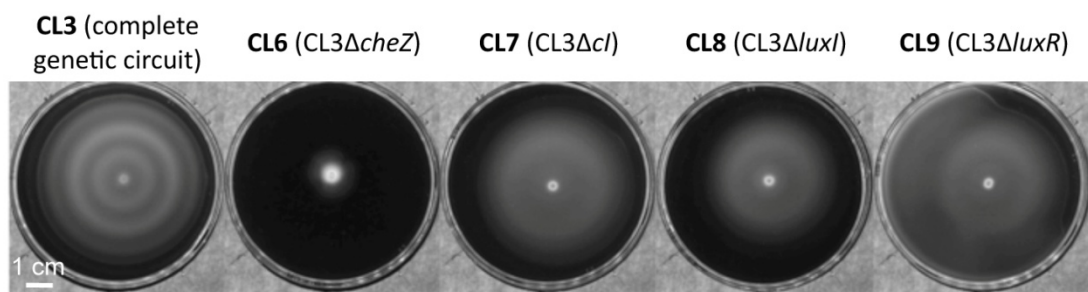


**Figure 4-10 Entire GC-I is required for stripe pattern formation.**

After seed culture and preculture, strain CL3 and the deletion mutants were diluted 200-fold into fresh medium and cultured till mid-exponential phase ( $OD_{600}=0.1\text{-}0.2$ ), then inoculated 2- $\mu\text{l}$  cell suspension at the center of 0.23% agar plates, followed by 20-h incubation at 37 °C. Photographs were taken against black background illuminated by a circular LED array from below. Property of each strain was indicated in the bracket.

#### 4.3.6 THE INTACT GENETIC CIRCUIT IS REQUIRED FOR THE PATTERN FORMATION

To verify that each gene in the designed genetic circuit was essential for the stripe pattern formation, pCIcheZΔcheZ was made by deleting *cheZ* gene from pCIcheZ, in brief; pCIcheZ was digested with *NheI* and *EcoRV*. The resultant fragment was blunted by T4 DNA polymerase, then self-ligated. pCIcheZΔcI was made by self-ligating inverse-PCR-amplified fragments from pCIcheZ to exclude the coding regions of *cI* with primers delcI-f-cla and delcI-r-cla. pLuxR was made by digesting pLuxRI2 with *BamHI* and *NotI* to delete *luxI*, blunting and self-ligating the resultant fragment. Similarly, pLuxI was made by digesting pLuxRI2 with *EcoRI* and *BamHI*. CL6, CL7, CL8, and CL9 were generated by transforming CL1 cells with pCIcheZΔcheZ and pLuxRI2, pCIcheZΔcI and pLuxRI2, pCIcheZ and pLuxR, and pCIcheZ and pLuxI, respectively. As anticipated, only cells harboring intact genetic circuit (CL3) formed stripe pattern. Other mutants formed either plain disks (CL7, CL8, and CL9) or spot (CL6) in semi-solid agar (**Fig. 4-10**).

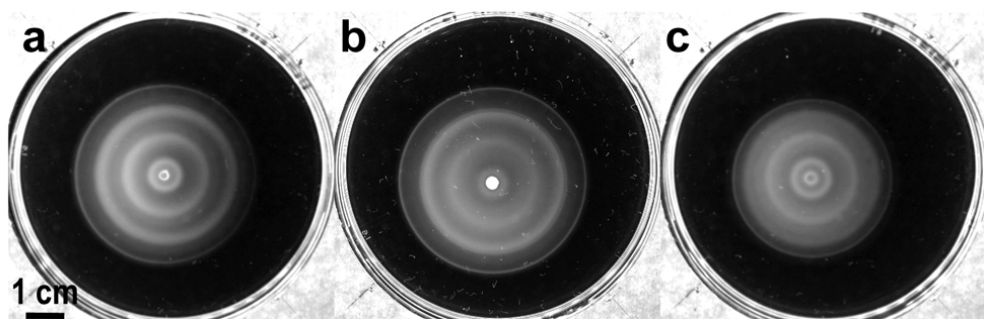


**Figure 4-11 Effects of host-encoded QS factors on stripe pattern formation.**  
**a**, CL3. **b**, CL18 (CL3Δ*sdiA*). **c**, CL19 (CL3Δ*luxS*). Cells were diluted 200-fold into fresh medium and cultured till mid-exponential phase ( $OD_{600}=0.1\text{--}0.2$ ), then inoculated 2- $\mu\text{l}$  cell suspension at the center of 0.25% agar plates, followed by 16-h incubation at 37 °C. Photographs were taken against black background illuminated by a circular LED array from below. Property of each strain was indicated in the bracket.

#### 4.3.7 INFLUENCE OF HOST-ENCODED QS FACTORS ON PATTERN FORMATION

A growing body of studies showed different QS systems might crosstalk with each other. So I next investigated whether the endogenous QS factors played a role during stripe pattern formation. To this end, full-length *sdiA* or *luxS* in CL1 was deleted “seamlessly” using a recombineering protocol as above. pCIcheZ and pLuxRI2 were then cotransformed into these null mutants, obtaining CL18 and CL19. As evident in **Fig.4-11**, similar geometry patterns were generated by the strains with the deletion of either *sdiA* or *luxS* (**Fig. 4-11**).

#### 4.3.8 INFLUENCE OF PHYSICAL FACTORS ON PATTERN FORMATION

To learn more about the stripe formation process, I surveyed the effect of agar thickness, humidity, starting cell number, volume, and phase. These results showed that the pattern formation was robust under most conditions tested (**Fig. 4-12**). Starting from different cell number/volume (to the extremely small microdrop) or different cell phase did not change the pattern, except for the morphology of the area of inoculation (**Fig. 4-12b, c, d**).

The generation of the periodic stripe pattern was robust with different thickness of agar layer (1-8 mm) (**Fig. 4-12e**), provided that limitation of oxygen is not essential to the patterning event. It was reproducibly observed that the velocity of pattern spreading increased as the agar thickness decreased. This phenomenon might be due to the decreased level of the initial nutrients at thinner layers as reported previously<sup>160</sup>.

The humidity, ranging from 25-88%, didn't affect the pattern formation either (**Fig. 4-12f**). The pattern formation occurred at the agar concentration widely ranging from 0.12% to 0.35% (**Fig. 4-12g**). As agar density lower than 0.12%, the convection could not be well prevented; higher than 0.35%, agar matrix did not allow cells to freely penetrate. In the range of 0.12-0.35%, the wavelength of the stripes increased as agar concentration decreased. Although pattern formation is robust in all above conditions; conditions that significantly affect cell growth (e.g., temperature) can affect the patterns in complex ways, presumably due to the cell's innate control on motility. As shown in **Fig. 4-12h**, the stripe number decreased to one when incubation temperature was adjusted to 28 °C or 32 °C.

Moreover, medium used in this study was half-strength LB broth/agar (see **Method 2.4** for details). The main reasons were that it gave rise to clearer patterns and caused less auto-fluorescence background, comparing with normal LB medium. As a control, **Fig. 4-12i** showed that the growth in normal LB medium did not change the stripe pattern.

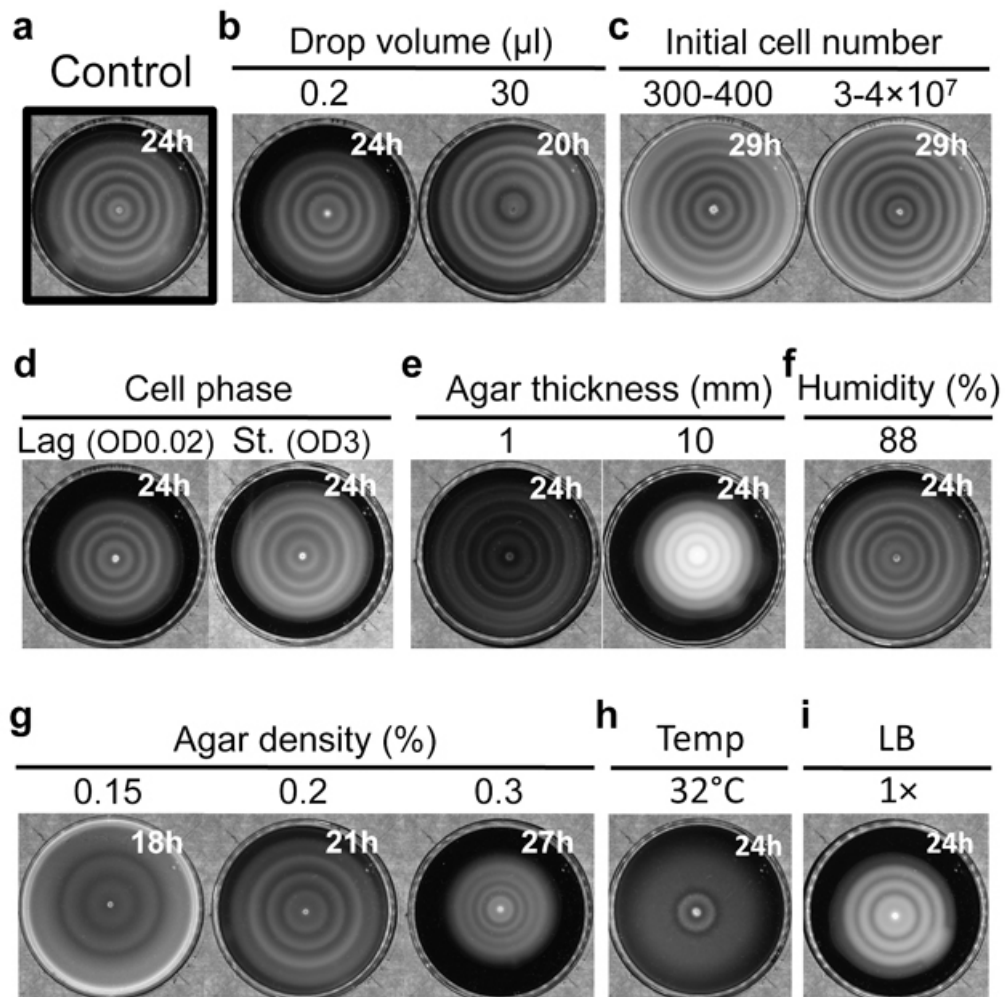


**Figure 4-12 Pattern formation under various conditions.**

**a**, The common experimental conditions applied in this study was used as the control, particularly, initial drop volume was 2  $\mu$ l; initial cell number was  $3\text{-}4 \times 10^5$ ; initial cell phase was mid-exponential phase ( $OD_{600}=0.1\text{-}0.2$ ); agar thickness is 2 mm; humidity is 30%; agar density is 0.25%; incubation temperature is 37 °C; medium is half-strength LB agar.

**b**, Initial drop volume. With other conditions unchanged, lower initial drop volume to 0.5 or higher to 30  $\mu$ l. **c**, initial cell number, cells were cultured till mid-exponential phase, 1000-fold diluted with experimental medium, or 100-fold concentrated by centrifuge. 2- $\mu$ l of cell suspension was inoculated. **d**, Initial cell phase, after seed-culture, subculture, cells were 200-fold diluted into fresh experimental medium and grown till lag-phase

(OD<sub>600</sub>=0.05), or stationary phase (OD<sub>600</sub>=3). **e**, Thickness of agar layer, LB medium supplemented with 0.1 M HEPES (pH 8.0) containing 0.25% agar in various volumes, ranging from 5- to 40-ml, were poured into Petri dishes (8.5-cm internal diameter) and the total height of the agar layer was set to 5 mm. Cells of *S. enterica* serovar Typhimurium were inoculated onto the agar surface at a density of 10<sup>6</sup> CFU/ml.

**f, Humidity.** Cells were spotted onto the semi-solid agar and placed into a plastic box (50 cm wide × 30 cm deep × 30 cm high) with a bottle of water (50-ml) inside. The box was covered and placed into warm room 5 h prior to inoculation. The humidity in balance is 92%. The number of the colonies was counted after 10 days at 37 °C.

~88%. g, The wavelength of the stripes increased as agar concentration decreased. 10-ml

experimental media containing various concentration of agar, ranging from 0.12- to -0.35%, were poured into Petri dishes and allowed to harden at room temperature for 90 min. h, Temperature. With other conditions unchanged, incubation temperature was 32 °C. i, LB strength. With other conditions unchanged, normal LB agar was used. The times in the figures indicate the duration of the agar plate incubated after cells were spotted.

#### 4.3.8.1 EFFECTS OF pH

I found the medium pH significantly changed from 7 to 9 after overnight culture in LB broth. Since cell motility is the key ingredient in my design, I sought to test the effects of pH on it. To this end, wildtype strain, CL-M, was spotted onto semi-solid agar plates with different pH values. As pH value of medium increased, cell motility in semi-solid agar decreased (**Fig. 4-14**).

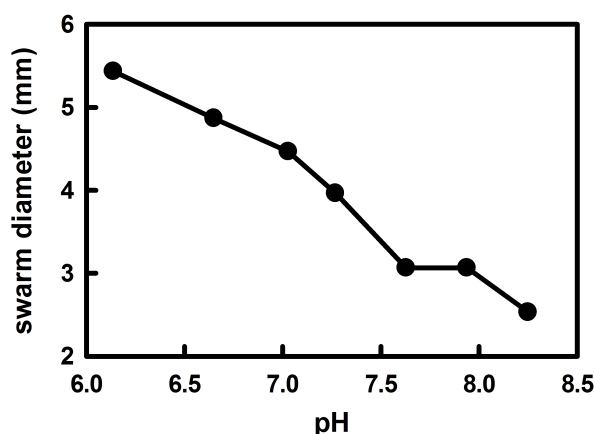


**Figure 4-14 The effect of pH on CL-M swarm distance**

Cells were cultured till mid-exponential phase ( $OD_{600}=0.1-0.2$ ), then inoculated  $2-\mu l$  cell suspension at the center of 0.3% agar plates, followed by 8-h incubation at 37 ° C. pH was buffered by 100 mM HEPES with different pH values.

The stripe pattern formation was also affected by the pH value of medium (**Fig. 4-15**). When pH value was lower than 7.0, the ring disappeared gradually. The clearest stripe pattern was observed at pH 8.0. Thus, throughout this study, the pH value of experimental medium was maintained around pH 8.0 (see **Method 2.4**).

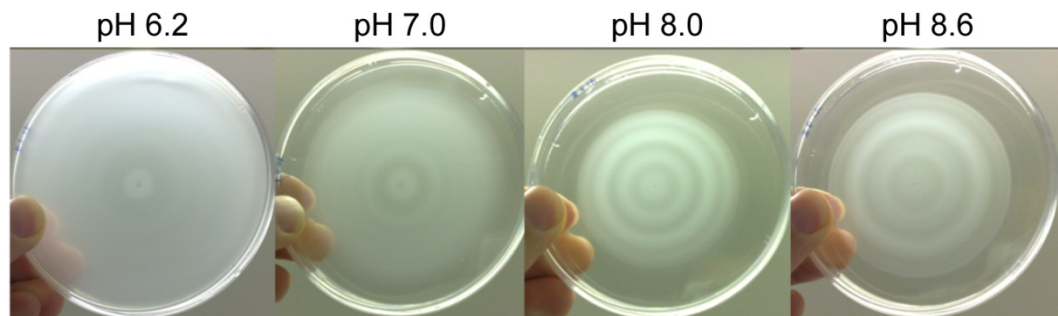


**Figure 4-15 Effects of medium pH on pattern formation**

Cells were cultured till mid-exponential phase ( $OD_{600}=0.1\text{--}0.2$ ), then inoculated 2- $\mu\text{l}$  cell suspension at the center of 0.25% agar plates, whose pH were adjusted by adding 100 mM HEPES with appropriate pH values, followed by 20-h incubation at 37 °C. Photographs were taken against a grey wall illuminated by a fluorescent lamp from below.

#### 4.3.8.2 CHARACTERIZATION OF “LOSS-OF-PATTERN” MUTATION OCCURRED DURING LONG TERM DEVELOPMENT

In addition, it is found that given larger space and longer time, “loss-of-pattern” mutations were observed during patterning process (Fig. 4-16). Further characterization suggested that the mutations occurred on the chromosome of strain CL3.

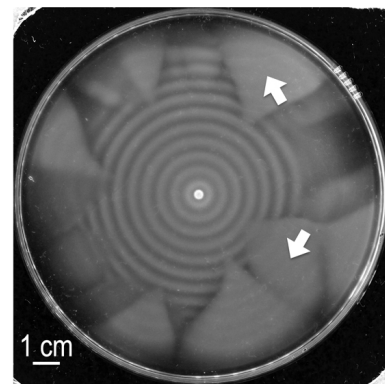


**Figure 4-16 “loss-of-pattern” mutation.**

2- $\mu\text{l}$  mid-exponential cell suspension was inoculated at the center of 0.25% agar plates (14-cm internal diameter), followed by 72-h incubation at 37 °C.

To characterize the “loss-of-pattern” phenomenon, cells from two non-stripe pattern regions (“b” and “c” in **Fig. 4-17**) and one stripe region (“a” in **Fig. 4-17**) were streaked onto selective LB plate. And then single colonies were inoculated into experimental medium, and cultured till mid-exponential phase. 2- $\mu$ l cell suspension was spotted at the center of 0.25% agar plates, followed by 20-h incubation at 37 °C.

As shown in **Fig. 4-17** cells from “a” region could form stripe as usual; cells from “b” and “c” regions, however, loss the stripe pattern forming ability. As a control, cells were homogeneously mixed with 0.25% LB agar, and incubated at 37 °C for 72 h, the same duration as the parental plate of “loss-of-pattern”. After that, cells were picked and followed the same procedure as those from “a”, “b”, or “c” region (**Fig. 4-17**, right panel). After cultured till mid-exponential phase, cells were spotted onto semi-solid agar and allowed to grow overnight at 37 °C. It is shown that the identical stripe pattern was developed (**Fig. 4-17**, right panel). These results indicated that the “loss-of-pattern” phenomenon was inherited; and that the process of expansion and development of stripe pattern might be required for the phenominum.

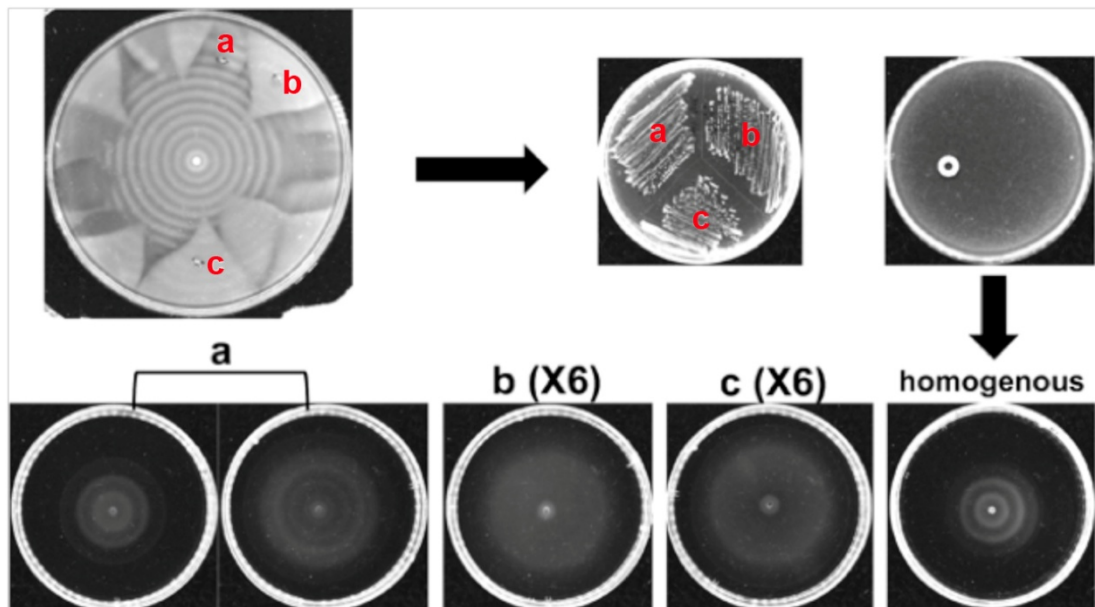


**Figure 4-17 Characterization of “loss-of-pattern” phenomenon.**

Cells from either non-stripe or stripe regions were streaked onto a fresh selective plate.

Single colonies were then picked, cultured and spotted onto semi-solid agar. For “a” region, 2 colonies were randomly picked; for “b” and “c” regions, 6 colonies were randomly picked. Homogeneous, cells were homogeneously mixed with 0.25% LB agar and grown overnight. Cells were then picked, cultured and spotted onto semi-solid agar. Plates were incubated at 37 °C for 20 h. Images were taken as described above.

Next, I sought to determine if the phenomenon was due to mutations on the genetic circuit. To this end, plasmids were extracted from single colonies of “b” and “c” regions, and retransformed into CL1 competent cells. The transformants were randomly picked, cultured, and spotted onto the semi-solid agar. Identical stripe patterns repeatedly formed as the parental strain CL3, suggesting that no essential mutations occurred in the DNA sequence of plasmids, and that the “loss-of-pattern” mutation(s) would be on the chromosome of host cells, either genetically or epigenetically.

#### 4.3.9 CELL AGGREGATION DRIVEN BY DENSITY-DEPENDENT MOTILITY

The formation of stripe pattern, involving regions of low densities sandwiched between regions of higher density, may be counter-intuitive since both diffusion and growth of cells tend to even out spatial variation in cell densities. The stability and robustness of the stripe patterns formed suggest the existence of counter mechanism(s) favoring cell aggregation. It was previously reported that *E. coli* cells could spontaneously aggregate when grown in specific poor-nutrient media due to the secretion of potent chemo-attractant<sup>44,45</sup>. But neither wild type cells nor the AHL-producing CL4 cells formed pattern in our experiments in rich medium (**Fig. 4-2b** and **4-5b**).

As stripe formation in these experiments depended on every component of the designed circuit in CL3 (**Fig. 4-10**), we infer this aggregation effect to result from density-dependent motility. A possible mechanism is illustrated in **Fig. 4-18**: Cells can diffuse freely in the semi-solid agar when cell density is low (**Fig. 4-18a**). As cells grow and the local density reaches high levels in some regions, e.g., above the threshold density of  $4 \times 10^8$  cells  $\text{ml}^{-1}$  shown in **Fig. 4-4b**, cell motility slows down as programmed (**Fig. 4-18b**, with non-motile cells in teal). These cells cannot move away but neighboring cells may continue to move into this high-density region and become non-motile (**Fig. 4-18c**). This would result in a net cell-flow towards the high-density region, seen macroscopically as an effective aggregation phenomenon. An aggregate initiated in this manner may be further amplified since growth in a region with a higher cell density will deplete nutrients from the neighboring low-density regions, thereby reducing the growth potential in the neighboring regions.

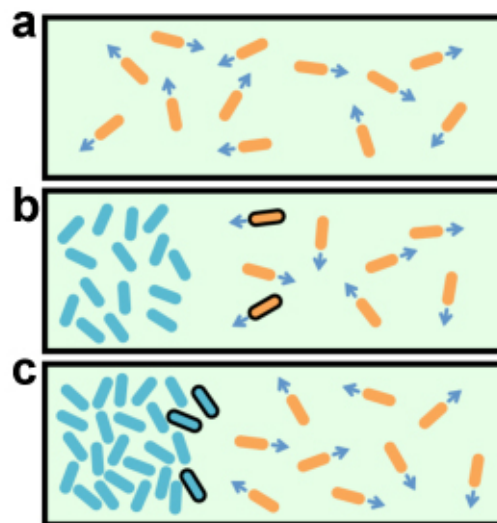


**Figure 4-18 Scheme showing the formation of aggregation (high-density region) in semi-solid agar.**

**a**, when cell-density is low, cells can move in the semi-solid agar readily. **b**, cells stop moving at high-density region. **c**, cells move towards high-density region, join it and stop moving. Cells in teal indicate non-motile, in khaki are motile. Outlined cells represent those moving towards high-density region.

To test the proposed aggregation mechanism, I created two strains, the senders (CL6) that synthesize AHL but are non-motile, and the receivers (CL8), capable of receiving AHL and regulating motility but incapable of AHL synthesis. The receiver cells were uniformly mixed with semi-solid agar. Subsequently, a drop of sender cells was spotted at the center of the hardened cell-agar mixture. The non-motile sender cells could not move away from where they were spotted, but were expected to synthesize and excrete AHL as they grew in number at the center of the plate. After 12-h incubation, a high-density band of receiver cells was observed to aggregate around the spotted sender cells (**Fig. 4-19**). No aggregation was observed in a control with receiver cells incapable of regulating motility (CL10), nor in other controls, such as receiver cells with AHL-producing ability, which might affect the formation of AHL gradient (CL3); receiver cells with native *cheZ* and AHL-producing ability (CL12); receiver cells with native *cheZ* but incapable of AHL synthesis (CL13) (**Fig. 4-19**). Thus, an effective aggregation phenomenon mediated by density-dependent motility was experimentally demonstrated.

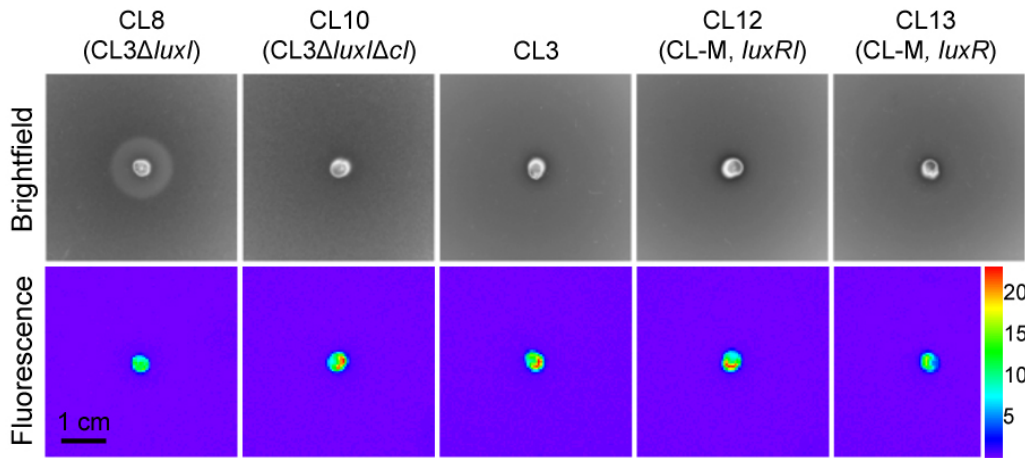
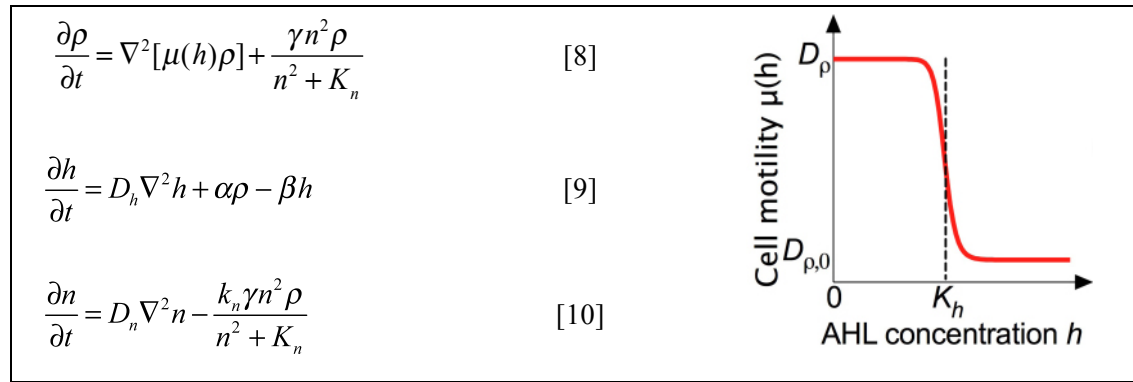


**Figure 4-19 Evidence of effective aggregation.**

All sender cells (CL6, non-motile but synthesizing AHL) were located at the position of inoculum as indicated by green fluorescence. Only those receiver cells with entire genetic circuit but lacking AHL-producing gene (*luxI*) formed a distinct cell aggregation around a group of sender cells (CL8). Aggregation could not occur under other conditions, such as receiver cells lacking *cl*, which failed to regulate *cheZ* (CL10); receiver cells with AHL-producing ability, which might affect the formation of AHL gradient (CL3); receiver cells with native *cheZ* and AHL-producing ability (CL12); receiver cells with native *cheZ* but incapable of AHL synthesis (CL13). Upper panel, bright field images. Lower panel, fluorescence images.

#### 4.3.10 THEORETICAL ANALYSIS OF THE PATTERNING PROCESS

From the studies so far, it is not yet clear why density-dependent aggregation can form highly regular patterns rather than just random high-density patches. To understand the formation of sequential and periodic stripes, we developed a mathematical model (Eqs. [8]-[10]) with the following key features: The stochastic swim-and-tumble motion of bacterial cells is described at the population level by a diffusion-like equation (Eq. [8]) for the cell density  $\rho(\vec{x}, t)$ , with an abrupt AHL-dependent motility coefficient  $\mu(h)$  (shown in Box). The synthesis, diffusion, and turnover of AHL ( $h$ ) are described by Eq. [9], while the consumption and diffusion of nutrient ( $n$ ) are described by Eq. [10]. Numerical simulations of Eqs. [8]-[10] using realistic parameter values generated patterns similar to the experimental observations in one- and two- dimensions (Fig. 4-20a).



Mathematical analysis of Eqs. [8]-[10] provides insights on the mechanism driving stripe formation by density-dependent motility. It turns out that there are competing scenarios for stripe formation, which can only be distinguished through a quantitative study of the temporal evolution of the density profiles. In the present problem, starting from an initial Gaussian profile, time-lapse plots of the simulated spatial cell-density profiles (**Fig. 4-20b**) shows that stripes initiate periodically from the propagating front and remain localized in space after formation; a similar picture is suggested from the experimentally observed density profiles (**Fig. 4-20c**).

Zooming into the propagating front generated by the model (red circle in **Fig. 4-20b**), an elaborate stripe initiation process is revealed: As shown by the black, orange, blue, cyan, magenta, green lines in **Fig. 4-20d**, the density profile of the front has the form of a bulge which propagates forward and increases very slowly in amplitude. When the bulge peak reaches a critical density (corresponding to the level in **Fig. 4-4b** where motility drops abruptly), a nipple forms and grows rapidly in peak amplitude and width (purple and blue lines), eventually developing into a high-density stripe. At the same time, a trough separating the nipple from the propagating front appears and grows into a low-density stripe. Steady lateral movement of the front (which has full mobility being below the critical density), gives rise to a new bulge (red arrow) and starts over the entire process. This stripe initiation and bulge regeneration process may be understood qualitatively from the balance of density-dependent aggregation and front propagation.

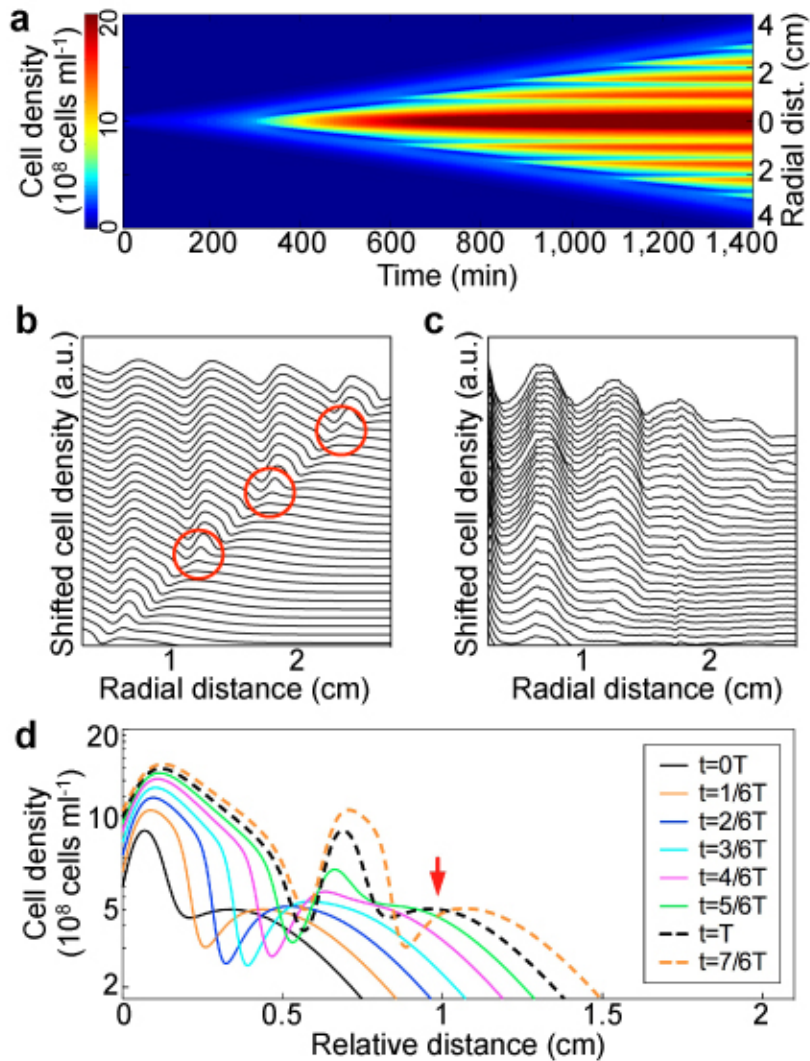


**Figure 4-20 Modeling of autonomous periodic stripe pattern formation.**

**a**, Spatiotemporal diagram of 1D simulated cell density profile corresponding to the experiments depicted in **Fig. 3-6, 3-7**. **b**, Time-lapse plots of the simulated spatial cell-density profiles. Red circles indicate the propagating front. **c**, Time-lapse plots of the experimental spatial cell-density profiles corresponding to simulation in **b**. For **b** and **c**, y-axis is shifted for every 30 min. **d**, Time-lapse plots of the simulated spatial cell-density profiles in the red circle region of **b**, showing the development of the leading bulge in one period ( $T$ ). When cell density reaches a critical level, the bulge rapidly increases peak amplitude (dashed lines). Red arrow indicates a new bulge is forming.

Eqs. [8]-[10] can also produce other behaviors depending on the values of two key dimensionless parameters,  $D_p / D_h$  and  $\gamma / \beta$  ( $D_p$ ,  $D_h$ ,  $\gamma$ , and  $\beta$  are diffusion coefficient of cells, AHL, cell growth rate, and AHL degradation rate, respectively), as summarized in the phase diagram (**Fig. 4-21**).

### 4.3.11 MODEL-GUIDED CONTROLLING OF STRIPE NUMBER

The above phase diagram (**Fig.4-20**) predicts that in addition to the periodic stripe phase discussed so far, the engineered strain may exhibit a qualitatively different behavior with no stripes, by passing through a transition region exhibiting a limited number of stripes. From the parameter dependences shown in the phase diagram, a simple direct way to test the occurrence of this phase transition is to vary the cell motility in the low-density regime ( $D_\rho$ ).

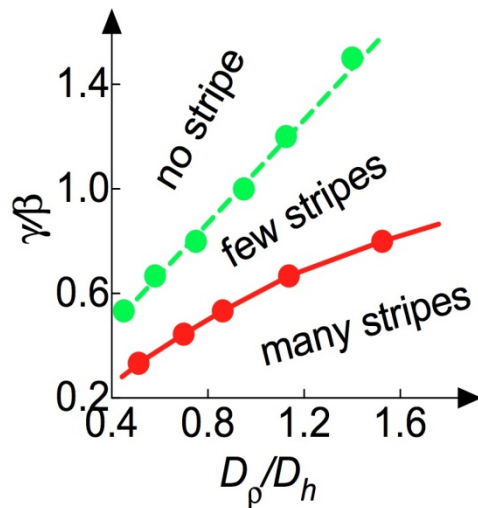


**Figure 4-21 Phase diagram of the stripe number.**

$D_\rho$ ,  $D_h$ ,  $\gamma$ , and  $\beta$  are diffusion coefficient of cells, AHL, growth rate, and AHL degradation rate, respectively.

To the right of the solid line, the system exhibits the periodic stripe phase with an infinite number of stripes (**Fig. 4-21**). Moving to the left of the solid line, there is a regime where the system can still generate a limited number of stripes for some initial conditions. Far away from the solid line no stripes can form (**Fig. 4-21**). The separation between the latter two regimes is not clear-cut and is indicated by the dashed line.

Within my experimental design in which the mobility  $D_\rho$  is set by *cheZ* expression, tuning of  $D_\rho$  can be implemented by adding a second *cI* gene, whose expression is titratable in an AHL-independent manner. I thus created strain CL2. Strain CL2 was constructed via P1 transduction with a recipient strain (CL1) and a donor strain (EQ44)<sup>145</sup>, by which the  $P_{LTet-O1}\text{-}tetR$  construct (containing the *tetR* gene driven by the synthetic, TetR-repressible  $P_{LTet-O1}$  promoter<sup>145</sup>) and the closely linked *bla* gene was integrated into the *attB* site.

Ampicillin-resistant colonies were verified for integration of  $P_{\text{Ltet-O1}}\text{-tetR}$  by PCR and sequencing. Subsequently, CL5 was made by transforming plasmid pLuxRI/CI into CL2. pLuxRI/CI is a variant of pLuxRI2 by harboring a *cI* gene whose expression is driven by a TetR-controlled promoter ( $P_{\text{Ltet-O1}}$ ) (Fig. 4-22a)

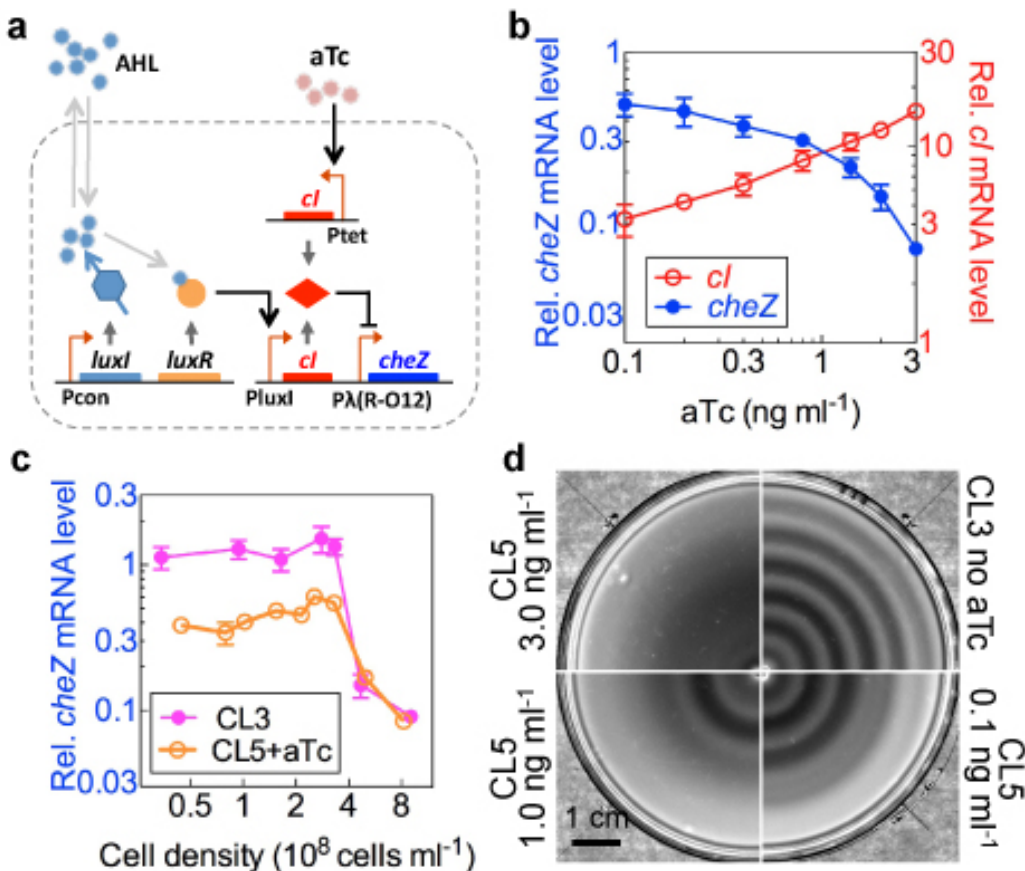


**Figure 4-22 Tunable periodic stripe patterns.**

**a**, Genetic circuit for tunable pattern formation. An additional tunable *cI* expression module was added. **b**, Relative *cheZ* and *cI* mRNA level of CL5 in bulk culture containing various concentrations of aTc (0.1–3 ng ml<sup>-1</sup>). Cells were cultured to OD<sub>600</sub>~0.05 and harvested for measurement. **c**, Relative *cheZ* mRNA level of CL5 as a function of cell density in bulk culture supplemented with 0.4 ng ml<sup>-1</sup> aTc. CL3 was included as a control. **d**, Experimental patterns of CL3 or CL5 inoculated at 0.25% agar containing various concentrations of aTc. Agar plates were incubated at 37 °C for 40 h. For **b** and **c**, data are normalized by the mean value of CL3 at 0.3×10<sup>8</sup> cells ml<sup>-1</sup>.

Fig. 4-22b shows that the basal *cI* expression level of CL5 cells (containing both

pLuxRI/CI and pCheZ/CI) could indeed be smoothly tuned by adjusting the dosage of anhydrotetracycline (aTc), the inducer of TetR, at a fixed cell density ( $0.3 \times 10^8$  cells  $\text{ml}^{-1}$ ); see red symbols. Corresponding changes in the high level of cheZ expression were also observed (blue symbols). Alternatively, for a fixed aTc level ( $0.4 \text{ ng ml}^{-1}$ ), the density dependence of cheZ expression exhibited a reduced high level as designed (Fig. 4-22c).

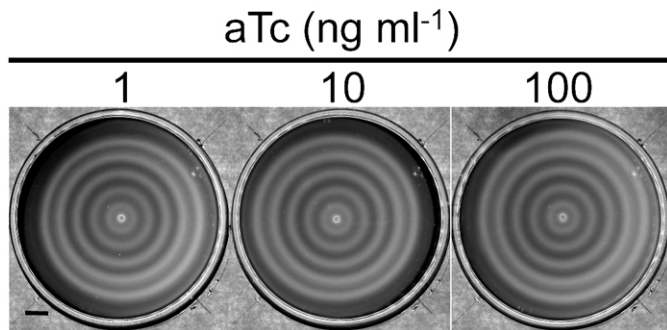


**Figure 4-23 Effect of aTc on the pattern formation of CL3.**

After seed-culture, CL3 cells subcultured into experimental medium supplemented with various concentrations of aTc, grown till mid-exponential phase. 2- $\mu\text{l}$  of cell suspension was spotted at the center of semi-solid agar containing the medium with the same concentration of aTc as subculture. Scale bar, 1 cm.

When strain CL5 was spotted at the center of semi-solid agar, consistent with the model predictions, the stripe number decreased gradually as aTc concentration increased from 0.1 to  $3.0 \text{ ng ml}^{-1}$  (Fig. 4-22d). As a control, the pattern of strain CL3 did not change even when aTc concentration increased to  $100 \text{ ng ml}^{-1}$  (Fig. 4-23).

## 4.4 GENETIC CIRCUIT II

### 4.4.1 RELATION BETWEEN CHEZ EXPRESSION LEVEL AND CELL MOTILITY IN SEMI-SOLID AGAR

In bulk culture, it has been shown that over-expression of *cheZ* inhibits tumbling, and cells overwhelmingly exhibit smooth run<sup>7</sup>. However, in semi-solid agar, only run or tumble

will make *E. coli* cells get trapped by obstructions in the agar. Successful switching between these two directions guarantee cells then can migrate in semi-solid agar<sup>1</sup>.

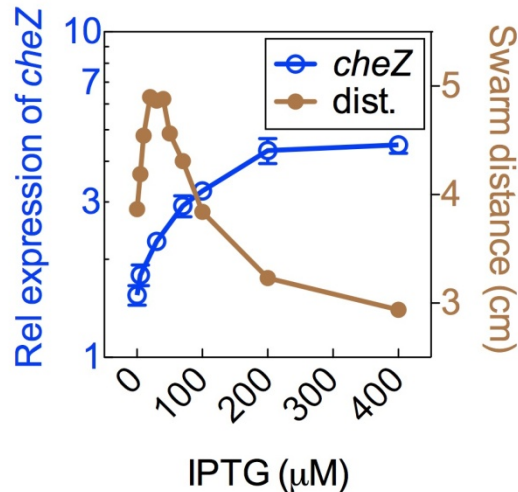


**Figure 4-24 Relative *cheZ* mRNA level or swarm distance of strain CL21 as a function of IPTG concentration.**

Cells in bulk culture containing various concentration of IPTG were cultured to  $OD_{600} \sim 0.3$  and harvested for RT-qPCR measurement. In parallel, 2- $\mu$ l of cell suspension was spotted at the center of semi-solid agar containing the medium with the same concentration of IPTG as subculture, followed by 12-h incubation at 32 °C. dist., swarm distance.

I then tested the motility of the cells in which *cheZ* was overexpressed. Strain CL21 (pLacheZ was transformed into CL20, in which *P<sub>lacIq</sub>-lacI* was integrated into the chromosome) was cultured in LB medium supplemented with various concentrations of IPTG to mid-exponential phase ( $OD_{600}=0.1-0.2$ ), and then spotted at the semi-solid agar plates supplemented the same concentration of IPTG, followed by 12-h incubation at 37°C. As shown in **Fig. 4-24**, the migration distances increased with IPTG at low concentrations, peaked at 30  $\mu$ M, and then decreased as IPTG concentration increased. On the other hand, mRNA level of *cheZ* was measured in parallel in bulk culture. *CheZ* expression was positively correlated with IPTG concentrations and saturated over 400  $\mu$ M (**Fig. 4-24**). Based on these findings, an alternative design is to simply put *cheZ* under the control of *P<sub>luxI</sub>* (**Fig. 4-25a**). Thus, if cell density were high, *cheZ* would be overexpressed, as a result, cells would stop in semi-solid agar.

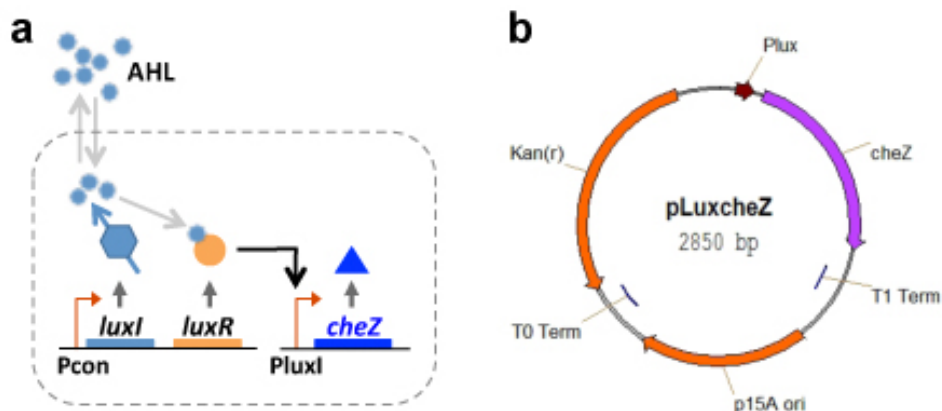


**Figure 4-25 GC-II.**

**a**, *cheZ* is driven by  $P_{luxI}$ <sup>3</sup>. The constitutively expressed LuxI synthesizes AHL, which diffuses freely across the cell membrane<sup>8</sup>. At high cell density, increased intracellular AHL binds to the cytoplasmic transcriptional regulator, LuxR, and the LuxR-AHL complex subsequently activates the *luxI* promoter<sup>3</sup>. Dashed line indicates cell membranes. **b**, map of pLuxcheZ. T0 and T1 indicate transcriptional terminators.

#### 4.4.2 CONSTRUCTION OF GENETIC CIRCUIT POSITIVELY REGULATING *CHEZ* (GC-II)

To make pLuxcheZ (**Fig. 4-25b**), pLuxccdB<sup>14</sup> was linearized by inverse PCR with primers plux-f and plux-r-xho, creating a blunt end and an *Xba*I site, and ligation with *cheZ* structure gene amplified by PCR from the genomic DNA of strain CL-M. pLuxcheZ and pLuxRI2 were then transformed into CL1, resulting CL22.

#### 4.4.3 CHARACTERIZATION OF GC-II

The expression profile of *cheZ* in CL22 was first measured in bulk culture at various cell densities using RT-qPCR. As shown in **Fig. 4-26**, *cheZ* expression level elevated over 20-fold as cell density increased from  $0.9 \times 10^8$  to  $1 \times 10^9$  cells ml<sup>-1</sup>.

To characterize cell motility in semi-solid agar quantitatively, CL22GFP cells were uniformly mixed with 0.25% agar at low density, and then at various times during the course of cell growth, laser was applied to photo-bleach fluorescent cells in small areas on the agar plate. The motility of strain CL22GFP (characterized by an effective diffusion coefficient  $D$ ) showed a bell-shaped curve when plotted as the function of cell densities. The cells began with a low  $D$ , followed by a steep increase to a level as high as the initial level of CL3 within a narrow density range ( $2.4 \times 10^8$  to  $3.5 \times 10^8$  cells  $\text{ml}^{-1}$ ), after that, a sudden drop immediately occurred to an extreme low level (Fig. 4-26), like the strain MGM, which is a flagella-lacking mutant, exhibiting only Brownian motion in either liquid culture or semi-solid agar. Thus, when cell density was high (over  $4 \times 10^8$  cells  $\text{ml}^{-1}$ ), strain CL22GFP exhibits a reduced motility as strain CL3 (Fig. 4-26).

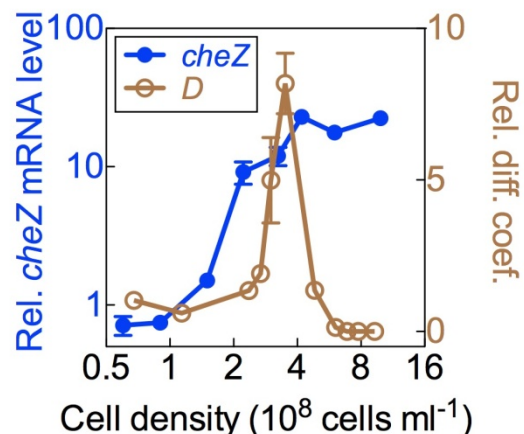


**Figure 4-26 Characterization of GC-II.**

Relative *cheZ* mRNA level in strain CL22 as a function of cell density in bulk culture determined by Quantitative Real-Time RT- PCR. Data are normalized by the mean value of cells at  $0.5 \times 10^8$  cells  $\text{ml}^{-1}$ . The relative diffusion coefficient of strain CL22GFP as a function of cell density for cells uniformly grown in 0.25% agar, measured by CPB method. Relative diffusion coefficient values are normalized by the mean value of CL3GFP at  $0.6 \times 10^8$  cells  $\text{ml}^{-1}$ . Results are representative data from three independent experiments. Error bars represent s.d. of three replicates.

#### 4.4.4 PATTERN FORMATION OF GC-II

I inoculated a suspension of exponentially growing CL22 cells ( $2 \mu\text{l}$ ,  $\text{OD}_{600} \sim 0.1\text{-}0.2$ ) at the center of a 8.5-cm Petri dish containing 10-ml LB medium and 0.25% agar. As shown in Fig. 4-27**b, e**, and **f**, the bands formed sequentially, a more striking stripe pattern formed.

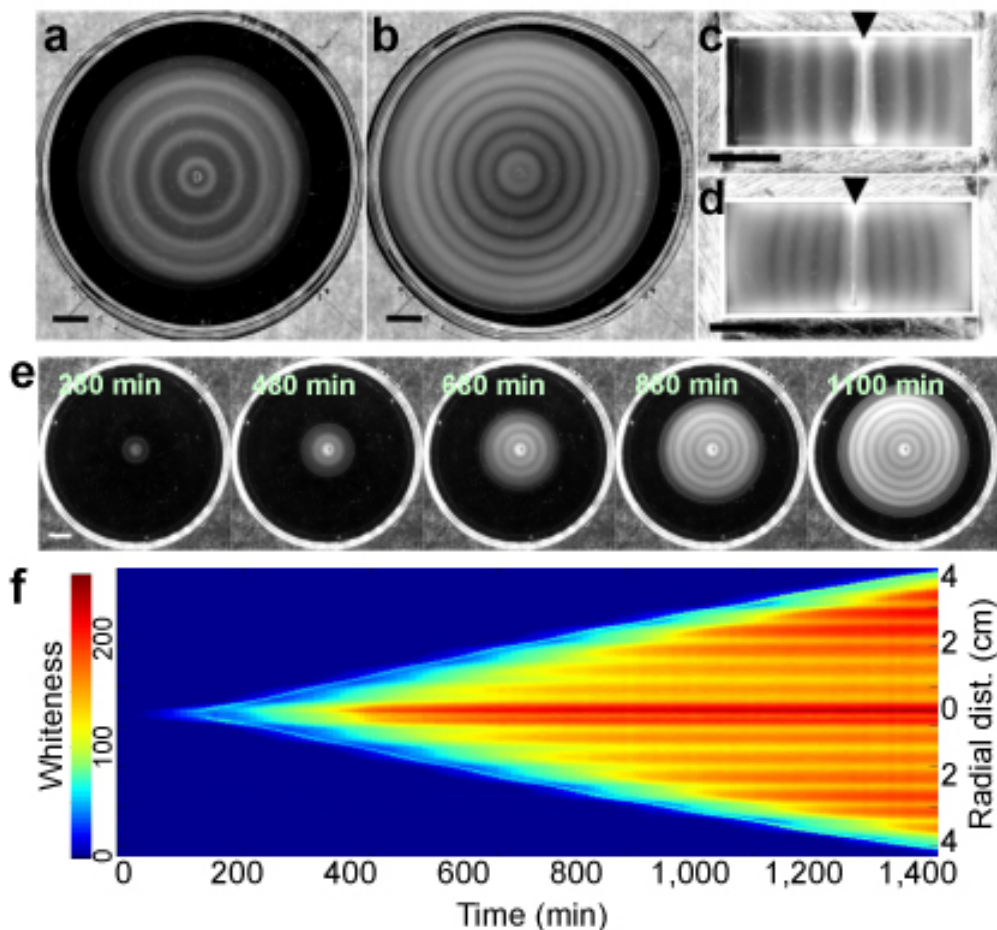


**Figure 4-27 Pattern formation of GC-II.**

**a, c, CL3. b, d, e, f, CL22.** **a, b**, photographs of a typical experimental pattern. Images were captured after 1,200 min growth at  $37^\circ\text{C}$ . **c, d**, One-dimensional pattern. Photographs were taken after 1,200 min growth at  $37^\circ\text{C}$ . The white boundary is an artifact due to the illumination. Arrow indicates the position of inoculation. **e**, Time-lapsed photographs of a typical experimental pattern. Images were captured every 10 min against a black background, illuminated from below by a circular LED array. **f**, Spatiotemporal diagram of **e**, showing the light intensity along a vertical line through the center of the Petri dish as a function of time. Scale bars, 1 cm

Similarly, in one-dimentional geometry, the stripe pattern of CL22 developed and propagated towards the two sides (Fig. 4-27d). These differed from that of CL3 (Fig. 4-27a

and c) with narrower wavelength (distance between the density peaks of two stripes, 0.4 mm) and shorter interval time of stripe generation (150 min), resulting more stripes in a certain space.

The spatiotemporal dynamics of the stripe formation process also was plotted as the colormap (**Fig. 4-27f**). The diagram clearly shows that the positions of the bands are fixed in space once formed. And the bands initiated at a regular time and spatial interval. Comparing to CL3 (**Fig. 4-6**), low-cell-density bands of CL22 were remarkably narrower.

#### 4.4.5 THE INTACT GENETIC CIRCUIT IS REQUIRED FOR THE PATTERN FORMATION

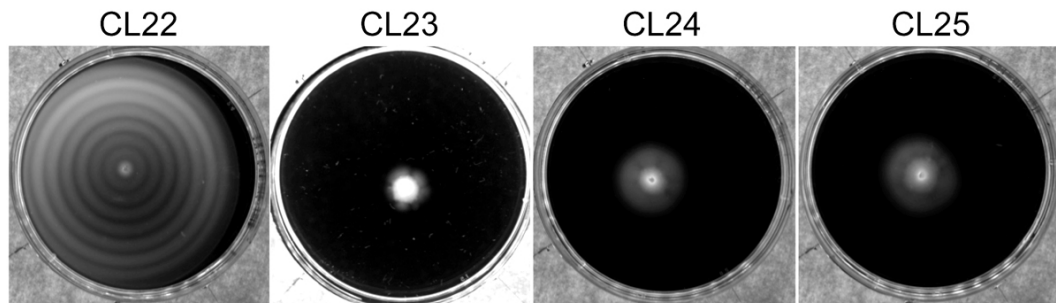


**Figure 4-28 Entire GC-II required for stripe pattern formation.**

After seed culture and preculture, strain CL22 and the deletion mutants were diluted 200-fold into fresh medium and cultured till mid-exponential phase ( $OD_{600}=0.1-0.2$ ), then inoculated 2- $\mu$ l cell suspension at the center of 0.25% agar plates, followed by 20-h incubation at 37 °C. Photographs were taken against black background illuminated by a circular LED array from below. Property of each strain was indicated in the bracket.

To determine the dependence of the pattern formation on GC-II, *luxR*, *luxI*, or *cheZ* was deleted from CL22. In brief, pLuxcheZΔcheZ was made by self-ligating inverse-PCR-amplified fragments from pLuxcheZ to exclude the coding regions of *cheZ* with primers plux-f and plux-r-xho. And then, pLuxRI2 and pLuxcheZΔcheZ, pLuxR and pLuxcheZ, pLuxI and pLuxcheZ were respectively cotransformed into CL1, creating CL23, CL24, and CL25. Cell suspensions of these mutants were spotted onto semi-solid agar, followed by 20-h incubation at 37 °C. As expected, all mutants formed no stripe patterns but spots at the position of inoculum (**Fig. 4-28**).

#### 4.4.6 EFFECT OF QS IN HOST ON THE PATTERN FORMATION

Similarly, to test the effect of QS system in host on the pattern formation, GC-II was introduced into CL16 (*sdiA*<sup>-</sup>) or CL17 (*luxS*<sup>-</sup>), creating CL26 and CL27, respectively. After spotted onto the semi-solid agar plates, either CL26 or CL27 developed identical stripe patterns as CL22 (Fig. 4-29), indicating pattern formation of CL22 is not dependent on these host factors.

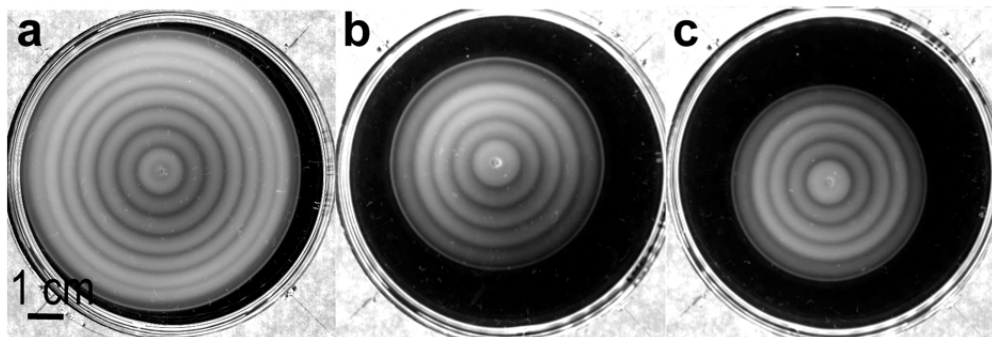


**Figure 4-29 Effects of host-encoded QS factors on GC-II stripe pattern formation.**

**a**, CL22. **b**, CL26 (CL22 $\Delta$ *sdiA*). **c**, CL27 (CL22 $\Delta$ *luxS*). Cells were diluted 200-fold into fresh medium and cultured till mid-exponential phase ( $OD_{600}=0.1\text{--}0.2$ ), then inoculated 2- $\mu\text{l}$  cell suspension at the center of 0.25% agar plates, followed by 20-h (**a**) or 16-h (**b**, **c**) incubation at 37 °C. Photographs were taken against black background illuminated by a circular LED array from below. Property of each strain was indicated in the bracket.

#### 4.4.7 CELL AGGREGATION DRIVEN BY GC-II

To test if the aggregation mechanism demonstrated in CL3 (see 4.3.9) was also the case of CL22, the receiver cells (CL24, CL25, or CL22) were uniformly mixed with semi-solid agar. Subsequently, a drop of sender cells (CL6) was spotted at the center of the hardened cell-agar mixture. After 12-h incubation, only a high-density band of CL24 cells was observed to aggregate around the spotted sender cells (Fig. 4-30), showing the effective aggregation phenomenon mediated by density-dependent motility also existed in cells harboring GC-II.

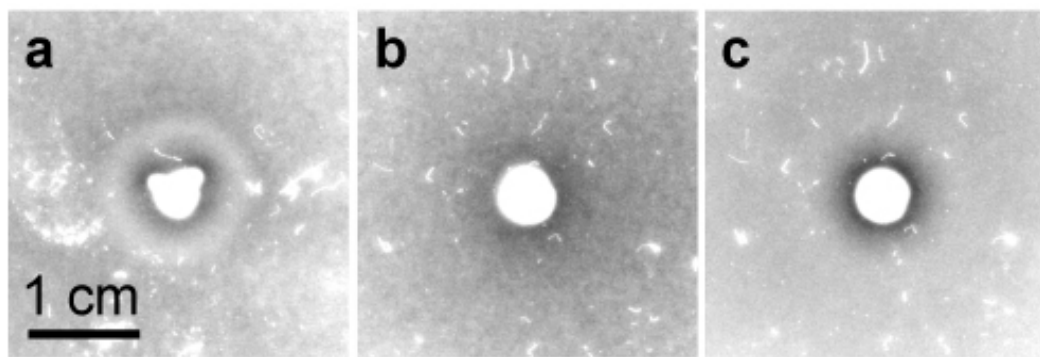


**Figure 4-30 Evidence of effective aggregation.**

All sender cells (CL6, non-motile but synthesizing AHL) were located at the position of inoculum. **a**, CL24, containing entire genetic circuit but lacking AHL-producing gene (*luxI*). **b**, CL25, lacking *luxR*, which failed to regulate *cheZ*. **c**, CL22, containing AHL-producing ability, which might affect the formation of AHL gradient.

## 4.5 “FUJI MOUNT”-LIKE PATTERN

Alternatively, I was curious as to what pattern would be formed if the pseudo-code of density-dependent motility were reversed (i.e., shown in **Fig. 4-31a**, if cell density is high, move; if cell density is low, stop). The modeling analysis predicts that this kind of regulation would give rise to a “Fuji mount”-like pattern (**Fig. 4-31b**).

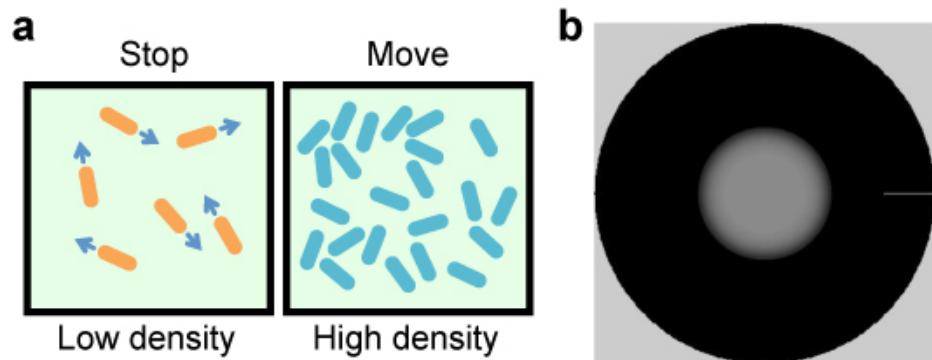


**Figure 4-31 The reversed design of programmed coupling of cell density and motility.**

**a**, Illustration of the design. **b**, Simulated “Fuji-mount” pattern.

Next, I sought to construct a genetic circuit to test if a “Fuji mount”-like pattern would

be formed. The aforesaid relationship between *cheZ* expression and cell motility in semi-solid agar showed a bell-shaped curve, in which a positive regulation was observed when cell density and *cheZ* expression level were low. As to GC-II, if the maximum *cheZ* level induced by cell density could be adjusted below the one that caused the largest  $D$ , then the positive regulation of motility then can be achieved. To this end, I reduced *cheZ* copy number by introducing  $P_{luxI}$ -*cheZ* onto the chromosome of CL1, generating CL28. CL29 was made by introducing pLuxRI2 into CL28. Here, *luxR* and *luxI* on pLuxRI2 presented as high copy number. To further lower the expression level of  $P_{lux}$ , *luxR* and *luxI* were integrated into the chromosome of CL28, creating CL30. As evident in **Fig. 4-32a** and **b**, a “Fuji-mount”-like pattern was generated by either CL29 or CL30.

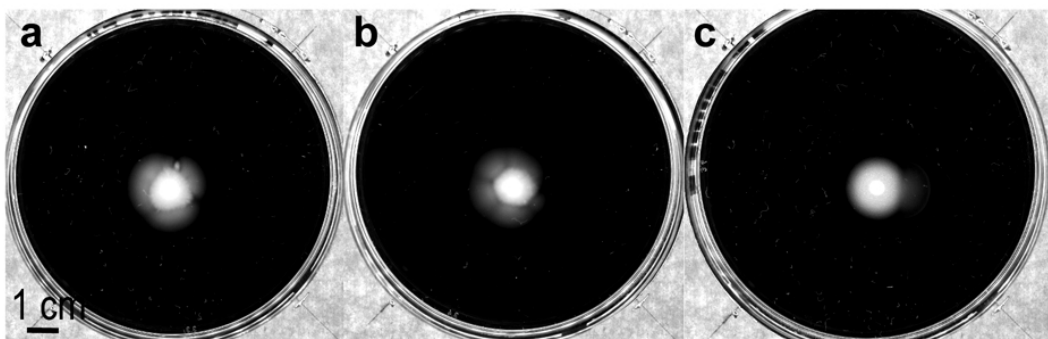


**Figure 4-32** “Fuji-mount”-like pattern.

**a**, CL29, **b**, CL30, **c**, CL31. Cells were cultured till mid-exponential phase ( $OD_{600}=0.1\text{-}0.2$ ), then inoculated 2- $\mu\text{l}$  cell suspension at the center of 0.25% agar plates, followed by 20-h incubation at 37 °C. Photographs were taken against black background illuminated by a circular LED array from below. Property of each strain was indicated in the bracket.

On the other hand, *cheZ* expression level can also be tuned at post-translational level by increasing the CheZ protein turn over rate. Protein stability can be altered by adding some short peptide sequences to their C-terminal. Keiler *et al* showed that some certain C-terminal oligopeptide extensions rendered stable proteins susceptible to protease digestions<sup>1</sup>. After that, Andersen *et al* tested several peptide sequences to change the half-life of GFP from weeks into a range from 40 min to hours<sup>2</sup>. Here, I added the peptide sequences named LAA to proteins CheZ, particularly, *cheZ* gene was PCR amplified from pLuxcheZ with primers cheZ-LAA-f and cheZ-LAA-r-Nhe (**Table 2-2**), which composed of a 39-bp LAA sequence

flanked by the sequence homologous to C-terminal of CheZ and a stop codon followed by a *NheI* site. The PCR fragment was digested with *NheI*, and then inserted into pLuxcheZ, creating pLuxcheZLAA. CL31 was made by cotransforming pLuxcheZLAA and pLuxRI2 into CL1. As predicted, a “Fuji mount”-like pattern was also formed after CL31 was spotted onto the center of semi-solid agar plates (Fig. 4-32c).

## 4.6 OTHER ATTEMPTS

### 4.6.1 REPLACE *CHEZ* BY *CHEY*\*\*

It has been shown that flagella rotation efficiency is not sensitive to the CheY level but the level of phosphorylated CheY<sup>161</sup>. Berg and his coworkers reported a double mutant of CheY, CheY\*\*, which is constantly active without phosphorylation<sup>162</sup>. They demonstrated that the flagella rotation bias was positively correlated with the level of CheY\*\* in cells<sup>162</sup>, i.e. when intracellular CheY\*\* level is low, flagella rotate counterclockwise; when CheY\*\* level is high, flagella rotate clockwise. So the regulation of cell motility also can be achieved by controlling *cheY*\*\* expression. I then sought to make a genetic circuit by replacing *cheZ* in GC-I with *cheY*\*\*.

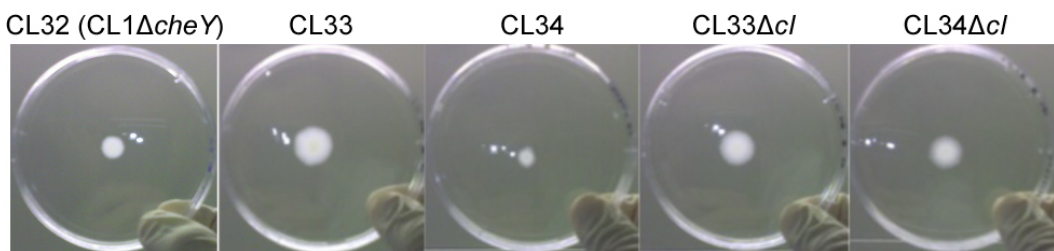


**Figure 4-33 Pattern formation of CL32 and its derivatives.**

Cells were cultured till mid-exponential phase, and spotted onto 0.25% agar plates, followed by incubation at 37 °C for 40 h (CL32), or 20 h (CL33, CL34, CL33Δcl, and CL34Δcl). The bright spots in images are artifact effects of the flashlight of camera.

First of all, full-length *cheY* in CL-M was deleted “seamlessly” using a recombineering protocol<sup>147</sup> with the aid of pSIM6<sup>146</sup>. Similar with the *cheZ*-knockout experiment, loxP flanked chloramphenicol resistance cassette was PCR amplified from pEGFP-loxP-CmR-loxP<sup>147</sup> with primers cheY-del-f and cheY-del-r (**Table 2-2**), each composed of a 50-bp sequence at the 5'-end homologous to the *cheY* gene region. The PCR products were treated with *Dpn*I, gel purified and then electroporated into CL-M cells containing pSIM6<sup>146</sup> that encodes lambda-Red proteins. Cm<sup>r</sup> colonies were verified for replacement of *cheY* with loxP-CmR-loxP cassette using colony PCR with primers cheY-del-conf-f and cheY-del-conf-r, and followed by direct sequencing. Removal of the chloramphenicol gene insertion was mediated by p705Cre as described previously<sup>147</sup>. pSIM6 and p705Cre were removed from the host by growing the mutants overnight at 37 °C. The mutant, designated as CL32. CL32 cells showed only smooth run motion in bulk culture. However, in semi-solid agar, they failed to migrate outwards (**Fig. 4-33**) and got trapped by the agar. Thus, the motility of CL32 in semi-solid agar was defective.

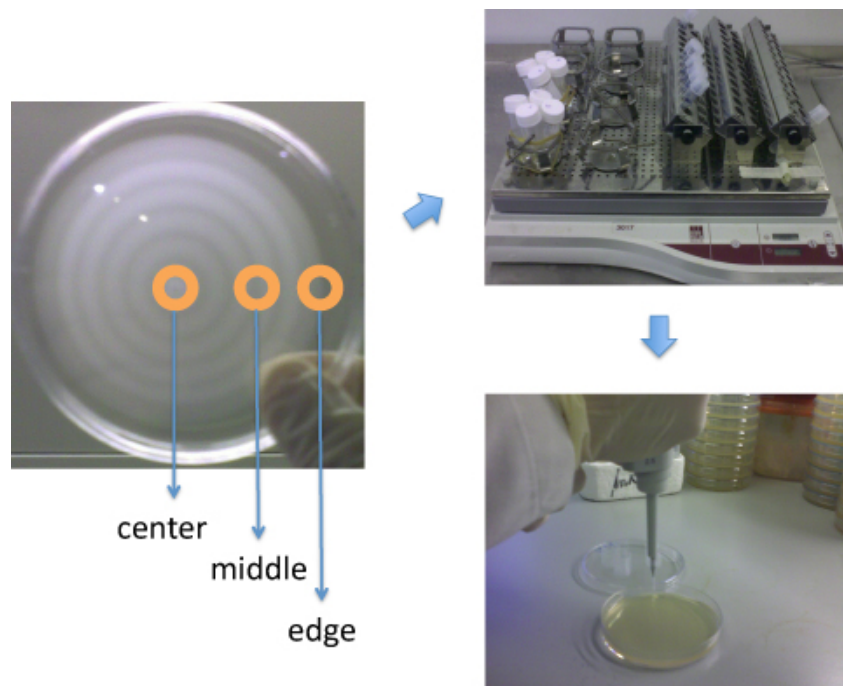


**Figure 4-34 Flow chart of repetitive spotting experiment.**

Cells from certain positions were picked, cultured, and spotted onto the center of fresh 0.25% agar plates. These steps were repeated for at least 16 rounds.

After that, *cheY* structure gene was amplified by PCR from the genomic DNA of strain CL-M with a pair of mutagenesis primers cheY-f-DM and cheY-r-DM, generating D13K and Y106W mutations, and inserted into pMD18-T vector. The resulting plasmid was inversely amplified with primers cheY-f and cheY-r-nhe. Subsequently, the *cheY\*\** fragment was digested and inserted into pCIcheZ at a blunt end and *NheI* sites, replacing *cheZ* with *cheY\*\**.

The resulting plasmid pCIcheY\*\* was transformed into strain CL32 without or with pLuxRI2, creating CL33 and CL34, respectively (**Table 2-1**). As shown in **Fig. 4-33**, CL33 (without *luxRI*) migrated around 1 cm in distance from the inoculum after 20-h incubation at 37 °C. When CL34 (pLuxRI2) was spotted at the center of semi-solid agar, it failed to migrate outwards and mainly stayed at the position of inoculation. Control strains were also included, in which *cI* was deleted. The patterns of these strains were identical to that of CL33 (without pLuxRI2), further indicating that the genetic circuit was functional.

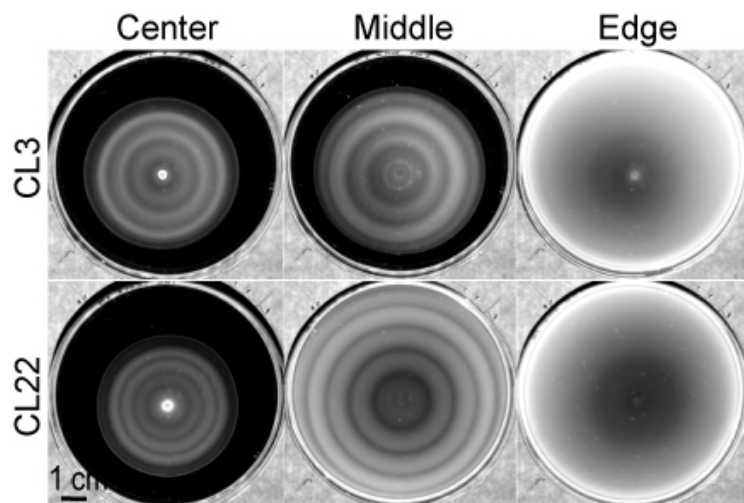


**Figure 4-35 Pattern formation of cells from different positions of developed stripe pattern**

After 10 rounds of picking, culture, and spotting. Images were taken after 30-h incubation at 37 °C.

#### 4.6.2 MUTATION-BASED CHANGE OF STRIPE WAVELENGTH

To test the repeatability of the stripe pattern formation, the cells from different positions

of the stripe patterns formed by CL3 and CL22 were picked separately (**Fig. 4-34**), cultured till mid-exponential phase and spotted at the center of a fresh semi-solid agar plate. After 20-h incubation at 37 °C, cells at the same positions (e.g. for the “center” plate, cells were still picked from the center in the following rounds) were picked again and repeated the culture, inoculation, and incubation procedure for at least 16 rounds.

Surprisingly, after 5 rounds, the patterns formed by cells from the middle and edge positions changed in terms of wavelength, particularly, the wavelength of stripe pattern increased slightly in the “middle” plates but strongly in the “edge” plates. Later on, the stripe pattern in “edge” plates disappeared; the increased-wavelength-pattern in the “middle” plates fixed in the following rounds (**Fig. 4-35**). For the “center” plates, the stripe pattern changed little, but cell density at the inoculum apparently increased (**Fig. 4-35**).

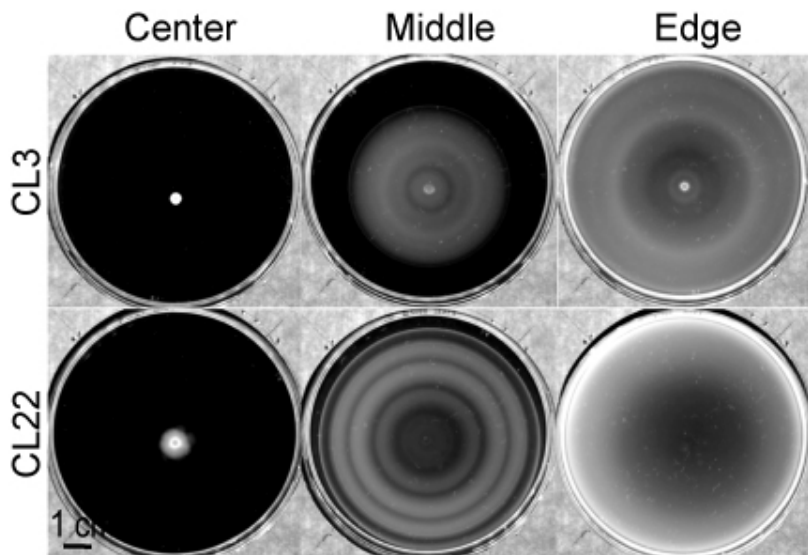


**Figure 4-36 Pattern formation of cells from single colonies isolated from different positions of developed stripe pattern after 15 rounds of picking, culture, and spotting.**

Images were taken after 24-h incubation at 37 °C.

Since the cells picked during each round were from an agar-cell mixture, the patterns observed in these plates might be a collective behavior of a mixture of heterogeneous cells. Thus, the cells from plates of 15<sup>th</sup> round were streaked onto LB agar supplemented with appropriate antibiotics. The single colonies were picked, cultured, and spotted onto the semi-solid agar. As shown in **Fig. 4-36**, cells from the “center” failed to migrate outwards;

cells from the “edge” migrated dramatically fast and formed a disk-like pattern as wild type cells; only cells from the “middle” still formed the increased-wavelength pattern. The cells from the “middle” plates were designated as CL3mid and CL22mid.

Next, I sought to determine if any mutations occurred on the introduced genetic circuit. The two plasmids were then extracted from the CL22mid cells, and transformed into fresh CL1 competent cells. The pattern formed by the resulting CL22\* cells was identical to the original CL22 cells with no change in wavelength, indicating the phenotype of increased wavelength was plasmid-independent (**Fig. 4-37**).

To further confirm this, plasmids in CL22mid were cured. The original pLuxRI2 and pLuxcheZ were transformed into the plasmid-free CL22mid cells, obtaining CL22midN. As anticipated, the pattern formed by CL22midN was identical to that of CL22mid (**Fig. 4-37**), suggesting that the mutations should occur in the chromosome.

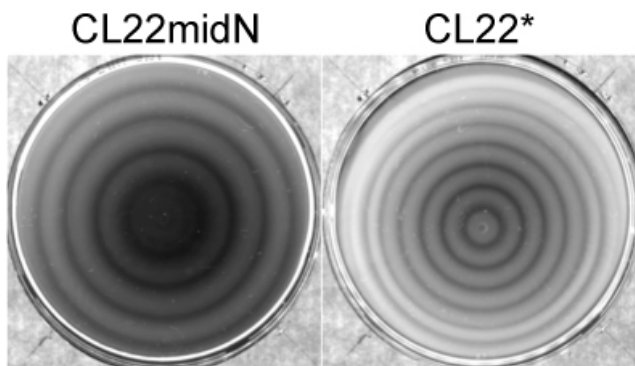


**Figure 4-37 Pattern formation of CL22midN and CL22\*.**

Cells were cultured till mid-exponential phase ( $OD_{600}=0.1-0.2$ ), then inoculated  $2\text{-}\mu\text{l}$  cell suspension at the center of 0.25% agar plates, followed by 30-h incubation at  $37\text{ }^{\circ}\text{C}$ . Photographs were taken against black background illuminated by a circular LED array from below.

## **CHAPTER 5**

## **DISCUSSION AND PERSPECTIVES**

## 5.1 DISCUSSION

Engineered *E. coli* strain with reduced motility at high cell densities exhibited crisp, periodic stripe patterns when spotted on semi-solid agar plates. The stripes formed sequentially during the outward expansion of the genetically identical cell population, and remained stable for weeks. Extensive characterization indicates that the observed phenomenon is not an endogenous response of *E. coli* cells but requires all components of the designed circuit. The stripe formation process can be well described by a mathematical model of density-dependent motility. Key ingredients for stripe formation include an effective aggregation mechanism due to reduced motility at high densities, and the lateral propagation of the low-density front in an outward expansion. In accordance with model prediction, the number of stripes exhibited by the system can be changed in a graded manner by titrating the expression of the regulator CheZ which controls the motility of the engineered strain.

### 5.1.1 EFFECTS OF CHEMOTAXIS

In our model, the stripe pattern formation is irrelevant with chemotaxis. Nevertheless, in **Fig. 3-5b**, two clear Adler rings were observed in CL4, showing an obvious chemotactic wave. As introduced above, CheZ exerts its effect on flagella rotation direction via regulating the phosphorylation status of CheY, which is the effector interacting with FliM (see **1.7.3**). So in CL3, together with the plasmid-born CheZ, endogeneous chemotactic proteins may still assemble a functional chemotaxis machinery.

To make the patterning system more clean (non-chemotactic) and consistent with the proposed model, I sought to test whether CheY can be directly controlled for regulating cell motility in our genetic circuits, excluding other upstream chemotactic effectors. I modified the GC-I by replacing *cheZ* with *cheY\*\**, whose function is independent of other chemotactic proteins<sup>162</sup>. In a *cheY*-knockout *cheZ*-wild type background, the likelihood of flagellar rotation direction is only correlated with the concentration of CheY\*\*. In the other words, CL32 and its derivatives are non-chemotactic strains. However, as shown in **Fig. 4-33**, although CheY\*\* expression partially restored CL32's motility in semi-solid agar, no ring patterns formed. A possible reason might be that the diffusion coefficient of the cells expressed *cheY\*\** was low. Before cells migrated outwards, cell density has become high enough to trigger *cI* expression and to inhibit *cheY\*\** expression. As a result, cells got trapped in the agar. Similarly, Scharf *et al* also showed that the cells expressing CheY\*\* migrated only 1.5 cm in distance from the inoculum after 40-h incubation at 33 °C. Thus,

further efforts need to be made to establish a non-chemotactic system with relatively high diffusion rate.

The stripe patterning process comprises of two key determinants: the effective aggregation and the propagating front (see **4.3.10** for details). In **Fig. 4-19** and **Fig. 4-30**, I demonstrated that the effective aggregation occurred when CL8 and CL24 cells are close enough to the AHL producing cells. I therefore deduce that aggregation arised from density-dependent suppression of cell motility as designed. Since in the aggregation experiments, receiver cells were initially homogeneously mixed with the semi-solid agar, there is no chemoattractant or chemorepellent gradient. One might argue that it may form a possible chemoattractant gradient that the AHL secreted by the sender cell localized at the center of the agar plate. This possibility was ruled out by using CL10 as receiver cells (**Fig. 4-19**), in which *cI* was deleted. Thus, the effective aggregation at least is chemotaxis-independent.

## 5.1.2 EFFECTS OF PH

In **Fig. 4-15**, the pH of medium significantly influences the patterning process. What's the mechanism responsible for this phenomenon? In my preliminary experiments, the LB medium pH was found to change during the bacterial culture, i.e. as cells grew, the pH of the medium increased from 7 to near 9. It was reported previously that the secretion of ammonium during the amino acid catabolism in LB broth results in the high alkalinity of the growth medium<sup>4</sup>. It is also shown that, when the environmental pH is as high as 9, *E. coli* is incapable to grow<sup>163</sup>. In this case, the growth rates changes caused by pH may be a reason to the result shown in **Fig. 4-14**. However, under the pH conditions used in **Fig. 4-14**, the growth rates of CL3 were comparable (data not shown). Although pH changes the growth rate little but dramatically affects the cell motility and AHL stability, the key factors in this pattern formation system. So throughout the study, the medium pH was maintained at near 8 by adding 100 mM HEPES (pH 8.0).

### 5.1.2.1 EFFECTS OF PH ON BACTERIAL MOTILITY

It has been reported that the bacterial migration distance in semi-solid agar decreased as the medium pH increased<sup>164</sup>. The same result was reproduced in CL-M (**Fig. 4-14**). The high motility at low pH condition can be easily reasoned as that the low medium pH causes the high pH difference between external and internal environments of cells, thus the high proton flux drives the flagellar rotation<sup>165</sup> (**1.7.3.5**). Recently, Maurer *et al* carried out a rather

comprehensive comparison of gene expression profiles under different external pH conditions<sup>164</sup>. They found that almost all genes involving flagellar regulon were repressed at high pH (8.7 in their case), e.g. *fliC*, the structure component of the flagellar filament, was downregulated 20 fold comparing to that at pH 7.0.

### 5.1.2.2 EFFECTS OF pH ON AHL STABILITY

On the other hand, another essential factor in the pattern formation system is AHL half-life (**4.3.10**). It has long been known that AHL stability is sensitive to environmental pH<sup>166,167</sup>. Yates *et al* applied <sup>13</sup>C NMR to investigate the turnover of AHL<sup>163</sup>. It is found that the lactone ring of AHL was intact at pH 2, and that the ring opening largely occurred from pH 5 to 8. As a result, the hydrolysis of AHL is pH-dependent, i.e. the turnover rate of AHL increases as the medium pH<sup>166-168</sup>. So if an aqueous solution was unbuffered, the half-life of AHL changed as the culture time increased.

### 5.1.3 WAVELENGTH

The wavelength of a periodic stripe pattern can be defined as the distance between the peaks of two neighboring stripes. It depends on the sizes of the stripe (high density region) and the interval region (low density region). As introduced in **1.4**, in some biological systems, given a fixed wavelength, the number of elements is body-size-dependent. Although the number of stripes has been successfully tuned in body-size-independent manner (see **4.3.11**), how to change the wavelength or the size of the stripe is still an interesting question to address.

As shown in **Fig. 4-12g**, the wavelength of the stripe pattern significantly increased as agar concentration decreased. It is intuitive that higher agar concentration, less convection. At 0.4% or higher agar concentration, the medium was almost solid. Cells were incapable to swim in the bulk, but migrate on the surface of the agar. When agar concentration was lower than 0.4%, cells swim in the agar, resulting a diffusion-like motion. So as agar concentration decreases, the viscosity of the medium decreases, thereby the diffusion rate of cells increases. However, as shown in the phase diagram (**Fig. 4-21**), keeping other parameter fixed, the low cell diffusion rate leads to the less stripe number, which has been experimentally demonstrated. This result is conflict with that of **Fig. 4-12g**, in which as agar concentration increased, cell diffusion coefficient decreased, but the number of stripe did not change. One possible explanation to this contradiction is that the diffusion rate of AHL may also change

with agar concentration. If the ratio of the cell to AHL diffusivity remains the same as agar concentration either increase or decrease, the number stripe would keep unchanged (**Fig. 4-21**). It has been shown that mannitol, a molecule smaller than AHL, has a diffusion coefficient  $\sim 600 \mu\text{m}^2 \text{s}^{-1}$  in liquid and  $\sim 200$  in 0.3% agar at 23 °C<sup>169</sup>. But the diffusivity of AHL in different agar concentration, to my best knowledge, has not been reported. Further efforts are required to investigate the dependency of AHL diffusion coefficient on agar concentration.

Different from the effects of physical conditions, the wavelength of CL22 (GC-II) is remarkably smaller than that of CL3 (GC-I) (**Fig. 4-27**). One possible reason might be that CL22 cells were only motile in a narrow range of cell density, out of which cells became immotile soon (**Fig. 4-26**).

Another possibility is that for CL3, cells need time to produce CI that repress *cheZ* expression. If even *cheZ* is suppressed, cell still need time to dilute out the CheZ proteins in cytoplasm, and then became immotile; on the contrary, the motility of CL22 responded to cell density much quicker without these delays. As a result, when AHL concentration reaches the critical level, the CL3 spends more time in “stopping” itself than CL22. This may cause the larger wavelength of CL3.

Although either physical or genetical approaches can change the wavelength of stripe pattern, the mechanism of wavelength controlling remains unknown. In our future work, the model and experiments needs further iterative development to make it clear.

### 5.1.4 ADAPTIVE MUTATION

In **4.3.8.2** and **4.6.2**, it is showed that the unexpected mutations leaded to the loss or changes of the patterns. I hypothesized the ‘loss of pattern’ might due to the so-called ‘adaptive mutation’, which indicates that bacteria are capable to increase their mutation rate under stress conditions<sup>170,171</sup>, e.g. starvation. Increased mutagenesis have been studied in many dense conditions, such as lawns on plates<sup>172</sup> and saturated culture in liquid<sup>173</sup>. In this study, the cells were also in dense in the semi-solid agar. Given larger space and longer time, more cells were trapped in the high-density stripe due to the designed density-dependent motility. It is obvious that when these trapped cells used up the local nutrients, they were unable to swim outwards to the place where the nutrient was plentiful, and therefore under starvation condition. The multicellular context is important in this case. For an individual cell, the hypermutable state is difficult to make it survive. However, given a mass of these kind of cells, the probability of survival would increase, i.e. the probability of the correct mutation

increase with cell number and duration. This may be the reason why the loss-of pattern phenomenon only happened when larger space and longer time were provided (**Fig. 4-15**). It was proposed that some cells in the mass extensively changing DNA did not survive, however, their rearranged DNA fragments could be donated to other cells whom keep on proliferation<sup>174,175</sup>. The survived cells no longer followed the density-dependent motility, and were able to seeking the nutrients outwards. The mutant cells often have more advantages than their parantal cells under the same conditions. They may become the predominant population in the system. As an evidence, the ‘triangle-like’ shape of the ‘loss-of-pattern’ in **Fig. 4-15** indicated the mutant cells had a clear advantage.

As to the mutants observed in **4.6.2**, they may be a different case. All cells in the certain region changed the phenotype progressively or simultaneously during the rounds of culture, inoculation, and incubation. This may due to the nature of the experimental setting, which is more likely a selective procedure. The cells from the outer and inner regions that can be easily recognized as the fastest and slowest swimmers, respectively, were repeatedly picked out. Finally, the cell from the inner region swims so slow that they get trapped at the inoculum because of the density-dependent motility (**Fig. 4-35**). On the contrary, the cell from the outer region propagates too faster to build up a threshod cell density that immobilize the cell (**Fig. 4-35**). For the cell from the middle region, they may be considered as an intermediate status between the slowest and fastest swimmer. Thus, an increased wavelength of stripe was observed.

However, what exact genetically changes lead to these inherited phenotypes is still unknow. The bottleneck is the high expense of the whole genome sequencing, which may be the most direct way to answer this question. Candidate-based tests might be an alternative approach if the regulative mechanism of these mutations were known.

## 5.2 PERSPECTIVES

### 5.2.1 A GENERAL PATTERN FORMATION STRATEGY

The spontaneous generation of such highly periodic patterns in space and time upon the inclusion of a simple open-loop circuit implementing density-dependent motility is very surprising. Precise patterns are not easy to produce by synthetic systems, in spatial or temporal domain alone<sup>10,13</sup>, not to mention coordinated spatiotemporal patterns. Natural

occurrences of well-coordinated spatial and/or temporal patterns are abundant in developmental systems, including the generation of spiral patterns in the differentiation of *Dictyostelium*<sup>176,177</sup>, the formation of body segments in *Drosophila* embryo<sup>178,179</sup>, and somitogenesis in vertebrate development<sup>180</sup>. Elaborate control and feedback circuits together with strategically placed external cues specifying positional information play critical roles in defining these patterns. In contrast, autonomous pattern formation systems, exemplified by the reaction-diffusion paradigm believed to underlie, e.g., hair follicle<sup>181,182</sup> and pigmentation patterns<sup>183,184</sup>, typically produce space-filling patterns which are at best only quasi periodic. Using synthetic circuit, we demonstrated that precise and robust spatiotemporal patterns could be generated in an autonomous system without explicit feedback. The key is the control of motility, which, as a general pattern formation strategy, has not been systematically explored or appreciated.

### 5.2.2 A SIMPLE WAY TO CHANGE THE NUMBER OF REPEATS

We note that the sequential patterns in nature are often tunable, e.g., the numbers of cervical vertebrae range from one in amphibians, to seven in almost all mammals, and as many as 25 in swans<sup>185</sup>. With the engineered strain, we demonstrated that changes in the number of stripes could be tuned gradually from many to a few by simply changing the basal expression level of a promoter. While this is clearly not the only mechanism to change the number of stripes, the ease with which stripe number can be changed offers the hope that simple evolvable mechanisms also exist in the tuning of the vertebrae number or other macroscopic body features in animal development.

### 5.2.3 IMPLICATION IN DEVELOPMENTAL BIOLOGY

In fact, the strategy of sequential stripe formation exposed by this work is not limited to cellular motility control. In the kinetic equations [1]-[3] which generate the stripe patterns, the cell density  $\rho(\bar{x},t)$  is merely a space- and time- dependent variable, which can equally well be the concentration of a regulator in another context. Thus, Eqs. [1]-[3] may be taken as a generalized reaction-diffusion system with the key feature that the mobility/transport of one of the diffusive species is regulated by another species. As regulated mobility of signaling molecules is a common strategy in metazoan development<sup>186,187</sup>. We believe the lessons from this work will stimulate new insights and inspire new directions in the studies of developmental systems.

In this regard, we mention that the sequential formation of periodic stripes observed here bear clear visual resemblance to the sequential formation of somites in vertebrate development. In the commonly accepted clock-wavefront model for somitogenesis, somites are produced from the posterior growth zone, through the interaction of time-periodic gene expression (the ‘clock’) with a morphogen wavefront that moves along with posterior growth<sup>64,188</sup>. At the phenomenological level, the output of our model (**Fig. 4-19d**) may also be described in terms of a ‘clock’ (the regularly spiking density profile), while the AHL profile may be viewed as a sweeping ‘morphogen wavefront’. However, the ‘clock’ and ‘wavefront’ are in this case self-generated features of a simple autonomous system, which does not need the external morphogen or the internal clock. It will thus be interesting to revisit the somitogenesis model in light of controlled regulator mobility.

Before this pattern formation project, I worked on two other projects, including:

1. Mechanism study of the cell death caused by single-stranded oligodeoxynucleotide-mediated targeted genomic sequence modification.
2. Mechanism study of protective effects of Danshen on cerebellum vascular diseases.

In the following chapters, the results of the two projects, which have been published in *Plos ONE* and *Oligonucleotides*, respectively, were introduced. Copy rights permission has been obtained from the publishers.

## **Appendix I**

**Salvianolic Acid B Inhibits Hydrogen Peroxide  
-Induced Endothelial Cell Apoptosis through  
Regulating PI3K/Akt Signaling**

# **1 INTRODUCTION**

## **1.1 APOPTOSIS**

Apoptosis is a process of programmed cell death in which defective and harmful cells are eliminated from a multicellular organism so as to maintain its homeostasis.

### **1.1.1 CASPASES**

Caspases, a family of specific cysteine proteases, are critical mediators of apoptosis. Fourteen members of the caspase family have been identified<sup>189</sup>. Among them, caspase-3 is a primary executioner of apoptosis induced by a variety of stimuli including H<sub>2</sub>O<sub>2</sub><sup>190,191</sup>. Caspase-9 is a major activator in intrinsic pathway. Following cerebral ischemia, cytochrome *c* is released from mitochondrial intermembrane space as a result of the changed mitochondrion permeability<sup>192</sup>. Released cytochrome *c* promotes the activation of caspase-9 through Apaf-1<sup>193</sup>. Activated caspase-9 subsequently activates caspase-3, which will in turn activate procaspase-9; this sequence forms positive feedback activation pathway.

### **1.1.2 DYSREGULATION OF APOPTOSIS**

Dysregulation of apoptotic signalling leads to pathological conditions, such as carcinoma (no apoptosis) and ischemia (enhanced apoptosis)<sup>194</sup>.

## **1.2 CEREBRAL MICROVASCULAR ENDOTHELIAL CELLS (CMECS)**

Cerebral microvascular endothelial cells (CMECs) and intercellular tight junctions constitute the basic structure of the blood-brain barrier (BBB) which is responsible for regulating the trafficking of cells, substrates, and other molecules into the brain<sup>195</sup>.

## **1.3 APOPTOSIS OF CMECS**

Apoptosis of CMECs may destroy the BBB and expose smooth muscle cells to neurotransmitters, toxins, and other vasoactive agents in the blood stream. Notably, CMECs apoptosis may lead to neuronal injury through the loss of BBB integrity and permit the extravasations of vascular inflammatory cells and proteins that are toxic to neurons. Hence, CMECs apoptosis is considered to be partially responsible for the pathogenesis of various

neurodisorders, such as cerebral ischemia, cerebral apoplexy, and Alzheimer's disease<sup>196,197</sup>.

## 1.4 REACTIVE OXYGEN SPECIES (ROS)

It has been demonstrated that reactive oxygen species (ROS) are involved in the apoptosis of CMECs<sup>198</sup>. Production of high quantities of ROS within the vasculature occurs in a wide array of pathological events<sup>199</sup>.

### 1.4.1. OXIDATIVE STRESS

The excessive accumulation of ROS results in oxidative stress, which is known to induce cell death in a wide variety of cell types by modulating a series of intracellular signaling pathways<sup>200</sup>. Among these pathways, the activation of mitogen-activated protein kinases (MAPKs) and phosphatidylinositol-3-kinase (PI3K)/Akt pathways are known to play major roles in cell growth, survival, differentiation and apoptosis responses<sup>201</sup>. ROS that are particularly responsible for oxidative stress include hydrogen peroxide ( $H_2O_2$ ), superoxide anions, and hydroxyl radicals. Among them,  $H_2O_2$ , the major source of endogenous ROS<sup>202</sup>, is generated during hypoxia and ischemia-reperfusion injury<sup>203</sup>, and has been extensively used to induce oxidative stress in *in vitro* models<sup>199,204</sup>.

## 1.5 SALVIA MILTIORRHIZA BUNGE (DANSHEN)

The dried root of *Salvia miltiorrhiza* Bunge (Danshen) (**Fig. AI-1**) is a popular traditional Chinese medicine and has been widely used in both Asian and Western countries for the treatment of various diseases including cerebrovascular diseases, coronary artery diseases, and myocardial infarction<sup>205,206</sup>.



**Figure AI-1 Photographs of *Salvia miltiorrhiza* Bunge (Danshen).**

**a**, Plant. **b**, Dried root. Figures are from web.

## 1.6 SALVIANOLIC ACID B (SAL B)

Salvianolic acid B (Sal B) (**Fig. AI-2**) is the most abundant and bioactive component of salvianolic acid in Danshen<sup>207</sup>. Extensive pharmacological studies have been carried out on this compound. It was shown that Sal B prevented ischaemia/reperfusion- induced rat brain injury by reducing lipid peroxidation, scavenging free radicals and improving energy metabolism<sup>208</sup>. In cerebral ischemia rats, Sal B reduced learning and memory dysfunctions induced by ischemia<sup>209</sup>. Moreover, salvianolic acids, including Sal B, were shown to improve regional cerebral blood flow in the ischemic hemisphere and inhibit platelet aggregation in rats<sup>210</sup>. More recently, Sal B was reported to be capable of improving the recovery of motor function after cerebral ischemia in rats<sup>211</sup>. At present, the molecular mechanisms responsible for the reported beneficial cerebrovascular effects of Sal B are relatively less studied. Considering the significance of oxidative stress-related cerebral vascular apoptosis, the present study was undertaken to examine the protective effects of Sal B on ROS (represented by H<sub>2</sub>O<sub>2</sub>)-induced rat cerebral microvascular endothelial apoptosis. We provide evidence that the anti-apoptotic effects of Sal B are at least in part mediated by altering the PI3K/Akt/Raf/MEK/ERK signaling pathway

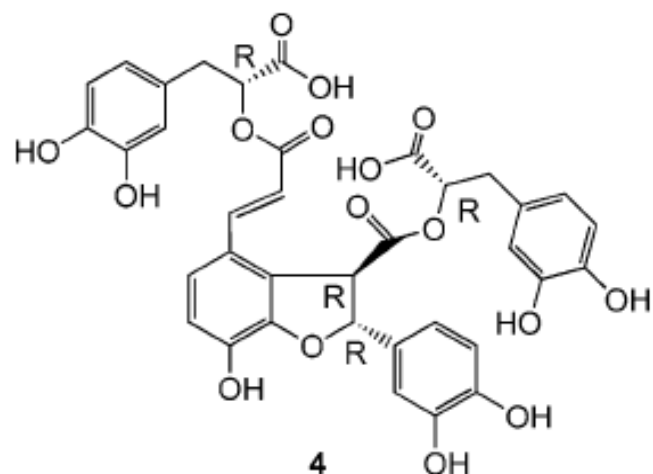


**Figure A1-2 Chemical structure of Sal B**

Figure is from the website of LookChem.com

## **2 MATERIAL AND METHODS**

## 2.1 REAGENTS

Salvianolic acid B (Sal B, purity > 99%) was purchased from the Chinese National Institute for the Control of Pharmaceutical and Biological Products (Beijing, China). When used, it was freshly prepared in phosphate buffer solution (PBS). Dulbecco's modified Eagle's medium (DMEM), medium 199 (M199), fetal bovine serum (FBS), PBS, Trypsin, EDTA, HEPES, PMSF, penicillin, and streptomycin were purchased from Gibco BRL (Grand Island, NY, USA). Endothelial cell growth factor (ECGF) was from Roche Diagnostics (Mannheim, Germany). U0126, LY294002 and antibodies for phospho-ERK1/2, phospho-c-Raf (Ser-259), phospho-Akt (Ser-473), caspase-3 and caspase-9 were obtained from Cell Signaling Technology (Beverly, MA). U0124 was from CalBiochem (San Diego, CA). Horseradish peroxidase (HRP)-conjugated secondary goat anti-mouse or anti-rabbit antibodies were from Invitrogen (S. San Francisco, USA); ECL reagent kit was from Pierce Biotechnology (Rockford, USA); Heparin, collagenase II, gelatin, H<sub>2</sub>O<sub>2</sub>, zVAD-fmk, GW5074, and antibodies for β-actin and γ-tubulin were purchased from Sigma (St. Louis, MO, USA). H<sub>2</sub>O<sub>2</sub> was freshly prepared for each experiment from a 33% stock solution.

## 2.2 MAMMALIAN PRIMARY CELL CULTURE AND DRUG TREATMENT

Rat cerebral microvascular endothelial cells (rCMECs) were isolated from Sprague-Dawley rat cerebral cortex microvessel segments, according to the method described by Bederson et al<sup>212</sup>. Briefly, the cortices were dissected free of meninges and white matter in M199 supplemented with 8% FBS, 10 U ml<sup>-1</sup> heparin and 100 U ml<sup>-1</sup> penicillin-streptomycin solution. The remaining gray matter was cut into small pieces and homogenized. Thereafter, the slurry was filtered consecutively through 145- and 75-mm nylon mesh screens to remove large vessels, tissue mass, single blood and nerve cells. The collected cerebral microvessels were treated with 0.1% collagenase at 37 °C for 15 min. After incubation, the detached cells were centrifuged and resuspended in DMEM supplemented with 25% FBS, 10 U ml<sup>-1</sup> heparin, 100 U ml<sup>-1</sup> penicillin-streptomycin solution and 150 mg ml<sup>-1</sup> ECGF, and were grown in monolayers at 37 °C in a humidified atmosphere of 5% CO<sub>2</sub> and 95% air. Cells from 4<sup>th</sup> and 7<sup>th</sup> passage were used in this study. For all experiments, rCMECs were grown to 80%–90% confluence and then pretreated with designated agents for 60 min prior to H<sub>2</sub>O<sub>2</sub> exposure in fresh medium.

## **2.3 ANALYSIS OF APOPTOSIS**

Apoptosis was detected by the DAPI staining, the TUNEL assay, and the PARP cleavage assay. For DAPI staining, harvested cells were washed with PBS, incubated in PBS containing 0.1% Triton X-100 for 10 min. And then cells were spun down and resuspended in 4% paraformaldehyde solution containing 10 µg ml<sup>-1</sup> DAPI. The morphology of the cells' nuclei was observed using a fluorescence microscope (Olympus, Center Valley, PA). Apoptotic nuclei were identified by the fragmented morphology of nuclear bodies. More than 200 green cells and 500 normal cells were counted.

TUNEL was performed as described<sup>213</sup>. In brief, after transfection, cells were harvested at the indicated time points, washed, fixed, permeabilized, and then resuspended in TdT reaction solution containing 80 µM BrdUTP and 12.5 U TdT. To distinguish corrected cells (GFP fluorescence) from apoptotic cells, cells were labeled with PE-conjugated anti-BrdU monoclonal antibody. Similarly, PARP cleavage assay was carried out with anti-PARP p85 fragment antibody<sup>214</sup> and Alexa Fluor 633-labeled secondary antibody. For both TUNEL and PARP cleavage assays, about 300,000 cells were analyzed on flow cytometer (Beckman Coulter, Fullerton, CA, USA). All assays were carried out in triplicate.

## **2.4 DATA ANALYSIS**

Data was analyzed with unpaired two-tailed Student's *t*-test or one-way ANOVA followed by Tukey's multiple comparison test with GraphPad Prism software (San Diego, CA, USA). Data were expressed as mean±SEM or SD derived from at least three independent experiments. Differences were considered significant at *P*<0.05.

## **3 RESULTS**

### 3.1 H<sub>2</sub>O<sub>2</sub>-INDUCED APOPTOSIS IN RCMECS

I first measured H<sub>2</sub>O<sub>2</sub>-induced apoptosis in rCMECs using the TUNEL assay. As shown in **Fig. AI-3**, the percentage of apoptotic (TUNEL-positive) cells increases dose-dependently with concentrations of H<sub>2</sub>O<sub>2</sub> ranging from 100 to 500 μM for 12 h. In addition, I also evaluated nuclear condensation, which is characteristic for apoptotic cell death, using DAPI staining.

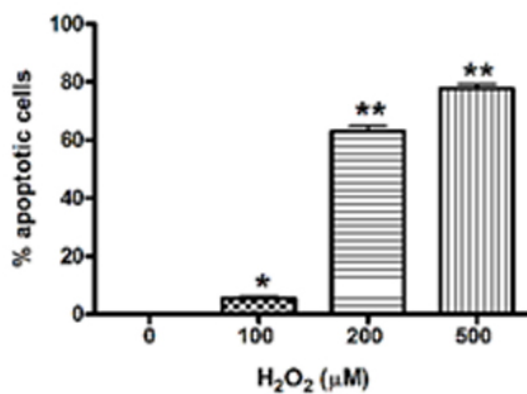


**Figure AI-3 H<sub>2</sub>O<sub>2</sub>-induced rCMECs apoptosis.**

Apoptosis was induced in rCMECs with 0-500 mM H<sub>2</sub>O<sub>2</sub> for 12 h and determined by TUNEL assay. \*P<0.05; \*\*P<0.01 versus control. Data are representative of three independent experiments.

### 3.2 EFFECTS OF SAL B ON H<sub>2</sub>O<sub>2</sub>-INDUCED APOPTOSIS IN RCMECS

To evaluate the effect of Sal B, cells were first pretreated with various concentrations of Sal B (from 10 to 100 μM), followed by treatment with H<sub>2</sub>O<sub>2</sub> (200 μM for 12 h) and apoptosis was then quantified by TUNEL assay and DAPI staining (**Fig. AI-4**). Unstressed cells showed no signs of morphological nuclear damage or chromatin condensation, which distinguished them from the stressed, H<sub>2</sub>O<sub>2</sub>-treated cells. The morphology of cells incubated with both H<sub>2</sub>O<sub>2</sub> and Sal B was comparable to that of unstressed cells.

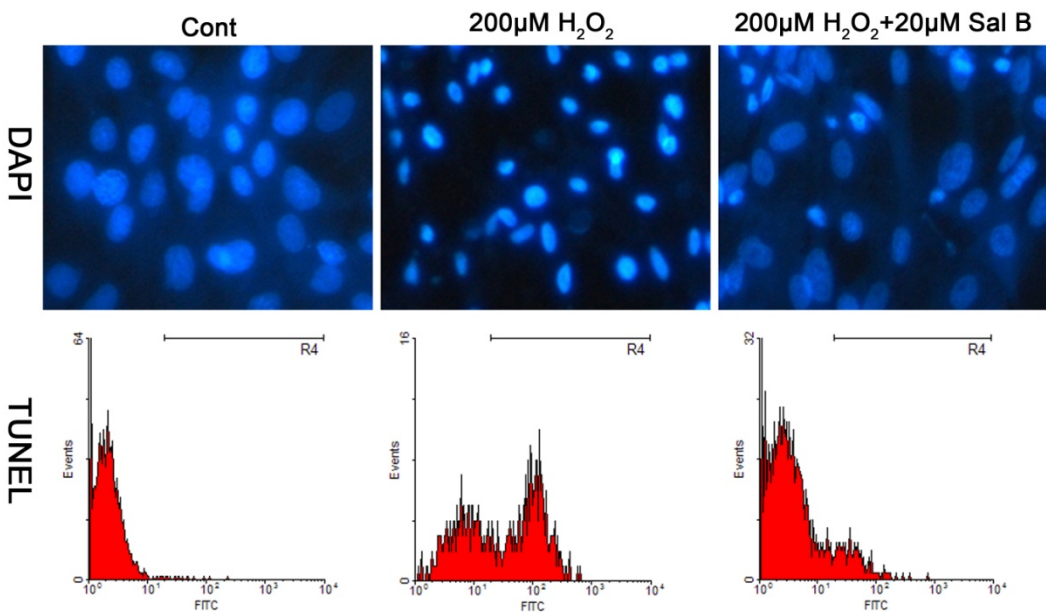
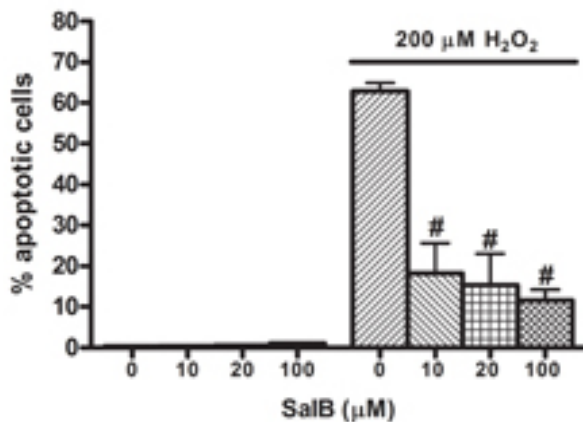


**Figure AI-4 Inhibition of H<sub>2</sub>O<sub>2</sub>-induced rCMECs apoptosis by Sal B.**  
rCMECs were analyzed by DAPI staining and TUNEL assay after a 12-h exposure to H<sub>2</sub>O<sub>2</sub> with or without Sal B pretreatment.

To further verify the effect of Sal B on apoptosis induced by H<sub>2</sub>O<sub>2</sub>, TUNEL assays were performed. The results show that pretreatment with Sal B dose-dependently reduced H<sub>2</sub>O<sub>2</sub>-induced apoptosis (**Fig. AI-5**).

### 3.3 INVOLVEMENT OF CASPASES

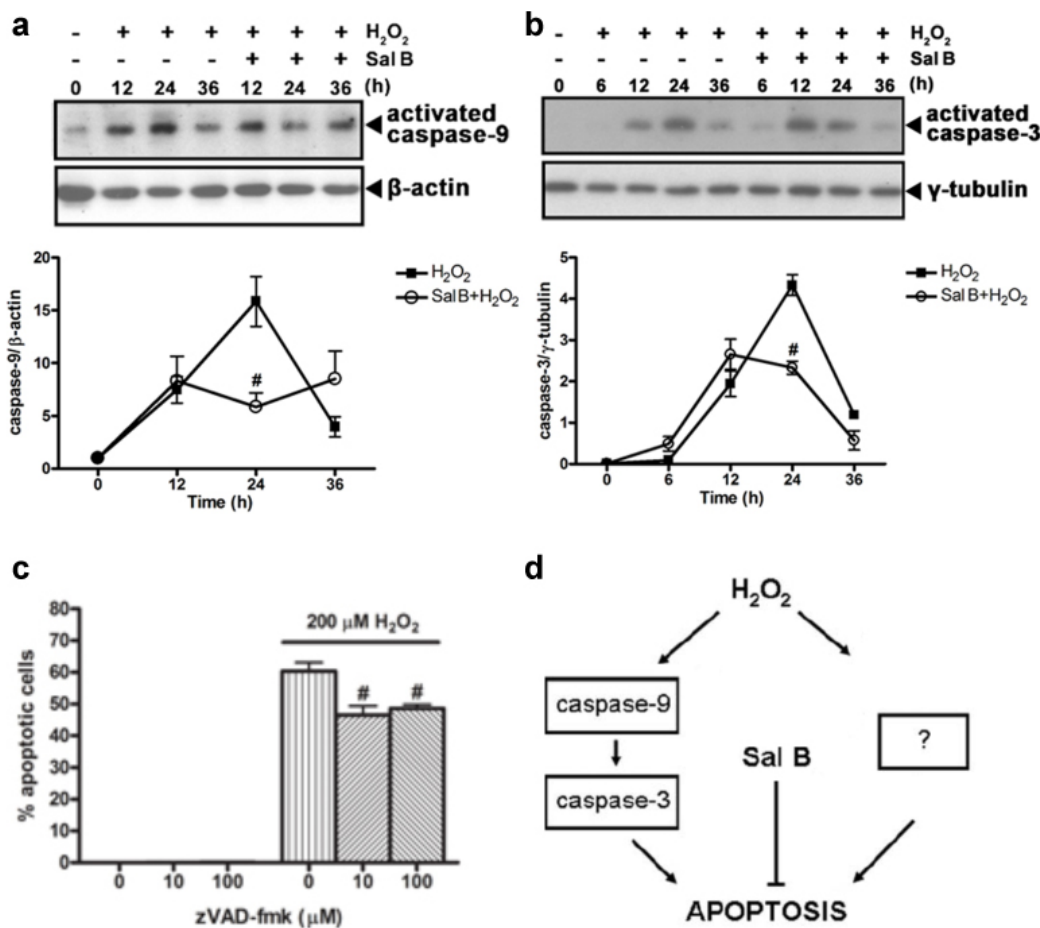
I next examined caspase-9 and -3 activation in H<sub>2</sub>O<sub>2</sub>-stimulated endothelial cells. Western blotting analysis revealed that amounts of cleaved caspase-9 and -3 in H<sub>2</sub>O<sub>2</sub>-stimulated rCMECs were maximal at 24 h and returned to near basal concentrations at 36 h (**Fig. AI-6a, b**). However, these effects of H<sub>2</sub>O<sub>2</sub> were attenuated by Sal B.



**Figure AI-5 The inhibition effect of Sal B is dose-dependent.**

rCMECs were pretreated with Sal B (0,100 mM) for 30 min, and then coincubated with or without 200 mM H<sub>2</sub>O<sub>2</sub> for 12 h, followed by apoptosis measurement using TUNEL assay. #, P<0.05 versus H<sub>2</sub>O<sub>2</sub> alone. Data are representative of three independent experiments.

Preincubation of cells with Sal B decreased the amounts of cleaved caspase-9 (**Fig. AI-6a**) and -3 (**Fig. AI-6b**), and also shortened the duration of their activation in response to exposure to H<sub>2</sub>O<sub>2</sub>. These data imply that Sal B may block the caspase-9 and -3 mediated apoptotic signaling pathways by acting on some upstream target(s). Given that activations of caspase-9 and -3 were still observed when Sal B significantly suppressed H<sub>2</sub>O<sub>2</sub>-induced apoptosis in the first 12 h, I sought to reveal the involvement of caspase. zVAD-fmk, a pan-caspase-inhibitor<sup>215</sup>, was employed to examine its ability to prevent apoptosis by H<sub>2</sub>O<sub>2</sub>. The data shown in Fig. AII-10c demonstrates that zVAD-fmk only slightly reduced the apoptotic percentage after exposure to H<sub>2</sub>O<sub>2</sub>, implying that the majority of rCMECs may undergo caspase-independent apoptosis when exposed to 200 μM H<sub>2</sub>O<sub>2</sub> (**Fig. AI-6d**).

**Figure AI-6 Involvement of caspases.**

**a**, Time course of caspase-9 activation in rCMECs incubated with H<sub>2</sub>O<sub>2</sub> (200 mM) alone or with H<sub>2</sub>O<sub>2</sub> (200 mM) and Sal B (20 mM). **b**, Time course of caspase-3 activation in rCMECs incubated with H<sub>2</sub>O<sub>2</sub> (200 mM) alone or with H<sub>2</sub>O<sub>2</sub> (200 mM) and Sal B (20 mM). Immunoblotting were carried out on cell lysate proteins from control cells or rCMECs pretreated with Sal B for 1 h and then exposed to H<sub>2</sub>O<sub>2</sub> for the indicated times. **c**, rCMECs were pretreated with zVAD-fmk (0,100 μM) for 60 min, and then coincubated with or without 200 mM H<sub>2</sub>O<sub>2</sub> for 12 h, followed by apoptosis measurement using TUNEL assay. #, P<0.05 versus H<sub>2</sub>O<sub>2</sub> alone. Data are representative of three independent experiments.

**d**, Scheme of signaling events I

### 3.4 H<sub>2</sub>O<sub>2</sub>-INDUCED MEK/ERK SIGNALING

To investigate the molecular mechanism by which Sal B exerts its anti-apoptotic effects, the activation of MAPK was examined. An increasing body of evidence has shown that H<sub>2</sub>O<sub>2</sub> stimulation increases extracellular signal-regulated kinase (ERK) activation and concomitant apoptosis<sup>216,217</sup>. I performed the apoptosis analysis using U0126, a specific inhibitor of ERK

upstream kinase MEK<sup>1</sup>. The increase of TUNEL-positive cells stimulated by H<sub>2</sub>O<sub>2</sub> was significantly inhibited by U0126, but not by its inactive analogue U0124<sup>1</sup> (**Fig. AI-7a**). These results indicated that H<sub>2</sub>O<sub>2</sub>-induced rCMECs apoptosis, which was attenuated by Sal B, was mediated through the MEK/ERK signaling pathway (**Fig. AI-7b**).

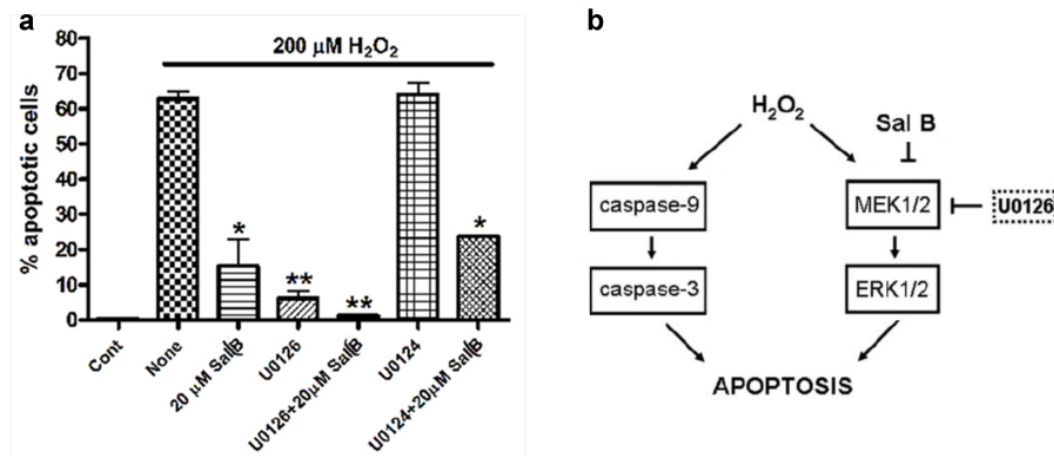


**Figure AI-7 Effects of Sal B, MEK inhibition, or their combination on H<sub>2</sub>O<sub>2</sub>-induced apoptosis.**

**a**, rCMECs were incubated with U0126 (10 nM) or U0124 (10 nM) for 1 h and then exposed to H<sub>2</sub>O<sub>2</sub> in the presence or absence of Sal B pretreatment for 12 h. \*P<0.05; \*\*P<0.01 versus H<sub>2</sub>O<sub>2</sub> alone. Data are representative of three independent experiments. U0126, specific inhibitor of MEK1/2. U0124, inactive analogue of U0126. **b**, Scheme of signaling events II

### 3.5 EFFECTS OF SAL B ON H<sub>2</sub>O<sub>2</sub>-INDUCED MEK/ERK SIGNALING

Therefore, I wondered what the action of Sal B on the modulation of ERK activation in rCMECs is and whether the anti-apoptotic effect of Sal B is mediated through ERK. I thus analyzed ERK activation by Western blotting analysis with phospho-ERK-specific antibody. The results showed that amounts of phosphorylated ERK in H<sub>2</sub>O<sub>2</sub>-stimulated cells peaked at 30 min, that they returned to near basal concentrations after 3 h, but that pretreatment with Sal B resulted in a marked inhibition of these cellular responses, and that incubation of rCMECs with Sal B alone significantly reduced basal ERK phosphorylation (**Fig. AI-8**).

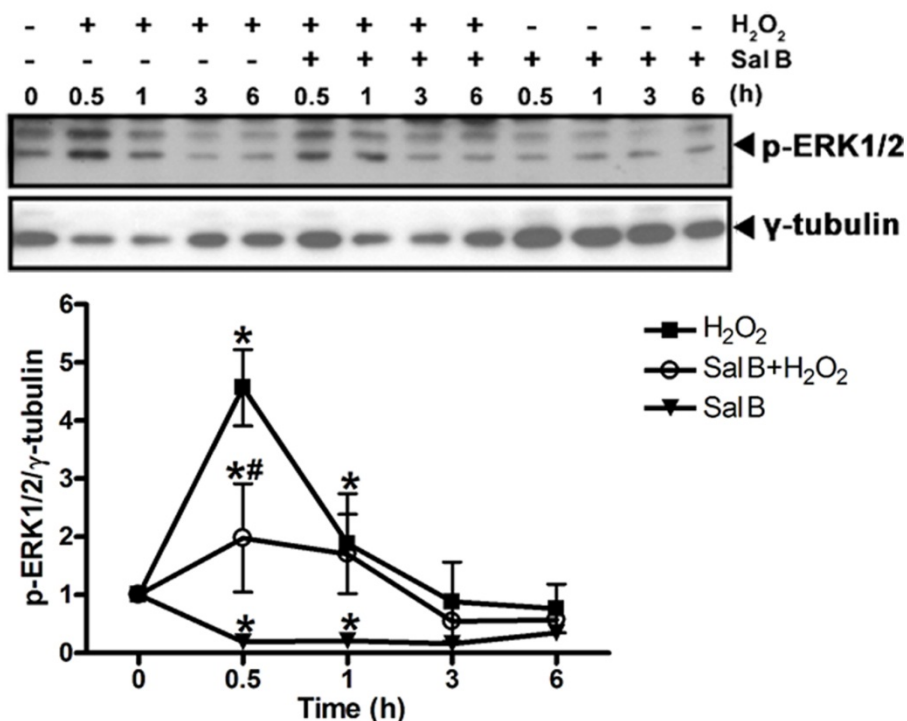


**Figure AI-8 Time course of phosphorylated ERK1/2 expression in rCMECs incubated with H<sub>2</sub>O<sub>2</sub> (200 mM) alone, or with H<sub>2</sub>O<sub>2</sub> (200 mM) and Sal B (20 mM), or with Sal B (20 mM) alone.**

Immunoblotting were carried out on cell lysate proteins from control cells or rCMECs pretreated with Sal B for 1 h and then exposed to H<sub>2</sub>O<sub>2</sub> for the indicated times. The representative Western blots and the quantitative analysis of protein expression (in relative protein density units). \*, P<0.05 versus control, #, P<0.05 versus H<sub>2</sub>O<sub>2</sub> alone. Data are representative of three independent experiments.

### 3.6 PI3K/AKT SIGNALING

I next examined the effect of Akt inhibition on ERK phosphorylation in rCMECs exposed to H<sub>2</sub>O<sub>2</sub>. Treatment with LY294002, a specific inhibitor of Akt upstream kinase PI3K<sup>7</sup>, resulted in the blockage of H<sub>2</sub>O<sub>2</sub>-induced ERK phosphorylation, as well as basal and H<sub>2</sub>O<sub>2</sub>-induced Akt phosphorylation. The basal level of ERK phosphorylation was also diminished (**Fig. AI-9**). In the presence of U0126, basal and H<sub>2</sub>O<sub>2</sub>-induced ERK phosphorylation were blocked. However, U0126 had no effect on either basal or H<sub>2</sub>O<sub>2</sub>-induced Akt phosphorylation (**Fig. AI-9**). These data clearly illustrate that PI3K acts upstream of ERK in the H<sub>2</sub>O<sub>2</sub>-induced signaling cascade.

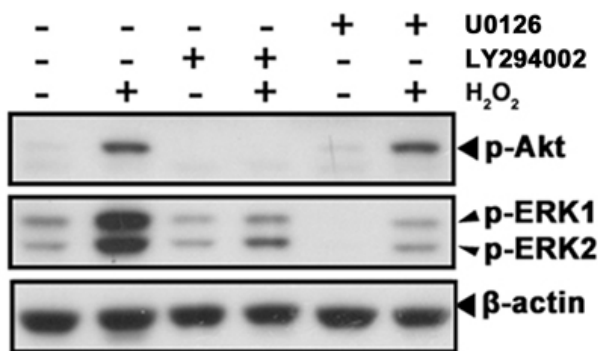


**Figure AI-9 Effects of PI3K or MEK inhibition on phosphorylated Akt (Ser-473) and phosphorylated ERK1/2 expression in the presence or absence of H<sub>2</sub>O<sub>2</sub> (200 mM).**

rCMECs were incubated with LY294002 (50 nM) or U0126 (10 nM) for 1 h and then exposed to H<sub>2</sub>O<sub>2</sub> for 30 min. Blot shown is representative of at least three independent experiments. U0126, a specific inhibitor of ERK upstream kinase MEK<sup>1</sup>. LY294002, a specific inhibitor of Akt upstream kinase PI3K<sup>7</sup>.

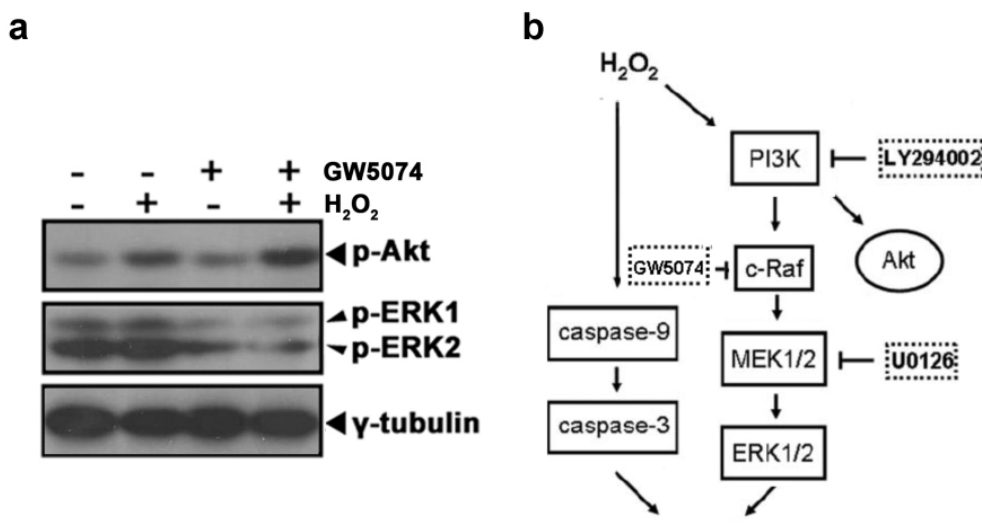


**Figure AI-10 Effects of c-Raf inhibition on apoptosis**

**a,** Effect of c-Raf inhibition on phosphorylated Akt (Ser-473) and phosphorylated ERK1/2 activation induced by H<sub>2</sub>O<sub>2</sub>. rCMECs were incubated with GW5074 (5 nM) and/or H<sub>2</sub>O<sub>2</sub> (200 nM) for 1 h. **b,** Scheme of signaling events involved in H<sub>2</sub>O<sub>2</sub>-induced rCMECs apoptosis.

Since c-Raf is known to lie downstream of Akt, and upstream of ERK<sup>218,219</sup>, I then sought to confirm that this was also the case in rCMECs. GW5074, a selective inhibitor of c-Raf, inhibits the Raf/MEK/ERK cascade in *in vitro* assays by 90% at 5  $\mu$ M<sup>220</sup>. Treatment with GW5074 had no effect on either basal or H<sub>2</sub>O<sub>2</sub>-induced Akt phosphorylation (Fig. AI-10a), but blocked H<sub>2</sub>O<sub>2</sub>-induced ERK phosphorylation (Fig. AI-10a). Thus, c-Raf acts upstream of ERK but downstream of PI3K in H<sub>2</sub>O<sub>2</sub>-induced rCMECs signaling cascade (Fig. AI-10b).

### 3.7 EFFECTS OF SALB ON PI3K/AKT/RAF/MEK/ERK SIGNALING

Previous studies have shown that Akt inhibited activation of the MEK/ERK signaling pathway by phosphorylating c-Raf at residue Ser-259<sup>219</sup>. To investigate whether in rCMECs Sal B inhibited H<sub>2</sub>O<sub>2</sub>-induced MEK/ERK activation through Akt, I therefore evaluated the effect of Sal B on Akt activation. Results showed that the phosphorylation of Akt peaked at 15 min in the cells incubated with Sal B alone, and then returned to basal level over 60 min (Fig. AI-11a). An elevated level of phosphorylated c-Raf at Ser-259 was also triggered by Sal B alone (Fig. AI-11a). Furthermore, LY294002 treatment completely blocked expressions of phosphorylated Akt (Ser-473) and c-Raf (Ser-259) induced by Sal B (Fig. AI-11b). This indicates PI3K is required for Sal B-induced Akt activation and c-Raf deactivation.

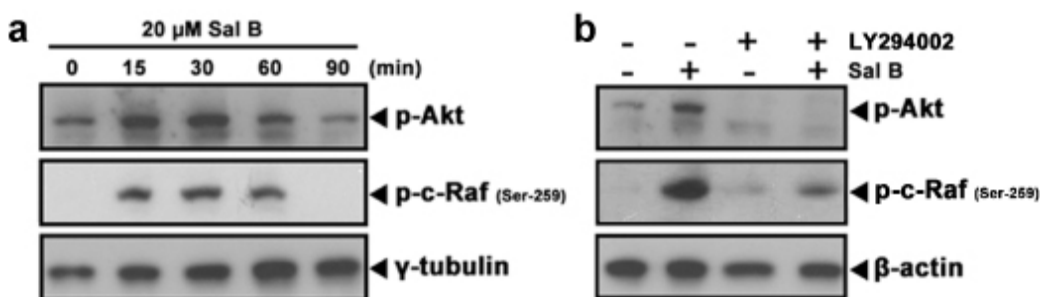


**Figure AI-11 Effects of Sal B on PI3K/Akt/Raf signaling.**

**a**, Phosphorylated Akt (Ser-473) and phosphorylated c-Raf (Ser-259) expressions in rCMECs incubated with Sal B (20 mM) for the indicated times. **b**, Effect of PI3K inhibition on phosphorylated Akt (Ser-473) and phosphorylated c-Raf (Ser-259) expressions induced by Sal B. rCMECs were incubated with LY294002 (50 mM) and/or Sal B (20 mM) for 1 h.

To further determine if the anti-apoptotic effects of Sal B were due to its effect on Akt, rCMECs were incubated with LY294002, with and without Sal B prior to H<sub>2</sub>O<sub>2</sub> treatment. Inhibition of PI3K completely ablated the anti-apoptotic effect of Sal B, as well as H<sub>2</sub>O<sub>2</sub>-induced apoptosis was potentiated (**Fig. AI-12a**). Thus, these results indicate that Sal B prevents H<sub>2</sub>O<sub>2</sub>-induced rCMECs apoptosis, at least in part, by altering PI3K/Akt/Raf/MEK/ERK activation (**Fig. AI-12b**).

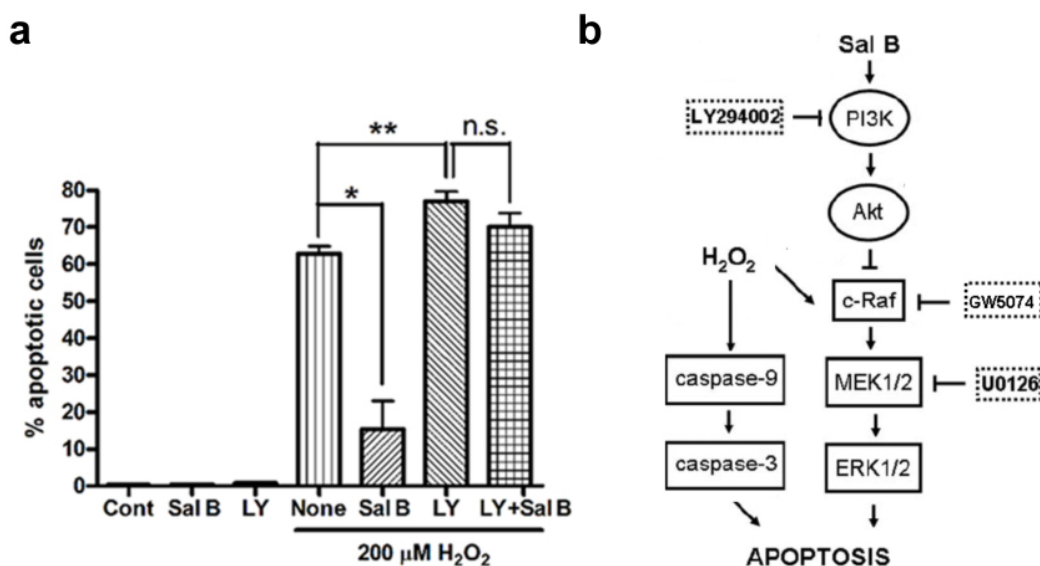


**Figure AI-12 Role of PI3K signaling.**

**a**, Effect of PI3K inhibition on H<sub>2</sub>O<sub>2</sub>-induced apoptosis in the presence or absence of Sal B (20 mM). rCMECs were incubated with LY294002 (50 nM) and/or Sal B (20 mM) for 1 h and then exposed to H<sub>2</sub>O<sub>2</sub> for 12 h. LY, indicates LY294002. \*P<0.05; \*\*P<0.01 versus H<sub>2</sub>O<sub>2</sub> alone; n.s., not significant. Data are representative of three independent experiments. **b**, Scheme of signaling events involved in Sal B prevention of H<sub>2</sub>O<sub>2</sub>-induced rCMECs apoptosis.

### 3.8 EFFECT OF SAL B ON BCL-2 EXPRESSION

To address the question whether Sal B exerts its anti-apoptotic effects only via PI3K-Akt-Raf-MEK-ERK signaling pathway, I pretreated rCMECs with U0126 or U0124 in the presence or absence of Sal B and found that the effect of Sal B on H<sub>2</sub>O<sub>2</sub>-induced apoptosis pronouncedly increased that of U0126 (**Fig. AI-7a**), indicating that there's other

mechanism contributing to the anti-apoptotic effects of Sal B. I next sought to determine which cellular signal transduction pathways other than MEK-ERK pathway were involved in it. I determined the levels of expression of Bcl-2, a well-known anti-apoptotic protein, by Western blot analysis. When rCMECs were incubated with Sal B alone, the Bcl-2 protein levels obviously increased and reached the peak at 30 min after H<sub>2</sub>O<sub>2</sub> treatment (**Fig. AI-13a, b**), and then slowly decreased over 6 h (**Fig. AI-13a**). In contrast, H<sub>2</sub>O<sub>2</sub> incubation induced a rapid decrease of levels of Bcl-2 protein, which was completely reversed by preincubation of Sal B (**Fig. AI-13a**). These data suggested that Bcl-2 might involve in the protective effect of Sal B against H<sub>2</sub>O<sub>2</sub>-induced rCMECs apoptosis. This needs further investigation (see AI section 4.8)

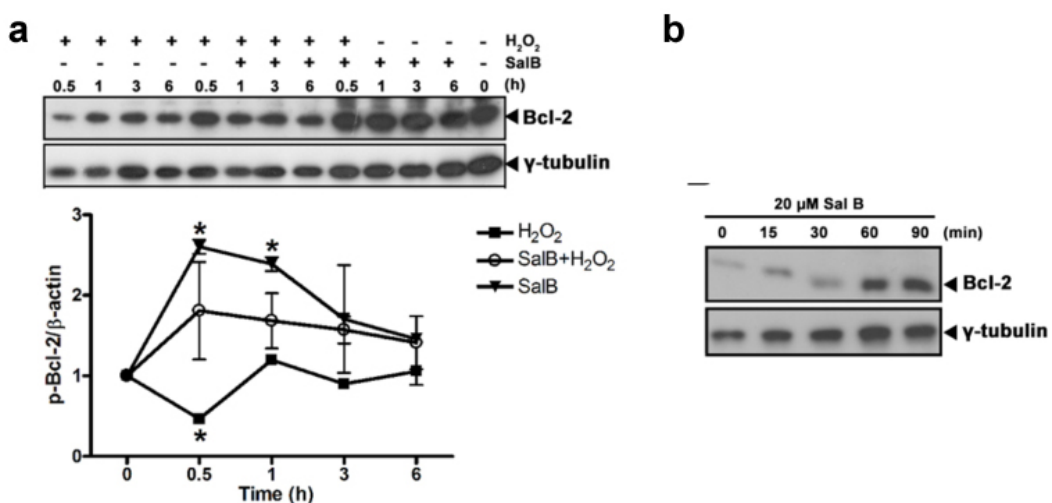


**Figure AI-13 Time course of Bcl-2 expression.**

**a**, rCMECs were incubated with H<sub>2</sub>O<sub>2</sub> (200 μM) alone or with H<sub>2</sub>O<sub>2</sub> (200 μM) and Sal B (20 μM) for 0.5, 1, 3, and 6 h. The representative Western blots and the quantitative analysis of protein expression (in relative protein density units). **b**, rCMECs were incubated with Sal B alone for 15, 30, 60, and 90 min. \*P<0.05 versus Control. Data are representative of three independent experiments.

## **4 DISCUSSION AND PERSPECTIVES**

This study yielded four major findings: (1) Exposure rCMECs to H<sub>2</sub>O<sub>2</sub> caused dose-dependent apoptosis, which could be prevented by pretreatment with Sal B. (2) Activation of the MEK/ERK pathway acted as a pro-apoptotic signal in H<sub>2</sub>O<sub>2</sub>-treated rCMECs; this activation was in turn dependent on PI3K activation. (3) The PI3K/Akt pathway acted as a survival signal upstream of c-Raf in H<sub>2</sub>O<sub>2</sub>-treated rCMECs. (4) Sal B exerted its preventive effects at least partly through the PI3K/Akt/Raf/MEK/ERK pathway.

## **4.1 CMECS AS A MODEL**

CMECs is a useful cell culture model for elucidating mechanisms of cerebral vascular diseases and protection that are extremely difficult to identify *in vivo*<sup>221</sup>. Apoptosis of CMECs plays a pivotal role in pathogenesis of these diseases. Accumulating evidence indicates that the elevated release of ROS from brain tissue under pathologic conditions is a fundamental mechanism leading to the apoptosis of CMECs. So protection of CMECs from ROS-induced apoptosis may provide beneficial therapeutic intervention to successfully combat cerebrovascular diseases. In this study, I demonstrated that Sal B was capable of saving rCMECs from apoptotic cell death caused by H<sub>2</sub>O<sub>2</sub>. This suggests that Sal B may have therapeutic use in the prevention of cerebrovascular diseases.

## **4.2 CASEPASE ACTIVATION BY H<sub>2</sub>O<sub>2</sub>**

To date, very little is known about apoptotic effects of H<sub>2</sub>O<sub>2</sub> in CMECs. Our results indicate that H<sub>2</sub>O<sub>2</sub> induced CMECs apoptosis in a dose-dependent manner; this apoptosis was characterized by condensation of the nucleus chromatin, fragmentation of the DNA, and activation of caspases-3 and -9. I showed that Sal B attenuated the activation of both caspases-3 and -9, and shortened their activation durations. The mechanisms by which H<sub>2</sub>O<sub>2</sub> induces caspase activation in endothelial cells are not fully understood. This activation could be due to direct oxidative stress, or it could be mediated by mitochondria or by other mechanisms; any of these mechanisms might be inhibited by Sal B. Although H<sub>2</sub>O<sub>2</sub> activated caspases in rCMECs, our data indicate that H<sub>2</sub>O<sub>2</sub>-induced apoptosis was mainly dependent on caspase-independent mechanisms but not caspase activation.

### **4.3 ERK: PRO-SURVIVAL OR PRO-APOPTOSIS**

Exposure of endothelial cells to H<sub>2</sub>O<sub>2</sub> activates several intricate cell signaling cascades that are crucial for determining whether a cell survives or dies. One such cascade involves ERK-mediated signaling [34]. The ERK pathway is most frequently associated with regulation of cell growth, survival, and differentiation<sup>222</sup>. A growing body of studies has revealed that ERK might play a role in apoptosis and pathogenesis. However the existing evidence is conflicting. For example, Yang et al.<sup>199</sup> reported that ERK served as pro-survival signaling mediators to alleviate H<sub>2</sub>O<sub>2</sub> cytotoxic effects in aortic endothelial cells. Oppositely, studies by Fischer et al. showed that in CMECs, paracellular permeability induced by H<sub>2</sub>O<sub>2</sub> was due to the activation of ERK. Similarly, I showed that inhibition of ERK by U0126 elicited cell survival, suggesting ERK was a pro-apoptosis signal mediator in H<sub>2</sub>O<sub>2</sub>-stimulated rCMECs. Taken together, these results suggest that the role of ERK under oxidative stress is cell-type specific. Our data further showed that ERK activation following oxidative injury was suppressed by Sal B treatment, which was consistent with data recently published by others in different cell culture models: human aortic smooth muscle cells<sup>223,224</sup>; hepatic stellate cells<sup>225</sup>; and human umbilical vein endothelial cells<sup>226</sup>. These results indicate that the ERK pathway may be a target of Sal B activity.

### **4.4 PI3K/AKT IS PRO-SURVIVAL**

To gain further insight into the mechanisms by which Sal B modulates ERK signalling and by which ERK mediates H<sub>2</sub>O<sub>2</sub>-induced apoptosis, I evaluated the role of the PI3K/Akt pathway. Akt is a serine/threonine kinase. It can be activated by phosphorylation and subsequently activates multiple downstream targets to enhance cell survival. PI3K, a lipid kinase, is largely responsible for Akt phosphorylation; it has three classes or subfamilies; I, II, and III. Each class of PI3K has unique preferences for phosphoinositide substrates and produces specific lipid second messengers<sup>227</sup>. In endothelial cells, PI3K/Akt elicits a survival signalling following various stresses, including exposure to H<sub>2</sub>O<sub>2</sub>, and this signaling leads to the inhibition of apoptosis<sup>228,229</sup>. Notably, following cerebral ischemia, Akt is responsible for the preventive effects on cerebrovascular endothelium apoptosis<sup>221</sup>. In rCMECs, I demonstrated that exposure to H<sub>2</sub>O<sub>2</sub> induced a transient activation of Akt, which peaked at 1 h. If PI3K/Akt plays an important survival role in rCMECs, inhibition of PI3K/Akt should potentiate H<sub>2</sub>O<sub>2</sub>-induced apoptosis; indeed this was observed.

## **4.5 AKT AND ERK REPRESENTED TWO INDEPENDENT PATHWAYS**

Given that activation of Akt was observed in the presence of significantly elevated levels of phosphorylated ERK in cells exposed to H<sub>2</sub>O<sub>2</sub>, I were curious as to whether Akt and ERK represented two independent pathways in apoptotic signaling cascades induced by H<sub>2</sub>O<sub>2</sub>. Zhuang et al.<sup>217</sup> and Sinha et al<sup>230</sup> recently reported that ERK was an upstream effector of Akt and that inhibition of ERK enhanced Akt activity. Unlike their observation, our data showed that Akt phosphorylation level was unaffected by ERK inhibition. In contrast, H<sub>2</sub>O<sub>2</sub>-induced activation of ERK was completely inhibited by the PI3K-inhibitor, LY294002, suggesting that PI3K was responsible for ERK activation. Thus, the activation of PI3K was an upstream event in H<sub>2</sub>O<sub>2</sub>-induced rCMECs apoptosis; it subsequently activated Akt and, through an unknown mechanism, ERK. Since LY294002 inhibits all classes of PI3Ks, activation of ERK and Akt might be induced by a different PI3K family member. It was recently reported that, although all class I PI3K family members are capable of activating Akt, only PI3K $\gamma$  is responsible for the activation of MEK/ERK<sup>231</sup>.

Clearly, although both PI3K/Akt and PI3K/ERK are activated following oxidant injury in rCMECs, they play opposite roles. PI3K/ERK signaling played an indispensably proapoptotic role in H<sub>2</sub>O<sub>2</sub>-induced rCMECs apoptosis. Sequentially activation of PI3K and Akt acted as survival signal to protect cells from apoptosis by deactivating c-Raf at Ser-259. In addition to this, Akt also promotes cell survival by its abilities to phosphorylate Bad at Ser136<sup>232</sup>; Akt also directly inhibits activation of caspase-9 by phosphorylating pro-caspase-9 at Ser-196 and by this inhibits proteolytic processing of pro-Caspase-9<sup>233</sup>.

## **4.6 A BALANCE BETWEEN PI3K/AKT AND PI3K/MEK/ERK**

I suppose that the status of rCMECs apoptosis is determined by the balance between the PI3K/Akt and PI3K/MEK/ERK pathways. In the presence of H<sub>2</sub>O<sub>2</sub>, the effects of PI3K/MEK/ERK overwhelm those of PI3K/Akt, so that the balance is tipped in favor of apoptosis. So Sal B may protect rCMECs from H<sub>2</sub>O<sub>2</sub>-induced apoptosis by restoring the PI3K/Akt and PI3K/MEK/ERK balance. Our hypothesis is supported by our findings that Sal B alone triggered a rapid activation of Akt, peaked at 15 min, which then initiated downstream signaling events including deactivation of c-Raf, and down-regulation of MEK and ERK. On the other hand, inhibition of PI3K completely blocked Sal B-mediated Akt

activation and all following effects. These data confirmed that PI3K/Akt is a particularly important signaling pathway in the mechanism by which Sal B promotes endothelium survival.

## **4.7 OTHER MECHANISM (S)**

With a dosage that completely suppressed ERK activation, U0126 showed a substantial but not complete effect on H<sub>2</sub>O<sub>2</sub>-induced apoptosis (**Fig. AI-7a**). This clearly indicated that MEK/ERK was not the sole pathway responsible for H<sub>2</sub>O<sub>2</sub>-induced apoptosis. Using both U0126 and Sal B, I then observed a complete rescue from apoptotic cell death caused by H<sub>2</sub>O<sub>2</sub>. Thus, it appears that in addition to the PI3K/Akt/Raf/MEK/ERK pathway, Sal B might protect rCMECs from apoptosis through other mechanism(s). To address this possibility, we examined the protein level of Bcl-2. As a potent suppressor of apoptosis, Bcl-2 plays an important role in endothelial cell death. H<sub>2</sub>O<sub>2</sub> was reported to down-regulate Bcl-2 level, which caused endothelial cells apoptosis<sup>234</sup>. Accordingly, over-expression of Bcl-2 inhibited apoptosis of cells exposed to H<sub>2</sub>O<sub>2</sub><sup>235</sup>. Indeed, Sal B not only reversed H<sub>2</sub>O<sub>2</sub>-induced decrease in Bcl-2 expression, but triggered a transient increase of Bcl-2 protein level. It is known that Bcl-2 prevents apoptosis by inhibiting the collapse of the mitochondrial membrane potential gradient and cytochrome c release to the cytosol<sup>236</sup>. A recent publication revealed that Bcl-2 might be a downstream effector of Akt in endothelial cells<sup>237</sup>. This possibility needs further investigation. The upstream regulator of Bcl-2 was not defined in this study.

In conclusion, our findings have potentially important implications for understanding the mechanisms by which H<sub>2</sub>O<sub>2</sub> induces rCMECs apoptosis and by which Sal B helps prevent apoptotic cell death (**Fig. AI-14**). To the best of our knowledge, this is the first report indicating the significance of PI3K/Akt and MEK/ERK signaling in H<sub>2</sub>O<sub>2</sub>-induced CMECs apoptosis and providing evidence that the PI3K signaling pathway is the mechanism by which Sal B acts as an anti-apoptotic agent in protecting cells from H<sub>2</sub>O<sub>2</sub> injury and prolonging cerebral endothelial survival.

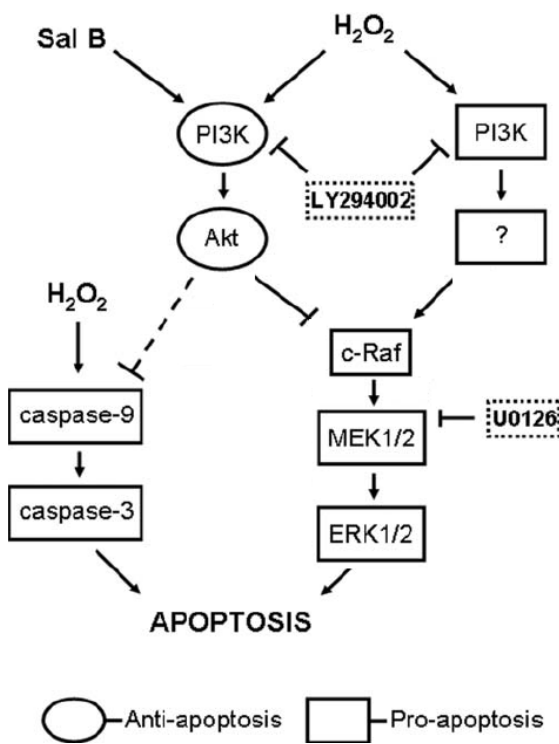


**Figure AI-14 Schematic model of signaling events involved in  $\text{H}_2\text{O}_2$ -induced rCMECs apoptosis and Sal B preventive mechanism.**

The broken line indicates a possible link of Akt and caspase-9.

## 4.8 FUTURE WORK

### 4.8.1 IS BCL-2 UPREGULATION RESPONSIBLE FOR THE PROTECTIVE AND ANTIOXIDANT EFFECTS OF SAL B?

#### 4.8.1.1 STUDY OF THE PROTECTIVE AND ANTIOXIDANT EFFECTS OF SAL B AGAINST $\text{H}_2\text{O}_2$ INDUCED CYTOTOXICITY IN rCMECs

##### a) Primary culture of rCMECs

rCMECs were cultured in DMEM supplemented with 25% FBS, 10 U/ml heparin, 100 U/ml penicillin-streptomycin solution and 150  $\mu\text{g}/\text{ml}$  ECGF, and were grown in monolayers at 37°C in a humidified atmosphere of 5% CO<sub>2</sub> and 95% air. Cells from 4<sup>th</sup> and 7<sup>th</sup> passage were used in following study.

##### b) Measurement of protective effects of Sal B against $\text{H}_2\text{O}_2$ induced cytotoxicity in rCMECs by MTT and TUNEL assays.

The viability of cells will be studied by MTT assay. Briefly, cultured rCMECs will be pre-treated with different doses of Sal B for 90 min, and then medium containing Sal B will be moved and replaced with the medium containing different concentration of H<sub>2</sub>O<sub>2</sub> for 12 h. Then, H<sub>2</sub>O<sub>2</sub> will be removed and the cells will be incubated with 100 µl 0.5 mg/ml MTT for 4 h at 37°C, and then washed and lysed with 100 µl DMSO. The reduced MTT will be measured at 570nm in a 96-microtiter plate.

H<sub>2</sub>O<sub>2</sub>-induced apoptosis was detected by performing the TUNEL assay using an Apo-Direct™ Kit. TUNEL was performed according to the manufacturer's instructions. Briefly, after pretreatments and exposure to H<sub>2</sub>O<sub>2</sub>, cells were harvested, washed, fixed, permeabilized, and labeled for DNA strand breaks, then analyzed on a Coulter Epics Elite flow cytometer.

**c) Measurement of intracellular ROS accumulation**

The carboxy derivative of fluorescein, carboxy-DCFDA is nonfluorescent until the acetate groups are removed by intracellular esterases and oxidation occurs within the cell. Thus Oxidation can be detected by monitoring the increase in fluorescence with a fluorescence microscope. In this study, carboxy-H2DCFDA will be used to monitor net intracellular accumulation of ROS within the cell. In brief, slides are washed with PBS and loaded with 10 µM Carboxy-DCFDA for 30 min at 37 °C. Images of fluorescence of Carboxy-2',7'-dichlorofluorescein (DCF) will be examined under a confocal microscope equipped with an argon laser (488 nm).

**d) Measurement of Lipid peroxidation by MDA assay**

Lipid peroxides will detected as malondialdehyde (MDA) reacting with thiobarbituric acid (TBA) to form a 1:2 adduct (colored complex, TBARS) measurable by spectrofluorometric analysis. Briefly, cells ( $2 \times 10^7$ ) will be lysed by sonicating on ice and whole homogenates will be used to quantify lipid peroxides using the TBARS assay [35]. The fluorescence in the supernatants will be read by a Microplate Spectrofluorometer with an excitation wavelength of 530 nm and an emission wavelength of 550 nm. The quantities of TBARS will be expressed in terms of amount (pmol) per mg protein.

**4.8.1.2 INHIBITION STUDY OF THE BCL-2 PROTEIN FUNCTION IN RCMECs.**

**a) Inhibition of the Bcl-2 protein function in rCMECs treated with Sal B**

Specific Bcl-2 inhibitor HA14-1, which could bind to the BH3 domain of Bcl-2, will be

used to block normal function of Bcl-2, thus abolish the effects of up-regulation of Bcl-2 conferred by Sal B. BH3 interact with the Glutathione (GSH) and regulates pool of mitochondrial GSH and has been considered as the most important antioxidant domain of Bcl-2. HA14-1 is a small cell-permeable, nonpeptidic ligand that binds to the Bcl-2 BH3 domain and has shown to be able to block transportation of GSH into mitochondria. In the study, cells will be incubated with Sal B for 90 min in the presence or absence of HA14-1 (15  $\mu$ M).

**b) Confirmation of Bcl-2 inhibition by measuring the mitochondria pool of GSH.**

Bcl-2 can directly regulate pool of mitochondrial GSH thus Mitochondrial GSH content could be determined to indicate Bcl-2 function. In brief, cells will be preincubated for 1 h with 250  $\mu$ M biotinylated GSH monoethyl ester (BioGEE) at 37°C, 10% CO<sub>2</sub> and then will be incubated with Sal B for 90 minute in the presence of either control or HA14-1. The cells will be fixed in 4% paraformaldehyde for 20 min and blocked/permeabilized for 1 h in 5% BSA and 0.2% Triton X-100 in PBS. The cells will then be incubated for 90 min at room temperature with 1 $\mu$ M Hoechst dye and streptavidin conjugated to Cy3 (1:200) to label the BioGEE. The images will be captured with either a 63 $\times$  or 100 $\times$  oil immersion objective. The Cy3-streptavidin staining will be quantified as either punctate or diffuse for 300 cells/condition from each of three independent experiments.

**c) Determine whether protective effects of Sal B will be affected when Bcl-2 is inhibited.**

After Bcl-2 is inhibited, rCMECs will be treated with Sal B and followed by treatment of H<sub>2</sub>O<sub>2</sub>. Cell viability, apoptosis, intracellular ROS level and MDA level will then be examined as previously described. Comparing the data with that from normal rCMECs that Bcl-2 is not inhibited, we would understand the role of Bcl-2 in the antioxidant effects of Sal B.

#### **4.8.2 TO TEST WHETHER THE RAPID UP-REGULATION OF BCL-2 PROTEIN IS MEDIATED BY AKT/CREB PATHWAY IN THE SAL B-TREATED RCMECS**

The major positive regulatory region in the 5'-flanking region of *bcl-2* gene for controlling of *bcl-2* expression has been identified in B cells, containing a cyclic AMP-responsive element (CRE). Transcript factor cyclic AMP-responsive element-binding protein (CREB), which bind to this region and activate expression of *bcl-2*, could be regulated by phosphorylation at ser-133<sup>238,239</sup>. CREB is generally a classic intracellular

secondary messenger. Several kinases including Akt/PKB are responsible for the phosphorylation of CREB under different stimuli<sup>240</sup>. It has been demonstrated that Bcl-2 might be a downstream effector of Akt in endothelial cells<sup>237,241</sup>. Thus, we want to understand whether Akt-induced CREB activation could be responsible for the up-regulation of Bcl-2.

Phosphorylation of CREB will be determined by western blot. If the activation of CREB were observed in rCMECs treated with Sal B, The CREB ShortCut siRNA Mix kit (New England Biolab) will be used to depletion CREB. In brief, Cells were transfected with siCREB (20 nM, 48 h) by using Lipofectamine 2000 (Invitrogen) following the manual's protocol. Bcl-2 protein level will then be analyzed by western blot. Akt inhibitor LY294002 will be used to block Sal B-induced activation of Akt, CREB phosphorylation and Bcl-2 protein level will then be examined by using western blot. A successful inhibition of CREB phosphorylation and Bcl-2 protein expression will provide evidence that Bcl-2 protein may be mediated by Akt/CREB pathway.

## **Appendix II**

**Cell death caused by single-stranded  
oligodeoxynucleotides mediated target  
ed genomic sequence modification**

## **1 INTRODUCTION**

Targeted gene repair mediated by single-stranded oligodeoxynucleotide (ssODN) offers a promising tool for biotechnology and gene therapy<sup>242-244</sup>. This approach has vast potentials, and in particular, to correct or introduce subtle mutations in desirable genomic DNA loci without introducing unwanted exogenous sequences. Despite its numerous advantages, its utility as a universal methodology for clinical therapeutic and research purposes is currently limited by its low frequency of repair events, variability amongst different experimental settings, and most importantly, low viability of “corrected” cells.

## 1.1 PROPOSED MECHANISMS OF SSODN-MEDIATED GENE REPAIR

The mechanism involved in ssODN-based gene repair has been postulated to occur in two steps, DNA strand pairing and DNA repair. During the strand pairing event, ssODN are introduced into cells and are aligned with a complementary DNA sequence on the target locus. It is now clear that this step is catalyzed by enzymes involved in homologous recombination (HR), such as RAD51<sup>245</sup> and XRCC<sup>246</sup>. This step creates a three- stranded intermediate, D-loop<sup>247</sup>. The event subsequent to the DNA strand pairing is the processing of these recombination intermediates, leading to modifications of the target sequence. Three possible models have been proposed for ssODN function<sup>248</sup>.

### 1.1.1 DIRECT NUCLEOTIDE EXCHANGE REACTION

One pathway involves a direct nucleotide exchange reaction that could be catalyzed by DNA repair enzymes, which are probably members of mismatch repair family (MMR). However, MMR appears to not play an important role in ssODN-based sequence alteration and in fact have an antagonistic effect<sup>246</sup>. In *E. coli*, some mismatches created by ODN and the target DNA were repaired more efficiently than others in MMR-proficient *E. coli* strains<sup>249</sup>. In mammalian cells, Embryonic stem (ES) cells lacking Msh2 activity showed levels of ODN-directed gene repair that were more than 100-fold greater than those in wild-type ES cells<sup>250</sup>. Recently, Drury *et al* showed that the correction efficiency in either Msh2<sup>-/-</sup> or Msh3<sup>-/-</sup> Mouse embryonic fibroblasts (MEFs) cells were much higher than that observed in the Msh<sup>WT</sup> cells<sup>251</sup>.

### 1.1.2 TRANSCRIPTION COUPLED REPAIR

Yoon and co-workers proposed another model that is based on transcription activity<sup>252</sup>. They proposed that during transcriptional elongation, a portion of the non-transcribed strand forms a transcription bubble that is accessible for strand pairing of an anti-sense ODN to form a D-loop. By using a transcription coupled repair (TCR) mechanism, the transcribed strand would be excised and physically substituted by the ssODN. This model suffices to explain the well known ‘strand bias’ effect in that an anti-sense ssODN always promote higher levels of gene repair than a sense ssODN<sup>253</sup>. Since there are exceptions to this ‘strand bias’ effect<sup>254</sup>, Kimec argued that only genes that are driven by highly active promoters follow this route<sup>248</sup>. Moreover, Olsen *et al* argued against this model as no targeted sequence alteration was observed during the G1 cell cycle phase, a phase with active transcription<sup>255</sup>. Anyhow, an actively transcribed region has been demonstrated to be more accessible to oligonucleotides binding because it provides an environment in which the chromatin structure surrounding the gene is loosen<sup>256</sup>. Active transcription might be critical for the DNA pairing step. As for the subsequent resolution of these recombination intermediates, there is no evidence to support a role of TCR. In addition, several cell lines lacking mismatch repair genes, *Msh2*, *Pms2* and *Mlh1*, were found to be deficient in TCR in mammalian cells<sup>257</sup>.

### 1.1.3 REPLICATION BASED MODEL

There is an increasing body of evidence that suggests DNA replication can strongly influence the process of gene repair<sup>258,259</sup>. Kimec’s group proposed a replication model for targeted gene repair<sup>248</sup>. In their model, D-loops can be enveloped or bypassed by the replication fork and assimilated into the daughter strand, generating a strand with a mismatched base pair complex and an unconverted copy of the gene. Assuming this mismatch is tolerated through a single round of replication, a second round of replication would generate a corrected gene allele in addition to an unconverted gene sequence.

Thus, DNA pairing and MMR might be two main limiting factors in targeted sequence correction. A deficiency in MMR machinery would increase the tolerance for a mismatch between ssODN and target sequences, which cause the ‘correct’ information to remain, while a functional MMR would, on the other hand, remove the mismatched base from the ssODN. Hence, the uncorrected cell might result from either the failure in pairing of ssODN or the removal of the ‘correct’ base by MMR. That could offer an explanation to why the targeted sequence alteration process does not work to any significant degree in the primary wt cells that have hitherto been analyzed. Only if *Msh2*, a central protein in MMR, is deleted can ssODN lead to a functional sequence alteration in mouse ES cells<sup>246</sup>.

## 1.2 THE FATE OF CORRECTED CELLS

While much effort has been devoted to increasing the rates of ssODN-based sequence correction and the understanding of its mechanisms, little is known with regard to the fate of the corrected cells. Previously, Olsen *et al* reported that the majority of corrected CHO-mEGFP cells were arrested in G2/M phase, and that only 1-2% cells were capable of forming viable colonies 24 h after ssODN transfection. Although treatment of cells with caffeine, an ATM/ATR inhibitor, attenuated the checkpoint arrest and a population of cells entered mitosis, the number of viable colonies did not increase<sup>255</sup>. Using HeLa-F5 and HEK-mEGFP cells as model systems, we previously reported a similar G2/M arrest phenomenon in corrected cells, and this inhibition of cell cycle progression was not noticeably affected by pretreatment of ATM/ATR inhibitors caffeine or pentoxyfylline<sup>260</sup>. More recently, the presence of phosphorylated H2AX was shown to be associated with this cell cycle arrest<sup>261</sup>.

## 1.3 THE POSSIBLE CAUSES

### 1.3.1 SSODN?

One might pose the question of what might have caused the cell death of corrected cells. Kimec suggested that this type of cellular response might be due to the introduction of the ssODN<sup>248</sup>. Recent experimentations, however, did not support this notion. Igoucheva *et al* investigated the differential cellular responses to exogenous DNA in mammalian cells and found that in either CHO, or HEK293, or NIH3T3 cells, the presence of ssODN did not trigger any cellular response when compared to controls<sup>262</sup>.

### 1.3.2 PHOSPHOROTHIOATE LINKAGES?

Olsen *et al* suggested that the presence of phosphorothioate (PS) linkages of ssODN might exert a cytotoxic effect to cells. Recently, it was shown that the number of viable corrected colonies mediated by ssODN without PS was a little higher (6%) than that by PS-protected ssODN (2%). However, the remaining 94-98% of corrected cells still did not survive<sup>263</sup>. So PS modification might exert an insignificant cytotoxic effect to the cell. Furthermore, if the introduction of PS-protected or unprotected ssODN would cause cell

cycle arrest or apoptosis, why can those uncorrected cells divide and survive well?

### 1.3.3 D-LOOP?

Another possibility that is attributable to the apparent cell death phenomenon is the functional intermediate ie. D-loop. It might interrupt the trafficking of RNA polymerase or DNA polymerase, and might be detected by cells as a form of DNA structural change and elicit various DNA repair activities<sup>264</sup>. However, Kaplan *et al* has shown that D-loops can be encompassed and bypassed by the replication machinery<sup>265</sup>. The D-loop then must have been repaired in the corrected cells that can generate functional mRNA. But its ability to trigger cell cycle arrest and cell death still cannot be arbitrarily excluded.

### 1.3.4 DNA MISMATCH

The most likely ‘offender’ is the DNA mismatch. As stated above, the tolerance to MMR of a mismatched base pair complex formed in the gene repair process is the prerequisite of the targeted sequence alteration. The mismatched base pair complex might remain and even be passed on to daughter cells. Meanwhile, the aberrant processing of mismatches can lead to MMR-dependent G2/M checkpoint activation and cell killing<sup>266,267</sup>. *Does cell death of corrected cells in gene repair correlate with MMR?*

There is a growing body of experimental evidence revealed that MMR proteins play an important role in recognizing and signaling DNA damage responses that is independent of the MMR catalytic repair process<sup>268</sup>.

As for the repair function of MMR, mismatch recognition is mediated by one of two heterodimers of MMR proteins. MutS-α (heterodimer of Msh2 and Msh6) binds to mismatches and small insertion/deletion loops, whereas hMutS-β (heterodimer of Msh2 and Msh3) recognizes larger insertion/deletion loops<sup>269</sup>. Following the recognition step, both MutS dimers recruit another heterodimeric complex, MutLα, which is composed of Mlh1 and Pms2. The formation of MutS-MutL complex activates the excision of up to 1 kb of the newly synthesized DNA strand containing the mismatch<sup>270</sup>. The single-stranded gap is filled in by a DNA polymerase, and DNA ligase restores the integrity of the DNA strand.

And for their function in DNA damage signaling, several models have been proposed to explain how DNA damage recognized by MMR proteins can lead to cell cycle checkpoint activation and cell death. In one model, MMR plays an indirect role by initiating futile cycles

of DNA repair. Mismatches cannot activate cell death pathway *per se*. As damage on the template strand is repeatedly processed that leads to the generation of secondary DNA damages (single-strand gaps and/or double strand breaks), provoking checkpoint activation and cell death<sup>266,267</sup>. Another model suggests a direct signaling role for MMR proteins<sup>271</sup>, which was supported by direct association of major MMR proteins with the components of stress signaling, such as ATM and Chk2<sup>272</sup>, ATR<sup>273</sup>.

The initial activation of the protein kinase cascade in response to DNA damage is not fully understood, although several protein kinases, such as ataxia telangiectasia, mutated (ATM) and ATM- and Rad3-related (ATR), as well as CHK1 and CHK2 are established as principal components involved in sensing and responding to DNA damage<sup>274,275</sup>. Single-strand DNA gaps lead to the recruitment of the ATR/ATR interacting protein (ATRIP) complex to these gaps. On the other hand, double strand breaks, another possible secondary DNA damage, results in the direct activation of ATM and subsequent replication fork arrest, thereby leading to ATR activation.

Stojic *et al* showed that low doses of MNNG induce a MMR-dependent G2 arrest that was ATR-dependent but was not dependent on ATM<sup>267</sup>. Recent studies provided a strong set of experimental evidence for the separate roles of MutS $\alpha$  complex in MMR and the induction of cell death. Lin *et al* showed that mutations in Msh2 and Msh6 proteins were still able to form heterodimers and bind DNA with the same affinity, but they were unable to repair mismatches. Although MMR was nonfunctional, the mutant protein retained the ability for DNA damage signaling<sup>276</sup>.

## 1.4 STUDY OBJECTIVES

In light of the data presented above, we propose a MMR-dependent model of ‘correction-induced’ cell death (**Fig. AII-1**).

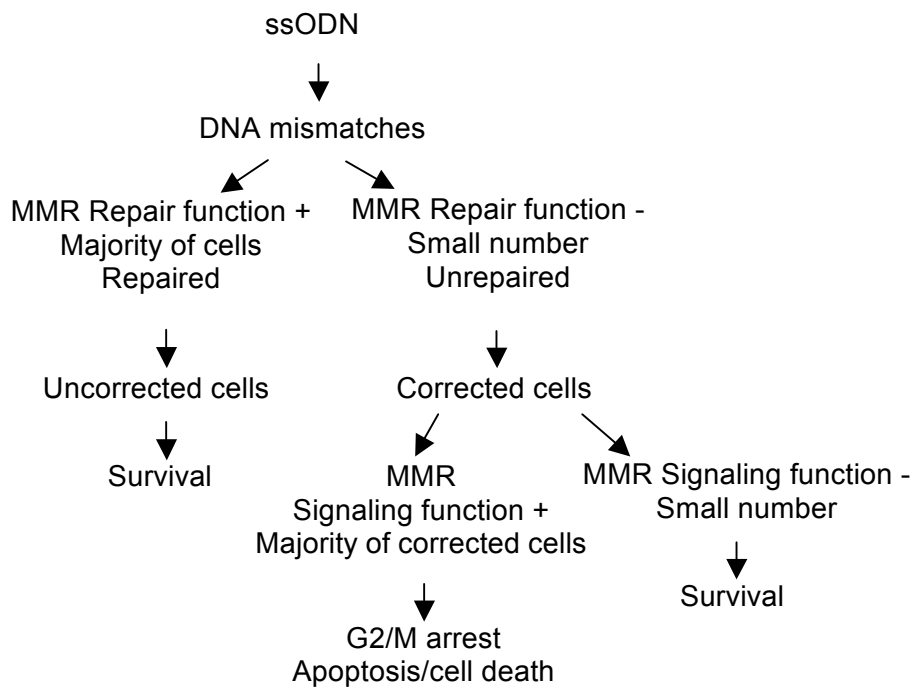


**Figure All-1 Proposed model of MMR-dependent 'correction-induced' cell death**

The objectives of this research are:

- (1) To confirm whether the 'correction-induced' cell death is MMR-dependent or -independent.
- (2) To determine whether the low viability of corrected cells is related to apoptosis? Which pathway and what factors are involved in this type of apoptosis?
- (3) To determine if ATM and/or ATR participate the cellular response to targeted sequence alteration.

This project aims to understand the mechanism of the cell death that occurs in the ssODN-based gene repair process.

## **2 MATERIAL AND METHODS**

## 2.1 CELL LINES

To detect ssODN-mediated gene repair, pmEGFP<sup>277</sup> with a mutant EGFP expression cassette was linearized by *Apa*LI and transfected into HeLa, HEK293T-Lα (kindly offered by Prof. Josef Jiricny)<sup>278</sup>, or Lovo cells (kindly offered by Prof. Stefan Zeuzem)<sup>279</sup>. The cells were cultured for 24 h before being seeded with the density of 100 cells/well in a 96-well plate and cultured in selective medium (supplemented with 600 µg/ml G418) for two weeks. At least 10 resistant clones were picked and examined for the ability of gene repair. Cell clones HeLa-F5<sup>277</sup>, HEK293T-Lα-mEGFP and Lovo-13-mEGFP cells were selected for further experiments. In the case of HEK293T-Lα-mEGFP, before transfection with the ssODN, cells were grown for at least 8 days in medium containing Tet Systems Approved FBS (Clontech) either in the absence or presence of 50 ng/ml doxycyclin (Sigma) to induce or repress expression of the central mismatch repair protein, hMLH1.

## 2.2 TARGET GENE CORRECTION ASSAY

Cells were seeded at  $2 \times 10^5$  in 12-well plates and grown for 24 h before transfection. For ssODN-mediated gene repair assay, a 25-mer phosphothioate-modified (underlined) antisense ssODN (E6: CCTTGCTCACCATGGTGGCGGAATT) was transfected into HeLa-F5, HEK293T-Lα-mEGFP, or Lovo-13-mEGFP cells. For each well, 0.8 µg DNA was transfected using Lipofectamine2000 (Invitrogen). zVAD-fmk (50 µM), Caffeine (3 mM), or pentoxyfylline (3 mM) (Sigma), was added to culture medium before transfection, where indicated. To measure gene repair efficiency, cells were trypsinized 36 h post-transfection and directly subjected to flow cytometry (Beckman Coulter) using a 488-nm argon-ion laser. Single cell population was ensured by FS/SS gating during analysis.

## 2.3 CLONOGENIC SURVIVAL ASSAY

Cells were seeded at  $8 \times 10^5$  per 60-mm dishes and grown for 24 h to reach 60-80% confluence. 36 h after transfection with ssODN, corrected cells were sorted by FACS, a total of 500 corrected (green) cells were seeded onto 10-cm dishes and allowed to attach overnight. Colonies were observed and counted after 7 to 14 days under the confocal microscope (Olympus).

## 2.4 SEQUENCING OF GENOMIC DNA

Genomic DNA was extracted from survival fluorescent colonies. A nested PCR was

used to amplify specific regions containing the target locus, followed by subcloning, and sequencing as described previously<sup>277</sup>.

## **2.5 STATISTICAL ANALYSIS**

Data was analyzed with unpaired two-tailed Student's t-test or one-way ANOVA followed by Tukey's multiple comparison test with GraphPad Prism software (San Diego, CA). Data were expressed as mean±SD derived from at least three independent experiments. Differences were considered significant at  $P<0.05$ .

### **3 RESULTS AND DISCUSSION**

### 3.1 CORRECTED CELLS WERE MORE PRONE TO UNDERGO APOPTOSIS THAN UNCORRECTED CELLS

An increasing number of studies have shown that the majority of corrected cells does not divide, and these cells died eventually<sup>255,261,280</sup>. To corroborate these findings, we first measured the time course of the corrected cells. As shown in **Fig. AII-2**, the percentage of corrected/green Hela-F5 cells was maximal at 36 h (0.13%) after transfection with ssODN, and decreased to 0.027% by 96 h post-transfection. Similarly, using Hela-F5 or HEK293T-Lα-mGFP as model systems, microscopic analyses revealed a substantial number of corrected green cells began to round up at 72 h and eventually detached from the plate. This indicated that ssODN-mediated correction reaction was associated with cell death.

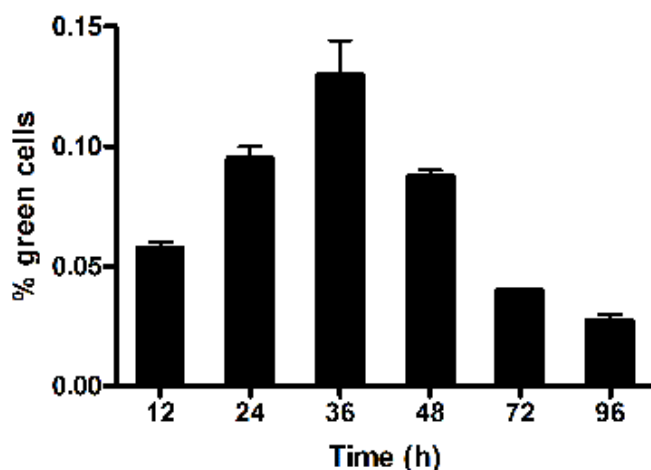


**Figure AII-2 Time course of green/corrected cells produced in single-stranded oligodeoxynucleotides (ssODN)-mediated target gene repair.**

HeLa-F5 cells were transfected with the ssODN-E6 and the number of green/corrected cells was quantified by flow cytometry at the indicated time points after transfection.

Our previous cell cycle analysis of corrected/green cells showed that the vast majority of the green (89.34%) cells were arrested at G2/M phase and failed to recover normal proliferation 24 h after transfection<sup>260</sup>. Transfection with either a control ssODN or a wild type EGFP plasmid did not affect cell cycle progression (data not shown), indicating that the G2/M arrest was not a result of the introduction of ssODN or the expression of the functional

EGFP gene, but was specifically happened in the corrected cells. So the cause of the cell cycle arrest herein might be the activation of DNA damage response pathways induced by the ssODN-mediated correction reaction.

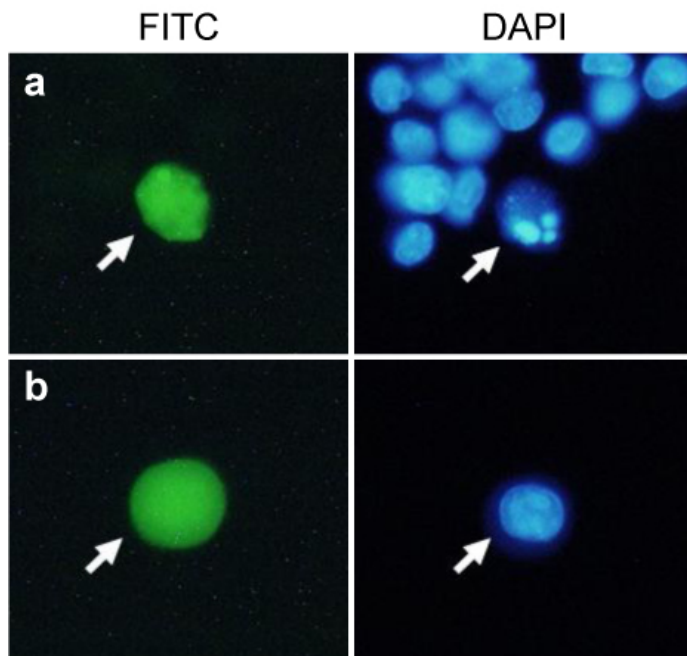


**Figure AII-3 Measurements of apoptosis in green cells.**

HeLa-F5 cells were analyzed by DAPI staining 12 h after transfection with the ssODN-E6. **a**, A typical photograph of apoptotic green cells. **b**, A typical photograph of normal green cells.

Recently, DNA damages, particularly DNA double-stand breaks (DSBs), have been directly detected in corrected cells<sup>261</sup>. The permanent existence of DNA damages led to cell death including apoptosis<sup>281</sup>. Several attempts have been made to detect apoptosis in various cell types<sup>246,261,282</sup>. However, apoptosis was only observed in CHO-mGFP cells when the cells were transfected with branched-ssODN<sup>246</sup>. To determine whether the low viability of corrected cells was related to apoptosis, we first evaluated the formation of apoptotic bodies using DAPI staining, which is characteristic for apoptotic cell death (**Fig. AII-3**). By direct counting, 17.23% green cells showed signs of morphological nuclear damage and formation of apoptotic body as early as 12 h after introduction of corrective oligonucleotides, which was significantly higher than that of non-green cells (1.34%).

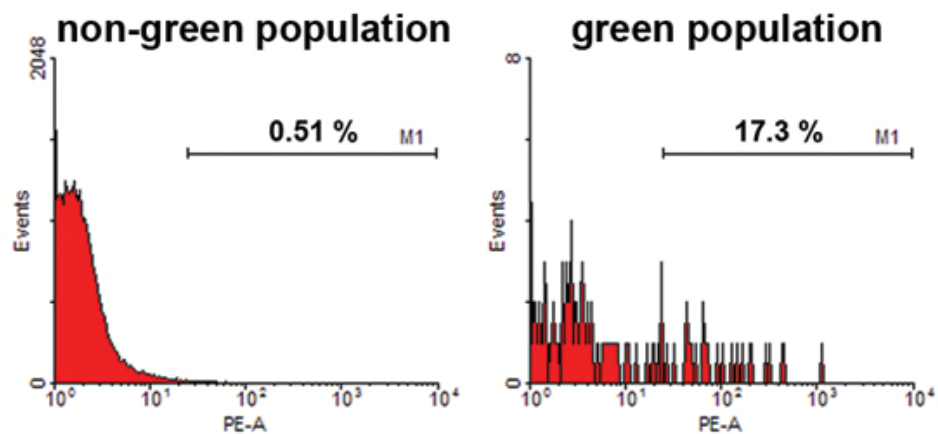


**Figure AII-4 Measurements of apoptosis in green cells.**

HeLa-F5 cells were analyzed by TUNEL assay 48 hours after transfection with the ssODN-E6.

To further verify apoptosis induced by ssODN-mediated correction reaction, TUNEL assays were performed. As shown in **Fig. AII-4**, only 0.5% total cells underwent apoptosis, whereas more than 20% green cells were TUNEL-positive (**Fig. AII-4**) 48 h after transfection. These results indicated that ssODN-corrected cells were much more prone to undergo apoptosis than uncorrected cells. Our data also suggested that activation of apoptosis might be a very early event.

### 3.2 THE APOPTOSIS OF CORRECTED CELLS WAS CASPASE-DEPENDENT AND ATM/ATR-INDEPENDENT

To determine the involvement of caspase in the observed apoptosis, zVAD-fmk, a pan-caspase-inhibitor<sup>215</sup>, was employed to examine its ability to prevent apoptosis of green cells. zVAD-fmk treatment significantly increased the number of green cells by around 1.5 times (data not shown). When green population was selected for analysis, untreated and zVAD-fmk-pretreated cells showed about 20.1% and 8.41% apoptosis index, respectively (**Fig. AII-5**). These data demonstrated that zVAD-fmk significantly reduced the apoptotic percentage of corrected cells by 58%, indicating that the majority of apoptotic green cells may undergo caspase-dependent apoptosis. The finding was verified by PARP cleavage

assay. Early in apoptosis, PARP is cleaved by caspases, primarily by caspase-3. Hence this assay can be used to determine the activation of caspase-3<sup>214</sup>. Results showed that the respective values for cleaved PARP were 8.97% for green cells and 0.92% for total cells.

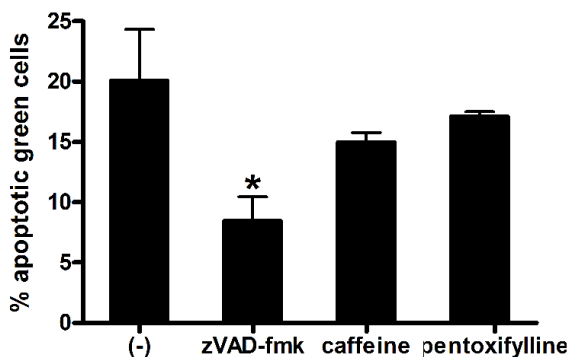


**Figure AII-5 Effects of caspases or ATM/ATR inhibitions on apoptosis caused by ssODN-mediated targeted gene repair.**

HeLa-F5 cells were pretreated with zVAD-fmk (50 µM), caffeine (3 mM), or pentoxifylline (3 mM) for 1 h and then transfected with ssODN-E6.

Apoptosis was measured 48 hours after transfection using TUNEL assay.

\*P<0.05 vs. control. Data were representative of three independent experiments.

ATM/ATR-dependent G2/M arrest has been suggested, at least in part, to be responsible for the abnormal cell cycle profile of green CHO-mGFP cells<sup>255</sup>. Likewise, Ferrara et al demonstrated that ATM/ATR downstream mediators Chk1 and/or Chk2 were specifically activated in corrected DLD-1 cells<sup>280</sup>. However, in Hela-F5 cells, we did not observe obvious release of arrested green cells by caffeine and pentoxifylline treatments<sup>260</sup>. Consistently, exposure of Hela-F5 cells to these two ATM/ATR inhibitors slightly but not significantly protected green cells from apoptosis (Fig. AII-5), implying ATM/ATR-mediated pathways does not play an important role in this apoptotic cell death.

### **3.3 HMLH1-DEFICIENCY INCREASED GENE CORRECTION EFFICIENCY, BUT NOT AFFECTED THE VIABILITY OF CORRECTED CELLS**

Our interest in exploring a role of MMR was based on the notion that the tolerance to MMR of a base mismatch is the prerequisite of the targeted sequence alteration. And the aberrant processing of mismatches can lead to mismatch repair (MMR)-dependent G2/M checkpoint activation and apoptosis<sup>266,267,283</sup>.

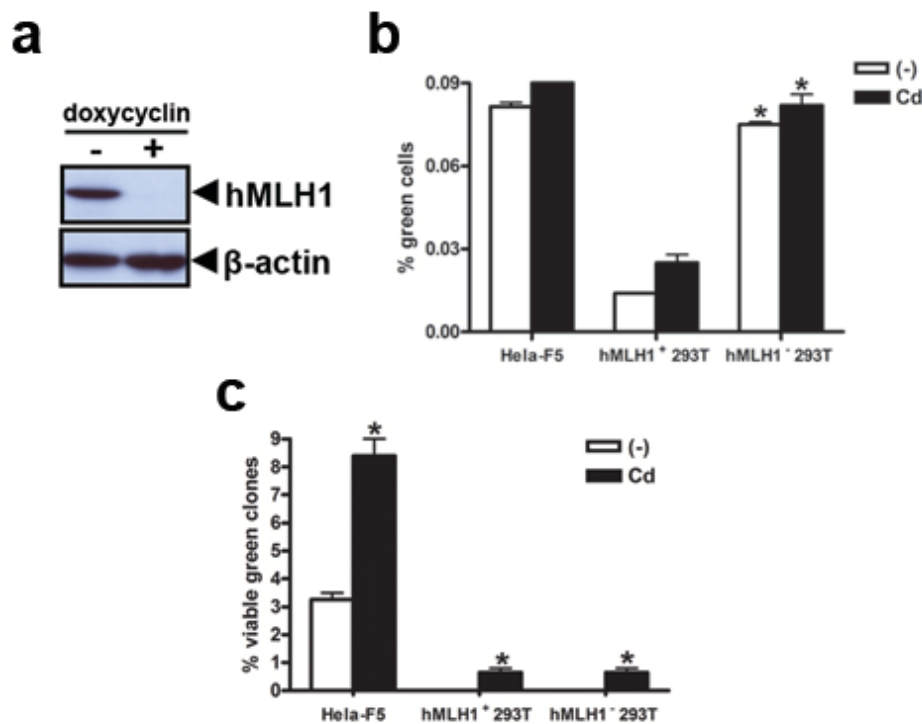


**Figure AII-6 Effects of hMLH1 deficiency**

a, hMLH1 expression was silenced by doxycycline. HEK293T-La-mGFP cells were cultured for 8 days in the absence or presence of 50 ng/mL doxycycline, and hMLH1 expressions were measured with MLH1 polyclonal antibody. Blot shown is representative of at least three independent experiments. b, Effects of zcadmium treatment or hMLH1 silencing on targeted gene repair efficiency. HeLa-F5, hMLH1-proficient, or hMLH1-deficient cells were incubated with or without cadmium (0.5 μM) for 1 h and then transfected with ssODN-E6. The numbers of green cells were quantified by flow cytometry 36 h after transfection. HEK293T-La-mGFP cells were labeled as 293T for short. \*P<0.05 vs. hMLH1-proficient HEK293T-La-mGFP cells. Data were representative of 3 independent experiments. c, Effects of cadmium treatment or hMLH1 silencing on viability of green/corrected cells. HeLa-F5, hMLH1-proficient, or hMLH1-deficient HEK293T-La-mGFP cells were incubated with or without cadmium (0.5 μM) for 1 h, followed by transfection with the ssODN-E6. Green colonies were counted by clonogenic survival assay after 7 days of continuous culture. \*P<0.05 vs. control. Data are representative of three independent experiments.

It was reported that hMLH1-deficient cells were less susceptible to apoptosis induced by lipoplatin than hMLH1-proficient cells<sup>284</sup>. To examine the possibility that MMR proteins function as activators of genotoxic responses to cell death induced by ssODN-mediated gene repair, we first isolated a clone of HEK293T-Lα-mEGFP cells with the mEGFP gene stably integrated into the chromosome of HEK293T-Lα cells. The expression of hMLH1 in this cell line can be controlled by doxycycline<sup>278</sup>. When HEK293T-Lα-mEGFP cells were treated with doxycycline for 8 days, the expression of hMLH1 was significantly reduced (**Fig. AII-6a**).

To measure ssODN-mediated gene repair efficiency, hMLH1-deficient or proficient cells were transfected with ssODN-E6 and were subjected to FACS analysis. A relatively low but reproducible repair frequency (0.02%) was observed in hMLH1-proficient cells. It has been shown that a defective MMR system would increase the repair efficiency<sup>248,250,261,263,285</sup>. As expected, comparing with hMLH1-proficient cells, a 5.4 times higher repair frequency was obtained in hMLH1-deficient cells (**Fig. AII-6b**). However, in clonogenic survival assay, neither hMLH1-deficient nor proficient cells could proliferate into visible colonies from at least 5 independent attempts (**Fig. AII-6c**). Results indicated that hMLH1 is not responsible for the observed cell death induced by ssODN-mediated gene repair.

### **3.4 CADMIUM TREATMENT DID NOT AFFECT THE VIABILITY OF CORRECTED CELLS**

It is known that the heavy metal cadmium can inhibit MMR by interfering with the binding of MSH2 and MSH6 complexes to mismatched DNA, and by inhibiting ATP hydrolysis of MSH6<sup>286</sup>. To assess if cadmium might prevent the cell death as described above, we next treated Hela-F5 and HEK293T-Lα-mEGFP cells with 0.5 μM cadmium 1 hour prior to transfection. After 36 h coincubation with cadmium, green cells were sorted by FACS and seeded in 10-cm dishes with fresh medium containing the same concentration of cadmium. Unlike the effects of MLH1-deficiency, cadmium treatment did not significantly increase the repair efficiency (**Fig. AII-6b**), but enhanced the viability of green cells. In Hela-F5 cells, there was a significant increase in the number of viable green clones in cadmium-treated cells compared with control cells ( $p<0.05$ ) (**Fig. AII-6c, Fig. AII-7a**). In the case of HEK293T-Lα-mEGFP cells, after 7 days of continuous cultures, 2-3 out of 500 green cells formed viable colonies in cadmium-treated cells (**Fig. AII-6c, Fig. AII-7a**).

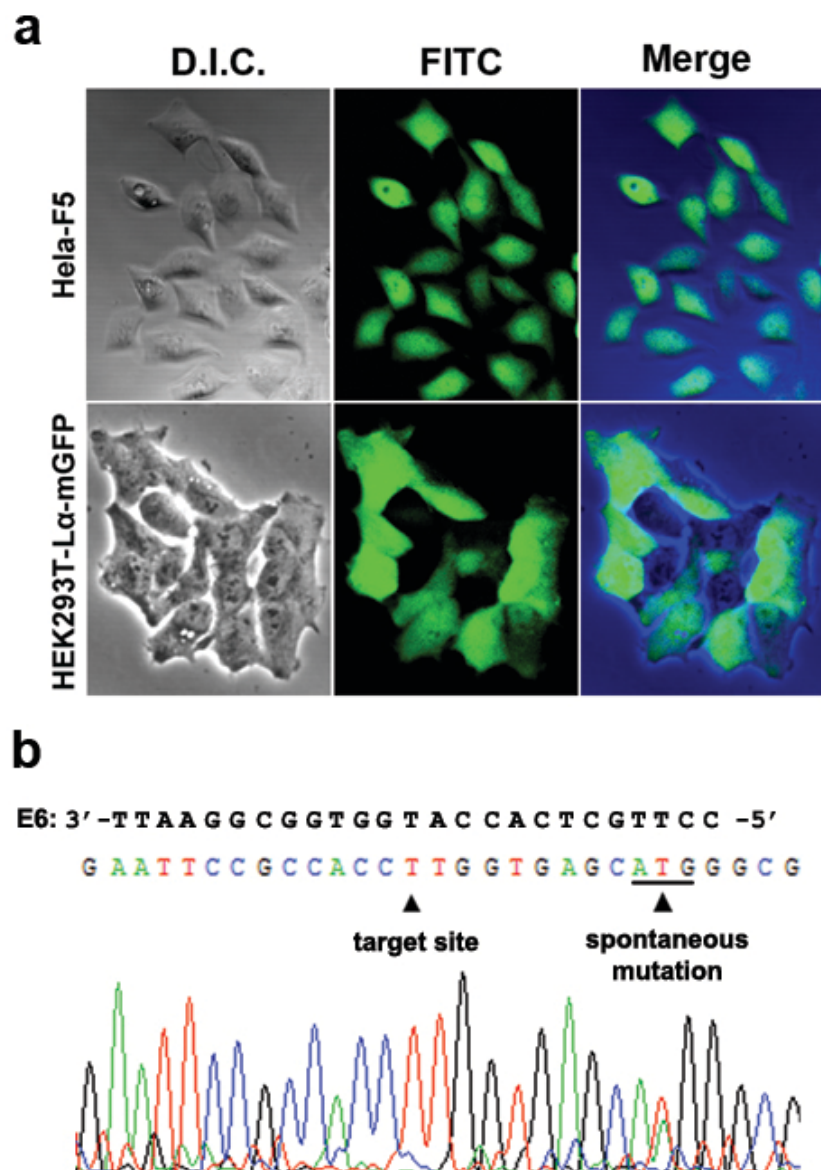


**Figure All-7 Effects of Cadmium treatment**

**a**, Colony formation of viable green cells. With cadmium treatment, green HeLa-F5 cells (upper panel) or hMLH1-deficient HEK293T-La-mGFP cells (lower panel) were imaged at  $\times 20$  original magnification after 7 days of continuous culture. Colonies shown are representatives of at least 3 independent experiments. **b**, Sequencing of mgfp gene fragments from viable green clones of HeLa-F5 or hMLH1- deficient HEK293T-La-mGFP cells. Single-stranded oligodeoxynucleotide-E6 was designed to be complementary to the untranscribed strand except for a "T-T" mismatch at the target site. The position of the spontaneous mutation that results in a fake start codon is underlined.

As described previously<sup>277</sup>, the target sequence was indeed repaired when the green cells were directly subjected to sequence analysis after sorting. Nevertheless, Sequence analysis revealed that the mGFP genes of all viable green clones, including both Hela-F5 and HEK293T-Lα-mEGFP cells, were not corrected at the desired site (**Fig. AII-7b**). An “A-T” point mutation was found at 10-bp downstream of the target site. This single point mutation resulted in start codon for a significant part of the mGFP gene, causing it to be transcribed and translated into a functional GFP polypeptide missing three amino acids (Met-Val-Ser) at its N-terminus. The defective repair system induced by cadmium treatment likely increased the spontaneous mutation rate in these cells. As a result, the “A-T” single point mutation was induced and caused the cells to turn green. Furthermore, these spontaneous mutants likely survived because the mutation might have bypassed or did not trigger the DNA damage responses. In addition, in **Fig. AII-7b**, a normal “A” signal was found beneath the mutated “T” one. Considering two copies of mGFP genes were stably integrated in the chromosome of Hela-F5 cells<sup>287</sup>, the suggested spontaneous mutation might only occur in one copy of them, leaving the other copy unchanged.

Accordingly, MMR proteins might not be required for the herein cellular genotoxic responses. This result was reminiscent to those using LoVo-mEGFP cells, which were generated by stably integrating the mGFP gene into the genome of MSH2-deficient LoVo cells<sup>279</sup>. Although a routine repair frequency of 0.05% was obtained 36 h after transfected with ssODN-E6, no green colony was observed in clonogenic survival assay (data not shown).

Taken together, in this ssODN-mediated gene repair event, activation of toxicity in corrected cells proceeded at least through the rapid activation of apoptosis and the cell cycle arrest. Neither ATM/ATR kinases nor MMR proteins play an important role. The mechanism underlying this cell death phenomenon is under investigation.

## References

- 1 Favata, M. F. et al., Identification of a novel inhibitor of mitogen-activated protein kinase kinase. *J Biol Chem* **273** (29), 18623-18632 (1998).
- 2 Peel, A. D., Chipman, A. D. & Akam, M., Arthropod segmentation: beyond the *Drosophila* paradigm. *Nat Rev Genet* **6** (12), 905-916 (2005).
- 3 Egland, K. A. & Greenberg, E. P., Quorum sensing in *Vibrio fischeri*: elements of the luxL promoter. *Mol Microbiol* **31** (4), 1197-1204 (1999).
- 4 Sezonov, G., Joseleau-Petit, D. & D'Ari, R., Escherichia coli physiology in Luria-Bertani broth. *J Bacteriol* **189** (23), 8746-8749 (2007).
- 5 Pedelacq, J. D., Cabantous, S., Tran, T., Terwilliger, T. C. & Waldo, G. S., Engineering and characterization of a superfolder green fluorescent protein. *Nat Biotechnol* **24** (1), 79-88 (2006).
- 6 Andersen, J. B. et al., New unstable variants of green fluorescent protein for studies of transient gene expression in bacteria. *Appl Environ Microbiol* **64** (6), 2240-2246 (1998).
- 7 Vlahos, C. J., Matter, W. F., Hui, K. Y. & Brown, R. F., A specific inhibitor of phosphatidylinositol 3-kinase, 2-(4-morpholinyl)-8-phenyl-4H-1-benzopyran-4-one (LY294002). *J Biol Chem* **269** (7), 5241-5248 (1994).
- 8 Kaplan, H. B. & Greenberg, E. P., Diffusion of autoinducer is involved in regulation of the *Vibrio fischeri* luminescence system. *J Bacteriol* **163** (3), 1210-1214 (1985).
- 9 Wolpert, L., Positional information and the spatial pattern of cellular differentiation. *J Theor Biol* **25** (1), 1-47 (1969).
- 10 Danino, T., Mondragon-Palomino, O., Tsimring, L. & Hasty, J., A synchronized quorum of genetic clocks. *Nature* **463** (7279), 326-330 (2010).
- 11 Tabor, J. J. et al., A synthetic genetic edge detection program. *Cell* **137** (7), 1272-1281 (2009).
- 12 Levskaya, A. et al., Synthetic biology: engineering *Escherichia coli* to see light. *Nature* **438** (7067), 441-442 (2005).
- 13 Basu, S., Gerchman, Y., Collins, C. H., Arnold, F. H. & Weiss, R., A synthetic multicellular system for programmed pattern formation. *Nature* **434** (7037), 1130-1134 (2005).
- 14 You, L., Cox, R. S., 3rd, Weiss, R. & Arnold, F. H., Programmed population control by cell-cell communication and regulated killing. *Nature* **428** (6985), 868-871 (2004).
- 15 Elowitz, M. B. & Leibler, S., A synthetic oscillatory network of transcriptional regulators. *Nature* **403** (6767), 335-338 (2000).
- 16 Elowitz, M. & Lim, W. A., Build life to understand it. *Nature* **468** (7326), 889-890 (2010).
- 17 Mukherji, S. & van Oudenaarden, A., Synthetic biology: understanding biological design from synthetic circuits. *Nat Rev Genet* **10** (12), 859-871 (2009).
- 18 Held, Lewis I., *Models for embryonic periodicity*. (Karger, Basel ; New York, 1992).
- 19 Nusslein-Volhard, C. & Wieschaus, E., Mutations affecting segment number and polarity in *Drosophila*. *Nature* **287** (5785), 795-801 (1980).
- 20 Lawrence, Peter A., *The making of a fly : the genetics of animal design*. (Blackwell Scientific Publications, Oxford, 1992).
- 21 Dequeant, M. L. & Pourquie, O., Segmental patterning of the vertebrate embryonic axis. *Nat Rev Genet* **9** (5), 370-382 (2008).
- 22 Schnell, S., Maini, P. K., McInerney, D., Gavaghan, D. J. & Houston, P., Models for pattern formation in somitogenesis: a marriage of cellular and molecular biology. *C R Biol* **325** (3), 179-189 (2002).
- 23 Sadler, T. W. & Langman, Jan, *Langman's medical embryology*, 8th ed. (Lippincott Williams & Wilkins, Philadelphia, 2000).
- 24 Palmeirim, I., Henrique, D., Ish-Horowicz, D. & Pourquie, O., Avian hairy gene expression identifies a molecular clock linked to vertebrate segmentation and somitogenesis. *Cell* **91** (5), 639-648 (1997).
- 25 Leimeister, C. et al., Oscillating expression of c-Hey2 in the presomitic mesoderm suggests that the segmentation clock may use combinatorial signaling through multiple interacting bHLH factors. *Dev Biol* **227** (1), 91-103 (2000).
- 26 Li, Y., Fenger, U., Niehrs, C. & Pollet, N., Cyclic expression of esr9 gene in *Xenopus* presomitic mesoderm. *Differentiation* **71** (1), 83-89 (2003).

- 27 McGrew, M. J., Dale, J. K., Fraboulet, S. & Pourquie, O., The lunatic fringe gene is a target of the molecular clock linked to somite segmentation in avian embryos. *Curr Biol* **8** (17), 979-982 (1998).
- 28 Holley, S. A., Geisler, R. & Nusslein-Volhard, C., Control of her1 expression during zebrafish somitogenesis by a delta-dependent oscillator and an independent wave-front activity. *Genes Dev* **14** (13), 1678-1690 (2000).
- 29 Jiang, Y. J. et al., Notch signalling and the synchronization of the somite segmentation clock. *Nature* **408** (6811), 475-479 (2000).
- 30 Oates, A. C. & Ho, R. K., Hairy/E(spl)-related (Her) genes are central components of the segmentation oscillator and display redundancy with the Delta/Notch signaling pathway in the formation of anterior segmental boundaries in the zebrafish. *Development* **129** (12), 2929-2946 (2002).
- 31 Holley, S. A., Julich, D., Rauch, G. J., Geisler, R. & Nusslein-Volhard, C., her1 and the notch pathway function within the oscillator mechanism that regulates zebrafish somitogenesis. *Development* **129** (5), 1175-1183 (2002).
- 32 Jouve, C. et al., Notch signalling is required for cyclic expression of the hairy-like gene HES1 in the presomitic mesoderm. *Development* **127** (7), 1421-1429 (2000).
- 33 Bessho, Y., Miyoshi, G., Sakata, R. & Kageyama, R., Hes7: a bHLH-type repressor gene regulated by Notch and expressed in the presomitic mesoderm. *Genes Cells* **6** (2), 175-185 (2001).
- 34 Forsberg, H., Crozet, F. & Brown, N. A., Waves of mouse Lunatic fringe expression, in four-hour cycles at two-hour intervals, precede somite boundary formation. *Curr Biol* **8** (18), 1027-1030 (1998).
- 35 Dale, J. K. et al., Periodic notch inhibition by lunatic fringe underlies the chick segmentation clock. *Nature* **421** (6920), 275-278 (2003).
- 36 Aulehla, A. et al., Wnt3a plays a major role in the segmentation clock controlling somitogenesis. *Dev Cell* **4** (3), 395-406 (2003).
- 37 Pourquie, O., The segmentation clock: converting embryonic time into spatial pattern. *Science* **301** (5631), 328-330 (2003).
- 38 Dubrulle, J., McGrew, M. J. & Pourquie, O., FGF signaling controls somite boundary position and regulates segmentation clock control of spatiotemporal Hox gene activation. *Cell* **106** (2), 219-232 (2001).
- 39 Takahashi, Y. et al., Mesp2 initiates somite segmentation through the Notch signalling pathway. *Nat Genet* **25** (4), 390-396 (2000).
- 40 Jen, W. C., Gawantka, V., Pollet, N., Niehrs, C. & Kintner, C., Periodic repression of Notch pathway genes governs the segmentation of Xenopus embryos. *Genes Dev* **13** (11), 1486-1499 (1999).
- 41 Le Douarin, N. M., Cell migrations in embryos. *Cell* **38** (2), 353-360 (1984).
- 42 De Felici, M., Dolci, S. & Pesce, M., Cellular and molecular aspects of mouse primordial germ cell migration and proliferation in culture. *Int J Dev Biol* **36** (2), 205-213 (1992).
- 43 McMahon, A., Supatto, W., Fraser, S. E. & Stathopoulos, A., Dynamic analyses of Drosophila gastrulation provide insights into collective cell migration. *Science* **322** (5907), 1546-1550 (2008).
- 44 Budrene, E. O. & Berg, H. C., Dynamics of formation of symmetrical patterns by chemotactic bacteria. *Nature* **376** (6535), 49-53 (1995).
- 45 Budrene, E. O. & Berg, H. C., Complex patterns formed by motile cells of Escherichia coli. *Nature* **349** (6310), 630-633 (1991).
- 46 Leptin, M., Gastrulation movements: the logic and the nuts and bolts. *Dev Cell* **8** (3), 305-320 (2005).
- 47 Elul, T. & Keller, R., Monopolar protrusive activity: a new morphogenic cell behavior in the neural plate dependent on vertical interactions with the mesoderm in Xenopus. *Dev Biol* **224** (1), 3-19 (2000).
- 48 Shook, D. & Keller, R., Mechanisms, mechanics and function of epithelial-mesenchymal transitions in early development. *Mech Dev* **120** (11), 1351-1383 (2003).
- 49 Yang, X., Dormann, D., Munsterberg, A. E. & Weijer, C. J., Cell movement patterns during gastrulation in the chick are controlled by positive and negative chemotaxis mediated by FGF4 and FGF8. *Dev Cell* **3** (3), 425-437 (2002).
- 50 Ben-Jacob, E. & Levine, H., The artistry of microorganisms. *Scientific American* **279** (4), 82-87 (1998).
- 51 Woodward, D. E. et al., Spatio-temporal patterns generated by *Salmonella typhimurium*. *Biophys J* **68** (5), 2181-2189 (1995).

- 52 Emerson, D., Complex pattern formation by *Pseudomonas* strain KC in response to nitrate and nitrite. *Microbiology* **145** ( Pt 3), 633-641 (1999).
- 53 Alon, Uri, *An introduction to systems biology : design principles of biological circuits.* (Chapman & Hall/CRC, Boca Raton, FL, 2007).
- 54 May, R. M., Simple mathematical models with very complicated dynamics. *Nature* **261** (5560), 459-467 (1976).
- 55 Murray, J. D., *Mathematical biology*, 3rd ed. (Springer, New York, 2002).
- 56 Wolpert, L., Positional information and pattern formation. *Curr Top Dev Biol* **6** (6), 183-224 (1971).
- 57 Kondo, S. & Miura, T., Reaction-diffusion model as a framework for understanding biological pattern formation. *Science* **329** (5999), 1616-1620 (2010).
- 58 Hodges, Andrew, *Alan Turing : the enigma*. (Simon and Schuster, New York, 1983).
- 59 Turing, A. M., The chemical basis of morphogenesis. 1953. *Bull Math Biol* **52** (1-2), 153-197; discussion 119-152 (1990).
- 60 Fitzhugh, R., Impulses and Physiological States in Theoretical Models of Nerve Membrane. *Biophys J* **1** (6), 445-466 (1961).
- 61 Maini, P. K., Myerscough, M. R., Winters, K. H. & Murray, J. D., Bifurcating spatially heterogeneous solutions in a chemotaxis model for biological pattern generation. *Bull Math Biol* **53** (5), 701-719 (1991).
- 62 Swindale, N. V., A model for the formation of ocular dominance stripes. *Proc R Soc Lond B Biol Sci* **208** (1171), 243-264 (1980).
- 63 Murray, J. D., Oster, G. F. & Harris, A. K., A mechanical model for mesenchymal morphogenesis. *J Math Biol* **17** (1), 125-129 (1983).
- 64 Cooke, J. & Zeeman, E. C., A clock and wavefront model for control of the number of repeated structures during animal morphogenesis. *J Theor Biol* **58** (2), 455-476 (1976).
- 65 Finney, M. & Ruvkun, G., The unc-86 gene product couples cell lineage and cell identity in *C. elegans*. *Cell* **63** (5), 895-905 (1990).
- 66 McKearin, D. M. & Spradling, A. C., bag-of-marbles: a *Drosophila* gene required to initiate both male and female gametogenesis. *Genes Dev* **4** (12B), 2242-2251 (1990).
- 67 Sussex, I. M., Developmental programming of the shoot meristem. *Cell* **56** (2), 225-229 (1989).
- 68 Cooke, J., Control of somite number during morphogenesis of a vertebrate, *Xenopus laevis*. *Nature* **254** (5497), 196-199 (1975).
- 69 Khalil, A. S. & Collins, J. J., Synthetic biology: applications come of age. *Nat Rev Genet* **11** (5), 367-379 (2010).
- 70 Benner, S. A. & Sismour, A. M., Synthetic biology. *Nat Rev Genet* **6** (7), 533-543 (2005).
- 71 Friedland, A. E. et al., Synthetic gene networks that count. *Science* **324** (5931), 1199-1202 (2009).
- 72 Skerker, J. M. et al., Rewiring the specificity of two-component signal transduction systems. *Cell* **133** (6), 1043-1054 (2008).
- 73 Kobayashi, H. et al., Programmable cells: interfacing natural and engineered gene networks. *Proc Natl Acad Sci U S A* **101** (22), 8414-8419 (2004).
- 74 Balagadde, F. K. et al., A synthetic *Escherichia coli* predator-prey ecosystem. *Mol Syst Biol* **4**, 187 (2008).
- 75 Lee, H. H., Molla, M. N., Cantor, C. R. & Collins, J. J., Bacterial charity work leads to population-wide resistance. *Nature* **467** (7311), 82-85 (2010).
- 76 Blattner, F. R. et al., The complete genome sequence of *Escherichia coli* K-12. *Science* **277** (5331), 1453-1462 (1997).
- 77 Butler, S. M. & Camilli, A., Going against the grain: chemotaxis and infection in *Vibrio cholerae*. *Nat Rev Microbiol* **3** (8), 611-620 (2005).
- 78 Berg, H., Motile behavior of bacteria. *Phys Today* **53** (1), 24-29 (2000).
- 79 Larsen, S. H., Reader, R. W., Kort, E. N., Tso, W. W. & Adler, J., Change in direction of flagellar rotation is the basis of the chemotactic response in *Escherichia coli*. *Nature* **249** (452), 74-77 (1974).
- 80 Macnab, R. M. & Ornston, M. K., Normal-to-curly flagellar transitions and their role in bacterial tumbling. Stabilization of an alternative quaternary structure by mechanical force. *J Mol Biol* **112** (1), 1-30 (1977).
- 81 Turner, L., Ryu, W. S. & Berg, H. C., Real-time imaging of fluorescent flagellar filaments. *J Bacteriol* **182** (10), 2793-2801 (2000).
- 82 Sourjik, V., Receptor clustering and signal processing in *E. coli* chemotaxis. *Trends Microbiol* **12** (12), 569-576 (2004).

- 83 Wadhams, G. H. & Armitage, J. P., Making sense of it all: bacterial chemotaxis. *Nat Rev Mol Cell Biol* **5** (12), 1024-1037 (2004).
- 84 Macnab, R. M., The bacterial flagellum: reversible rotary propellor and type III export apparatus. *J Bacteriol* **181** (23), 7149-7153 (1999).
- 85 Aldridge, P. & Hughes, K. T., Regulation of flagellar assembly. *Curr Opin Microbiol* **5** (2), 160-165 (2002).
- 86 Reid, S. W. et al., The maximum number of torque-generating units in the flagellar motor of Escherichia coli is at least 11. *Proc Natl Acad Sci U S A* **103** (21), 8066-8071 (2006).
- 87 Kojima, S. & Blair, D. F., Solubilization and purification of the MotA/MotB complex of Escherichia coli. *Biochemistry* **43** (1), 26-34 (2004).
- 88 Kojima, S. et al., Stator assembly and activation mechanism of the flagellar motor by the periplasmic region of MotB. *Mol Microbiol* **73** (4), 710-718 (2009).
- 89 Zhao, R., Amsler, C. D., Matsumura, P. & Khan, S., FliG and FliM distribution in the Salmonella typhimurium cell and flagellar basal bodies. *J Bacteriol* **178** (1), 258-265 (1996).
- 90 Zhao, R., Pathak, N., Jaffe, H., Reese, T. S. & Khan, S., FliN is a major structural protein of the C-ring in the Salmonella typhimurium flagellar basal body. *J Mol Biol* **261** (2), 195-208 (1996).
- 91 Manson, M. D., Dynamic motors for bacterial flagella. *Proc Natl Acad Sci U S A* **107** (25), 11151-11152 (2010).
- 92 Berg, H. C., The rotary motor of bacterial flagella. *Annu Rev Biochem* **72**, 19-54 (2003).
- 93 Namba, K. & Vonderviszt, F., Molecular architecture of bacterial flagellum. *Q Rev Biophys* **30** (1), 1-65 (1997).
- 94 Suzuki, T., Iino, T., Horiguchi, T. & Yamaguchi, S., Incomplete flagellar structures in nonflagellate mutants of Salmonella typhimurium. *J Bacteriol* **133** (2), 904-915 (1978).
- 95 Suzuki, T. & Komeda, Y., Incomplete flagellar structures in Escherichia coli mutants. *J Bacteriol* **145** (2), 1036-1041 (1981).
- 96 Kubori, T., Shimamoto, N., Yamaguchi, S., Namba, K. & Aizawa, S., Morphological pathway of flagellar assembly in Salmonella typhimurium. *J Mol Biol* **226** (2), 433-446 (1992).
- 97 Kubori, T., Yamaguchi, S. & Aizawa, S., Assembly of the switch complex onto the MS ring complex of Salmonella typhimurium does not require any other flagellar proteins. *J Bacteriol* **179** (3), 813-817 (1997).
- 98 Larsen, S. H., Adler, J., Gargus, J. J. & Hogg, R. W., Chemomechanical coupling without ATP: the source of energy for motility and chemotaxis in bacteria. *Proc Natl Acad Sci U S A* **71** (4), 1239-1243 (1974).
- 99 Imae, Y. & Atsumi, T., Na<sup>+</sup>-driven bacterial flagellar motors. *J Bioenerg Biomembr* **21** (6), 705-716 (1989).
- 100 Macnab, R. M., How bacteria assemble flagella. *Annu Rev Microbiol* **57**, 77-100 (2003).
- 101 Boesch, K. C., Silversmith, R. E. & Bourret, R. B., Isolation and characterization of nonchemotactic CheZ mutants of Escherichia coli. *J Bacteriol* **182** (12), 3544-3552 (2000).
- 102 Sanna, M. G. & Simon, M. I., In vivo and in vitro characterization of Escherichia coli protein CheZ gain- and loss-of-function mutants. *J Bacteriol* **178** (21), 6275-6280 (1996).
- 103 Topp, S. & Gallivan, J. P., Guiding bacteria with small molecules and RNA. *J Am Chem Soc* **129** (21), 6807-6811 (2007).
- 104 Vladimirov, N. & Sourjik, V., Chemotaxis: how bacteria use memory. *Biol Chem* **390** (11), 1097-1104 (2009).
- 105 Buja, L. M., Ferrans, V. J. & Maron, B. J., Intracytoplasmic junctions in cardiac muscle cells. *Am J Pathol* **74** (3), 613-647 (1974).
- 106 Simpson, D. G., Decker, M. L., Clark, W. A. & Decker, R. S., Contractile activity and cell-cell contact regulate myofibrillar organization in cultured cardiac myocytes. *J Cell Biol* **123** (2), 323-336 (1993).
- 107 Blair, S. S., Wing vein patterning in Drosophila and the analysis of intercellular signaling. *Annu Rev Cell Dev Biol* **23**, 293-319 (2007).
- 108 Gray, K. M., Intercellular communication and group behavior in bacteria. *Trends Microbiol* **5** (5), 184-188 (1997).
- 109 Kaiser, D. & Losick, R., How and why bacteria talk to each other. *Cell* **73** (5), 873-885 (1993).
- 110 Wirth, R., Muscholl, A. & Wanner, G., The role of pheromones in bacterial interactions. *Trends Microbiol* **4** (3), 96-103 (1996).
- 111 Lin, J. C., Duell, K. & Konopka, J. B., A microdomain formed by the extracellular ends of the transmembrane domains promotes activation of the G protein-coupled alpha-factor

- receptor. *Mol Cell Biol* **24** (5), 2041-2051 (2004).
- 112 Bassler, B. L. & Losick, R., Bacterially speaking. *Cell* **125** (2), 237-246 (2006).
- 113 Miller, M. B. & Bassler, B. L., Quorum sensing in bacteria. *Annu Rev Microbiol* **55**, 165-199 (2001).
- 114 Kleerebezem, M., Quadri, L. E., Kuipers, O. P. & de Vos, W. M., Quorum sensing by peptide pheromones and two-component signal-transduction systems in Gram-positive bacteria. *Mol Microbiol* **24** (5), 895-904 (1997).
- 115 Fuqua, C. & Greenberg, E. P., Listening in on bacteria: acyl-homoserine lactone signalling. *Nat Rev Mol Cell Biol* **3** (9), 685-695 (2002).
- 116 Felkner, I. C. & Wyss, O., A substance produced by competent *Bacillus cereus* 569 cells that affects transformability. *Biochem Biophys Res Commun* **16** (1), 94-99 (1964).
- 117 Tomasz, A., Control of the competent state in *Pneumococcus* by a hormone-like cell product: an example for a new type of regulatory mechanism in bacteria. *Nature* **208** (5006), 155-159 (1965).
- 118 Schauder, S., Shokat, K., Surette, M. G. & Bassler, B. L., The LuxS family of bacterial autoinducers: biosynthesis of a novel quorum-sensing signal molecule. *Mol Microbiol* **41** (2), 463-476 (2001).
- 119 Herzberg, M., Kaye, I. K., Peti, W. & Wood, T. K., YdgG (TqsA) controls biofilm formation in *Escherichia coli* K-12 through autoinducer 2 transport. *J Bacteriol* **188** (2), 587-598 (2006).
- 120 Taga, M. E., Miller, S. T. & Bassler, B. L., Lsr-mediated transport and processing of AI-2 in *Salmonella typhimurium*. *Mol Microbiol* **50** (4), 1411-1427 (2003).
- 121 Xavier, K. B. & Bassler, B. L., Regulation of uptake and processing of the quorum-sensing autoinducer AI-2 in *Escherichia coli*. *J Bacteriol* **187** (1), 238-248 (2005).
- 122 Sperandio, V., Torres, A. G., Giron, J. A. & Kaper, J. B., Quorum sensing is a global regulatory mechanism in enterohemorrhagic *Escherichia coli* O157:H7. *J Bacteriol* **183** (17), 5187-5197 (2001).
- 123 Lazdunski, A. M., Ventre, I. & Sturgis, J. N., Regulatory circuits and communication in Gram-negative bacteria. *Nat Rev Microbiol* **2** (7), 581-592 (2004).
- 124 Wang, L. H., Weng, L. X., Dong, Y. H. & Zhang, L. H., Specificity and enzyme kinetics of the quorum-quenching N-Acyl homoserine lactone lactonase (AHL-lactonase). *J Biol Chem* **279** (14), 13645-13651 (2004).
- 125 Ruby, E. G. & Nealson, K. H., Symbiotic association of *Photobacterium fischeri* with the marine luminous fish *Monocentris japonica*; a model of symbiosis based on bacterial studies. *Biol Bull* **151** (3), 574-586 (1976).
- 126 Weiss, R. & Knight, T. F., Engineered communications for microbial robotics. *Lect Notes in Comp Sci* **2054**, 1-16 (2001).
- 127 Meighen, E. A., Molecular biology of bacterial bioluminescence. *Microbiol Rev* **55** (1), 123-142 (1991).
- 128 Fernandez-Pinas, F. & Wolk, C. P., Expression of luxCD-E in *Anabaena* sp. can replace the use of exogenous aldehyde for in vivo localization of transcription by luxAB. *Gene* **150** (1), 169-174 (1994).
- 129 Fuqua, W. C. & Winans, S. C., A LuxR-LuxI type regulatory system activates *Agrobacterium* Ti plasmid conjugal transfer in the presence of a plant tumor metabolite. *J Bacteriol* **176** (10), 2796-2806 (1994).
- 130 Fuqua, W. C., Winans, S. C. & Greenberg, E. P., Quorum sensing in bacteria: the LuxR-LuxI family of cell density-responsive transcriptional regulators. *J Bacteriol* **176** (2), 269-275 (1994).
- 131 Choi, S. H. & Greenberg, E. P., The C-terminal region of the *Vibrio fischeri* LuxR protein contains an inducer-independent lux gene activating domain. *Proc Natl Acad Sci U S A* **88** (24), 11115-11119 (1991).
- 132 Hanzelka, B. L. & Greenberg, E. P., Evidence that the N-terminal region of the *Vibrio fischeri* LuxR protein constitutes an autoinducer-binding domain. *J Bacteriol* **177** (3), 815-817 (1995).
- 133 Devine, J. H., Shadel, G. S. & Baldwin, T. O., Identification of the operator of the lux regulon from the *Vibrio fischeri* strain ATCC7744. *Proc Natl Acad Sci U S A* **86** (15), 5688-5692 (1989).
- 134 Choi, S. H. & Greenberg, E. P., Genetic dissection of DNA binding and luminescence gene activation by the *Vibrio fischeri* LuxR protein. *J Bacteriol* **174** (12), 4064-4069 (1992).
- 135 Van Houdt, R., Aertsen, A., Moens, P., Vanoirbeek, K. & Michiels, C. W., N-acyl-L-homoserine lactone signal interception by *Escherichia coli*. *FEMS Microbiol Lett*

- 256 (1), 83-89 (2006).
- 136 Chuang, J. S., Rivoire, O. & Leibler, S., Simpson's paradox in a synthetic microbial system. *Science* **323** (5911), 272-275 (2009).
- 137 Davidson, E. H. & Erwin, D. H., Gene regulatory networks and the evolution of animal body plans. *Science* **311** (5762), 796-800 (2006).
- 138 Wolpert, L., *Principles of development*, 3rd ed. (Oxford University Press, Oxford ; New York, 2007).
- 139 Meinhardt, H. & Gierer, A., Pattern formation by local self-activation and lateral inhibition. *Bioessays* **22** (8), 753-760 (2000).
- 140 Maini, P. K., Baker, R. E. & Chuong, C. M., Developmental biology. The Turing model comes of molecular age. *Science* **314** (5804), 1397-1398 (2006).
- 141 Rorth, P., Collective guidance of collective cell migration. *Trends Cell Biol* **17** (12), 575-579 (2007).
- 142 Montell, D. J., The social lives of migrating cells in Drosophila. *Curr Opin Genet Dev* **16** (4), 374-383 (2006).
- 143 Buchholz, F., Ringrose, L., Angrand, P. O., Rossi, F. & Stewart, A. F., Different thermostabilities of FLP and Cre recombinases: implications for applied site-specific recombination. *Nucleic Acids Res* **24** (21), 4256-4262 (1996).
- 144 Sambrook, J., Fritsch, E.F. & Maniatis, T. eds., *Molecular cloning,a laboratory manual* 2nd ed. (Science Press, Beijing, 1993).
- 145 Klumpp, S., Zhang, Z. & Hwa, T., Growth rate-dependent global effects on gene expression in bacteria. *Cell* **139** (7), 1366-1375 (2009).
- 146 Datta, S., Costantino, N. & Court, D. L., A set of recombineering plasmids for gram-negative bacteria. *Gene* **379**, 109-115 (2006).
- 147 Watt, R. M. et al., Visualizing the proteome of Escherichia coli: an efficient and versatile method for labeling chromosomal coding DNA sequences (CDSs) with fluorescent protein genes. *Nucleic Acids Res* **35** (6), e37 (2007).
- 148 Zhang, Y., Buchholz, F., Muylers, J. P. & Stewart, A. F., A new logic for DNA engineering using recombination in Escherichia coli. *Nat Genet* **20** (2), 123-128 (1998).
- 149 Lee, C., Lee, S., Shin, S. G. & Hwang, S., Real-time PCR determination of rRNA gene copy number: absolute and relative quantification assays with Escherichia coli. *Appl Microbiol Biotechnol* **78** (2), 371-376 (2008).
- 150 Berg, Howard C., (Springer, New York, 2004), pp. xi, 133 p., [131] col. plate.
- 151 Slade, K. M., Steele, B. L., Pielak, G. J. & Thompson, N. L., Quantifying green fluorescent protein diffusion in Escherichia coli by using continuous photobleaching with evanescent illumination. *J Phys Chem B* **113** (14), 4837-4845 (2009).
- 152 Shaner, N. C., Steinbach, P. A. & Tsien, R. Y., A guide to choosing fluorescent proteins. *Nat Methods* **2** (12), 905-909 (2005).
- 153 Otsu, N., Threshold Selection Method from Gray-Level Histograms. *Ieee Transactions on Systems Man and Cybernetics* **9** (1), 62-66 (1979).
- 154 Wolfe, A. J. & Berg, H. C., Migration of bacteria in semisolid agar. *Proc Natl Acad Sci U S A* **86** (18), 6973-6977 (1989).
- 155 Kuo, S. C. & Koshland, D. E., Jr., Roles of cheY and cheZ gene products in controlling flagellar rotation in bacterial chemotaxis of Escherichia coli. *J Bacteriol* **169** (3), 1307-1314 (1987).
- 156 Parkinson, J. S. & Houts, S. E., Isolation and behavior of Escherichia coli deletion mutants lacking chemotaxis functions. *J Bacteriol* **151** (1), 106-113 (1982).
- 157 Adler, J., Chemotaxis in bacteria. *Science* **153** (737), 708-716 (1966).
- 158 Girgis, H. S., Liu, Y., Ryu, W. S. & Tavazoie, S., A comprehensive genetic characterization of bacterial motility. *PLoS Genet* **3** (9), 1644-1660 (2007).
- 159 Lutz, R. & Bujard, H., Independent and tight regulation of transcriptional units in Escherichia coli via the LacR/O, the TetR/O and AraC/I1-I2 regulatory elements. *Nucleic Acids Res* **25** (6), 1203-1210 (1997).
- 160 Sekowska, A., Masson, J. B., Celani, A., Danchin, A. & Vergassola, M., Repulsion and metabolic switches in the collective behavior of bacterial colonies. *Biophys J* **97** (3), 688-698 (2009).
- 161 McEvoy, M. M., Bren, A., Eisenbach, M. & Dahlquist, F. W., Identification of the binding interfaces on CheY for two of its targets, the phosphatase CheZ and the flagellar switch protein fliM. *J Mol Biol* **289** (5), 1423-1433 (1999).
- 162 Scharf, B. E., Fahrner, K. A., Turner, L. & Berg, H. C., Control of direction of flagellar rotation in bacterial chemotaxis. *Proc Natl Acad Sci U S A* **95** (1), 201-206 (1998).

- 163 Neidhardt, Frederick C., Ingraham, John L. & Schaechter, Moselio, *Physiology of the bacterial cell : a molecular approach.* (Sinauer Associates, Sunderland, Mass., 1990).
- 164 Maurer, L. M., Yohannes, E., Bondurant, S. S., Radmacher, M. & Slonczewski, J. L., pH regulates genes for flagellar motility, catabolism, and oxidative stress in *Escherichia coli* K-12. *J Bacteriol* **187** (1), 304-319 (2005).
- 165 Khan, S. & Macnab, R. M., Proton chemical potential, proton electrical potential and bacterial motility. *J Mol Biol* **138** (3), 599-614 (1980).
- 166 Yates, E. A. et al., N-acylhomoserine lactones undergo lactonolysis in a pH-, temperature-, and acyl chain length-dependent manner during growth of *Yersinia pseudotuberculosis* and *Pseudomonas aeruginosa*. *Infect Immun* **70** (10), 5635-5646 (2002).
- 167 Horswill, A. R., Stoodley, P., Stewart, P. S. & Parsek, M. R., The effect of the chemical, biological, and physical environment on quorum sensing in structured microbial communities. *Anal Bioanal Chem* **387** (2), 371-380 (2007).
- 168 Byers, J. T., Lucas, C., Salmond, G. P. & Welch, M., Nonenzymatic turnover of an *Erwinia carotovora* quorum-sensing signaling molecule. *J Bacteriol* **184** (4), 1163-1171 (2002).
- 169 Hoistad, M., Chen, K. C., Nicholson, C., Fuxe, K. & Kehr, J., Quantitative dual-probe microdialysis: evaluation of [<sup>3</sup>H]mannitol diffusion in agar and rat striatum. *J Neurochem* **81** (1), 80-93 (2002).
- 170 Foster, P. L., Adaptive mutation: the uses of adversity. *Annu Rev Microbiol* **47**, 467-504 (1993).
- 171 Rosenberg, S. M., Harris, R. S. & Torkelson, J., Molecular handles on adaptive mutation. *Mol Microbiol* **18** (2), 185-189 (1995).
- 172 Cairns, J. & Foster, P. L., Adaptive reversion of a frameshift mutation in *Escherichia coli*. *Genetics* **128** (4), 695-701 (1991).
- 173 Maenhaut-Michel, G. & Shapiro, J. A., The roles of starvation and selective substrates in the emergence of araB-lacZ fusion clones. *EMBO J* **13** (21), 5229-5239 (1994).
- 174 Higgins, N. P., Death and transfiguration among bacteria. *Trends in Biochemical Sciences* **17** (6), 207-211 (1992).
- 175 Redfield, R. J., Evolution of bacterial transformation: is sex with dead cells ever better than no sex at all? *Genetics* **119** (1), 213-221 (1988).
- 176 Elliott, S., Joss, G. H., Spudich, A. & Williams, K. L., Patterns in *Dictyostelium discoideum*: the role of myosin II in the transition from the unicellular to the multicellular phase. *J Cell Sci* **104** (Pt 2), 457-466 (1993).
- 177 Rieddorf, J., Siegert, F., Dharmawardhane, S., Firtel, R. A. & Weijer, C. J., Analysis of cell movement and signalling during ring formation in an activated G alpha $\delta$  mutant of *Dictyostelium discoideum* that is defective in prestalk zone formation. *Dev Biol* **181** (1), 79-90 (1997).
- 178 Kang, S. Y., Kim, S. N., Kim, S. H. & Jeon, S. H., Temporal and spatial expression of homeotic genes is important for segment-specific neuroblast 6-4 lineage formation in *Drosophila*. *Mol Cells* **21** (3), 436-442 (2006).
- 179 Knipple, D. C., Seifert, E., Rosenberg, U. B., Preiss, A. & Jackle, H., Spatial and temporal patterns of Kruppel gene expression in early *Drosophila* embryos. *Nature* **317** (6032), 40-44 (1985).
- 180 Nagahara, H., Ma, Y., Takenaka, Y., Kageyama, R. & Yoshikawa, K., Spatiotemporal pattern in somitogenesis: a non-Turing scenario with wave propagation. *Phys Rev E Stat Nonlin Soft Matter Phys* **80** (2 Pt 1), 021906 (2009).
- 181 Schlake, T. & Sick, S., Canonical WNT signalling controls hair follicle spacing. *Cell Adh Migr* **1** (3), 149-151 (2007).
- 182 Nagorcka, B. N. & Mooney, J. R., From stripes to spots: prepatterns which can be produced in the skin by a reaction-diffusion system. *IMA J Math Appl Med Biol* **9** (4), 249-267 (1992).
- 183 Kondo, S., Iwashita, M. & Yamaguchi, M., How animals get their skin patterns: fish pigment pattern as a live Turing wave. *Int J Dev Biol* **53** (5-6), 851-856 (2009).
- 184 Nakamasu, A., Takahashi, G., Kanbe, A. & Kondo, S., Interactions between zebrafish pigment cells responsible for the generation of Turing patterns. *Proc Natl Acad Sci U S A* **106** (21), 8429-8434 (2009).
- 185 Galis, F., Why do almost all mammals have seven cervical vertebrae? Developmental constraints, Hox genes, and cancer. *J Exp Zool* **285** (1), 19-26 (1999).
- 186 Gritli-Linde, A., Lewis, P., McMahon, A. P. & Linde, A., The whereabouts of a morphogen: direct evidence for short- and graded long-range activity of hedgehog signaling peptides. *Dev Biol* **236** (2), 364-386 (2001).
- 187 Koyama, E. et al., Polarizing activity, Sonic hedgehog, and tooth development in embryonic

- and postnatal mouse. *Dev Dyn* **206** (1), 59-72 (1996).
- 188 Dequeant, M. L. et al., A complex oscillating network of signaling genes underlies the mouse segmentation clock. *Science* **314** (5805), 1595-1598 (2006).
- 189 Cryns, V. & Yuan, J., Proteases to die for. *Genes Dev* **12** (11), 1551-1570 (1998).
- 190 Boatright, K. M. & Salvesen, G. S., Mechanisms of caspase activation. *Curr Opin Cell Biol* **15** (6), 725-731 (2003).
- 191 Fadeel, B. & Orrenius, S., Apoptosis: a basic biological phenomenon with wide-ranging implications in human disease. *J Intern Med* **258** (6), 479-517 (2005).
- 192 Fujimura, M., Morita-Fujimura, Y., Murakami, K., Kawase, M. & Chan, P. H., Cytosolic redistribution of cytochrome c after transient focal cerebral ischemia in rats. *J Cereb Blood Flow Metab* **18** (11), 1239-1247 (1998).
- 193 Li, P. et al., Cytochrome c and dATP-dependent formation of Apaf-1/caspase-9 complex initiates an apoptotic protease cascade. *Cell* **91** (4), 479-489 (1997).
- 194 Mehta, S. L., Manhas, N. & Raghbir, R., Molecular targets in cerebral ischemia for developing novel therapeutics. *Brain Res Rev* **54** (1), 34-66 (2007).
- 195 Warner, T. D., Relationships between the endothelin and nitric oxide pathways. *Clin Exp Pharmacol Physiol* **26** (3), 247-252 (1999).
- 196 Shi, L. G., Zhang, G. P. & Jin, H. M., Inhibition of microvascular endothelial cell apoptosis by angiopoietin-1 and the involvement of cytochrome C. *Chin Med J (Engl)* **119** (9), 725-730 (2006).
- 197 Zipser, B. D. et al., Microvascular injury and blood-brain barrier leakage in Alzheimer's disease. *Neurobiol Aging* **28** (7), 977-986 (2007).
- 198 Bresgen, N. et al., Oxidative stress in cultured cerebral endothelial cells induces chromosomal aberrations, micronuclei, and apoptosis. *J Neurosci Res* **72** (3), 327-333 (2003).
- 199 Yang, B., Oo, T. N. & Rizzo, V., Lipid rafts mediate H<sub>2</sub>O<sub>2</sub> prosurvival effects in cultured endothelial cells. *FASEB J* **20** (9), 1501-1503 (2006).
- 200 Abe, J.I. & Berk, B.C., Reactive oxygen species as mediators of signal transduction in cardiovascular disease. *Trends Cardiovasc Med* **8**, 59-64 (1998).
- 201 Blanc, A., Pandey, N. R. & Srivastava, A. K., Synchronous activation of ERK 1/2, p38mapk and PKB/Akt signaling by H<sub>2</sub>O<sub>2</sub> in vascular smooth muscle cells: potential involvement in vascular disease (review). *Int J Mol Med* **11** (2), 229-234 (2003).
- 202 Nohl, H., Kozlov, A. V., Gille, L. & Staniek, K., Cell respiration and formation of reactive oxygen species: facts and artefacts. *Biochem Soc Trans* **31** (Pt 6), 1308-1311 (2003).
- 203 Hashimoto, Y. et al., Rapid superoxide production by endothelial cells and their injury upon reperfusion. *J Surg Res* **57** (6), 693-697 (1994).
- 204 Xiao, X. Q., Lee, N. T., Carlier, P. R., Pang, Y. & Han, Y. F., Bis(7)-tacrine, a promising anti-Alzheimer's agent, reduces hydrogen peroxide-induced injury in rat pheochromocytoma cells: comparison with tacrine. *Neurosci Lett* **290** (3), 197-200 (2000).
- 205 Jiang, R. W. et al., Chemistry and biological activities of caffeic acid derivatives from *Salvia miltiorrhiza*. *Curr Med Chem* **12** (2), 237-246 (2005).
- 206 Zhou, L., Zuo, Z. & Chow, M. S., Danshen: an overview of its chemistry, pharmacology, pharmacokinetics, and clinical use. *J Clin Pharmacol* **45** (12), 1345-1359 (2005).
- 207 Watzke, A., O'Malley, S. J., Bergman, R. G. & Ellman, J. A., Reassignment of the configuration of salvianolic acid B and establishment of its identity with lithospermic acid B. *J Nat Prod* **69** (8), 1231-1233 (2006).
- 208 Chen, Y. H., Du, G. H. & Zhang, J. T., Salvianolic acid B protects brain against injuries caused by ischemia-reperfusion in rats. *Acta Pharmacol Sin* **21** (5), 463-466 (2000).
- 209 Du, G. H., Qiu, Y. & Zhang, J. T., Salvianolic acid B protects the memory functions against transient cerebral ischemia in mice. *J Asian Nat Prod Res* **2** (2), 145-152 (2000).
- 210 Tang, M. K., Ren, D. C., Zhang, J. T. & Du, G. H., Effect of salvianolic acids from *Radix Salviae miltorrhizae* on regional cerebral blood flow and platelet aggregation in rats. *Phytomedicine* **9** (5), 405-409 (2002).
- 211 Tang, M., Feng, W., Zhang, Y., Zhong, J. & Zhang, J., Salvianolic acid B improves motor function after cerebral ischemia in rats. *Behav Pharmacol* **17** (5-6), 493-498 (2006).
- 212 Bederson, J. B. et al., Rat middle cerebral artery occlusion: evaluation of the model and development of a neurologic examination. *Stroke* **17** (3), 472-476 (1986).
- 213 Li, X. & Darzynkiewicz, Z., Labelling DNA strand breaks with BrdUTP. Detection of apoptosis and cell proliferation. *Cell Prolif* **28** (11), 571-579 (1995).
- 214 Li, X. & Darzynkiewicz, Z., Cleavage of Poly(ADP-ribose) polymerase measured in situ in individual cells: relationship to DNA fragmentation and cell cycle position during apoptosis.

- 215      *Exp Cell Res* **255** (1), 125-132 (2000).  
Slee, E. A. et al., Benzyloxycarbonyl-Val-Ala-Asp (OMe) fluoromethylketone (Z-VAD.FMK) inhibits apoptosis by blocking the processing of CPP32. *Biochem J* **315** ( Pt 1), 21-24 (1996).
- 216      Lee, J. S., Kim, S. Y., Kwon, C. H. & Kim, Y. K., EGFR-dependent ERK activation triggers hydrogen peroxide-induced apoptosis in OK renal epithelial cells. *Arch Toxicol* **80** (6), 337-346 (2006).
- 217      Zhuang, S., Yan, Y., Daubert, R. A., Han, J. & Schnellmann, R. G., ERK promotes hydrogen peroxide-induced apoptosis through caspase-3 activation and inhibition of Akt in renal epithelial cells. *Am J Physiol Renal Physiol* **292** (1), F440-447 (2007).
- 218      Rommel, C. et al., Differentiation stage-specific inhibition of the Raf-MEK-ERK pathway by Akt. *Science* **286** (5445), 1738-1741 (1999).
- 219      Zimmermann, S. & Moellering, K., Phosphorylation and regulation of Raf by Akt (protein kinase B). *Science* **286** (5445), 1741-1744 (1999).
- 220      Lackey, K. et al., The discovery of potent cRaf1 kinase inhibitors. *Bioorg Med Chem Lett* **10** (3), 223-226 (2000).
- 221      Zhang, Y., Park, T. S. & Gidday, J. M., Hypoxic preconditioning protects human brain endothelium from ischemic apoptosis by Akt-dependent survivin activation. *Am J Physiol Heart Circ Physiol* **292** (6), H2573-2581 (2007).
- 222      Yang, J. Y., Michod, D., Walicki, J. & Widmann, C., Surviving the kiss of death. *Biochem Pharmacol* **68** (6), 1027-1031 (2004).
- 223      Chen, Y. L. et al., Salviaolic acid B attenuates cyclooxygenase-2 expression in vitro in LPS-treated human aortic smooth muscle cells and in vivo in the apolipoprotein-E-deficient mouse aorta. *J Cell Biochem* **98** (3), 618-631 (2006).
- 224      Lin, S. J. et al., Salviaolic acid B attenuates MMP-2 and MMP-9 expression in vivo in apolipoprotein-E-deficient mouse aorta and in vitro in LPS-treated human aortic smooth muscle cells. *J Cell Biochem* **100** (2), 372-384 (2007).
- 225      Cheng, Y., Ping, J., Liu, C., Tan, Y. Z. & Chen, G. F., Study on effects of extracts from *Salvia Miltiorrhiza* and *Curcuma Longa* in inhibiting phosphorylated extracellular signal regulated kinase expression in rat's hepatic stellate cells. *Chin J Integr Med* **12** (3), 207-211 (2006).
- 226      Ding, M., Ye, T. X., Zhao, G. R., Yuan, Y. J. & Guo, Z. X., Aqueous extract of *Salvia miltiorrhiza* attenuates increased endothelial permeability induced by tumor necrosis factor-alpha. *Int Immunopharmacol* **5** (11), 1641-1651 (2005).
- 227      Stein, R. C. & Waterfield, M. D., PI3-kinase inhibition: a target for drug development? *Mol Med Today* **6** (9), 347-357 (2000).
- 228      Kontos, C. D., Cha, E. H., York, J. D. & Peters, K. G., The endothelial receptor tyrosine kinase Tie1 activates phosphatidylinositol 3-kinase and Akt to inhibit apoptosis. *Mol Cell Biol* **22** (6), 1704-1713 (2002).
- 229      Ohashi, H. et al., Phosphatidylinositol 3-kinase/Akt regulates angiotensin II-induced inhibition of apoptosis in microvascular endothelial cells by governing survivin expression and suppression of caspase-3 activity. *Circ Res* **94** (6), 785-793 (2004).
- 230      Sinha, D., Bannerjee, S., Schwartz, J. H., Lieberthal, W. & Levine, J. S., Inhibition of ligand-independent ERK1/2 activity in kidney proximal tubular cells deprived of soluble survival factors up-regulates Akt and prevents apoptosis. *J Biol Chem* **279** (12), 10962-10972 (2004).
- 231      Schmidt, E. K., Fischelson, S. & Feller, S. M., PI3 kinase is important for Ras, MEK and Erk activation of Epo-stimulated human erythroid progenitors. *BMC Biol* **2**, 7 (2004).
- 232      Datta, S. R. et al., Akt phosphorylation of BAD couples survival signals to the cell-intrinsic death machinery. *Cell* **91** (2), 231-241 (1997).
- 233      Cardone, M. H. et al., Regulation of cell death protease caspase-9 by phosphorylation. *Science* **282** (5392), 1318-1321 (1998).
- 234      Motoyama, S. et al., Hydrogen peroxide-dependent declines in Bcl-2 induces apoptosis in hypoxic liver. *J Surg Res* **110** (1), 211-216 (2003).
- 235      Matsushita, H. et al., Hypoxia-induced endothelial apoptosis through nuclear factor-kappaB (NF-kappaB)-mediated bcl-2 suppression: in vivo evidence of the importance of NF-kappaB in endothelial cell regulation. *Circ Res* **86** (9), 974-981 (2000).
- 236      Shimizu, S., Narita, M. & Tsujimoto, Y., Bcl-2 family proteins regulate the release of apoptotic cytochrome c by the mitochondrial channel VDAC. *Nature* **399** (6735), 483-487 (1999).
- 237      Liu, D. et al., Dehydroepiandrosterone protects vascular endothelial cells against apoptosis

- through a Galphai protein-dependent activation of phosphatidylinositol 3-kinase/Akt and regulation of antiapoptotic Bcl-2 expression. *Endocrinology* **148** (7), 3068-3076 (2007).
- 238 Wilson, B. E., Mochon, E. & Boxer, L. M., Induction of bcl-2 expression by phosphorylated CREB proteins during B-cell activation and rescue from apoptosis. *Mol Cell Biol* **16** (10), 5546-5556 (1996).
- 239 Riccio, A., Ahn, S., Davenport, C. M., Blendy, J. A. & Ginty, D. D., Mediation by a CREB family transcription factor of NGF-dependent survival of sympathetic neurons. *Science* **286** (5448), 2358-2361 (1999).
- 240 Mayr, B. & Montminy, M., Transcriptional regulation by the phosphorylation-dependent factor CREB. *Nat Rev Mol Cell Biol* **2** (8), 599-609 (2001).
- 241 Kumar, P., Miller, A. I. & Polverini, P. J., p38 MAPK mediates gamma-irradiation-induced endothelial cell apoptosis, and vascular endothelial growth factor protects endothelial cells through the phosphoinositide 3-kinase-Akt-Bcl-2 pathway. *J Biol Chem* **279** (41), 43352-43360 (2004).
- 242 Agarwal, S., Gamper, H. B. & Kmiec, E. B., Nucleotide replacement at two sites can be directed by modified single-stranded oligonucleotides in vitro and in vivo. *Biomol Eng* **20** (1), 7-20 (2003).
- 243 Liu, L., Parekh-Olmedo, H. & Kmiec, E. B., The development and regulation of gene repair. *Nat Rev Genet* **4** (9), 679-689 (2003).
- 244 Alexeev, V., Igoucheva, O. & Yoon, K., Simultaneous targeted alteration of the tyrosinase and c-kit genes by single-stranded oligonucleotides. *Gene Ther* **9** (24), 1667-1675 (2002).
- 245 Thorpe, P., Stevenson, B. J. & Porteous, D. J., Optimising gene repair strategies in cell culture. *Gene Ther* **9** (11), 700-702 (2002).
- 246 Olsen, P. A., McKeen, C. & Krauss, S., Branched oligonucleotides induce in vivo gene conversion of a mutated EGFP reporter. *Gene Ther* **10** (21), 1830-1840 (2003).
- 247 Igoucheva, O., Alexeev, V., Pryce, M. & Yoon, K., Transcription affects formation and processing of intermediates in oligonucleotide-mediated gene alteration. *Nucleic Acids Res* **31** (10), 2659-2670 (2003).
- 248 Parekh-Olmedo, H., Ferrara, L., Brachman, E. & Kmiec, E. B., Gene therapy progress and prospects: targeted gene repair. *Gene Ther* **12** (8), 639-646 (2005).
- 249 Li, X. T. et al., Identification of factors influencing strand bias in oligonucleotide-mediated recombination in Escherichia coli. *Nucleic Acids Res* **31** (22), 6674-6687 (2003).
- 250 Dekker, M., Brouwers, C. & te Riele, H., Targeted gene modification in mismatch-repair-deficient embryonic stem cells by single-stranded DNA oligonucleotides. *Nucleic Acids Res* **31** (6), e27 (2003).
- 251 Drury, M. D., Skogen, M. J. & Kmiec, E. B., A tolerance of DNA heterology in the mammalian targeted gene repair reaction. *Oligonucleotides* **15** (3), 155-171 (2005).
- 252 Igoucheva, O., Alexeev, V. & Yoon, K., Oligonucleotide-directed mutagenesis and targeted gene correction: a mechanistic point of view. *Curr Mol Med* **4** (5), 445-463 (2004).
- 253 Igoucheva, O., Alexeev, V. & Yoon, K., Targeted gene correction by small single-stranded oligonucleotides in mammalian cells. *Gene Ther* **8** (5), 391-399 (2001).
- 254 Radecke, F., Radecke, S. & Schwarz, K., Unmodified oligodeoxynucleotides require single-strandedness to induce targeted repair of a chromosomal EGFP gene. *J Gene Med* **6** (11), 1257-1271 (2004).
- 255 Olsen, P. A., Randol, M. & Krauss, S., Implications of cell cycle progression on functional sequence correction by short single-stranded DNA oligonucleotides. *Gene Ther* **12** (6), 546-551 (2005).
- 256 Brachman, E. E. & Kmiec, E. B., DNA replication and transcription direct a DNA strand bias in the process of targeted gene repair in mammalian cells. *J Cell Sci* **117** (Pt 17), 3867-3874 (2004).
- 257 Mellon, I., Rajpal, D. K., Koi, M., Boland, C. R. & Champe, G. N., Transcription-coupled repair deficiency and mutations in human mismatch repair genes. *Science* **272** (5261), 557-560 (1996).
- 258 Ferrara, L. & Kmiec, E. B., Camptothecin enhances the frequency of oligonucleotide-directed gene repair in mammalian cells by inducing DNA damage and activating homologous recombination. *Nucleic Acids Res* **32** (17), 5239-5248 (2004).
- 259 Brachman, E. E. & Kmiec, E. B., Gene repair in mammalian cells is stimulated by the elongation of S phase and transient stalling of replication forks. *DNA Repair (Amst)* **4** (4), 445-457 (2005).
- 260 Wang, Z., Zhou, Z. J., Liu, D. P. & Huang, J. D., Single-stranded oligonucleotide-mediated gene repair in mammalian cells has a mechanism distinct from homologous recombination

- repair. *Biochem Biophys Res Commun* **350** (3), 568-573 (2006).
- 261 Olsen, P. A., Solhaug, A., Booth, J. A., Gelazauskaite, M. & Krauss, S., Cellular responses to targeted genomic sequence modification using single-stranded oligonucleotides and zinc-finger nucleases. *DNA Repair (Amst)* (2008).
- 262 Igoucheva, O., Alexeev, V. & Yoon, K., Differential cellular responses to exogenous DNA in mammalian cells and its effect on oligonucleotide-directed gene modification. *Gene Ther* **13** (3), 266-275 (2006).
- 263 Olsen, P. A., Randol, M., Luna, L., Brown, T. & Krauss, S., Genomic sequence correction by single-stranded DNA oligonucleotides: role of DNA synthesis and chemical modifications of the oligonucleotide ends. *J Gene Med* **7** (12), 1534-1544 (2005).
- 264 Igoucheva, O., Alexeev, V. & Yoon, K., Mechanism of gene repair open for discussion. *Oligonucleotides* **14** (4), 311-321 (2004).
- 265 Kaplan, D. L. & O'Donnell, M., Twin DNA pumps of a hexameric helicase provide power to simultaneously melt two duplexes. *Mol Cell* **15** (3), 453-465 (2004).
- 266 Kaina, B., Ziouta, A., Ochs, K. & Coquerelle, T., Chromosomal instability, reproductive cell death and apoptosis induced by O6-methylguanine in Mex-, Mex+ and methylation-tolerant mismatch repair compromised cells: facts and models. *Mutat Res* **381** (2), 227-241 (1997).
- 267 Stojic, L. et al., Mismatch repair-dependent G2 checkpoint induced by low doses of SN1 type methylating agents requires the ATR kinase. *Genes Dev* **18** (11), 1331-1344 (2004).
- 268 Palombo, F. et al., GTBP, a 160-kilodalton protein essential for mismatch-binding activity in human cells. *Science* **268** (5219), 1912-1914 (1995).
- 269 Genschel, J., Littman, S. J., Drummond, J. T. & Modrich, P., Isolation of MutSbeta from human cells and comparison of the mismatch repair specificities of MutSbeta and MutSalpha. *J Biol Chem* **273** (31), 19895-19901 (1998).
- 270 Kolodner, R. D. & Marsischky, G. T., Eukaryotic DNA mismatch repair. *Curr Opin Genet Dev* **9** (1), 89-96 (1999).
- 271 Fishel, R., Mismatch repair, molecular switches, and signal transduction. *Genes Dev* **12** (14), 2096-2101 (1998).
- 272 Brummelkamp, T. R., Bernards, R. & Agami, R., A system for stable expression of short interfering RNAs in mammalian cells. *Science* **296** (5567), 550-553 (2002).
- 273 Wang, Y. & Qin, J., MSH2 and ATR form a signaling module and regulate two branches of the damage response to DNA methylation. *Proc Natl Acad Sci U S A* **100** (26), 15387-15392 (2003).
- 274 Zhou, B. B. & Elledge, S. J., The DNA damage response: putting checkpoints in perspective. *Nature* **408** (6811), 433-439 (2000).
- 275 Bartek, J. & Lukas, J., Chk1 and Chk2 kinases in checkpoint control and cancer. *Cancer Cell* **3** (5), 421-429 (2003).
- 276 Lin, D. P. et al., An Msh2 point mutation uncouples DNA mismatch repair and apoptosis. *Cancer Res* **64** (2), 517-522 (2004).
- 277 Wu, X. S. et al., Increased efficiency of oligonucleotide-mediated gene repair through slowing replication fork progression. *Proc Natl Acad Sci U S A* **102** (7), 2508-2513 (2005).
- 278 Cejka, P. et al., Methylation-induced G(2)/M arrest requires a full complement of the mismatch repair protein hMLH1. *EMBO J* **22** (9), 2245-2254 (2003).
- 279 Brieger, A., Trojan, J., Raedle, J., Plotz, G. & Zeuzem, S., Transient mismatch repair gene transfection for functional analysis of genetic hMLH1 and hMSH2 variants. *Gut* **51** (5), 677-684 (2002).
- 280 Ferrara, L. & Kmiec, E. B., Targeted gene repair activates Chk1 and Chk2 and stalls replication in corrected cells. *DNA Repair (Amst)* **5** (4), 422-431 (2006).
- 281 Plesca, D., Mazumder, S. & Almasan, A., DNA damage response and apoptosis. *Methods Enzymol* **446**, 107-122 (2008).
- 282 Ferrara, L., Engstrom, J. U., Schwartz, T., Parekh-Olmedo, H. & Kmiec, E. B., Recovery of cell cycle delay following targeted gene repair by oligonucleotides. *DNA Repair (Amst)* **6** (10), 1529-1535 (2007).
- 283 Yan, T., Berry, S. E., Desai, A. B. & Kinsella, T. J., DNA mismatch repair (MMR) mediates 6-thioguanine genotoxicity by introducing single-strand breaks to signal a G2-M arrest in MMR-proficient RKO cells. *Clin Cancer Res* **9** (6), 2327-2334 (2003).
- 284 Fedier, A., Poyet, C., Perucchini, D., Boulikas, T. & Fink, D., MLH1-deficient tumor cells are resistant to lipoplatin, but retain sensitivity to lipoxal. *Anticancer Drugs* **17** (3), 315-323 (2006).
- 285 Radecke, S., Radecke, F., Peter, I. & Schwarz, K., Physical incorporation of a single-stranded oligodeoxynucleotide during targeted repair of a human chromosomal locus. *J Gene Med* **8**

- 286 (2), 217-228 (2006).  
Clark, A. B. & Kunkel, T. A., Cadmium inhibits the functions of eukaryotic MutS complexes.  
*J Biol Chem* **279** (52), 53903-53906 (2004).
- 287 Yin, W. X. et al., Targeted correction of a chromosomal point mutation by modified single-stranded oligonucleotides in a GFP recovery system. *Biochem Biophys Res Commun* **334** (4), 1032-1041 (2005).

## Publications

- 1 **Liu C**, Fu X, Chau CKL, Li S, Xiang L, Zheng H, Zhang F, Chen G, Tang L, Lenz P, Cui X, Huang W, Hwa T, Huang JD. Autonomous formation of sequential periodic stripes from density-dependent motility. *Science*. (Under Revision)
- 2 **Liu C**, Wang Z, Huen MS, Lu LY, Liu DP, Huang JD. Cell death caused by single-stranded oligodeoxynucleotide-mediated targeted genomic sequence modification. *Oligonucleotides*. 2009, 19(3): 281-6.
- 3 **Liu C**, Xie LX, Li M, Durairajan SS, Goto S, Huang JD. Salvianolic acid B inhibits hydrogen peroxide-induced endothelial cell apoptosis through regulating PI3K/Akt signaling. *PLoS One*. 2007, 2(12): e1321.
- 4 **Liu C**, Yu B, Fu X, Huang JD. A synthetic magnetic bacteria. (Manuscript in preparation)
- 5 Xie LX, Durairajan SS, Lu JH, **Liu C**, Kum WF, Wang Y, Koo I, Wu WK, Han D, Lao F, Huang JD, Li M. The effect of salvianolic acid B combined with laminar shear stress on TNF-alpha-stimulated adhesion molecule expression in human aortic endothelial cells. *Clin Hemorheol Microcirc*. 2010, 44(4): 245-58.
- 6 Durairajan SS, Yuan Q, Xie L, Chan WS, Kum WF, Koo I, **Liu C**, Song Y, Huang JD, Klein WL, Li M. Salvianolic acid B inhibits Abeta fibril formation and disaggregates preformed fibrils and protects against Abeta-induced cytotoxicity. *Neurochem Int*. 2008, 52(4-5): 741-5